UNIVERSITY OF CALIFORNIA SAN DIEGO

Molecular Gas and Star Formation in Nearby Galaxy Centers

A dissertation submitted in partial satisfaction of the
requirements for the degree Doctor of Philosophy

in

Physics

by

Yu-Hsuan Teng

Committee in charge:

Professor Karin M. Sandstrom, Chair
Professor Alison L. Coil
Professor James M. D. Day
Professor Raphael M. Flauger
Professor Shelley A. Wright

2024

The Dissertation of Yu-Hsuan Teng is approved, and it is acceptable in quality and form for publication on microfilm and electronically.

University of California San Diego

2024

DEDICATION

To Herman Dong, and to my parents.

EPIGRAPH

It is the stars, The stars above us, govern our conditions.

—William Shakespeare, “King Lear”

TABLE OF CONTENTS

Dissertation Approval Page iii

Dedication iv

Epigraph v

Table of Contents vi

List of Figures viii

List of Tables xii

Acknowledgements xiii

Vita xvi

Abstract of the Dissertation xx

Chapter 1 Introduction 1
- 1.1 Overview and Motivation 1
- 1.2 Star Formation in a Galactic Context 2
- 1.3 Tracing Molecular Gas in Galaxies 3
  - 1.3.1 Challenge of ^{12}CO Observations 3
  - 1.3.2 CO Isotopologues 4
  - 1.3.3 Multi-line Radiative Transfer Modeling 5
  - 1.3.4 The CO-to-H_2 Conversion Factor 7
- 1.4 Dissertation Organization 9

Chapter 2 Molecular Gas Properties and CO-to-H_2 Conversion Factors in the Central Kiloparsec of NGC 3351 10
- Abstract 10
- 2.1 Introduction 11
- 2.2 Observations and Data Reduction 15
  - 2.2.1 ALMA Observations 17
  - 2.2.2 Calibration and Imaging 18
  - 2.2.3 Product Creation and Error Estimation 19
- 2.3 Results 20
- 2.4 Multi-line Modeling 26
  - 2.4.1 Modeling Setup 26
  - 2.4.2 One-Component Models 30
  - 2.4.3 Two-Component Models 37
  - 2.4.4 Marginalized 1D Likelihoods 42
- 2.5 CO-to-H_2 Conversion Factor 44
  - 2.5.1 α_{CO} from the Modeling Results 46

2.5.2 α_{CO} in the Inflow Arms 49
2.5.3 Comparison with Other CO Isotopologue Transitions 55
2.6 Discussion 56
2.7 Conclusion 60
2.8 Acknowledgements 62

Chapter 3 The Physical Drivers and Observational Tracers of α_{CO} Variations in Nearby Barred Galaxy Centers 65
Abstract 65
3.1 Introduction 66
3.2 Observations and Data 70
3.3 Results 73
3.4 Multi-line Bayesian Modeling 83
3.4.1 Modeling Setup 83
3.4.2 Molecular Gas Physical Conditions 86
3.4.3 CO-to-H_2 Conversion Factors 93
3.5 Discussion 96
3.5.1 α_{CO} Distribution and Environmental Dependence 96
3.5.2 Comparison to α_{CO} Measurements in Literature 102
3.5.3 Observational Tracers for α_{CO} Variations 105
3.5.4 Comparison with Existing α_{CO} Prescriptions 111
3.5.5 Multi-line Constraints in the Modeling 116
3.6 Conclusions 119
3.7 Acknowledgements 122
Appendices 125

Chapter 4 Star Formation Efficiency in Nearby Galaxies Revealed with a New α_{CO} Prescription 135
Abstract 135
4.1 Introduction 136
4.2 Data and Measurements 139
4.2.1 PHANGS Datasets 139
4.2.2 Dust-based α_{CO} Measurements 145
4.3 Results 146
4.3.1 A Velocity Dispersion-based α_{CO} Prescription 146
4.3.2 Comparison to Previous Literature 149
4.3.3 Star Formation Efficiency in Galaxy Centers 152
4.3.4 Systematic Impact on Star Formation Efficiency 155
4.4 Discussion 156
4.5 Conclusions 159
4.6 Acknowledgments 160

Chapter 5 Conclusion 163
5.1 Summary 163
5.2 Future Directions 164

LIST OF FIGURES

Figure 2.1. Integrated intensity maps of several CO isotopologues and rotational transitions (in units of K km s^{-1}). 20

Figure 2.2. (a) Intensity-weighted velocity (moment 1) and (b) effective line width of CO 2–1, both in units of km s^{-1}. (c) Definition of the center, ring, and arm regions. 21

Figure 2.3. Line ratio maps. A 3σ mask in both relevant lines is applied to each panel, except for the $C^{18}O$ lines where a 1σ cutoff is applied. 22

Figure 2.4. Shifted and stacked spectra over the center region, overlaid with the best-fit Gaussian profiles. All six lines show a single-peaked spectrum that can be well-described by a Gaussian function. 23

Figure 2.5. Marginalized 1D and 2D likelihood distributions of a bright pixel at $(\mathrm{R.A.}, \mathrm{Decl.}) = (10^{\mathrm{h}}43^{\mathrm{m}}57\overset{\mathrm{s}}{.}9, 11^{\circ}42'19\overset{''}{.}5)$ in the northern contact point. . 31

Figure 2.6. Marginalized 1D and 2D likelihood distributions of a faint pixel at $(\mathrm{R.A.}, \mathrm{Decl.}) = (10^{\mathrm{h}}43^{\mathrm{h}}57\overset{\mathrm{s}}{.}8, 11^{\circ}42'15\overset{''}{.}5)$ in the gap region between the ring and the nucleus. See the caption of Figure 2.5 for more information. 32

Figure 2.7. Best-fit (i.e. highest likelihood) constraints from the six observed line fluxes at the same pixel as in (a) Figure 2.5 and (b) Figure 2.6. 33

Figure 2.8. Maps of the 1DMax physical conditions derived from the one-component model. 34

Figure 2.9. Maps of the 1DMax physical conditions derived from the two-component model. The top row shows the denser component having higher $n_{\mathrm{H_2}}$ and the bottom row shows the more diffuse gas phase. 39

Figure 2.10. α_{CO} variations determined by the one-component modeling results. . . . 45

Figure 2.11. α_{CO} variations determined by the two-component modeling results. . . . 46

Figure 2.12. Shifted and averaged spectra over the inflow arms, overlaid with the best-fit Gaussian profiles. 49

Figure 2.13. Marginalized 1D and 2D likelihood distributions of the stacked spectra from inflow arms. See the caption of Figure 2.5 for more information. Note that some of the parameters are less-constrained in these faint regions and thus pushing the solutions to the boundaries of the grid. . . 50

Figure 2.14. Constraints on the T_k–n_{H_2} slice where the best-fit parameter (red box) lies assuming a 10% flux uncertainty. See the caption of Figure 2.7 for more information. 51

Figure 2.15. Optical depth (τ) map of CO 1–0 determined from the one-component 1DMax physical conditions. 51

Figure 2.16. Marginalized 1D likelihoods of the ^{13}CO and C^{18}O 1–0 intensities in the (a) center and (b) arms regions. 55

Figure 2.17. Relation between α_CO and (a) T_k or (b) $\tau_{\mathrm{CO}(1-0)}$. The contours show density of points from 1000 likelihood-weighted random draws from the one-component model grids for all pixels in each region. 57

Figure 3.1. Integrated intensity maps of NGC 4321 (in units of K km s^{-1}). The white areas lie outside the field of view of ALMA observations, while the gray areas show the pixels with $< 3\sigma$ detection. 73

Figure 3.2. Same as Figure 3.1, but for NGC 3627. The matched beam size of 2.0″ and a scale bar of 1 kpc are shown in panel (c). The central nucleus with a size of ~300 pc is securely detected in all six lines, while the inner spiral arms are not bright enough to be detected in C^{18}O. 74

Figure 3.3. Definition of the nucleus, inner arms, and outer arms regions based on the galactocentric radius, which will be used for regional statistics and analysis. The black contours represent the CO 2–1 integrated intensity at 50, 100, 200, 300, 500, 700 (and 900 for NGC 3627) K km s^{-1}. 75

Figure 3.4. Line ratio maps of NGC 4321. Any region with < 70% flux recovered rate or $< 3\sigma$ detection in either relevant line is masked out in each panel. 76

Figure 3.5. Line ratio maps of NGC 3627. Contour levels represent the CO 2–1 integrated intensity at $I_{\mathrm{CO}(2-1)} = 50, 100, 200, 300, 500, 700, 900$ K km s^{-1}. See the caption of Figure 3.4 for more information. 77

Figure 3.6. Shifted and averaged spectra over the whole kpc regions of NGC 4321 (top row) and NGC 3627 (bottom row), using the moment 1 of CO 2–1 as the fiducial velocity. The intensity of CO 2–1 is scaled down by a factor of 15 (60) in the middle (right) column. 78

Figure 3.7. Best-fit (i.e. lowest χ^2) constraints from the six observed line fluxes at (a) the central pixel and (b) a pixel in the northern, inner arm of NGC 4321. Contours show the ranges of observed line intensities $\pm 1\sigma$ uncertainties, including the measurement and calibration uncertainties. 86

Figure 3.8. Marginalized 1D and 2D probability distributions of the central pixel of NGC 4321. In the panels of 1D PDFs (on the diagonal), the dashed lines represent the 50th percentile (i.e., median) values of the cumulative 1D PDFs, and the dotted lines label the best-fit solution as in Figure 3.7(a). 87

Figure 3.9. Maps of the 1DMax physical conditions derived from the modeling for NGC 4321. Panel (a) shows $\log(N_{\rm CO})$ normalized to a fiducial line width of 15 km s^{-1} over the whole region. 88

Figure 3.10. Same as Figure 3.9 but for NGC 3627. 89

Figure 3.11. Spatial variation of $\alpha_{\rm CO}$ in NGC 4321. (a) 1DMax $\log(\alpha_{\rm CO})$ map in units of $M_\odot$ (K km s^{-1} $pc^2)^{-1}$; the contours represent the moment 0 of CO 2–1. (b) Relation between the modeled $\alpha_{\rm CO}$ and galactocentric radius. 92

Figure 3.12. Spatial variation of $\alpha_{\rm CO}$ in NGC 3627. See the caption of Figure 3.11 for more information. The derived $\alpha_{\rm CO}$ values are generally lower than NGC 4321 and substantially lower than the Galactic disk average. 93

Figure 3.13. Medians of the modeled (a) $\alpha_{\rm CO}$ in units of $M_\odot$ (K km s^{-1} $pc^2)^{-1}$ and (b) line center $\tau_{\rm CO(2-1)}$ within ~100 pc galactocentric radii bins in the centers of NGC 3351 (red), NGC 3627 (blue), and NGC 4321 (green). Shaded areas span the 25th and 75th percentile ranges. 96

Figure 3.14. Modeled $\alpha_{\rm CO}$ and $\tau_{\rm CO(2-1)}$, color-coded by (a) three galaxies and (b) 2D-binned medians of the observed CO/^{13}CO 2–1 ratios. 97

Figure 3.15. Relation of the modeled $\log(\alpha_{\rm CO})$ with (a) $\log(T_{\rm k})$ and (b) $\log(\sqrt{n_{\rm H_2}}/T_{\rm k})$ for NGC 3351 (red), NGC 3627 (blue), and NGC 4321 (green). 97

Figure 3.16. Ratio of the modeled and fitting-predicted $\alpha_{\rm CO}$ (by Equation 3.4) versus the CO optical depth, colorcoded by the modeled gas temperature. The dashed line indicates perfect agreement between the modeled and predicted $\alpha_{\rm CO}$. 102

Figure 3.17. Relation of the modeled $\log(\alpha_{\rm CO})$ with the observed (a) CO/^{13}CO 2–1 line ratio and (b) CO 2–1 effective line width in optically thick regions with $\tau_{\rm CO(2-1)} > 5$. The dashed lines represent the best-fit power law relations (Equations 3.5 and 3.6). 105

Figure 3.18. Galactocentric radial profiles of the CO 2–1 (a) effective line widths with a $\sqrt{\cos(i)}$ inclination correction and (b) spectral peak intensities for NGC 3351 (red), NGC 3627 (blue), and NGC 4321 (green). 108

Figure 3.19. $\alpha_{\rm CO}$ relations with the observed (a) CO 2–1/1–0 ratio, (b) peak temperature of CO 1–0, and (c) CO 1–0 integrated intensity, comparing our observations (colored lines as before) with the simulations. 113

Figure 3.20. Median solutions of $T_{\rm k}$ (first row), $n_{\rm H_2}$ (middle row), and $N_{\rm CO}/\Delta v$ (bottom row) determined by multi-line modeling with different sets of emission lines in the central kpc regions of NGC 3351 (red), NGC 3627 (blue), and NGC 4321 (green). 117

Figure 4.1. Column (a): Dust-based $\alpha_{\rm CO}$ measurements show a strong anti-correlation with the intensity-weighted average of 150-pc scale molecular gas velocity dispersion (top), consistent with the result from T23 on barred galaxy centers 147

Figure 4.2. (a) Comparison of the derived $\alpha_{\rm CO}$ using our Δv-based prescription (Equation 4.2) and the Z' plus $\Sigma_{\rm star}$-based prescription (Equation 4.3; B13), applied to 65 galaxies. 148

Figure 4.3. The molecular Kennicutt-Schmidt (mKS) relation across 65 PHANGS galaxies, where the $\alpha_{\rm CO}$ used to derive $\Sigma_{\rm mol}$ is based on (a) Equation 4.2 or (b) the MW value. 153

Figure 4.4. Molecular gas velocity dispersion and the derived depletion time of PHANGS galaxies using four different $\alpha_{\rm CO}$ prescriptions. The upper/lower panels show the centers/disks regions. 154

LIST OF TABLES

Table 2.1. ALMA Observations 16

Table 2.2. Regional Line Ratios in NGC 3351. 24

Table 2.3. Model Grid Parameters 27

Table 2.4. 1DMax Solutions from One-Component Modeling 33

Table 2.5. 1DMax Solutions from Two-Component Modeling 38

Table 3.1. Source Information 70

Table 3.2. Regional Line Ratios and CO Line Width in NGC 4321. 79

Table 3.3. Regional Line Ratios and CO Line Width in NGC 3627. 80

Table 3.4. RADEX Input Parameters 82

Table 3.5. Regional Averages and Standard Deviations of the 1D PDF Solutions . . 90

Table 4.1. Galaxy Sample and Properties in the Central 1.5 kpc Regions 140

ACKNOWLEDGEMENTS

I would like to express my deepest gratitude to my advisor, Karin Sandstrom, without whom this dissertation would not have been possible. Karin has provided an ideal mix of guidance and freedom for me to develop my research. She always keeps me motivated, respects my work style, and makes herself available whenever I need help. Her thoughtful advice and ways to address science questions taught me a lot, and I appreciate all the connections and resources she has brought to me. I am fortunate to have such an amazing advisor guiding and supporting me throughout these five years.

I would also like to acknowledge Alison Coil, James Day, Raphael Flauger, and Shelley Wright for serving on my doctoral committee and providing feedback that improves the dissertation. Additionally, I am thankful for Alison's support during my second year, when I was a bit frustrated with coursework and TAing but was excited to work with her on another research topic I wanted to explore. I also remember Raphael's interesting lectures for the Cosmology class, which made my second year more enjoyable as well.

My dissertation also involved many co-authors who have provided constructive input. Every individual discussion with Alberto Bolatto, Adam Leory, and Jiayi Sun has been incredibly helpful, and I greatly appreciate their insightful comments. I am also grateful for critical feedback from other collaborators in the PHANGS Team, particularly Simon Glover, Munan Gong, Ralf Klessen, Daizhong Liu, Eve Ostriker, Miguel Querejeta, Eva Schinnerer, and Antonio Usero. In addition, thanks to Jakob den Brok, Cosima Eibensteiner, Maria Jimenez-Donaire, Jaeyeon Kim, Eric Koch, and Jiayi Sun for all the discussions and funs we had during each conference and/or visit.

I would also like to thank my research group colleagues at UCSD, including I-Da Chiang, Jeremy Chastenet, Petia Yanchulova Merica-Jones, Michael Busch, Jessica Sutter, Ryan Rickards Vaught, Lindsey Hands, Ilyse Clark, and Hannah Koziol. Conversations with them in and outside group meetings have been useful. Thank you especially to I-Da for tremendous help when I was new to the group and to UCSD, not only academically but in almost every aspect of my life. Thanks also to my other friends, particularly Annie C-J Lai, Dino Hsu, Fang-Chi Leong, I-Lin Yeh, and Yueh-Hua Wu, for enriching my life in San Diego.

Finally, my sincere gratitude goes to my family, who have always been there and believed in me. Huge thanks to my mother and father for their constant love and support that have shaped me into who I am today. I also thank my brother and sister for calling/texting me from time to time and sharing interesting things in their lives with me. Special thanks to my beloved cat Meow Meow – I was fortunate to have spent much time with you during the pandemic; you live in my heart forever. Above all, I want to thank my partner and best friend, Herman Dong. Thank you for bringing immense joy to my life and always encouraging me in my academic pursuits, without which I would not have made it through my PhD. I am truly blessed to be able to start and finish a PhD together with you at UCSD and have your warm company throughout all these years.

* * *

My dissertation research was supported by the National Radio Astronomical Observatory (NRAO) through Student Observing Support grant SOSPADA-012, and by the National Science Foundation (NSF) through grant No. 2108081. I also acknowledge the Ministry of Education of Taiwan for their generous support of my PhD study through the Government Scholarship to Study Abroad.

This dissertation contains material from the following publications:

- Chapter 2, in full, is a reprint of the material as it appears in “Molecular Gas Properties and CO-to-H_2 Conversion Factors in the Central Kiloparsec of NGC 3351” by Yu-Hsuan Teng, Karin M. Sandstrom, Jiayi Sun, Adam K. Leroy, L. Clifton Johnson, Alberto D. Bolatto, J. M. Diederik Kruijssen, Andreas Schruba, Antonio Usero, Ashley T. Barnes, Frank Bigiel, Guillermo A. Blanc, Brent Groves, Frank P. Israel, Daizhong Liu, Erik Rosolowsky, Eva Schinnerer, J. D. Smith, and Fabian Walter, which was published in The Astrophysical Journal in 2022.

- Chapter 3, in full, is a reprint of the material as it appears in “The Physical Drivers and Observational Tracers of CO-to-H_2 Conversion Factor Variations in Nearby Barred Galaxy Centers” by Yu-Hsuan Teng, Karin M. Sandstrom, Jiayi Sun, Munan Gong, Alberto D. Bolatto, I-Da Chiang, Adam K. Leroy, Antonio Usero, Simon C. O. Glover, Ralf S. Klessen, Daizhong Liu, Miguel Querejeta, Eva Schinnerer, Frank Bigiel, Yixian Cao, M´elanie Chevance, Cosima Eibensteiner, Kathryn Grasha, Frank P. Israel, Eric J. Murphy, Lukas Neumann, Hsi-An Pan, Francesca Pinna, Mattia C. Sormani, J. D. T. Smith, Fabian Walter, and Thomas G. Williams, which was published in The Astrophysical Journal in 2023.
- Chapter 4, in full, is a reprint of the material as it appears in “Star Formation Efficiency in Nearby Galaxies Revealed with a New CO-to-H_2 Conversion Factor Prescription” by Yu-Hsuan Teng, I-Da Chiang, Karin M. Sandstrom, Jiayi Sun, Adam K. Leroy, Alberto D. Bolatto, Antonio Usero, Eve C. Ostriker, Miguel Querejeta, Jeremy Chastenet, Frank Bigiel, Mederic Boquien, Jakob den Brok, Yixian Cao, Melanie Chevance, Ryan Chown, Dario Colombo, Cosima Eibensteiner, Simon C. O. Glover, Kathryn Grasha, Jonathan D. Henshaw, Marıa J. Jimenez-Donaire, Daizhong Liu, Eric J. Murphy, Hsi-An Pan, Sophia K. Stuber, and Thomas G. Williams, which was published in The Astrophysical Journal in 2024.

In these publications, the dissertation author was the lead author who conducted all the data analysis, led the scientific interpretation of the results, created all figures and plots, and wrote the large majority of the text. The other co-authors either contributed to the observations/measurements used in these work or provided comments and edits to the final manuscripts that were accepted by The Astrophysical Journal.

VITA

Education

2019 – 2024 *Doctor of Philosophy in Physics*, University of California San Diego

2017 – 2019 *Master of Science in Physics*, National Taiwan University

2013 – 2017 *Bachelor of Science in Electrical Engineering*, National Taiwan University

Refereed Publications

First-Authored

Teng, Y.-H., Chiang, I.-D., Sandstrom, K. M., Sun, J., Leroy, A. K., Bolatto, A. D., Usero, A., Ostriker, E. C., Querejeta, M., Chastenet, J., Bigiel, F., Boquien, M., den Brok, J., Cao, Y., Chevance, M., Chown, R., Colombo, D., Eibensteiner, C., Glover, S. C. O., Grasha, K., Henshaw, J. D., Jimenez-Donaire, M. J., Liu, D., Murphy, E. J., Pan, H.-A., Stuber, S. K., & Williams, T. G., "Star Formation Efficiency in Nearby Galaxies Revealed with a New CO-to-H_2 Conversion Factor Prescription", 2024, *The Astrophysical Journal (**ApJ**)*, 961, 42.

Teng, Y.-H., Sandstrom, K. M., Sun, J., Gong, M., Bolatto, A. D., Chiang, I.-D., Leroy, A. K., Usero, A., Glover, S. C. O., Klessen, R. S., Liu, D., Querejeta, M., Schinnerer, E., Bigiel, F., Cao, Y., Chevance, M., Eibensteiner, C., Grasha, K., Israel, F. P., Murphy, E. J., Neumann, L., Pan, H.-A., Pinna, F., Sormani, M. C., Smith, J. D., Walter, F., & Williams, T. G., "The Physical Drivers and Observational Tracers of CO-to-H_2 Conversion Factor Variations in Nearby Barred Galaxy Centers", 2023, *The Astrophysical Journal (**ApJ**)*, 950, 119.

Teng, Y.-H., Sandstrom, K. M., Sun, J., Leroy, A. K., Johnson, L. C., Bolatto, A. D., Kruijssen, J. M. D., Schruba, A., Usero, A., Barnes, A. T., Bigiel, F., Blanc, G. A., Groves, B., Israel, F. P., Liu, D., Rosolowsky, E., Schinnerer, E., Smith, J. D., & Walter, F., "Molecular Gas Properties and CO-to-H_2 Conversion Factors in the Central Kiloparsec of NGC 3351", 2022, *The Astrophysical Journal (**ApJ**)*, 925, 72.

Teng, Y.-H., & Hirano, N., "Physical Conditions and Kinematics of the Filamentary Structure in Orion Molecular Cloud 1", 2020, *The Astrophysical Journal (**ApJ**)*, 893, 63.

Co-Authored

He, H., Wilson, C., Sun, J., **Teng, Y.-H.**, Rosolowsky, E., & Bemis, A. R., "Unraveling the Mystery of the Low CO-to-H_2 Conversion Factor in Starburst Galaxies: RADEX Modeling of the Antennae", 2024, *The Astrophysical Journal (**ApJ**)*, in press; *arXiv:2401.16476*.

Williams, T. G., Lee, J. C., Larson, K. L., Leroy, A. K., Sandstrom, K., Schinnerer, E., Thilker, D. A., Belfiore, F., Egorov, O. V., Rosolowsky, E., Sutter, J., DePasquale, J., Pagan, A., Anand, G. S., Barnes, A. T., Bigiel, F., Boquien, M., Cao, Y., Chastenet, J., Chevance, M., Chown, R., Dale, D. A., Eibensteiner, C., Emsellem, E., Faesi, C. M., Glover, S. C. O., Grasha, K., Hannon, S., Hassani, H., Henshaw, J. D., Jiménez-Donaire, M. J., Kim, J., Klessen, R. S., Koch, E. W., Li, J., Liu, D., Meidt, S. E., Méndez-Delgado, J. E., Murphy, E. J., Neumann, J., Neumann, L., Neumayer, N., Oakes, E. K., Pathak, D., Pety, J., Pinna, F., Querejeta, M., Ramambason, L., Romanelli, A., Sormani, M. C., Stuber, S. K., Sun, J., **Teng, Y.-H.**, Usero, A., Watkins, E. J., & Weinbeck, T. D., “PHANGS-JWST: Data Processing Pipeline and First Full Public Data Release”, 2024, *The Astrophysical Journal Supplement Series (**ApJS**)*, in press; *arXiv:2401.15142*.

Chiang, I.-D., Sandstrom, K. M., Chastenet, J., Bolatto, A. D., Koch, E. W., Leroy, A. K., Sun, J., **Teng, Y.-H.**, & Williams, T. G., “Resolved Measurements of the CO-to-H_2 Conversion Factor in 37 Nearby Galaxies”, 2024, *The Astrophysical Journal (**ApJ**)*, 964, 18.

Stuber, S. K., Pety, J., Schinnerer, E., Bigiel, F., Usero, A., Beslic, E., Querejeta, M., Jimenez-Donaire, M. J., Leroy, A., den Brok, J., Neumann, L., Eibensteiner, C., **Teng, Y.-H.**, Barnes, A., Chevance, M., Colombo, D., Dale, D. A., Glover, S. C. O., Liu, D., Pan, H.-A., “Surveying the Whirlpool at Arcseconds with NOEMA (SWAN) I. Mapping the HCN and N_2H^+ 3mm lines”, 2023, *Astronomy & Astrophysics (**A&A**)*, 680, L20.

den Brok, J. S., Leroy, A. K., Usero, A., Schinnerer, E., Rosolowsky, E., Koch, E. W., Querejeta, M., Liu, D., Bigiel, F., Barnes, A. T., Chevance, M., Colombo, D., Dale, D. A., Glover, S. C. O., Jimenez-Donaire, M. J., **Teng, Y.-H.**, & Williams, T. G., “Resolved low-J ^{12}CO excitation at 190 parsec resolution across NGC2903 and NGC3627”, 2023, *Monthly Notices of the Royal Astronomical Society (**MNRAS**)*, 526, 6347.

Querejeta, M., Pety, J., Schruba, A., Leroy, A. K., Herrera, C. N., Chiang, I.-D., Meidt, S. E., Rosolowsky, E., Schinnerer, E., Schuster, K., Sun, J., Herrmann, K. A., Barnes, A. T., Beslic, I., Bigiel, F., Cao, Y., Chevance, M., Eibensteiner, C., Emsellem, E., Faesi, C. M., Hughes, A., Kim, J., Klessen, R. S., Kreckel, K., Kruijssen, J. M. D., Liu, D., Neumayer, N., Pan, H.-A., Saito, T., Sandstrom, K., **Teng, Y.-H.**, Usero, A., Williams, T. G., & Zakardjian, A., “A sensitive, high resolution, wide field IRAM NOEMA CO(1-0) survey of the very nearby spiral galaxy IC 342”, 2023, *Astronomy & Astrophysics (**A&A**)*, 680, A4.

Sormani, M. C., Barnes, A. T., Sun, J., Stuber, S. K., Schinnerer, E., Emsellem, E., Leroy, A. K., Glover, S. C. O., Henshaw, J. D., Meidt, S. E., Neumann, J., Querejeta, M., Williams, T. G., Bigiel, F., Eibensteiner, C., Fragkoudi, F., Levy, R. C., Grasha, K., Klessen, R. S., Kruijssen, J. M. D., Neumayer, N., Pinna, F., Rosolowsky, E. W., Smith, R. J., **Teng, Y.-H.**, Tress, R. G., & Watkins, E. J., “Fuelling the nuclear ring of NGC 1097”, 2023, *Monthly Notices of the Royal Astronomical Society (**MNRAS**)*, 523, 2918.

Sun, J., Leroy, A. K., Ostriker, E. C., Meidt, S., Rosolowsky, E., Schinnerer, E., Wilson, C. D., Utomo, D., Belfiore, F., Blanc, G. A., Emsellem, E., Faesi, C., Groves, B., Hughes, A., Koch, E. W., Kreckel, K., Liu, D., Pan, H.-A., Pety, J., Querejeta, M., Razza, A., Saito, T., Sardone, A., Usero, A., Williams, T. G., Bigiel, F., Bolatto, A. D., Chevance, M., Dale, D. A., Gensior, J., Glover, S. C. O., Grasha, K., Henshaw, J. D., Jiménez-Donaire, M. J., Klessen, R. S., Kruijssen, J. M. D., Murphy, E. J., Neumann, L., **Teng, Y.-H.**, & Thilker, D. A., “Star Formation Laws and Efficiencies across 80 Nearby Galaxies", 2023, *The Astrophysical Journal Letters (**ApJL**)*, 945, 19.

den Brok, J. S., Bigiel, F., Chastenet, J., Sandstrom, K., Leroy, A., Usero, A., Schinnerer, E., Rosolowsky, E. W., Koch, E. W., Chiang, I.-D., Barnes, A. T., Puschnig, J., Saito, T., Bešlić, I., Chevance, M., Dale, D. A., Eibensteiner, C., Glover, S., Jiménez-Donaire, M. J., **Teng, Y.-H.**, & Williams, T. G., "Wide-Field CO Isotopologue Emission and the CO-to-H_2 Factor across the Nearby Spiral Galaxy M101", 2023, *Astronomy & Astrophysics (**A&A**)*, 676, A93.

Neumann, L., Gallagher, M. J., Bigiel, F., Leroy, A. K., Barnes, A. T., Usero, A., den Brok, J. S., Belfiore, F., Bešlić, I., Cao, Y., Chevance, M., Dale, D. A., Eibensteiner, C., Glover, S. C. O., Grasha, K., Henshaw, J. D., Jiménez-Donaire, M. J., Klessen, R. S., Kruijssen, J. M. D., Liu, D., Meidt, S., Pety, J., Puschnig, J., Querejeta, M., Rosolowsky, E., Schinnerer, E., Schruba, A., Sormani, M. C., Sun, J., **Teng, Y.-H.**, & Williams, T. G., "The ALMOND Survey: Molecular cloud properties and gas density tracers across 25 nearby spiral galaxies with ALMA", 2023, *Monthly Notices of the Royal Astronomical Society (**MNRAS**)*, 521, 3348.

Liu, D., Schinnerer, E., Saito, T., Rosolowsky, E., Leroy, A., Usero, A., Sandstrom, K., Klessen, R. S., Glover, S. C. O., Ao, Y., Bešlić, I., Bigiel, F., Cao, Y., Chastenet, J., Chevance, M., Dale, D. A., Gao, Y., Hughes, A., Kreckel, K., Kruijssen, J. M. D., Pan, H.-A., Pety, J., Salak, D., Santoro, F., Schruba, A., Sun, J., **Teng, Y.-H.**, & Williams, T., "CI and CO in Nearby Spiral Galaxies - I. Line Ratio and Abundance Variations at ~200 pc Scales", 2023, *Astronomy & Astrophysics (**A&A**)*, 672, A36.

Liu, D., Schinnerer, E., Cao, Y., Leroy, A., Usero, A., Rosolowsky, E., Kruijssen, J. M. D., Chevance, M., Glover, S. C. O., Sormani, M. C., Bolatto, A. D., Sun, J., Stuber, S. K., **Teng, Y.-H.**, Bigiel, F., Bešlić, I., Grasha, K., Henshaw, J. D., Barnes, A. T., den Brok, J. S., Saito, T., Dale, D. A., Watkins, E. J., Pan, H.-A., Klessen, R. S., Emsellem, E., Anand, G. S., Deger, S., Egorov, O. V., Faesi, C. M., Hassani, H., Larson, K. L., Lee, J. C., Lopez, L. A., Pety, J., Sandstrom, K., Thilker, D. A., Whitmore, B. C., & Williams, T. G., "PHANGS-JWST First Results: Stellar Feedback-Driven Excitation and Dissociation of Molecular Gas in the Starburst Ring of NGC 1365?", 2023, *The Astrophysical Journal Letters (**ApJL**)*, 944, 19.

Lee, J. C., Sandstrom, K. M., Leroy, A. K., Thilker, D. A., Schinnerer, E., Rosolowsky, E., Larson, K. L., Egorov, O. V., Williams, T. G., Schmidt, J., Emsellem, E., Anand, G. S., Barnes, A. T., Belfiore, F., Bešlić, I., Bigiel, F., Blanc, G. A., Bolatto, A. D., Boquien, M., den Brok, J., Cao, Y., Chandar, R., Chastenet, J., Chevance, M., Chiang, I.-D., Congiu, E., Dale, D. A., Deger, S., Eibensteiner, C., Faesi, C. M., Glover, S. C. O., Grasha, K., Groves, B., Hassani, H., Henny, K. F., Henshaw, J. D., Hoyer, N., Hughes, A., Jeffreson, S., Jiménez-Donaire, M. J., Kim, J., Kim, H., Klessen, R. S., Koch, E. W., Kreckel, K., Kruijssen, J. M. D., Li, J., Liu, D., Lopez, L. A., Maschmann, D., Chen, N. M., Meidt, S. E., Murphy, E. J., Neumann, J., Neumayer, N., Pan, H.-A., Pessa, I., Pety, J., Querejeta, M., Pinna, F., Rodríguez, M. J., Saito, T., Sánchez-Blázquez, P., Santoro, F., Sardone, A., Smith, R. J., Sormani, M. C., Scheuermann, F., Stuber, S. K., Sutter, J., Sun, J., **Teng, Y.-H.**, Treß, R. G., Usero, A., Watkins, E. J., Whitmore, B. C., & Razza, A., "The PHANGS-JWST Treasury Survey: Star Formation, Feedback, and Dust Physics at High Angular resolution in Nearby GalaxieS", 2023, *The Astrophysical Journal Letters (**ApJL**)*, 944, 17.

García-Rodríguez, A., Usero, A., Leroy, A. K., Bigiel, F., Jiménez-Donaire, M. J., Liu, D., Querejeta, M., Saito, T., Schinnerer, E., Barnes, A., Belfiore, F., Bešlić, I., Cao, Y., Chevance, M., Dale, D. A., den Brok, J. S., Eibensteiner, C., García-Burillo, S., Glover, S. C. O., Klessen, R. S., Pety, J., Puschnig, J., Rosolowsky, E., Sandstrom, K., Sormani, M. C., **Teng, Y.-H.**, & Williams, T. G., "Sub-kpc empirical relations and excitation conditions of HCN and HCO^+ J=3-2 in nearby star-forming galaxies", 2023, *Astronomy & Astrophysics (**A&A**)*, 672, A96.

Eibensteiner, C., Barnes, A. T., Bigiel, F., Schinnerer, E., Liu, D., Meier, D. S., Usero, A., Leroy, A. K., Rosolowsky, E., Puschnig, J., Lazar, I., Pety, J., Lopez, L. A., Emsellem, E., Bešlić, I., Querejeta, M., Murphy, E. J., den Brok, J., Schruba, A., Chevance, M., Glover, S. C. O., Gao, Y., Grasha, K., Hassani, H., Henshaw, J. D., Jimenez-Donaire, M. J., Klessen, R. S., Kruijssen, J. M. D., Pan, H.-A., Saito, T., Sormani, M. C., **Teng, Y.-H.**, & Williams, T. G., "A 2-3 mm high-resolution molecular line survey towards the centre of the nearby spiral galaxy NGC 6946", 2022, *Astronomy & Astrophysics (**A&A**)*, 659, A173.

ABSTRACT OF THE DISSERTATION

Molecular Gas and Star Formation in Nearby Galaxy Centers

by

Yu-Hsuan Teng

Doctor of Philosophy in Physics

University of California San Diego, 2024

Professor Karin M. Sandstrom, Chair

Star formation in galaxies is governed by the amount of molecular gas and the efficiency that gas is converted into stars. However, assessing the amount of molecular gas relies on the CO-to-H_2 conversion factor ($\alpha_{\rm CO}$), which is known to vary with molecular gas conditions like density, temperature, and dynamical state – the same conditions that also alter star formation efficiency. The variation of $\alpha_{\rm CO}$, particularly in galaxy centers where $\alpha_{\rm CO}$ can drop by nearly an order of magnitude, thus causes major uncertainties in current molecular gas and star formation efficiency measurements. Using ALMA observations of multiple low-J ^{12}CO, ^{13}CO, and C^{18}O lines in several barred galaxy centers, we found that $\alpha_{\rm CO}$ is primarily driven by CO opacity changes and therefore shows strong correlations with observables like velocity dispersion and ^{12}CO/^{13}CO line ratio. Motivated by these results, we have constructed a new α_{CO} prescription which accounts for emissivity effects in galaxy centers and verified it on a set of barred and non-barred galaxies with measured α_{CO} values from dust. Applying our new prescription to 65 galaxies from the PHANGS-ALMA survey, we found an overall three times higher star formation efficiency in barred galaxy centers than in non-barred galaxy centers, and such a trend is obscured when using a constant α_{CO} or other existing prescriptions. Our results suggest that the high star formation rate observed in barred galaxy centers is due to an enhanced star formation efficiency compared to non-barred galaxy centers or the disk regions, rather than a substantially increased amount of molecular gas in barred galaxy centers.

Chapter 1

Introduction

1.1 Overview and Motivation

Among the phases of gas in the interstellar medium (ISM), molecular gas plays a critical role in star formation and galaxy evolution. As stars are born in cold and dense molecular clouds, the star formation process should be governed by (1) the amount of molecular gas and (2) the efficiency of that gas being converted into stars. Therefore, measuring molecular gas mass and its star formation efficiency (SFE) is fundamental to understanding the physics and interplay between small-scale star formation and large-scale galactic environments (e.g., Leroy et al., 2008; Saintonge and Catinella, 2022).

However, the estimations of molecular gas mass and SFE are both entangled with the variation of the CO-to-H_2 conversion factor ($\alpha_{\rm CO}$; see also review by Bolatto et al., 2013), a factor that has long been used to derive molecular gas mass in galaxies (Solomon et al., 1987). Because assessing these important quantities relies heavily on the value of $\alpha_{\rm CO}$, and the physical or dynamical processes driving SFE variations are the same conditions that also alter $\alpha_{\rm CO}$, such an entanglement between $\alpha_{\rm CO}$ and SFE can lead to biased SFE estimates due to significant uncertainties in $\alpha_{\rm CO}$ (e.g., Utomo et al., 2017; den Brok et al., 2023; Sun et al., 2023). Therefore, to break through the current limitation in understanding molecular gas and star formation in galaxies, it is critical to fully understand the variation of $\alpha_{\rm CO}$ and its relationship with gas physical conditions across different environments.

Studies have shown that many galaxy centers, especially those with stellar bars, have substantially lower α_{CO} than the standard Milky Way disk value which is commonly assumed in most studies (Sandstrom et al., 2013; Israel, 2020). As galaxy centers tend to have very different environmental properties than those in the disks (e.g., gas concentration and dynamics; Sun et al., 2020b), they are ideal test beds for understanding the mechanisms of star formation in galaxies. Therefore, as a first step to investigate the physical causes of α_{CO} variations, we utilize state-of-the-art mm/sub-mm telescope, Atacama Large Millimeter/submillimeter Array (ALMA), to observe the centers of several nearby galaxies in multiple CO isotopologue lines. With such high-resolution data, detailed variation of α_{CO} can be revealed and giant molecular clouds (GMCs) can be resolved, we can then test various hypotheses for why α_{CO} is generally lower in galaxy centers and further develop a reliable α_{CO} prescription for future studies.

1.2 Star Formation in a Galactic Context

In galaxies like our Milky Way, it is known that stars are formed in the molecular gas phase which is mainly composed of molecular hydrogen (H_2). This is supported not only by theoretical models (Schmidt, 1959), but also by many pieces of observational evidence. For example, spatial correlations have been observed between molecular gas and newly formed stars, and studies have found a tight correlation between star formation rates and the amount of molecular gas across a wide range of environments (i.e., the molecular Kennicutt-Schmidt relation, or mKS relation; Kennicutt, 1998; Bigiel et al., 2008; Schruba et al., 2011). In the mKS relation, the roughly constant ratio between star formation rate and molecular gas mass suggests that the star formation efficiency (SFE) is consistent throughout different regions or different types of galaxies. This empirical scaling relation, linking small-scale star formation physics to large-scale galactic environments, has therefore laid an important foundation for extragalactic star formation studies.

However, the mKS relation depends on molecular gas measurements and thereby the $\alpha_{\rm CO}$ conversion factor. The involvement of $\alpha_{\rm CO}$ is essential because tracing molecular gas in galaxies is typically done by observing the lowest rotational line emission from carbon monoxide (CO; the second most abundant molecule in the molecular phase of the ISM). The most abundant H_2, on the other hand, is not directly observable in the cold star-forming gas at few tens of K, because even its lowest energy transition requires at least $\sim$100 K to be excited (Togi and Smith, 2016). Thus, the common practice for tracing H_2 is simply to convert the observed CO line flux into molecular gas mass via a *constant* CO-to-H_2 conversion factor $\alpha_{\rm CO}$, even if the factor is known to vary with environmental conditions.

Studies have also shown that global galaxy properties (e.g., structural/dynamical features) can affect various molecular gas properties (Kennicutt and Evans, 2012; Sun et al., 2020b). However, the link between these local and large-scale processes is still unclear. To understand the physics and interplay from small-scale star formation to large-scale galaxy evolution, it is important to obtain information such as molecular cloud free-fall time, virial parameter, turbulent pressure, and gas inflow rates. Unfortunately, similar to the mKS relation, all these quantities have direct dependence on molecular gas measurements, implying that $\alpha_{\rm CO}$ variations is the current big challenge that hampers us from achieving an accurate and comprehensive view of galactic-scale star formation (Feldmann et al., 2012b; Leroy et al., 2013; Sormani and Barnes, 2019; Ellison et al., 2020b; Pessa et al., 2021; Sun et al., 2022). Therefore, to bring the field to the next level, it is key to establish how $\alpha_{\rm CO}$ behaves in different environmental regimes and account for the systematic effect of $\alpha_{\rm CO}$ variation on all these important star formation quantities.

1.3 Tracing Molecular Gas in Galaxies

1.3.1 Challenge of ^{12}CO Observations

Observationally, the low rotational levels of ^{12}CO are almost always optically thick in molecular clouds (e.g., Shetty et al., 2011a). For an optically thick molecular line, the peak intensity of the observed line profile does not reflect the true amount of that molecule along the observed line of sight. Instead, the observed emission comes only from the surface of molecular cloud where the optical depth is low, and thus the peak intensity is set by the brightness temperature at the surface layer. Then, one might ask: why can the predominantly opaque ^{12}CO $J = 1$–0 or 2–1 line be used as a workhorse tracer for H_2 mass?

While it is true that the peak intensity of CO is saturated in most cases, it is worth noting that the CO emission can still escape through the spectral (or velocity) domain in the case of a larger linewidth or increased velocity dispersion. Observationally, molecular clouds have been found to approximately follow an empirical size-linewidth relation of $\sigma \propto R^{0.5}$, where R is the cloud size and σ is the cloud velocity dispersion (Larson, 1981; Heyer et al., 2009). Theoretically, such a relation is also supported by the well-known Kolmogorov's law for subsonic turbulent flows, which predicts a similar power-law dependence between turbulent velocity and its length scale. All together, these suggest that larger molecular clouds have increased velocity dispersion due to the superposition of small-scale turbulence.

As the size of a molecular cloud also scales with its mass (through a density term), the size-linewidth relation explains why CO intensities may approximately trace the entire H_2 mass even if the emission is optically thick. This also shows that $\alpha_{\rm CO}$ is far more than a constant factor, but a relation tied to the physical conditions of molecular gas (e.g., temperature and turbulence). Thus, to obtain precise measurements of molecular gas mass, it would be best to incorporate optically thin tracers such as the CO isotopologues.

1.3.2 CO Isotopologues

Isotopologues are molecules with different isotopic compositions. For carbon monoxide, the most abundant composite is ^{12}C^{16}O, which is what "CO" or "^{12}CO" usually refers to. The second and third abundant composite is ^{13}C^{16}O and ^{12}C^{18}O, which is generally abbreviated as ^{13}CO and C^{18}O, respectively. Studying these rarer isotopologues can provide useful information in the chemical enrichment process associated with star formation and galaxy evolution. However, depending on their difference in abundances, the rareness of certain isotopologues also results in fainter line emission from them. This explains why extensive studies of CO isotopologues like ^{13}CO and C^{18}O have been limited to molecular clouds in the Milky Way (e.g., Wilson and Rood, 1994; Milam et al., 2005).

Because low-J rotational lines of CO are normally optically thick, it is important to observe optically thin CO isotopologues to investigate the physical condition of molecular gas and the cause for α_{CO} variation. For ^{13}CO, the CO/^{13}CO abundance ratios ranges from ~20 at the Galactic Center to ~70 near the solar neighborhood (Milam et al., 2005). With such a low abundance, ^{13}CO is generally optically thin in molecular clouds except for the densest regions. As for C^{18}O, it is approximately an order of magnitude less abundant than ^{13}CO, and is therefore always optically thin with only few exceptions (Areal et al., 2018).

While several studies have used the lowest-J transitions of CO isotopologues to constrain physical conditions in nearby galaxy centers at $\gtrsim$kpc scales (Israel, 2009b; Eckart et al., 1990; Israel, 2020), it is only recently that observations of CO isotopologues on cloud-scales (~100 pc) have become routinely possible toward nearby galaxy centers. Thanks to ALMA's high sensitivity and resolution in mm/sub-mm wavelengths, it is now possible to obtain multiple rotational levels of optically thin CO isotopologue lines resolved in external galaxies, allowing for more reliable physical results and revealing the detailed variation of gas conditions and α_{CO} in different galactic environments.

1.3.3 Multi-line Radiative Transfer Modeling

With observations of multiple molecular lines, it is possible to accurately constrain the physical conditions of molecular gas by comparing to radiative transfer models. The observed line intensity from a molecular species can be predicted via radiative transfer equations with knowledge and/or assumptions on the structure, velocity distribution, temperature, and column and volume densities of the observed molecular cloud. On such a basis, we can create a multi-dimensional model grid that contains predicted molecular line emission under varying combinations of physical parameters. Then, we can compare the model-predicted line intensity with our observation and determine what parameter set best describes the physical conditions of the observed cloud. With only a single molecular line observation, the constraint can be poor, but the more molecular lines we observe and compare to models, the higher chance we can narrow down the constraint and obtain a reliable estimate of the gas conditions.

A detailed explanation of how radiative transfer models works can be found in textbooks (e.g., Draine, 2011), but the concept is briefly described below. In principle, the radiation field is emitted via de-population from an upper to a lower energy level of an atom or molecule. The strength of that radiation is governed by the level populations, which can be described by the Boltzmann equation (as a function of the excitation temperature and level energies) in the case of local thermodynamic equilibrium (LTE). On the other hand, the *measured* strength of radiation is also affected by the absorption from the outer-layer cloud along the line of sight, and this determines the optical depth in the radiative transfer equation. Both the emission and absorption rates can be described by combinations of the Einstein coefficients, which represent different mechanisms of the excitation or de-excitation process (including spontaneous, stimulated, and collisional).

Another way to solve the level population is to estimate the probability that a photon can escape from the cloud using Large Velocity Gradient (LVG) approximation (Sobolev, 1960), where the escape probability can be expressed as a function of optical depth. This approach is particularly useful in the case of non-LTE, where gas temperature deviates from the excitation temperature and thus the level population can no longer be derived from the Boltzmann equation. A public and widely used non-LTE radiative transfer code, RADEX (van der Tak et al., 2007), utilizes this escape probability method to iteratively solve for a converged solution of the excitation and radiation field assuming a homogeneous medium. Specifically, it produces an initial guess of level population by assuming LTE, calculates the resulting optical depth to obtain the escape probability and update the level population, and then re-estimate the optical depth and excitation temperature until they reach convergence.

By observing multiple transitions of ^{12}CO, ^{13}CO, and C^{18}O with ALMA, my work jointly model these lines with RADEX to determine the physical properties of molecular gas in three nearby barred galaxy centers (see Chapters 2 and 3 for more details). The same modeling also allows us to derive spatial distributions of the CO-to-H$_2$ conversion factor, which can be further linked to various environmental conditions and observable properties. My multi-line modeling code in these work, incorporating RADEX and Bayesian probabilistic analysis, is publicly available on GitHub and Zenodo (Teng, 2024), and it has been referenced or used by researchers around the world to explore molecular gas conditions and $\alpha_{\rm CO}$ in diverse galaxies, including early-type galaxy and starburst galaxy mergers (Young et al., 2022; He et al., 2024).

1.3.4 The CO-to-H$_2$ Conversion Factor

The CO-to-H$_2$ conversion factor ($\alpha_{\rm CO}$) is defined as the ratio of molecular gas mass to the ^{12}CO 1–0 luminosity (Bolatto et al., 2013), which is also equivalent to the ratio of molecular gas mass surface density (in units of M$_\odot$/pc^2) to ^{12}CO 1–0 integrated intensity (in units of K km s^{-1}):

$$\alpha_{\rm CO} = \frac{M_{\rm mol}}{L_{\rm CO(1-0)}} = \frac{\Sigma_{\rm mol}}{I_{\rm CO(1-0)}} \left(\frac{\rm M_\odot}{\rm K\ km\ s^{-1}\ pc^2} \right) . \tag{1.1}$$

The CO 1–0 luminosity is the CO 1–0 intensity multiplied by the area of beam size, and the molecular gas mass ($M_{\rm mol}$) is proportional to the product of CO column density ($N_{\rm CO}$) and the beam-filling factor ($\Phi_{\rm bf}$) times the area (Kamenetzky et al., 2014):

$$M_{\rm mol} = 1.36\, m_{\rm H_2}\, N_{\rm CO}\, A\, \Phi_{\rm bf}\, x_{\rm CO}^{-1} , \tag{1.2}$$

where A is the same area as that in CO 1–0 luminosity, the 1.36 factor accounts for the contribution from Helium to the total molecular gas, and $x_{\rm CO}$ is the CO/H$_2$ abundance ratio that is commonly assumed at ~10^{-4} for Galactic disk-like environments.

There are many ways to measure $\alpha_{\rm CO}$. The basic idea is to estimate the molecular gas mass via various methods and then compare to CO observations. For example, the optically thin isotopologues of CO, such as ^{13}CO, can trace the column density of molecular gas (e.g., Cormier et al., 2018). In addition, tracers like dust, γ-ray, and [C II] may also be optically thin, so they can be used to trace the total gas and estimate the amount of molecular gas by subtracting the emission contributed by atomic gas (e.g., Leroy et al., 2011; Accurso et al., 2017b; Remy et al., 2017). We may also assume that molecular clouds are in virial balance and then use the measured line widths and sizes to determine the virial masses of the clouds (e.g., Donovan Meyer et al., 2013). Or, some studies assume that all galaxies have a predictable star formation efficiency based on the mKS relation, so that molecular gas mass can be inferred from measured star formation rates (e.g., Blanc et al., 2013). Studies that applied these different methods have found a roughly consistent $\alpha_{\rm CO}$ value of $\sim$4.35 $M_\odot$ (K km s^{-1} pc^2)$^{-1}$ in molecular clouds in the disks of the Milky Way or other local spiral galaxies. As a result, many studies simply assume a constant, Milky Way-like $\alpha_{\rm CO}$ to derive molecular gas mass in different regions or types of galaxies.

However, $\alpha_{\rm CO}$ can actually vary by orders of magnitude in different environments. In theory, the value of $\alpha_{\rm CO}$ is known to depend on molecular gas conditions such as density, temperature, metallicity, and velocity dispersion (Narayanan et al., 2012; Bolatto et al., 2013; Gong et al., 2020). Observations have also revealed large $\alpha_{\rm CO}$ variations within and between galaxies (Papadopoulos et al., 2012a; Sandstrom et al., 2013; Kamenetzky et al., 2017). For instance, galaxy centers tend to have lower $\alpha_{\rm CO}$ due to higher temperatures and/or dynamical effects in galaxy centers, and previous kpc-scale observations in nearby galaxy centers also revealed substantially lower $\alpha_{\rm CO}$ values than the Milky Way average (Israel, 2009b; Blanc et al., 2013; Sandstrom et al., 2013; Israel, 2020). Similarly, both theoretical and observational work have shown that $\alpha_{\rm CO}$ is also lower in (ultra-)luminous infrared galaxies ((U)LIRGs) and/or galaxy mergers due to their gas being warmer, denser, and having higher CO isotopologue abundances (e.g., Downes and Solomon, 1998; Papadopoulos et al., 2012b; Sliwa et al., 2017). To understand how molecular gas properties and its distribution within galaxies shape the star formation processes and impact the secular evolution of galaxies, improved knowledge of α_{CO} variation and its relation to environmental conditions is of crucial importance.

1.4 Dissertation Organization

In this dissertation, I aim to address the long-standing issue of α_{CO} variation in current star formation studies. Specifically, I have (1) measured molecular gas properties and α_{CO} across a sample of galaxies, (2) disentangled the physical drivers of α_{CO} and found out what processes control α_{CO} in galaxy centers, (3) identified key observational tracers of α_{CO} and developed a widely applicable α_{CO} prescription for future studies, and (4) investigated the systematic impact of α_{CO} correction on past and current SFE estimations.

Chapter 2 presents a comprehensive case study on NGC 3351, demonstrating our established models and techniques for measuring molecular gas properties and α_{CO} (Teng et al., 2022). Based on the approach and measurements, Chapter 3 further shows how we identified the physical drivers and key observables for tracing α_{CO} variations in barred galaxy centers (Teng et al., 2023). In Chapter 4, we describe our development of a new α_{CO} prescription for star-forming galaxies, which reveals systematic impacts of α_{CO} on the estimation of SFE (Teng et al., 2024). Finally, I summarize all these work and discuss possible future directions in Chapter 5.

Chapter 2

Molecular Gas Properties and CO-to-H_2 Conversion Factors in the Central Kiloparsec of NGC 3351

Abstract

The CO-to-H_2 conversion factor (α_{CO}) is critical to studying molecular gas and star formation in galaxies. The value of α_{CO} has been found to vary within and between galaxies, but the specific environmental conditions that cause these variations are not fully understood. Previous observations on ~kpc scales revealed low values of α_{CO} in the centers of some barred spiral galaxies, including NGC 3351. We present new ALMA Band 3, 6, and 7 observations of ^{12}CO, ^{13}CO, and C^{18}O lines on 100 pc scales in the inner ~2 kpc of NGC 3351. Using multi-line radiative transfer modeling and a Bayesian likelihood analysis, we infer the H_2 density, kinetic temperature, CO column density per line width, and CO isotopologue abundances on a pixel-by-pixel basis. Our modeling implies the existence of a dominant gas component with a density of $2–3 \times 10^3$ cm^{-3} in the central ~1 kpc and a high temperature of 30–60 K near the nucleus and near the contact points that connect to the bar-driven inflows. Assuming a CO/H_2 abundance of 3×10^{-4}, our analysis yields α_{CO}~0.5–2.0 M$_\odot$ (K km s^{-1} pc^2)$^{-1}$ with a decreasing

trend with galactocentric radius in the central ~1 kpc. The inflows show a substantially lower $\alpha_{\rm CO}\lesssim 0.1$ M$_\odot$ (K km s^{-1} pc^2)$^{-1}$, likely due to lower optical depths caused by turbulence or shear in the inflows. Over the whole region, this gives an intensity-weighted $\alpha_{\rm CO}$ of ~1.5 M$_\odot$ (K km s^{-1} pc^2)$^{-1}$, which is similar to previous dust modeling based results at kpc scales. This suggests that low $\alpha_{\rm CO}$ on kpc scales in the centers of some barred galaxies may be due to the contribution of low optical depth CO emission in bar-driven inflows.

2.1 Introduction

Stars are born in cold and dense molecular clouds that are mainly composed of molecular hydrogen, H_2. It is therefore known that molecular clouds play an important role in star formation and galaxy evolution (see review by Kennicutt and Evans, 2012). However, emission from the most abundant molecule, H_2, is not directly observable in cold molecular gas, since its lowest energy transition has an upper energy level $E/k \approx 510$ K and can only be seen in gas with temperatures above ~80 K (Togi and Smith, 2016). Therefore, to trace cold molecular gas, the most common approach is to observe the low-J rotational lines of the second most abundant molecule, carbon monoxide ($^{12}C^{16}O$; hereafter CO), and then apply a CO-to-H_2 conversion factor to infer the total amount of molecular gas (see review by Bolatto et al., 2013). The CO-to-H_2 conversion factor is formally defined as the ratio between H_2 column density and the integrated intensity of CO 1–0:

$$X_{\rm CO} = \frac{N_{\rm H_2}}{I_{\rm CO(1-0)}} \left(\frac{\rm cm^{-2}}{\rm K\ km\ s^{-1}}\right) . \tag{2.1}$$

In mass units, Equation 2.1 can be rewritten as

$$\alpha_{\rm CO} = \frac{M_{\rm mol}}{L_{\rm CO(1-0)}} \left(\frac{\rm M_\odot}{\rm K\ km\ s^{-1}\ pc^2}\right) , \tag{2.2}$$

where M_{mol} is the total molecular mass including the contribution from Helium ($M_{\mathrm{mol}} \sim 1.36\,M_{\mathrm{H_2}}$), and $L_{\mathrm{CO(1-0)}}$ is the CO 1–0 luminosity. X_{CO} can be converted to α_{CO} by multiplying by a factor of 4.5×10^{19} (see Section 2.5 for more details).

Various methods have been used to measure the value of α_{CO} by estimating the total gas mass, including: using measured line-widths and sizes with the assumption of virial balance in giant molecular clouds (GMCs) (Scoville et al., 1987; Solomon et al., 1987; Bolatto et al., 2008; Donovan Meyer et al., 2013); dust emission or extinction converted to gas mass with various assumptions on the dust-to-gas ratio (Pineda et al., 2008; Leroy et al., 2011; Planck Collaboration et al., 2011; Imara, 2015); γ-ray emission converted to gas mass with knowledge of the cosmic ray flux (Abdo et al., 2010; Ackermann et al., 2012b; Remy et al., 2017); and the use of ^{13}CO (Cormier et al., 2018), [C II] (Accurso et al., 2017b; Bigiel et al., 2020; Madden et al., 2020), or the Kennicutt-Schmidt law based on star formation rate measurements (Schruba et al., 2012; Blanc et al., 2013). These studies have found a roughly constant α_{CO} value of ~4.4 $\mathrm{M_\odot}$ (K km s^{-1} pc^2)$^{-1}$ (or $X_{\mathrm{CO}} \sim 2 \times 10^{20}$ cm^{-2} (K km s^{-1})$^{-1}$ in molecular clouds in the disks of the Milky Way or other nearby spiral galaxies. As a result, many studies assume a constant α_{CO} value similar to the Milky Way average. However, α_{CO} may depend on gas conditions such as density, temperature, metallicity, and velocity dispersion (e.g., Narayanan et al., 2012; Bolatto et al., 2013), and the α_{CO} values could vary by orders of magnitude in different environments as predicted from hydrodynamical simulations (Feldmann et al., 2012a; Gong et al., 2020). For instance, a low α_{CO} value could be caused by conditions such as: (1) enhanced temperature and/or decreased density in GMCs that are virialized (e.g., Bolatto et al., 2013), (2) GMCs with increased velocity dispersion relative to mass, which alters their virial balance (e.g., Watanabe et al., 2011), or (3) CO emission from molecular gas that is not associated with GMCs (e.g., Leroy et al., 2015). On the other hand, α_{CO} can also be extremely high in low-metallicity galaxies (e.g., Papadopoulos et al., 2018; Madden et al., 2020) due to envelopes of "CO-dark H_2" (Wolfire et al., 2010).

Studies have shown that galaxy centers tend to have lower $\alpha_{\rm CO}$, which may be due to higher temperatures and/or dynamical effects in galaxy centers (e.g., Sandstrom et al., 2013; Israel, 2020). The value of $\alpha_{\rm CO}$ in the Galactic Center was found to be 3–10 times lower than in the Galactic disk (Blitz et al., 1985; Sodroski et al., 1995; Oka et al., 2001; Ackermann et al., 2012a). In addition, previous kpc-scale observations also revealed substantially lower $\alpha_{\rm CO}$ values than the Milky Way average in many nearby galaxy centers, especially those with nuclear gas concentrations (Meier and Turner, 2004; Israel, 2009b; Blanc et al., 2013; Sandstrom et al., 2013; Israel, 2020). As stellar bars or spiral arms funnel gas to the centers and create concentrations of gas and star formation, galaxy centers frequently host the most active star formation in disk galaxies (e.g. Davies et al., 2007; Callanan et al., 2021). Feedback from starburst and active galactic nuclei (AGNs) could also lead to significantly different physical conditions in the central kpc of galaxies. In (ultra-)luminous infrared galaxies (U/LIRGs) and/or galaxy mergers, $\alpha_{\rm CO}$ values were also found to be lower than those of the Milky Way clouds, with the gas usually being warmer, denser, and having higher CO isotopologue abundances (Downes and Solomon, 1998; Papadopoulos et al., 2012b; Sliwa et al., 2014; Sliwa et al., 2017; König et al., 2016). To understand molecular gas and star formation in galaxies, it is critical to study the variation of $\alpha_{\rm CO}$ and its relation to environmental conditions. Galaxy centers, having conditions of high gas surface density, high excitation, and/or altered molecular gas dynamics compared to the simple picture of isolated virialized GMCs, are thus ideal test beds for studying the influence of physical properties on $\alpha_{\rm CO}$.

In order to best diagnose the physical state of the molecular gas and reasons for $\alpha_{\rm CO}$ variation, it is necessary to observe the optically thin isotopologues of CO. Since the low-J rotational lines of CO are optically thick in molecular clouds, this leads to a degeneracy in CO excitation and subsequently to uncertain column densities. Therefore, optically thin tracers are crucial for self-consistent measurements of excitation conditions or molecular gas column densities. One of the CO isotopologues, ^{13}CO, has CO/^{13}CO abundance ratios ranging from ~20 at the Galactic Center to ~70 near the solar neighborhood (Langer and Penzias, 1990; Milam et al., 2005). With such a low abundance, ^{13}CO is generally optically thin in molecular clouds except for the densest regions (Tan et al., 2011; Shimajiri et al., 2014; Barnes et al., 2020). Another CO isotopologue, C^{18}O, is approximately an order of magnitude less abundant than ^{13}CO, and is therefore optically thin with only few exceptions (Wouterloot et al., 2008; Areal et al., 2018). Several studies have used the lowest-J transitions of CO isotopologues to constrain physical conditions in nearby galaxy centers at $\gtrsim$kpc scales (Eckart et al., 1990; Israel, 2009b; Jiménez-Donaire et al., 2017; Israel, 2020). However, it is only recently that observations of CO isotopologues on cloud-scales (~100 pc) have become routinely possible toward nearby galaxy centers, thanks to the high sensitivity and resolution of the Atacama Large Millimeter/submillimeter Array (ALMA). Therefore, it is now possible to obtain multiple rotational levels of optically thin CO isotopologue lines resolved in a galaxy center, which not only allows for more reliable physical results but also reveals the detailed variation of conditions in the galaxy center.

In this study, we investigate cloud-scale variation of molecular gas properties and $\alpha_{\rm CO}$ using ALMA observations of CO isotopologues toward the center of NGC 3351. NGC 3351 is a barred spiral galaxy located at a distance of 9.96 ± 0.33 Mpc (Anand et al., 2021), with a (photometric) disk inclination of 45.1° and position angle of 188.4° (Lang et al., 2020). It has a total stellar mass of 2.3×10^{10} M$_\odot$ and a star formation rate of 1.3 M$_\odot$ yr^{-1} (Leroy et al., 2021b). Early studies have found a circumnuclear ring[1] with a diameter of ~20″ (~1 kpc) in the center of NGC 3351, harboring intense massive star formation activity (e.g., Alloin and Nieto, 1982; Leroy et al., 2009). Previous observations in UV, Hα, Paα, and radio continuum also identified multiple star-forming complexes at 100 pc scales along the ring (Colina et al., 1997; Planesas et al., 1997; Hägele et al., 2007; Linden et al., 2020; Calzetti et al., 2021). The star formation rate and the stellar mass are estimated to be

---

[1] With higher resolution, it might be revealed as a tightly wound double spiral emanating from the inner region of the bar instead of a continuous ring-like structure. See Helfer and Blitz (1995) for an example in NGC 1068.

~0.4 $M_\odot$ yr^{-1} and 3–10 × 10^8 $M_\odot$ in the central few kpc region (Elmegreen et al., 1997; Planesas et al., 1997; Calzetti et al., 2021). In addition, recent studies that analyzed the kinematics in the center of NGC 3351 have revealed bar-driven inflows that funnel gas/dust into the ring (e.g. Leaman et al., 2019; Lang et al., 2020). Notably, there are no signs of AGN activity in the nucleus of NGC 3351 (Goulding and Alexander, 2009; Grier et al., 2011; Gadotti et al., 2019), while Lin et al. (2018) showed that the nucleus may be a recent star formation site. This indicates that emission from the center of NGC 3351 is dominated by star formation. Leaman et al. (2019) also showed that stellar feedback processes may drive a nuclear outflow in NGC 3351 even without an AGN host. At an angular resolution of ~40″, Sandstrom et al. (2013) found a $\alpha_{\rm CO}$ value ~6× lower than the standard Milky Way value in the central 1.7 kpc of NGC 3351 with an uncertainty of < 0.2 dex. This region has an oxygen abundance similar to the solar value, so the contrast cannot be explained by a metallicity difference (Moustakas et al., 2010).

In this paper, we present new ALMA observations toward the inner ~2 kpc of NGC 3351 with the CO isotopologues ^{12}CO, ^{13}CO, and C^{18}O in their lowest rotational transitions J=1–0, 2–1, and 3–2 at a matched angular resolution of 2.1″ (~100 pc). To understand what physical processes control $\alpha_{\rm CO}$ in galaxy centers, we study the distribution of environmental conditions and $\alpha_{\rm CO}$ values in this region and investigate the possible causes of such variations. In Section 2.2, we describe the details of observations and data reduction. The resulting spectra, images and line ratios are shown in Section 2.3. In Section 2.4, we present non-local thermodynamic equilibrium (non-LTE) radiative transfer modeling and results. Section 2.5 shows our analysis of $\alpha_{\rm CO}$ variation and its possible implications. Finally, we compare our results with other literature or observations in Section 2.6, and summarize our findings in Section 2.7.

2.2 Observations and Data Reduction

Table 2.1. ALMA Observations

Line	Project Code	Rest Frequency (GHz)	n_{crit} at 20 K (cm^{-3})	Array	Beam Size (″)	LAS (″)	rms per channel (K $(2.5\ \mathrm{km\ s}^{-1})^{-1}$)
CO J=1–0	(1)	115.27	2.2×10^{3}	12m	2.1	11.9	0.320
CO J=2–1	(2)	230.54	1.1×10^{4}	12m+7m+TP	1.5	–	0.108
^{13}CO J=2–1	(1)	220.40	9.4×10^{3}	12m	1.8	10.4	0.036
^{13}CO J=3–2	(3)	330.59	3.1×10^{4}	12m	1.2	7.6	0.032
C^{18}O J=2–1	(1)	219.56	9.3×10^{3}	12m	1.8	10.4	0.036
C^{18}O J=3–2	(3)	329.33	3.1×10^{4}	12m	1.2	7.6	0.032

ALMA project codes: (1) 2013.1.00885.S, (2) 2015.1.00956.S, (3) 2016.1.00972.S. Critical densities (n_{crit}) are calculated from the Einstein-A and collisional rate coefficients provided by the Leiden Atomic Molecular Database (Schöier et al., 2005). In optically thick cases with $\tau_0 = 5$, n_{crit} of CO 1–0 and 2–1 at 20 K decrease to 6.1×10^{2} and $3.1 \times 10^{3}\ \mathrm{cm}^{-3}$, respectively (see Shirley, 2015). The rms of CO 1–0 is higher due to it being observed in a more extended array configuration, which has lower surface brightness sensitivity.

2.2.1 ALMA Observations

We obtained ALMA Band 3, 6, and 7 observations to capture CO, ^{13}CO, and C^{18}O lines as well as millimeter continuum emission from the central ~2 kpc of NGC 3351 (see Table 2.1). These observations were designed to resolve the gas structures around the starburst ring at 1–2″ (~50–100 pc) resolution. In this paper, we focus on the molecular line observations and their implied gas conditions. Results of the dust continuum will be included in a future work.

Our Band 3 observation targets the CO 1–0 line and 100–115 GHz continuum. It uses the C43-3 configuration of the ALMA 12m array to reach an angular resolution of 2.1″×1.3″ for the CO line, and a single 12m pointing covered the entire central region (~30″ in diameter). The achieved root-mean-square (rms) noise level is 0.32 K per 2.5 km s^{-1} channel (averaged across the field-of-view, out to a primary beam response threshold of 0.25). We note that Band 3 has the lowest frequency, and thus it requires a more extended array configuration to achieve an angular resolution similar to the Band 6 or 7 observations. With a more extended array configuration, the surface brightness sensitivity decreases, which leads to a higher rms level for our Band 3 data compared to the other bands for a given integration time. Although a longer integration time in Band 3 observations can reduce the noise level, the rms of 0.32 K per channel is already sufficient for secure detection of CO 1–0 over the central kpc region of NGC 3351.

Our Band 6 observation targets the $J=2$–1 transition of the ^{13}CO and C^{18}O lines as well as the 215–235 GHz continuum. With the C43-1 configuration of the ALMA 12m array, it achieves an angular resolution of 1.8″ × 1.2″ and uses a 7-pointing mosaic to cover the central 30″ × 30″ area. The achieved rms noise level is 0.036 K per 2.5 km s^{-1} channel.

Our Band 7 observation targets the $J=3$–2 transition of the ^{13}CO and C^{18}O lines and the 325–345 GHz continuum. The ALMA C40-1 configuration provides an angular resolution of 1.2″ × 1.0″ and a 14-pointing mosaic covers the central 30″ × 30″ area. The achieved rms noise level is 0.032 K per 2.5 km s^{-1} channel.

To complement these observations obtained specifically for this project, we also include the PHANGS–ALMA CO 2–1 data (Leroy et al., 2021b) in our analysis to aid the imaging and provide additional constraints on the gas temperature and isotopologue ratios. This data set was observed in Cycle 3 (project code: 2015.1.00956.S) and it reaches a similar angular resolution as the other observations used in this project. It combines ALMA 12m, 7m, and total-power (TP) observations to ensure a complete u–v coverage. The characteristics of the PHANGS–ALMA data are described in detail in Leroy et al. (2021b).

Our Band 3, 6, and 7 observations were taken with the 12m array alone and thus lack short-spacing information (see Table 2.1 for the largest angular structure (LAS) recoverable for each line). To estimate how much emission these 12m-only observations can recover, we perform a test with the PHANGS CO 2–1 data, which includes coverage of all u–v scales with 12m and 7m arrays as well as TP observations. We imaged the 12m-only PHANGS data and the 12m+7m+TP and compared the resulting maps to check flux recovery. By dividing the 12m-only image by the combined image, we find a flux recovered ratio of ~97% over the entire observed region. The analyses presented in this paper include only the pixels within a flux recovered ratio of 1 ± 0.3.

2.2.2 Calibration and Imaging

We calibrate the raw data with the calibration scripts provided by the observatory. We use the appropriate versions of the CASA pipeline to calibrate the Cycle 2 and Cycle 5 observations as recommended by the observatory (version 4.2.2 and 5.1.1, respectively).

We then image the CO lines and continuum separately with the CASA task `tclean` in two steps, as inspired by the PHANGS-ALMA imaging scheme (Leroy et al., 2021a). We weight the u–v data according to the "Briggs" scheme with a robustness parameter $r = 0.5$, which offers a good compromise between noise and resolution. We first perform a shallow, multi-scale cleaning to pick up both compact and extended emission down to a signal-to-noise ratio (S/N) of three throughout the entire field of view. After that, we perform a deep, single-scale cleaning to capture all remaining emission down to $S/N \sim 1$. This second step is restricted to within a cleaning mask, which is constructed based on the presence of significant CO 2–1 detection in the PHANGS–ALMA data. This way, the deep cleaning process can efficiently recover most remaining signals at their expected position-position-velocity (*ppv*) locations.

These calibration and imaging procedures produce high-quality data cubes for the CO lines as well as 2D images for the continuum emission.

2.2.3 Product Creation and Error Estimation

From the CO line data cubes, we derive 2D maps of integrated line intensity (moment 0), intensity-weighted velocity (moment 1), and velocity dispersion estimated using the effective line width estimator, as well as their associated uncertainties. We describe our methodology here, and note that it is very similar to that adopted in the PHANGS–ALMA pipeline (Leroy et al., 2021a; also see Sun et al., 2018).

First, we convolve all data cubes to the finest possible round beam (FWHM = 2.1″; set by the CO 1–0 resolution) to ensure that all CO line data probe the same spatial scale. Second, we estimate the local rms noise in the data cubes by iteratively rejecting CO line detection and calculating the median absolute deviation (MAD) for the signal-free *ppv* pixels. Third, we create a signal mask for each data cube by finding all *ppv* positions with $S/N > 5$ detection in more than two consecutive channels, and then expanding this signal mask to include all morphologically connected *ppv* positions with $S/N > 2$ detection in more than two consecutive channels. Fourth, we combine the signal masks for all CO lines in "union" (i.e., logical OR) to generate a master signal mask. Fifth, we collapse all CO line data cubes within this master signal mask to create moment maps, and calculate the associated uncertainties based on Gaussian error propagation. Finally, we regrid all the data products such that the new grid Nyquist-samples the beam (i.e., grid spacing equals half of the beam FWHM).

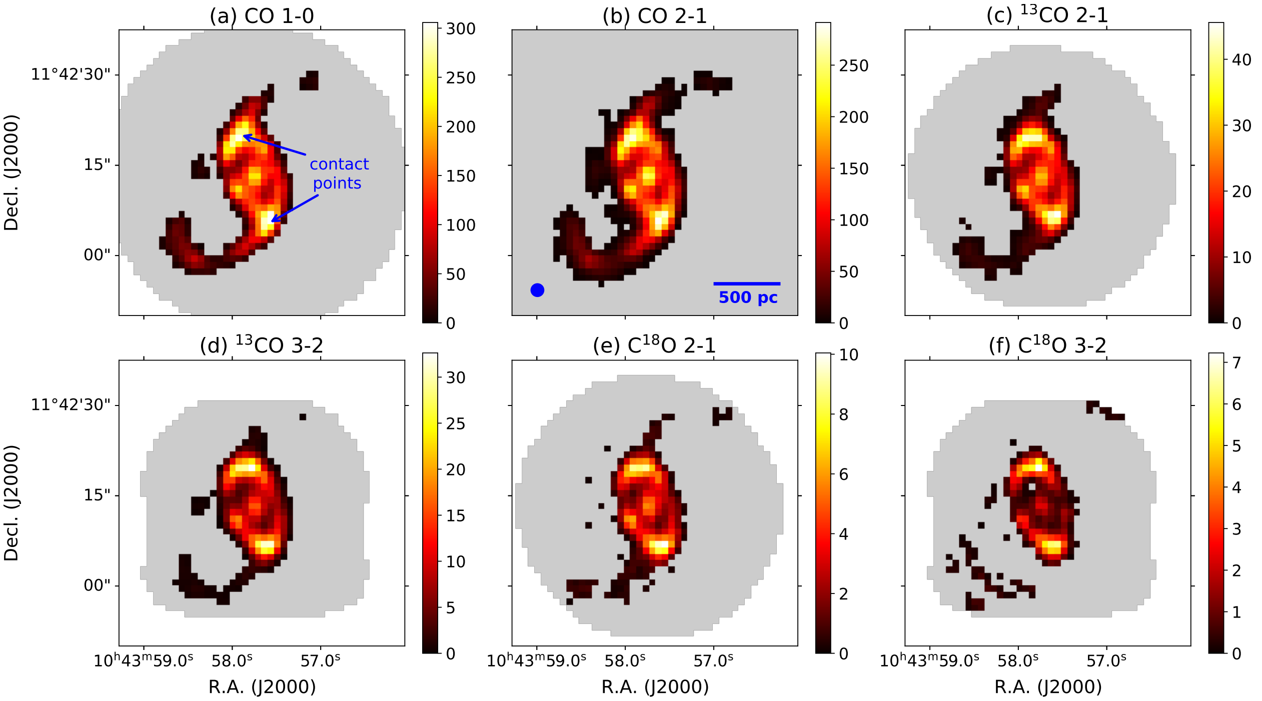

Figure 2.1. Integrated intensity maps of several CO isotopologues and rotational transitions (in units of K km s^{-1}). The matched beam size of 2.1″ and a scale bar of 500 pc is shown in panel (b). The white areas lie outside the field of view of ALMA observations, while the gray areas show the pixels without confident detection (i.e. $< 3\sigma$ for ^{12}CO and ^{13}CO and $< 1\sigma$ for C^{18}O). These images resolve a circumnuclear star-forming ring with ~20″ or 1 kpc in diameter, a gap between the ring and the nucleus, and two bar-driven inflows connected to the "contact points" at the northern and southern parts of the ring.

This product creation scheme yields a coherent set of moment maps and uncertainty maps for all the CO lines, which have matched resolution and consistently cover the same *ppv* footprint.

2.3 Results

Figure 2.1 shows the moment 0 maps of the observed CO lines. In these images, we blank pixels with $S/N < 3$ in moment 0, except for the two C^{18}O images where pixels with $S/N < 1$ are blanked. All six images resolve the circumnuclear star-forming ring structure and a gap between the ring and the nucleus. The images also reveal two spiral arm-like structures, which are gas inflows driven by the bar (also see Leaman et al., 2019; Lang et al., 2020). Note that the pixels in the central ~20″ region have $S/N > 3$ even in the

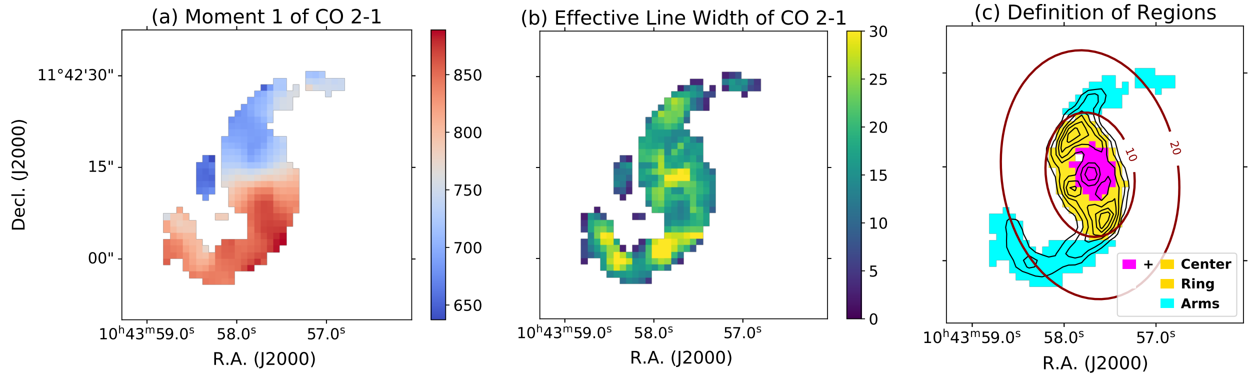

Figure 2.2. (a) Intensity-weighted velocity (moment 1) and (b) effective line width of CO 2–1, both in units of km s^{-1}. The moment 1 shows a clear sign of counterclockwise gas rotation, and the line widths are broader at the nucleus and along the arms. (c) Definition of the center, ring, and arm regions, overlaid with contour levels of the CO 2–1 integrated intensity at $I_{\rm CO(2-1)}$ = $20, 50, 100, 150, 200, 250$ K km s^{-1} and the galactocentric radius at 10″ and 20″, respectively. We will present various regional statistics based on these defined regions.

C^{18}O images, but a S/N > 1 cutoff in C^{18}O further reveals parts of the inflow arms. We will show that constraints from the C^{18}O lines are not critical to our results for the arms (Section 2.5.2), so we do not exclude pixels from the analysis based on $< 3\sigma$ detection in C^{18}O lines. The moment 1 map in Figure 2.2a shows blue-shifted spectra in the northern half of the galaxy and red-shifted spectra in the southern half, indicating a counterclockwise gas rotation along the ring. Figure 2.2b shows the effective line widths[2] of CO 2–1. The rotation also causes a large line width around the nucleus, likely due to strong, unresolved gas motions within the central beam. As marked up in Figure 2.1a, the two "contact points" connecting the ring and the inflows have the brightest emission in all the lines.

---

[2] The effective line width is defined as $\Sigma I/(\sqrt{2\pi}\,T_{\rm peak})$, where ΣI is the integrated line intensity and $T_{\rm peak}$ is the line peak temperature in K. It is referred to as "equivalent width" in Heyer et al. (2001) and subsequent works. Sun et al. (2018); Sun et al. (2020b) also introduced this quantity in detail.

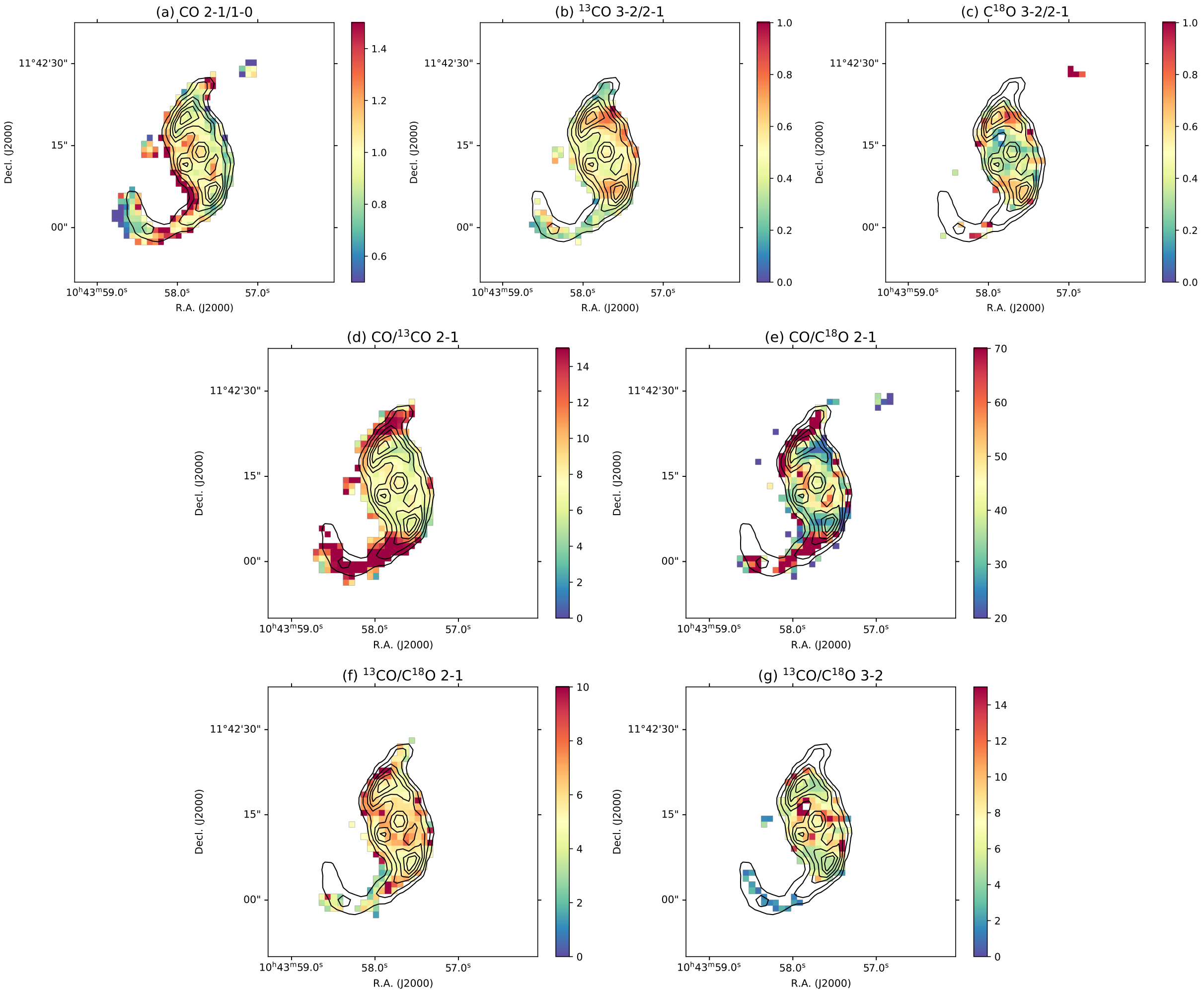

Figure 2.3. Line ratio maps. A 3σ mask in both relevant lines is applied to each panel, except for the C^{18}O lines where a 1σ cutoff is applied. Contour levels of the CO 2–1 emission are the same as in Figure 2.2c. (a)–(c) show the primarily temperature-sensitive line ratios, and (d)–(g) show the line ratios primarily sensitive to isotopologue abundances or optical depths. The CO 2–1/1–0 ratio of ~1 suggests optically thick and thermalized emission in this region. Notably, the arm regions show significantly higher CO/^{13}CO and CO/C^{18}O line ratios than the center.

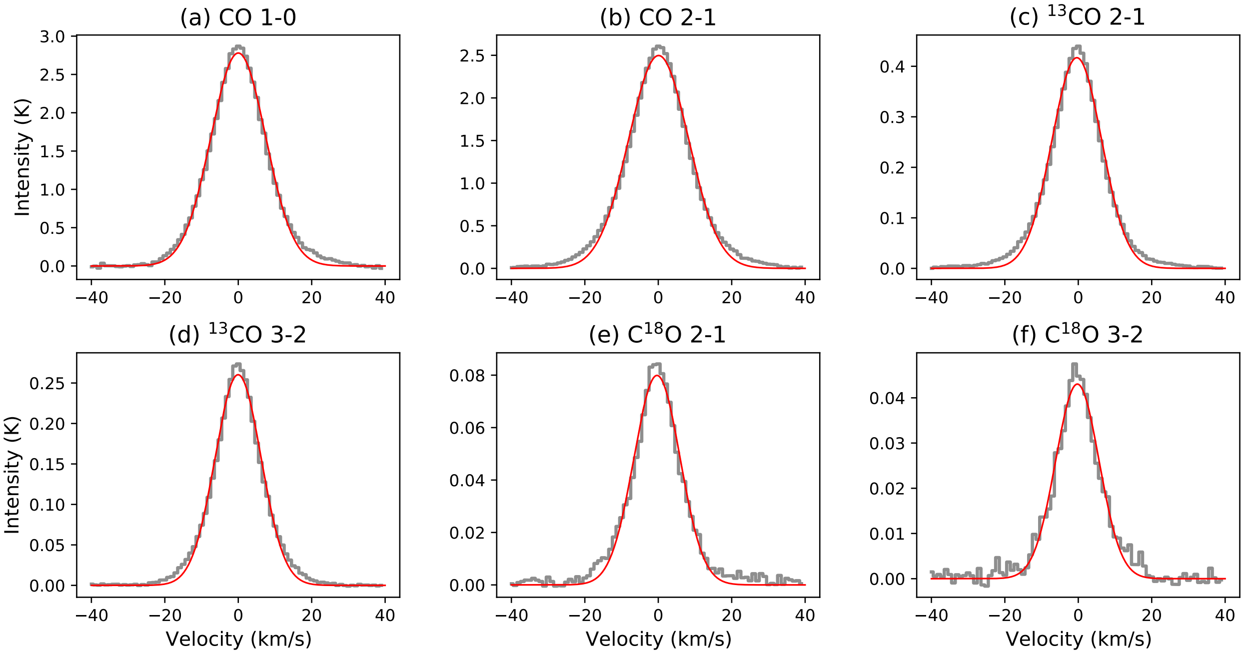

Figure 2.4. Shifted and stacked spectra over the center region, overlaid with the best-fit Gaussian profiles. All six lines show a single-peaked spectrum that can be well-described by a Gaussian function. The ring region also shows similar spectra, except having a slightly higher peak temperature and a ~1 km s^{-1} narrower line width. The averaged spectra for the arms region is presented in Figure 2.12.

Table 2.2. Regional Line Ratios in NGC 3351.

Region		CO $\frac{2-1}{1-0}$	^{13}CO $\frac{3-2}{2-1}$	C^{18}O $\frac{3-2}{2-1}$	$\frac{\mathrm{CO}}{^{13}\mathrm{CO}}$ 2–1	$\frac{\mathrm{CO}}{\mathrm{C^{18}O}}$ 2–1	$\frac{^{13}\mathrm{CO}}{\mathrm{C^{18}O}}$ 2–1	$\frac{^{13}\mathrm{CO}}{\mathrm{C^{18}O}}$ 3–2
Whole	Median	0.99	0.51	0.47	7.99	42.86	5.69	6.48
	Mean	1.03	0.50	0.51	10.67	53.63	5.92	7.08
	Std. Dev.	0.31	0.14	0.23	5.67	38.56	2.10	3.63
	Integrated Mean	1.01	0.55	0.50	8.06	45.68	5.67	6.22
Center	Median	0.99	0.54	0.46	7.02	41.10	5.75	6.89
	Mean	1.01	0.55	0.48	7.38	46.21	6.06	7.75
	Std. Dev.	0.21	0.10	0.18	1.86	23.45	1.51	3.30
	Integrated Mean	0.98	0.57	0.51	7.11	39.41	5.54	6.25
Ring	Median	0.99	0.56	0.52	7.01	40.33	5.57	6.37
	Mean	1.01	0.57	0.52	7.49	47.24	6.04	7.27
	Std. Dev.	0.23	0.10	0.18	2.10	26.91	1.69	3.11
	Integrated Mean	0.98	0.60	0.55	7.13	38.65	5.42	5.86
Arms	Median	0.98	0.33	0.87	15.67	60.25	4.53	1.92
	Mean	1.00	0.35	0.88	16.71	69.36	5.11	1.84
	Std. Dev.	0.33	0.14	0.38	6.05	49.30	2.17	0.60
	Integrated Mean	1.06	0.25	0.52	20.21	141.97	7.02	3.33

Line ratios are calculated using the moment 0 maps in units of K km s^{-1}. The integrated means are calculated by first averaging the integrated intensities in each region and then dividing to obtain the ratios, while the mean, median and standard deviation are for the individual pixels of the map. Due to poor detection of C^{18}O 3–2 in the arms, the statistics for C^{18}O 3–2/2–1 and ^{13}CO/C^{18}O 3–2 in the arms are only based on a few pixels.

Using the six moment 0 maps in units of K km s^{-1}, we generate seven line ratio maps as shown in Figure 2.3: the primarily temperature sensitive line ratios are presented in the top row (a–c) as CO 2–1/1–0, ^{13}CO 3–2/2–1, and C^{18}O 3–2/2–1; the following rows (d–g) show CO/^{13}CO 2–1, CO/C^{18}O 2–1, ^{13}CO/C^{18}O 2–1, and ^{13}CO/C^{18}O 3–2, which are primarily sensitive to isotopologue abundance ratios and/or optical depths. There are notable variations in the line ratios throughout the map. The main trends appear to be increased ^{13}CO 3–2/2–1 and C^{18}O 3–2/2–1 in regions of the star-forming ring, potentially revealing higher temperatures, though it is interesting to note that these trends are not mirrored in CO 2–1/1–0 likely due to the emission being optically thick and thermalized. In addition, the west side of the northern contact point near $(\mathrm{R.A.}, \mathrm{Decl.}) = (10^{\mathrm{h}}43^{\mathrm{m}}57\overset{\mathrm{s}}{.}7, 11^{\circ}42'20'')$ shows enhanced ratios in 3–2/2–1 of ^{13}CO and C^{18}O, which may imply a change in excitation conditions. The region also has lower ratios in the CO/^{13}CO and CO/C^{18}O 2–1 maps due to fainter emission in CO lines. There is a clear trend for both CO/^{13}CO and CO/C^{18}O 2–1 to increase in the arms, possibly indicating a significant change of abundance ratios or optical depths. As star formation occurs only in the ring/nucleus but not the inflows, enrichment of ^{13}C or ^{18}O could lower the CO/^{13}CO or CO/C^{18}O abundances and thus lower the CO/^{13}CO and CO/C^{18}O line ratios in the ring/nucleus. On the other hand, the enhanced velocity dispersion in the arms as shown in Figure 2.2b may also lower the optical depths, leading to more escape CO emission and higher CO/^{13}CO and CO/C^{18}O line ratios in the arms. Note that higher line ratios are not observed in the nucleus where the effective line widths are also broader, which is likely due to beam smearing effects. More details will be discussed in Section 2.5.2.

We define three regions for our analysis: the center, ring, and arms. Figure 2.2c illustrates the definition of these regions. The center is defined as the central 20″ or ~1 kpc (in galactocentric diameter) where $\mathrm{S/N} > 3$ in the moment 0 maps of all six lines. The ring region shares the same outer edge as the center, but excludes the inner 9″ or ~450 pc region of the center. The arms region includes only the pixels outside a 20″ diameter but excludes the “blob” that lies to the east of the center. Figure 2.4 shows the averaged spectra over the center region, where we applied the stacking approach by Schruba et al. (2011) and used the moment 1 of CO 2–1 as velocity centroids. The shapes of the averaged spectra over the ring are almost identical to the center, while they show slightly higher peak intensities and ~1 km s^{-1} narrower line widths. This is because the ring region excludes the emission-faint “gap” region and the nucleus which has high velocity dispersion. The spectra of the arms are presented and analyzed in Section 2.5.2.

Table 2.2 lists the line ratios averaged over the whole map and for the center, ring, and arm regions separately. The means, medians and standard deviations are calculated with the ensemble of line ratio in each pixel, and we also present the integrated means where the line fluxes are first summed up in each region to calculate the ratios. We note that due to poor detection of $C^{18}O$ in the arms, the averaged $C^{18}O$ 3–2/2–1 ratio of the arms is based on only few pixels. As shown in Table 2.2, the CO 2–1/1–0 ratio is ~1.0 in all regions, which would indicate optically thick, thermalized emission. The $CO/^{13}CO$ and $CO/C^{18}O$ ratios vary the most from the center/ring to the arms. Also, the ^{13}CO 3–2/2–1 ratio is lower in the arms compared to the rest, which may indicate changes in temperature or density. As these line ratio variations may imply variations in environmental conditions, we investigate the spatial distribution of multiple physical parameters through joint analysis of all the observed lines using non-LTE radiative transfer modeling and Bayesian likelihood analyses in Section 2.4.

2.4 Multi-line Modeling

2.4.1 Modeling Setup

We use the non-LTE radiative transfer code RADEX (van der Tak et al., 2007) to model the observed line intensities under various combinations of H_2 density (n_{H_2}), kinetic temperature (T_k), CO column density per line width ($N_{CO}/\Delta v$), $CO/^{13}CO$ ($X_{12/13}$) and $^{13}CO/C^{18}O$ ($X_{13/18}$) abundance ratios, and the beam-filling factor (Φ_{bf}). The beam-filling

Table 2.3. Model Grid Parameters

Parameter	Range	Step Size
	One-Component Models	
$\log(n_{\mathrm{H_2}}\ [\mathrm{cm^{-3}}])$	2.0–5.0	0.2 dex
$\log(T_{\mathrm{k}}\ [\mathrm{K}])$	1.0–2.3	0.1 dex
$\log(N_{\mathrm{CO}}\ [\mathrm{cm^{-2}}])$	16.0–21.0	0.2 dex
$X_{12/13}$	10–200	10
$X_{13/18}$	2–20	1.5
Φ_{bf}	0.05–1.0	0.05
$\Delta v\ [\mathrm{km\ s^{-1}}]$	15.0	–
	Two-Component Models	
$\log(n_{\mathrm{H_2}}\ [\mathrm{cm^{-3}}])$	2.0–5.0	0.25 dex
$\log(T_{\mathrm{k}}\ [\mathrm{K}])$	1.0–2.0	0.1 dex
$\log(N_{\mathrm{CO}}\ [\mathrm{cm^{-2}}])$	16.0–19.0	0.25 dex
$\log(\Phi_{\mathrm{bf}})$	$-1.3 \ldots -0.1$	0.1
$X_{12/13}$	25	–
$X_{13/18}$	8	–
$\Delta v\ [\mathrm{km\ s^{-1}}]$	15.0	–

factor is a fractional area of the beam covered by the emitting gas, and thus it should be ≤ 1. Tests of the recoverability of model parameters with RADEX fitting have shown that modeling the isotopologue abundance ratio as a free parameter leads to more accurate results than assuming a fixed ratio (Tunnard and Greve, 2016). With six measured lines, we construct two different models with a one-component or two-component assumption on gas phases. The setup for these models are described separately in Section 2.4.2 and 2.4.3.

The input to RADEX includes a molecular data file specifying the energy levels, statistical weights, Einstein A-coefficients, and collisional rate coefficients of each specific molecule. The data files we use for CO, ^{13}CO, and C^{18}O are from the Leiden Atomic and Molecular Database (Schöier et al., 2005) with collisional rate coefficients taken from Yang et al. (2010). To run RADEX, we directly input the T_{k}, $n_{\mathrm{H_2}}$, molecular species column density (N), and line width (Δv). The input T_{k} and $n_{\mathrm{H_2}}$ are used to set collisional excitation, while N and Δv are the radiative transfer parameters that determine the optical depth and escape probability for the modeled molecular emission line.

RADEX assumes a homogeneous medium and uses radiative transfer equations based on the escape probability formalism (Sobolev, 1960) to find a converged solution for the excitation and radiation field. Initially, RADEX guesses the population of each energy level under LTE assumption and then computes for each transition the resultant optical depth at the line center (τ_0) by

$$\tau_0 = \frac{A_{ij}}{8\pi\tilde{\nu}^3}\,\frac{N}{\Delta v}\left(x_j\frac{g_i}{g_j} - x_i\right)\ , \tag{2.3}$$

where A_{ij} is the Einstein A-coefficient, $\tilde{\nu}$ is the wave number, and x_i and g_i are the fractional population and statistical weight, respectively, in level i. The optical depth then determines the escape probability (β) for a uniform sphere:

$$\beta = \frac{1.5}{\tau}\left[1 - \frac{2}{\tau^2} + \left(\frac{2}{\tau} + \frac{2}{\tau^2}\right)e^{-\tau}\right]\ , \tag{2.4}$$

which estimates the fraction of photons that can escape the cloud (Osterbrock and Ferland, 2006). This directly constrains the radiation field, and thus a new estimation of level population and excitation temperature, leading to new optical depth values. This procedure is done iteratively until convergence is reached.

We first run RADEX with CO to build up a 3D grid with varying $N_{\mathrm{CO}}/\Delta v$, $n_{\mathrm{H_2}}$, and T_{k}. To construct a model grid with $X_{12/13}$ and $X_{13/18}$ axes, we calculate the column densities of ^{13}CO and C^{18}O that correspond to each varying $N_{\mathrm{CO}}/\Delta v$ and abundance ratios, and then re-run RADEX with the calculated $N_{^{13}\mathrm{CO}}/\Delta v$ and $N_{\mathrm{C^{18}O}}/\Delta v$ values. The RADEX output of the three molecules predicts a Rayleigh–Jeans equivalent temperature (T_{RJ}) for each line under the varied parameters. Assuming a Gaussian profile, the predicted line fluxes can then be estimated using a Gaussian integral:

$$\int T_{\mathrm{RJ}}\,\mathrm{d}v = \frac{\sqrt{\pi}}{2\sqrt{\ln 2}}\,T_{\mathrm{RJ}}\,\Delta v\ , \tag{2.5}$$

where Δv is the FWHM line width. Finally, we expand the grid with an additional axis of beam-filling factor (Φ_{bf}) by multiplying the predicted line integrated intensities with the varying $\Phi_{\rm bf}$. This assumes the same beam-filling factor among all six emission lines. Note that since we are essentially fitting $N_{\rm CO}/\Delta v$ with RADEX (see Equation 2.3), the estimation of $N_{\rm CO}$ would vary with line widths in different regions. Thus, when $N_{\rm CO}$ values are needed in further analyses, we multiply $N_{\rm CO}/\Delta v$ with the observed CO 1–0 line width for each pixel. This assumes all six lines to have the same line width, which is consistent with our assumption of single-component gas in Section 2.4.2. We have checked that adopting the CO 2–1 line width also results in similar $N_{\rm CO}$, as the line widths of 1–0 and 2–1 agree to within 50%. The high-S/N emission in ^{13}CO also yields similar line widths to those from the low-J CO emission - e.g., the mean CO 1–0/^{13}CO 2–1 line width ratio is 1.07 ± 0.21. We do not consider the low-S/N pixels because the line widths are very uncertain at low S/N and therefore do not provide a strong constraint.

To evaluate the goodness of fit for each parameter set $\theta = (n_{\rm H_2}$, $T_{\rm k}$, $N_{\rm CO}/\Delta v$, $X_{12/13}$, $X_{13/18}$, $\Phi_{\rm bf})$, we compute the χ^2 values at each point in the model grid:

$$\chi^2(\theta) = \sum_{i=1}^{n} \frac{\left[S_i^{\rm mod}(\theta) - S_i^{\rm obs}\right]^2}{\sigma_i^2} \ , \tag{2.6}$$

where $S^{\rm mod}$ and $S^{\rm obs}$ are the modeled and observed line integrated intensities with uncertainty σ_i, and $n = 6$ since we consider six lines. To include both the measurement and calibration uncertainties, σ_i can be written as $\sigma_i^2 = \sigma_{{\rm noise},\,i}^2 + \sigma_{\rm cal}^2$, where $\sigma_{{\rm noise},\,i}$ is simply the measurement uncertainty of the ith observed line intensity and $\sigma_{\rm cal}$ represents the calibration uncertainty. For ALMA Band 3, 6, and 7 observations, a flux calibration uncertainty of $\gtrsim$5% is suggested for point sources (Bonato et al., 2018; Bonato et al., 2019), and an additional few percent should be added for extended sources (e.g., Tunnard and Greve, 2016; Leroy et al., 2021a). Thus, we adopt a 10% calibration uncertainty (i.e., $\sigma_{\rm cal} = 0.1 \times$ flux) for each line and assume independent calibrations. Although there should exist correlations between the calibration uncertainties for lines observed in the same spectral setup with the same calibrator, assuming independent calibrations is a less stringent constraint and therefore more conservative for the modeling.

The best-fit parameter set can be determined by selecting the combination with the lowest χ^2 value. By assuming a multivariate Gaussian probability distribution, the χ^2 value for each parameter set can be converted to the probability as

$$P(S^{\mathrm{obs}}|\theta) = \frac{1}{Q}\ \exp\left[-\frac{1}{2}\chi^2(\theta)\right] , \tag{2.7}$$

where $Q^2 = \Pi_i(2\pi\sigma_i)$. We calculate this probability for each grid point in the model parameter space, and we make our grid space wide enough to cover all grid points with reasonably high likelihood. Next, we generate the marginalized 1D or 2D likelihood distributions for any given parameter(s) by summing the joint probability distribution over the full range of all other parameters except the one(s) of interest. With such marginalized 1D likelihood distributions, we find the "1DMax" solutions that give the highest 1D likelihood in each parameter. We also determine the 50th percentile values (i.e., medians) of the cumulative 1D likelihoods and compare them with the 1DMax values to better understand the probability distributions. This procedure of computing the χ^2 values and the likelihood distributions is applied to every pixel of the galaxy image in order to generate maps of the galaxy showing the derived physical parameters. In Sections 2.4.2 and 2.4.3, we present these results based on a one-component model with six free parameters and a two-component model with eight free parameters, respectively. For reproducibility, we release all the source code and parameters in a GitHub repository[3].

2.4.2 One-Component Models

Assuming that the gas along each line of sight is uniform and that the emission can be described by a single physical condition ($n_{\mathrm{H_2}}$, T_{k}, $N_{\mathrm{CO}}/\Delta v$, $X_{12/13}$, $X_{13/18}$) with an identical filling factor Φ_{bf} across all lines, we create intensity model grids for each observed transition. As listed in Table 2.3, the model can be represented by a six-dimensional grid

---

[3] https://github.com/ElthaTeng/multiline-ngc3351

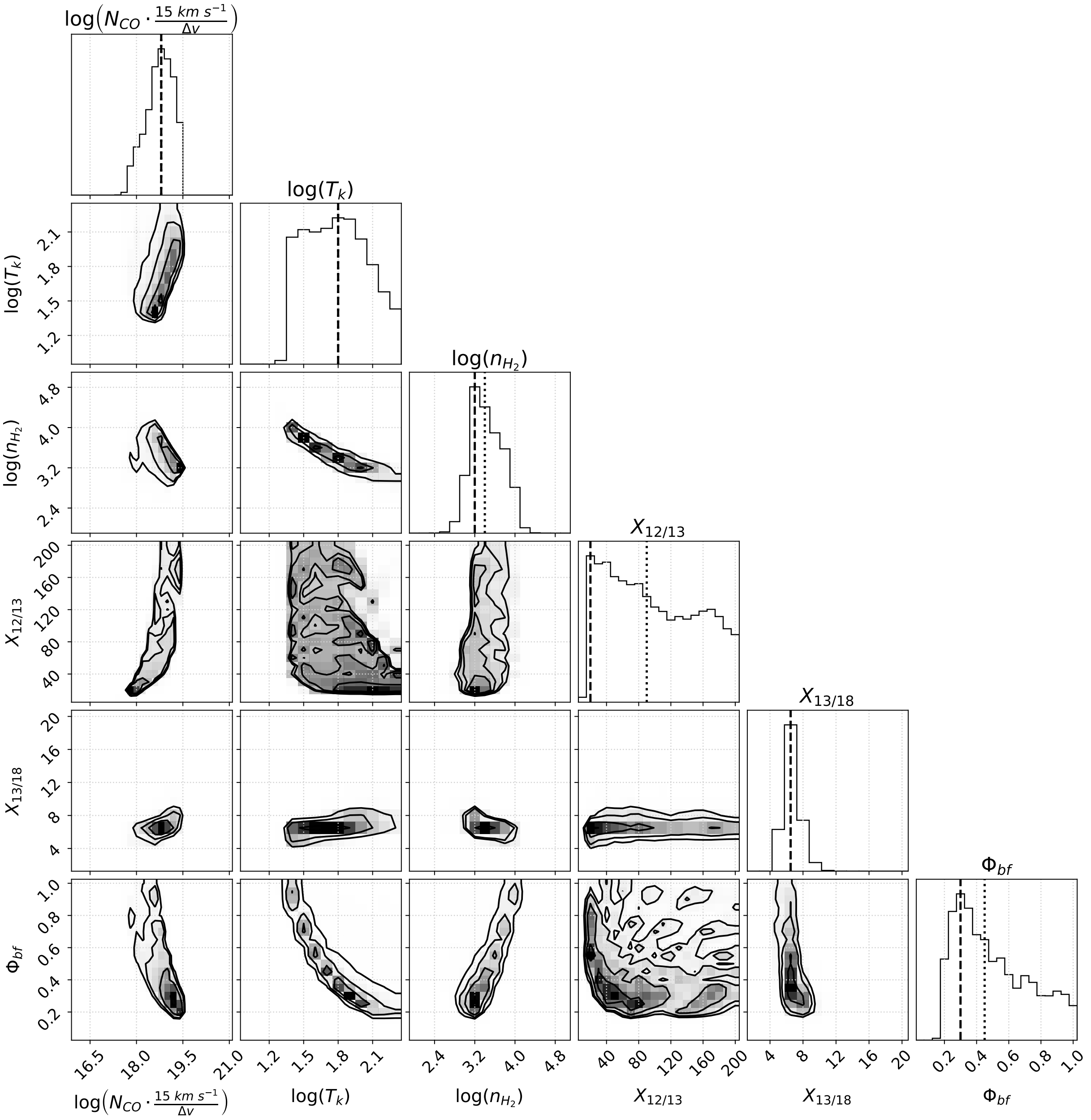

Figure 2.5. Marginalized 1D and 2D likelihood distributions of a bright pixel at (R.A., Decl.) = $(10^{\mathrm{h}}43^{\mathrm{m}}57\overset{\mathrm{s}}{.}9, 11^\circ42'19\overset{''}{.}5)$ in the northern contact point. The dashed lines on the 1D likelihood plots (in diagonal) represent the "1DMax" values that correspond to the peaks of each 1D likelihood. The dotted lines show the medians of the cumulative probability density function. For a less-constrained parameter like $X_{12/13}$, the median (~90) can substantially deviate from the 1DMax value (~20). However, the 1DMax solutions of $X_{12/13}$ are found to be consistent over the central ~1 kpc region, as shown in Figure 2.8.

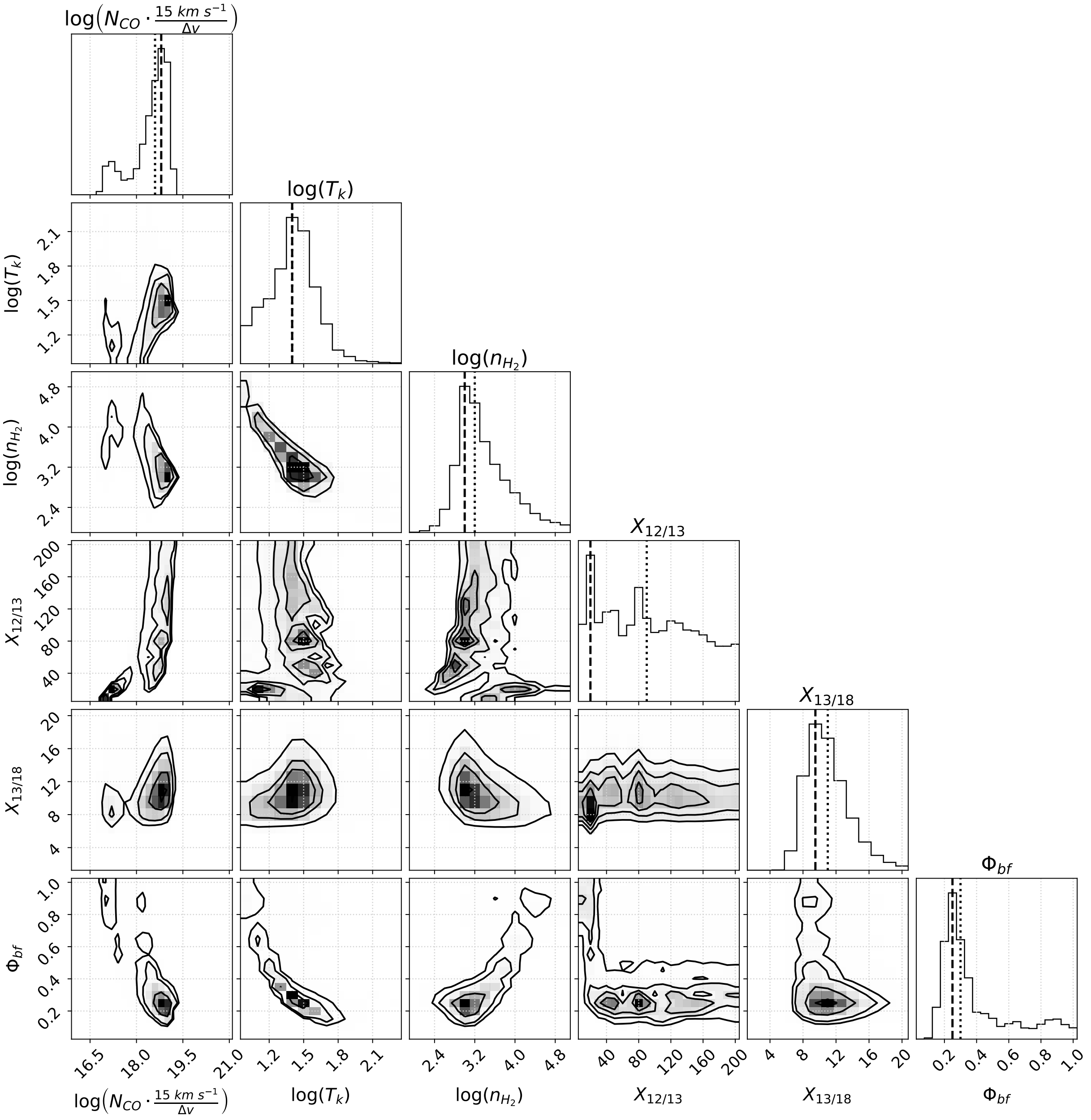

Figure 2.6. Marginalized 1D and 2D likelihood distributions of a faint pixel at (R.A., Decl.) = $(10^{\mathrm{h}}43^{\mathrm{h}}57\overset{\mathrm{s}}{.}8, 11^{\circ}42'15\overset{''}{.}5)$ in the gap region between the ring and the nucleus. See the caption of Figure 2.5 for more information.

Table 2.4. 1DMax Solutions from One-Component Modeling

Region		$\log\left(N_{\rm CO}\,\frac{15\ {\rm km\ s^{-1}}}{\Delta v}\right)$ (cm^{-2})	$\log T_{\rm k}$ (K)	$\log n_{\rm H_2}$ (cm^{-3})	$X_{12/13}$	$X_{13/18}$	$\Phi_{\rm bf}$
Whole	Median	17.8	1.2	3.2	30	8.0	0.20
	Mean	17.46	1.35	3.46	51.46	10.43	0.23
	Std. Dev.	1.13	0.41	0.76	58.31	6.48	0.19
Center	Median	18.4	1.3	3.2	20	6.5	0.25
	Mean	18.30	1.34	3.33	22.42	7.38	0.26
	Std. Dev.	0.59	0.22	0.40	14.64	1.66	0.16
Ring	Median	18.4	1.3	3.2	20	6.5	0.20
	Mean	18.21	1.33	3.38	22.94	7.12	0.26
	Std. Dev.	0.65	0.22	0.43	16.66	1.74	0.18
Arms	Median	16.2	1.1	3.2	40	15.5	0.15
	Mean	16.83	1.35	3.48	78.56	12.38	0.21
	Std. Dev.	0.99	0.51	0.93	67.51	7.86	0.20

The statistics are determined for the ensemble of 1DMax solutions across the pixels. The standard deviation does not reflect the uncertainties in the 1D likelihoods of each pixel.

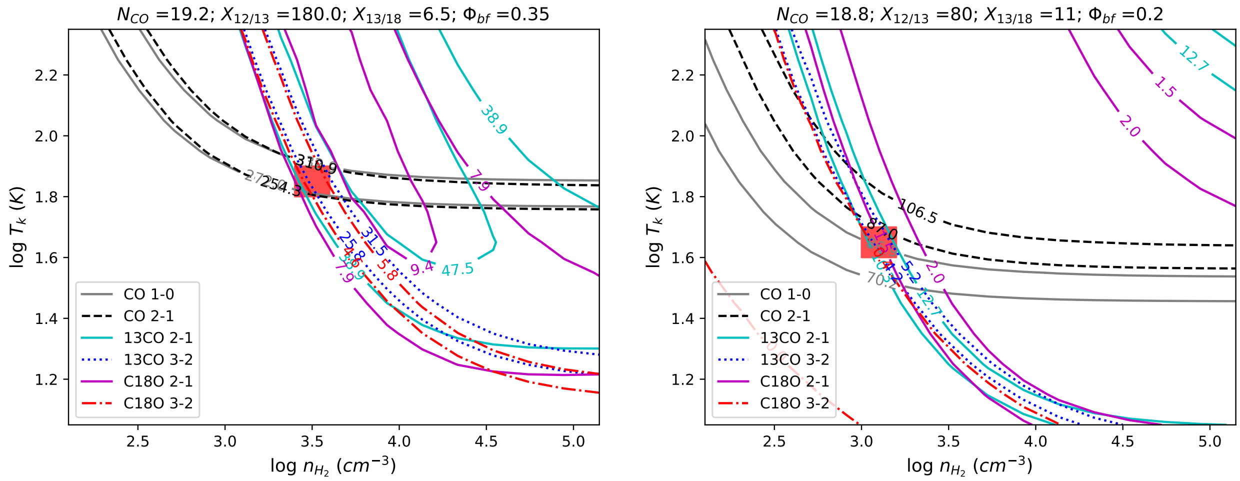

(a)

(b)

Figure 2.7. Best-fit (i.e. highest likelihood) constraints from the six observed line fluxes at the same pixel as in (a) Figure 2.5 and (b) Figure 2.6. Contours show the ranges of observed line intensities ±1σ uncertainties, including the measurement uncertainty from the data and a 10% flux calibration uncertainty. Red boxes represent the best-fit solutions. Note that these are the solutions with the lowest χ^2 value in the full grid, not the 1DMax solutions based on marginalized probability distributions, and thus the $X_{12/13}$ values here deviate from the lower $X_{12/13} \sim 20$ suggested by 1DMax solutions. Except for $X_{12/13}$, other parameters are similar to the 1DMax solutions as their 1D likelihoods are single-peaked and well-constrained.

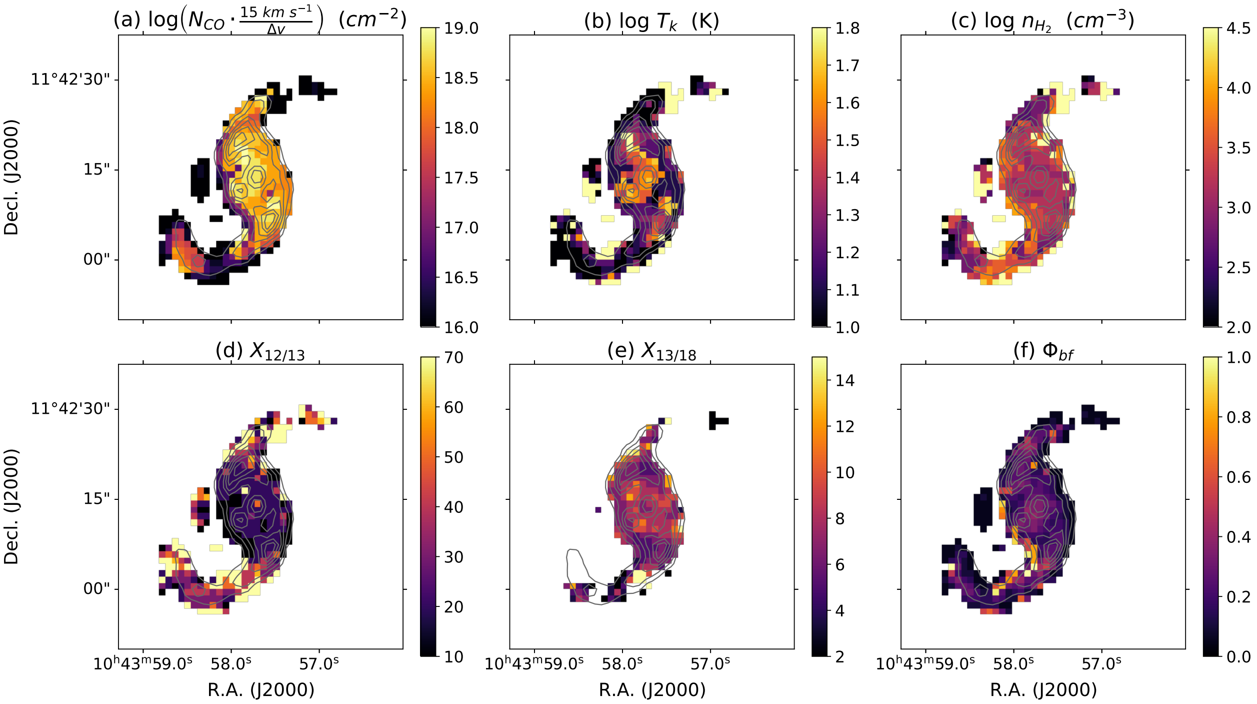

Figure 2.8. Maps of the 1DMax physical conditions derived from the one-component model. Panel (a) shows log(N_{CO}) assuming a constant line width of 15 km s^{-1} over the whole region. Contours represent the CO 2–1 emission shown in Figure 2.1b. A 1σ mask of the C^{18}O 2–1 image is applied to (e). These results show that N_{CO} is higher in the center, T_{k} is higher near the nucleus and the contact points, and $n_{\mathrm{H_2}}$ is overall $\sim 2 \times 10^3$ cm^{-3}. The $X_{12/13}$ and $X_{13/18}$ abundances are found to be consistent with those in the center of Milky Way.

with $\log(n_{\mathrm{H_2}}\ [\mathrm{cm^{-3}}])$ varied from 2 to 5 in steps of 0.2 dex, T_{k} from 10 to 200 K in steps of 0.1 dex, $N_{\mathrm{CO}}/\Delta v$ from $10^{16}/15$ to $10^{21}/15$ $\mathrm{cm^{-2}}$ $(\mathrm{km\ s^{-1}})^{-1}$ in steps of 0.2 dex, $X_{12/13}$ from 10 to 200 in steps of 10, $X_{13/18}$ from 2 to 20 in steps of 1.5, and Φ_{bf} from 0.05 to 1 in steps of 0.05. The range of $N_{\mathrm{CO}}/\Delta v$ covers reasonable $N_{\mathrm{H_2}}$ ranges of $\sim 10^{20}$–10^{25} $\mathrm{cm^{-2}}$ with typical CO/H$_2$ abundance ratios of $\sim 10^{-4}$, and all the parameter ranges were optimized from representative pixels such that the shapes of the 1D likelihood distributions are well-covered for typical bright and faint regions in the galaxy.

We apply a prior on the path length of the molecular gas along the line of sight. The idea of applying priors on line-of-sight lengths to avoid unrealistic solutions was also adopted in Kamenetzky et al. (2014) and is supported by Tunnard and Greve (2016). The line-of-sight path length is calculated by $\ell_{\mathrm{los}} = N_{\mathrm{CO}}(\sqrt{\Phi_{\mathrm{bf}}}\, n_{\mathrm{CO}})^{-1}$, where $n_{\mathrm{CO}} = n_{\mathrm{H_2}}\, x_{\mathrm{CO}}$ and x_{CO} is the CO/H$_2$ abundance ratio which we assume a typical value of 3×10^{-4} for starburst regions (Lacy et al., 1994; Ward et al., 2003; Sliwa et al., 2014). The $\sqrt{\Phi_{\mathrm{bf}}}$ factor can be interpreted as the one-dimensional filling factor along the line of sight to match the area filling factor Φ_{bf}, and the same equation was also adopted by Ward et al. (2003) and Kamenetzky et al. (2012); Kamenetzky et al. (2014). With an angular resolution of $\sim$100 pc, we require all parameter sets in our model grids to have line-of-sight path length $\ell_{\mathrm{los}} \leq 100$ pc. The 100 pc path length is also consistent with the vertical height (thickness) of CO observed in the central few kpc of Milky Way and other nearby edge-on galaxies (Yim et al., 2014; Heyer and Dame, 2015). We have checked that relaxing the constraint to 200 pc results in similar best-fit and 1DMax solutions, and thus the result is not sensitive to factor of $\sim$2 changes in the line-of-sight constraint. The change in the gas thickness along the line of sight due to galaxy inclination would not alter the results. We note that all the parameters for calculating ℓ_{los} are the varied inputs of our model except for the constant x_{CO} and the observed line width to obtain N_{CO} from $N_{\mathrm{CO}}/\Delta v$. In other words, we adopt $\ell_{\mathrm{los}} < 100$ pc as a prior by setting a zero probability to all the parameter sets that violate this constraint, and then investigate the resultant likelihood distributions. This prior generally rules out solutions with $N_{\rm CO} \gtrsim 10^{19}$ cm^{-2} or $n_{\rm H_2} \lesssim 3 \times 10^2$ cm^{-3}, as either a high column density or a low volume density would lead to large $\ell_{\rm los}$. We also find that the primary effect of allowing larger path lengths would be to shift the solutions to higher $N_{\rm CO}$ while $n_{\rm H_2}$ and $T_{\rm k}$ stay roughly constant, and we do not think that such large $N_{\rm CO}$ values and path lengths are reasonable solutions.

Figures 2.5 and 2.6 are two corner plots (Foreman-Mackey, 2016) showing the marginalized likelihood distributions of a bright pixel at (R.A., Decl.) = ($10^{\rm h}43^{\rm m}57\overset{\rm s}{.}9$, $11^\circ42'19\overset{''}{.}5$) in the northern contact point and a faint pixel at ($10^{\rm h}43^{\rm m}57\overset{\rm s}{.}8, 11^\circ42'15\overset{''}{.}5$) in the gap region between the ring and the nucleus. The 1D likelihoods of $N_{\rm CO}$, $T_{\rm k}$, $n_{\rm H_2}$, and $X_{13/18}$ are well-constrained in both pixels. On the other hand, $X_{12/13}$ is loosely constrained compared to other parameters, and the peaks in both 1D likelihoods (i.e. 1DMax, indicated by the dashed lines) are consistently at a lower $X_{12/13}$ of ~20–30. This leads to a deviation between the 1DMax solutions and the medians (median $X_{12/13} \sim$ 90–100, indicated by the dotted lines). Even though the 1D likelihoods of $X_{12/13}$ along each sight line may be less-constrained than other parameters, we will show that the 1DMax solutions of $X_{12/13}$ are consistent over the central ~1 kpc region.

We note that some parameters show correlations in their 2D likelihoods, including $N_{\rm CO}$–$n_{\rm H_2}$, $T_{\rm k}$–$n_{\rm H_2}$, and $N_{\rm CO}$–$\Phi_{\rm bf}$. Below the critical densities of the optically thin lines (see Table 2.1), the emissivity depends on the density. Therefore, the anti-correlation between $N_{\rm CO}$ and $n_{\rm H_2}$ is expected, as a larger column density is needed to produce the same emission if we decrease the volume density with all other parameters fixed. Similarly, as $n_{\rm H_2}$ decreases, $T_{\rm k}$ has to increase to produce the same intensity if all other parameters remain unchanged. The inversely correlated $N_{\rm CO}$–$\Phi_{\rm bf}$ may imply well-constrained total mass of CO, as $M_{\rm mol} \propto N_{\rm CO}\,\Phi_{\rm bf}$ (see Equation 2.9). In Figure 2.7, we show how well the best-fit (i.e. highest likelihood in the grid) solutions for the two corresponding pixels in Figures 2.5 and 2.6 match the constraints given by the observed line fluxes. The contour values are set as the ranges of observed line intensities $\pm 1\sigma$ uncertainties, which include the measurement uncertainty from the data and a 10% flux calibration uncertainty. Note that the best-fit solutions of $X_{12/13}$ also deviate from the 1DMax solutions at ~20–30.

We present the pixel-by-pixel maps and regional statistics of all six 1DMax parameters in Figure 2.8 and Table 2.4, respectively. It is clear that the CO column densities are highest in the center and the ring, while the average H_2 densities are similar in all regions. Although the average temperatures from Table 2.4 are also similar in each region, Figure 2.8b reveals a higher kinetic temperature of ~30–60 K near the nucleus and both contact points. High-resolution studies at pc scales toward the inner ~500 pc (Central Molecular Zone, CMZ) of the Milky Way suggested a dominant gas component with a temperature of ~25–50 K (Longmore et al., 2013; Ginsburg et al., 2016; Krieger et al., 2017), which is consistent with the temperatures we find near the nucleus and contact points. In addition, we find that these peaks in the T_k map cover several circumnuclear star-forming regions identified by previous UV, Hα, near-infrared or radio observations (Colina et al., 1997; Planesas et al., 1997; Hägele et al., 2007; Linden et al., 2020; Calzetti et al., 2021), and thus higher temperatures could be related to the heating from young stars. We also find consistent 1DMax values of $X_{12/13} \sim 20$–30 and $X_{13/18} \sim 6$–10 inside the central ~1 kpc region. Unlike $X_{12/13}$, the 1DMax solutions for $X_{13/18}$ are consistent with the medians and are very well constrained over the central region. Both the 1DMax $X_{12/13}$ and $X_{13/18}$ abundance ratios are consistent with those found in the central kpc of the Milky Way (Langer and Penzias, 1990; Wilson and Rood, 1994; Milam et al., 2005; Wouterloot et al., 2008; Areal et al., 2018). We note that only the "center" pixels defined in Figure 2.2c have $\mathrm{S/N} > 3$ in the $\mathrm{C^{18}O}$ images, and thus pixel-by-pixel estimation beyond this region could be subject to larger uncertainties. Therefore, to examine our pixel-based results in the arm regions, we conduct similar analysis using stacked spectra in Section 2.5.2.

2.4.3 Two-Component Models

Table 2.5. 1DMax Solutions from Two-Component Modeling

Region		$\log\left(N_1\,\frac{15\ \mathrm{km\ s^{-1}}}{\Delta v}\right)$ (cm^{-2})	$\log T_1$ (K)	$\log n_1$ (cm^{-3})	$\log\Phi_1$	$\log\left(N_2\,\frac{15\ \mathrm{km\ s^{-1}}}{\Delta v}\right)$ (cm^{-2})	$\log T_2$ (K)	$\log n_2$ (cm^{-3})	$\log\Phi_2$
Whole	Median	17.00	1.1	3.75	-0.6	17.00	2.0	3.25	-0.8
	Mean	17.01	1.27	3.55	-0.68	17.17	1.74	3.00	-0.79
	Std. Dev.	0.85	0.31	0.74	0.42	1.00	0.36	0.64	0.40
Center	Median	17.75	1.3	3.50	-0.5	18.25	2.0	3.25	-0.7
	Mean	17.80	1.38	3.61	-0.55	18.11	1.90	3.15	-0.71
	Std. Dev.	0.53	0.25	0.48	0.30	0.45	0.24	0.39	0.26
Ring	Median	17.75	1.4	3.75	-0.5	18.00	2.0	3.25	-0.7
	Mean	17.83	1.42	3.65	-0.57	18.11	1.89	3.16	-0.74
	Std. Dev.	0.58	0.26	0.94	0.34	0.47	0.27	0.39	0.29
Arms	Median	16.25	1.0	3.50	-0.6	16.25	1.9	3.25	-0.8
	Mean	16.38	1.13	3.36	-0.71	16.39	1.67	2.88	-0.77
	Std. Dev.	0.45	0.25	0.83	0.48	0.55	0.37	0.70	0.47

The denser component is represented as the first component, i.e., (N_1, T_1, n_1, Φ_1).

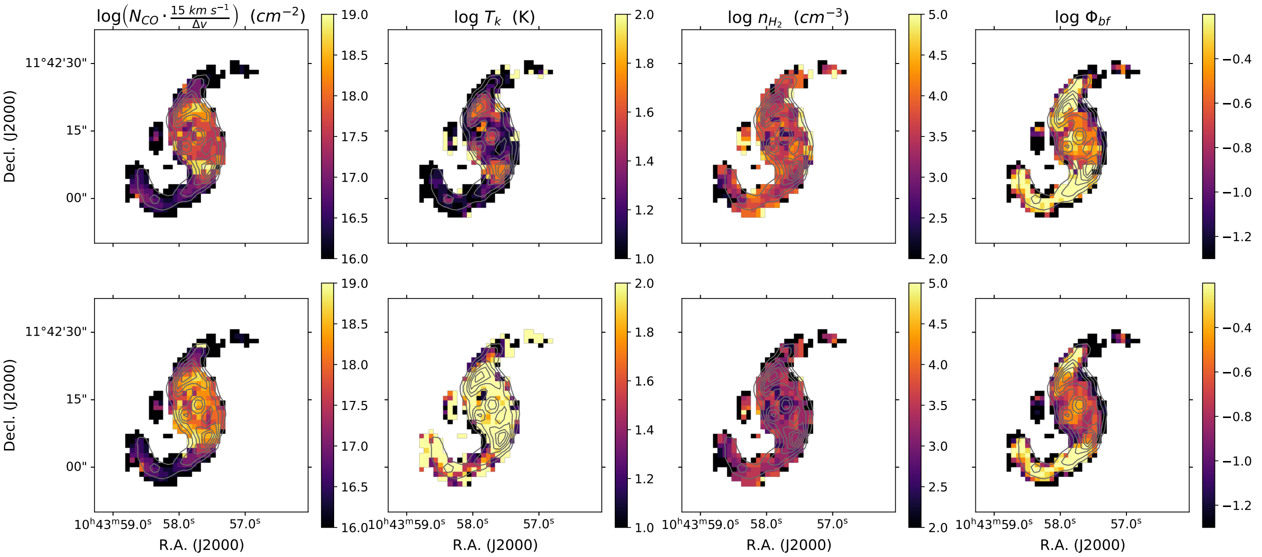

Figure 2.9. Maps of the 1DMax physical conditions derived from the two-component model. The top row shows the denser component having higher $n_{\mathrm{H_2}}$ and the bottom row shows the more diffuse gas phase. The two components have similar physical properties, with a ≤0.5 dex difference in each parameter. This is likely the reason why the two-component model results in similar solutions and spatial variations compared to the one-component model.

While single-component modeling has been widely used to determine physical properties of molecular gas in various galaxies (e.g., Topal et al., 2014; Sliwa et al., 2017; Imanishi et al., 2018; Teng and Hirano, 2020), it is likely that the molecular line emission comes from multiple gas components with different physical conditions (e.g., Ginsburg et al., 2016; Barnes et al., 2017; Krieger et al., 2017). Some studies have modeled the gas with smoothly varying distributions of temperatures and densities (e.g., Leroy et al., 2017; Bisbas et al., 2019; Liu et al., 2021), while others modeled the emission with a warm and cold or dense and diffuse component (e.g., Kamenetzky et al., 2014; Schirm et al., 2014; Liu et al., 2015). In addition, theoretical expectation for isolated and virialized molecular clouds and suggestively some observational studies of galaxy centers imply a two-phase molecular gas with a high-α_{CO} dense component and a low-α_{CO} diffuse component (e.g. Papadopoulos et al., 2012a; Leroy et al., 2015). Israel (2020) also conducted a two-phase analysis toward the centers of ~100 galaxy samples with single dish measurements, although NGC 3351 was not included. To test how multiple gas components could change our results, we construct a two-component model of $N_{\rm CO}/\Delta v$, $T_{\rm k}$, $n_{\rm H_2}$, and $\Phi_{\rm bf}$. This is primarily to see if we get dramatically different results if we change our assumptions about the gas components.

Based on the consistent 1DMax values of $X_{12/13}$ and $X_{13/18}$ from the one-component modeling and their consistency with the values of the Milky Way center, we assume fixed isotopologue abundances of $X_{12/13} = 25$ and $X_{13/18} = 8$ for both gas phases. The two-component model can thus be described by eight parameters, namely, four parameters for each gas phase. We remind the readers that even if the 1DMax values of $X_{12/13}$ are consistently at ~25 in the one-component modeling, the 1D likelihoods of $X_{12/13}$ are loosely constrained; the $X_{13/18}$ likelihoods, on the other hand, are well-constrained at 6–10 (see Figure 2.5 and 2.6). Jiménez-Donaire et al. (2017) have observed the central kpc of NGC 3351 at a 8″ resolution with ^{13}CO and C^{18}O 1–0 and suggested a $X_{13/18}$ value that is also consistent with our one-component modeling as well as the Galactic Center value. Nevertheless, we note that applying fixed, Galactic Center-like abundance ratios to the two-component modeling may be a rather strict assumption. We emphasize that the primary goal of our two-component model is to test if the solutions will differ substantially after altering the assumption in the numbers of gas components, and this goal can be achieved by comparing the solutions of $N_{\rm CO}/\Delta v$, $T_{\rm k}$, or $n_{\rm H_2}$ while fixing the isotopologue abundances to remain consistent with the one-component modeling.

Due to large grid size of the 8D model, we slightly adjust the parameter ranges and step sizes (see Table 2.3): $N_{\rm CO}/\Delta v$ ranges from $10^{16}/15$ to $10^{19}/15$ cm^{-2} (km s^{-1})$^{-1}$ in steps of 0.25 dex, $T_{\rm k}$ ranges from 10 to 100 K in steps of 0.1 dex, $\log(n_{\rm H_2}\ [{\rm cm}^{-3}])$ ranges from 2 to 5 in steps of 0.25 dex, and $\log(\Phi_{\rm bf})$ ranges from −1.3 to −0.1 in steps of 0.1 dex. We lower the upper limit of $T_{\rm k}$ to 100 K in the two-component model grids because the sensitivity to distinguish different temperatures above 100 K is very weak with J=3–2 as the highest transition. In addition, the one-component modeling results show that $T_{\rm k}$ is well below 100 K across the whole region. We also lower the upper limit of $N_{\rm CO}/\Delta v$ to $10^{19}/15$ because a higher value is normally ruled out by the line-of-sight constraint of $\ell_{\rm los} < 100$ pc as mentioned in Section 2.4.2.

The 8D model grid consists of all combinations of either two components from the 4D parameter space. By summing up the predicted intensities of both components, each grid point has a prediction of the total integrated intensity. Since the two components are interchangeable under summation, nearly half of the grid points are redundant, and we thus require the first component to have higher T_k than the second component. This not only allows us to distinguish between warm and cold or dense and diffuse components, but also avoids getting the exact same marginalized likelihoods for both components due to symmetric model grids. Similar to the 6D one-component modeling, we include a 10% flux calibration uncertainty and the measurement uncertainties for fitting.

When deriving the values of N_CO, we assume both components to have the same line widths as the observed CO 1–0 line width. This assumption has negligible effect on our α_CO results in Section 2.5, as N_CO and Φ_bf are being fit simultaneously to determine α_CO values, which means that the two parameters can adjust themselves to fit best with the line intensities. In addition, we mostly observed a single-peaked spectrum which can be well represented by a single line width (see Figure 2.4), so assuming the same line widths as the measured line width is likely the most feasible thing we could do in the two-component analysis. If both components have Gaussian spectra, this assumption would imply that both components are at the same velocity.

Figure 2.9 shows the 1DMax solutions from the two-component modeling, where the component with higher n_{H_2} is shown in the top row. Regional statistics are also summarized in Table 2.5 with the denser component being presented as the first component. We note that the separation by density is made for visualization purposes and has no role in the subsequent calculation of α_CO. In general, the dense components correspond to lower T_k and N_CO values than the diffuse components, which is similar to the correlations observed in the one-component result within the probability distribution of a single pixel. From the regional averages of both components (see Table 2.5), we find that the differences in N_{CO}, $n_{\mathrm{H_2}}$ and Φ_{bf} between the two components are all less than ~0.5 dex. Moreover, the difference between their masses, which are proportional to their N_{CO} and Φ_{bf} (see Equation 2.9), is even found to be less than ~0.3 dex. This means that the two components have similar physical properties. We also find these properties to be similar to those suggested by the one-component model. For example, the 1DMax $n_{\mathrm{H_2}}$ distribution from the two-component model suggests a density of $\sim 2\text{–}3 \times 10^3$ cm^{-3} in the center, which is consistent with $\sim 2 \times 10^3$ cm^{-3} suggested by the one-component model. These are also similar to the average gas density of $\sim 5 \times 10^3$ cm^{-3} found in the Milky Way's CMZ (e.g., Longmore et al., 2013). The only substantial difference between our two-component solutions is the kinetic temperature. While the denser component has a similar range of temperature and region-by-region variations as observed in the one-component model (see Figure 2.8b), the other component shows evidently higher kinetic temperature of ~100 K over the whole region. These temperatures are quantitatively similar to previous two-component studies toward the GMCs in our Galactic Center, which suggest a dominant component by mass with T_{k} ~25–50 K and a less-dominant warm component with $T_{\mathrm{k}} \gtrsim 100$ K (e.g., Huettemeister et al., 1993; Krieger et al., 2017). We thus conclude that the dominant component in our two-component model is well-represented by the one-component model alone, but there might be a secondary, warmer component unaccounted for in the one-component model, as previously seen in the Galactic CMZ.

2.4.4 Marginalized 1D Likelihoods

In this subsection, we describe the unified procedure of how we generate and deal with the marginalized likelihoods and then derive plausible solutions for parameters like α_{CO}. This is fundamental to the results presented in Section 2.5.

In Sections 2.4.2 and 2.4.3, we derived the marginalized 1D likelihoods for each input parameter. In both cases, we have a full 6D or 8D grid, with each grid point having an associated probability. Since our input parameters are sampled uniformly, their marginalized

1D likelihood distribution is simply a probability-weighted histogram, where the probability value of each grid point is reflected proportionally in the number of counts toward each bin. On the other hand, to derive the marginalized likelihoods of parameters that are functions of the intrinsic grid parameters (e.g., the modeled line intensities or α_{CO}), an additional normalization on the histograms would be needed due to the possibility of irregular sampling on the derived parameter grid space. For instance, given the grids of modeled line integrated intensities, we could determine 1D likelihoods for each line intensity with some chosen bin spacing and range. However, since multiple combinations of parameters in the 6D or 8D grid space could produce the same integrated intensity, and some line intensities may only be produced by a small subset of the parameter combinations, the resulting 1D likelihoods will have an additional non-uniform weighting due to the starting grid. To properly deal with the grid irregularity, we can generate a uniformly weighted histogram for line intensities under the same parameter range and bin size, treating that as a normalization. To obtain the marginalized 1D likelihood of any derived parameter from the original grid, we divide the probability-weighted histogram by the uniformly weighted histogram to normalize out any grid irregularity. The marginalized likelihoods of α_{CO}, which is a function of N_{CO}, Φ_{bf}, and the CO 1–0 line intensity, can also be derived in this way (see Section 2.5).

Once the 1D likelihood distributions of a parameter are obtained, we can determine either the 1DMax solutions by finding the values that correspond to the peaks, or the medians, and $\pm 1\sigma$ values by finding the 16th and 84th percentiles of the cumulative 1D likelihood distribution. Then, maps of the 1DMax solutions or medians $\pm 1\sigma$ can be generated by iterating over each pixel. While we could look individually into the likelihood distributions at each pixel, comparing between these maps is a more simple and feasible way to get a sense of the probability distribution in different regions of the galaxy. With this procedure, it is important to note that our solutions for α_{CO} in Section 2.5 do not rely on the individually derived N_{CO} and Φ_{bf} distributions presented in Sections 2.4.2 and 2.4.3, since those parameters are being fit simultaneously within the full grid before we obtain the marginalized likelihoods of α_{CO}.

2.5 CO-to-H$_2$ Conversion Factor

The CO-to-H$_2$ conversion factor (α_{CO}) is defined as the ratio of molecular gas mass to CO 1–0 luminosity (Dickman et al., 1986; Bolatto et al., 2013), which is also equivalent to the ratio of molecular gas mass surface density to CO 1–0 intensity:

$$\alpha_{\mathrm{CO}} = \frac{M_{\mathrm{mol}}}{L_{\mathrm{CO(1-0)}}} = \frac{\Sigma_{\mathrm{mol}}}{I_{\mathrm{CO(1-0)}}} \left(\frac{\mathrm{M}_\odot}{\mathrm{K\ km\ s^{-1}\ pc^2}}\right) . \tag{2.8}$$

The CO 1–0 luminosity is the CO 1–0 intensity multiplied by the area in square parsecs, and the molecular gas mass is proportional to the product of CO column density and the filling factor times the area (Kamenetzky et al., 2014):

$$M_{\mathrm{mol}} = 1.36\, m_{\mathrm{H_2}}\, N_{\mathrm{CO}}\, A\, \Phi_{\mathrm{bf}}\, x_{\mathrm{CO}}^{-1} , \tag{2.9}$$

where A is the same area as that in CO 1–0 luminosity. Therefore, Equation 2.8 can be rewritten as

$$\begin{aligned} \alpha_{\mathrm{CO}} &= \frac{1.36\, m_{\mathrm{H_2}}\, (\mathrm{M}_\odot)\, N_{\mathrm{CO}}\, (\mathrm{cm^{-2}})\, A\, (\mathrm{cm^2})\, \Phi_{\mathrm{bf}}}{x_{\mathrm{CO}}\, I_{\mathrm{CO(1-0)}}\, (\mathrm{K\ km\ s^{-1}})\, A\, (\mathrm{pc^2})} \\ &= \frac{1}{4.5 \times 10^{19}} \cdot \frac{N_{\mathrm{CO}}\, (\mathrm{cm^{-2}})\, \Phi_{\mathrm{bf}}}{x_{\mathrm{CO}}\, I_{\mathrm{CO(1-0)}}\, (\mathrm{K\ km\ s^{-1}})} , \end{aligned} \tag{2.10}$$

where $m_{\mathrm{H_2}}$ is the mass of molecular hydrogen, 1.36 is the factor after including the mass contribution from Helium, and x_{CO} is the CO-to-H$_2$ abundance ratio. The x_{CO} value in different galaxies or metallicity conditions can vary from $0.5\text{–}5 \times 10^{-4}$ (e.g., Frerking et al., 1982; Black et al., 1990; Downes and Solomon, 1998; Sliwa et al., 2012) and is commonly assumed as $\sim 10^{-4}$. In our analysis, we assume a higher x_{CO} value of 3×10^{-4}, which is typically found and/or adopted in starburst regions (Lacy et al., 1994; Ward et al., 2003;

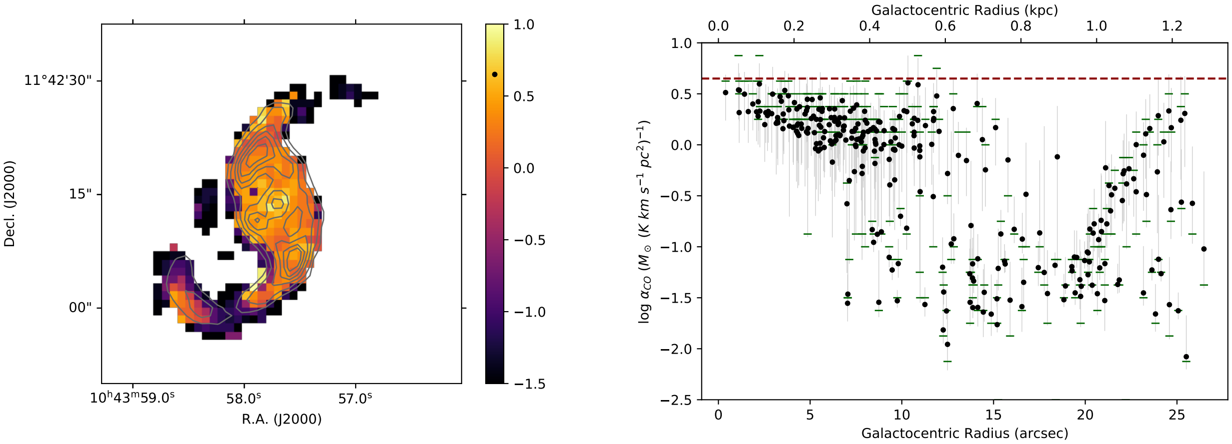

(a)

(b)

Figure 2.10. α_{CO} variations determined by the one-component modeling results. (a) 1DMax $\log(\alpha_{\mathrm{CO}})$ map in units of $\mathrm{M}_\odot$ (K km s^{-1} pc^2)$^{-1}$; the contours show zeroth moment of CO 1–0 and the black dot on the color bar indicates the Galactic average value of $\alpha_{\mathrm{CO}} \sim 4.4$ $\mathrm{M}_\odot$ (K km s^{-1} pc^2)$^{-1}$. (b) Relation between the median α_{CO} (black dots) and galactocentric radius; the green horizontal lines represent the 1DMax α_{CO} and the vertical lines show the 1σ ranges (16th–84th percentiles); the red dashed line shows the Galactic disk average value of $\alpha_{\mathrm{CO}} \sim 4.4$ $\mathrm{M}_\odot$ (K km s^{-1} pc^2)$^{-1}$. In the center, the median and 1DMax α_{CO} values are only slightly below the Galactic disk average, and decrease slowly from the nucleus to the ring. Beyond a galactocentric radius of ~10″, α_{CO} drops significantly to a value that is approximately an order of magnitude lower than the Galactic disk average.

Kamenetzky et al., 2012; Kamenetzky et al., 2014; Sliwa et al., 2014; Sliwa et al., 2017). This means that the absolute value of our derived α_{CO} is accurate only when $x_{\mathrm{CO}} = 3 \times 10^{-4}$, and the true α_{CO} can be represented as $\alpha_{\mathrm{CO}}^{\mathrm{true}} = \alpha_{\mathrm{CO}} \times (3 \times 10^{-4}/x_{\mathrm{CO}})$. Therefore, we note that our results on the α_{CO} values depend inversely on any variation of x_{CO}, and that the spatial variation of our derived α_{CO} could partially result from spatial variations in x_{CO}.

With Equation 2.10, we derive the spatial distribution of α_{CO} using the approach described in Section 2.4.4: for each pixel, we first calculate an α_{CO} value for every grid point in the model using the corresponding N_{CO}, Φ_{bf}, and predicted CO intensity S^{mod}, and then marginalize over the whole grid to obtain the 1DMax value of α_{CO}. We apply this method to both one- and two-component modeling results and compare the derived α_{CO} distributions.

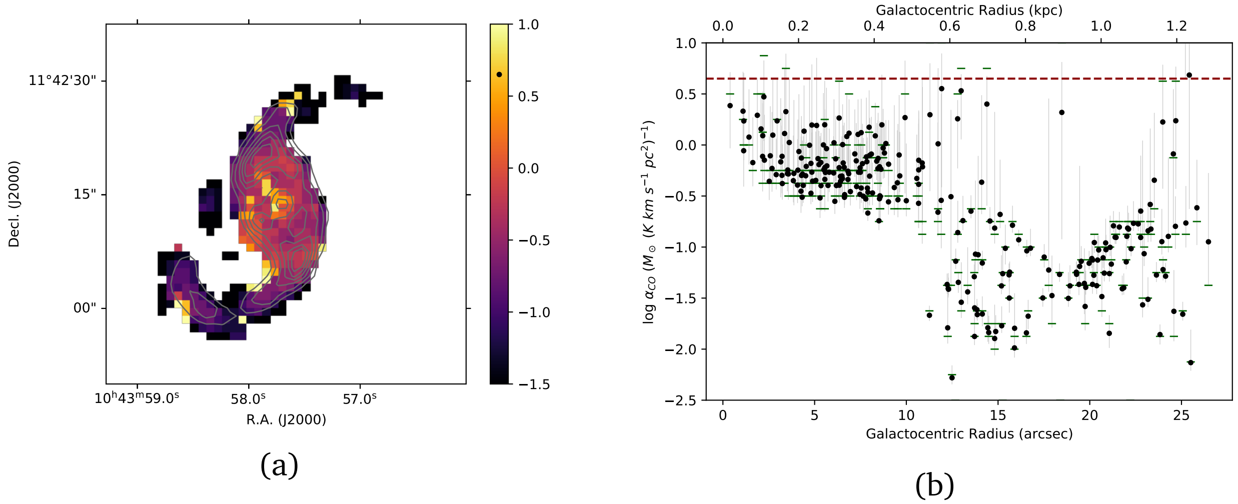

(a)

(b)

Figure 2.11. α_{CO} variations determined by the two-component modeling results. (a) 1DMax $\log(\alpha_{\text{CO}})$ map in units of $\text{M}_\odot$ (K km s^{-1} pc^2)$^{-1}$. (b) Relation between the median/1DMax α_{CO} and galactocentric radius, determined by the marginalized α_{CO} likelihoods from the two-component models. See the caption of Figure 2.10 for more information. The spatial variation of α_{CO} and the values in the arms are similar to that derived from the one-component model, while the values in the center are a factor of 2–3 lower.

2.5.1 α_{CO} from the Modeling Results

Using the method described in Section 2.4.4, we derive the marginalized 1D likelihoods of $\log(\alpha_{\text{CO}})$ for each pixel with $\log(\alpha_{\text{CO}})$ ranging from −2.5 to 2.5 in steps of 0.125. Figures 2.10 and 2.11 present the α_{CO} variations derived from the one-component and two-component modeling, respectively. The marginalized 1DMax α_{CO} shown in Figure 2.10a reveals an average of ∼2 $\text{M}_\odot$ (K km s^{-1} pc^2)$^{-1}$ in the inner 1 kpc region, while the α_{CO} along the arms is a factor of ∼10 lower than the center. Figure 2.10b shows how the median and 1DMax α_{CO} vary with the galactocentric radius of NGC 3351. Both the median and 1DMax α_{CO} values exhibit a slow decrease from the nucleus to the ring and a significant drop at a radius of ∼10″ (∼0.5 kpc), which is where the ring and the arms intersect. Interestingly, while α_{CO} remains roughly constant at a radius of ∼10–20″, it starts to increase beyond a radius of ∼20″. We find that the $\gtrsim$ 20″ region corresponds to the curved-up feature in the southern arm (see Figure 2.2c). This region is called the "transverse dust lane" in Leaman et al. (2019), where they suggested the feature as evidence for an outflow pushing gas/dust away from the nuclear ring via stellar feedback processes.

Overall, all the pixels in our observed region show at least factor of ~2–3 (0.3–0.5 dex) lower $\alpha_{\rm CO}$ values than the Milky Way average at the assumed $x_{\rm CO}$ of 3×10^{-4}. If $x_{\rm CO}$ were set to be 10^{-4}, $\alpha_{\rm CO}$ would increase by a factor of three. In such a case, the central 1 kpc region would have a nearly Galactic $\alpha_{\rm CO}$, whereas the $\alpha_{\rm CO}$ is still substantially lower in the inflow arms since a global change in $x_{\rm CO}$ would not change the relative drop in $\alpha_{\rm CO}$. Note that if there were spatial variations of $x_{\rm CO}$ across this region, it could alter our $\alpha_{\rm CO}$ variation results. Leaman et al. (2019) estimated the circular rotational velocity to be 150–200 km s^{-1} on the circumnuclear ring of NGC 3351, implying a gas rotation period of 15−20 Myr. Since this orbital time scale is much shorter than the stellar evolution time scale that can cause a difference in chemical abundances, we expect the abundances of carbon and oxygen to be well-mixed in the central kpc of NGC 3351, and thus sub-kpc scale variations of $x_{\rm CO}$ should be small if $x_{\rm CO}$ is essentially determined by the availability of carbon and oxygen. Despite such expectation, we emphasize that disentangling $x_{\rm CO}$ variations and $\alpha_{\rm CO}$ is infeasible under current modeling and measurements. Therefore, our estimated $\alpha_{\rm CO}$ distribution can be affected if there is any $x_{\rm CO}$ variation on sub-kpc scales.

The 1DMax $\alpha_{\rm CO}$ distributions derived from the two-component modeling results, as shown in Figure 2.11a, suggest a similar spatial variation to that determined by the one-component results, while the $\alpha_{\rm CO}$ values in the center are generally lower than those in Figure 2.10a. Figure 2.11b shows the median and 1DMax solutions determined from the marginalized $\alpha_{\rm CO}$ likelihoods and their variation with galactocentric radius. The $\alpha_{\rm CO}$ solutions inside the central 1 kpc region are shifted ~0.3−0.5 dex downward compared with Figure 2.10b. On the other hand, the $\alpha_{\rm CO}$ solution in the inflow arms is consistent with Figure 2.10b, and we can see a clear distinction between $\alpha_{\rm CO}$ values in the center and inflow regions, which are separated at the 10″ or 0.5 kpc radius. We note that the possible cause for a ~0.3−0.5 dex shift of $\alpha_{\rm CO}$ solutions in the center may originate from the assumption of a fixed $X_{12/13}$ at 25. The 2D correlations in Figure 2.5 and 2.6 show that

$X_{12/13} = 25$ corresponds to a lower $N_{\rm CO}/\Delta v$ and a higher $\Phi_{\rm bf}$ compared with the 1DMax solutions, which may altogether result in a 0.3–0.5 dex offset in $\alpha_{\rm CO}$. In general, both our one- and two-component models result in lower-than-Galactic $\alpha_{\rm CO}$ values for the entire observed region and significantly ($\gtrsim 10\times$) lower $\alpha_{\rm CO}$ values in the inflow arms. Furthermore, by comparing with the derived $T_{\rm k}$ distributions shown in Figure 2.8b, there is no sign that lower $\alpha_{\rm CO}$ are associated with higher temperatures (see discussion in Section 2.6). In Section 2.5.2, we will discuss possible scenarios that cause the $\alpha_{\rm CO}$ variation and such low $\alpha_{\rm CO}$ values in the arms.

To compare the derived $\alpha_{\rm CO}$ with those observed previously at kpc scales, we compute the intensity-weighted mean $\alpha_{\rm CO}$ over our entire observed region of ~2 kpc. The intensity-weighted mean $\alpha_{\rm CO}$ is calculated as the ratio of total molecular mass to the total luminosity over the whole region. Based on Equation 2.10, this can be done with the full grids of the modeled $N_{\rm CO}$, $\Phi_{\rm bf}$, and intensity of CO 1–0 ($S^{\rm mod}$) at every pixel. For each pixel, we first perform a likelihood-weighted random draw from the model grids to obtain $N_{\rm CO}$, $\Phi_{\rm bf}$, and the corresponding modeled $I_{\rm CO(1-0)}$ value. Next, we sum up the values over the pixels to derive the total molecular mass and CO intensity, and then calculate the resulting intensity-weighted mean $\alpha_{\rm CO}$. We then perform another random draw and repeat 2000 times. Finally, the mean and standard deviation over the 2000 measurements of $\alpha_{\rm CO}$ are obtained. This approach is a combination of Monte Carlo sampling with likelihood weighting of the model grids, and is similar to the "realize" method used by Gordon et al. (2014) for dust spectral energy distribution (SED) fitting.

The intensity-weighted mean $\alpha_{\rm CO}$ of the entire region is 1.79 ± 0.10 and 1.11 ± 0.09 $M_\odot$ (K km s^{-1} pc^2)$^{-1}$ based on the one- and two-component models, respectively. Since the sum of our $I_{\rm CO(1-0)}$ and $I_{\rm CO(2-1)}$ over the entire observed region are similar, weighting either by the CO 1–0 or 2–1 intensities give approximately the same intensity-weighted mean $\alpha_{\rm CO}$. With an angular resolution of ~40″, Sandstrom et al. (2013) found an $\alpha_{\rm CO(2-1)}$ of $1.0^{+0.4}_{-0.3}$ $M_\odot$ (K km s^{-1} pc^2)$^{-1}$ in the central 1.7 kpc of NGC 3351 using dust modeling with CO 2–1

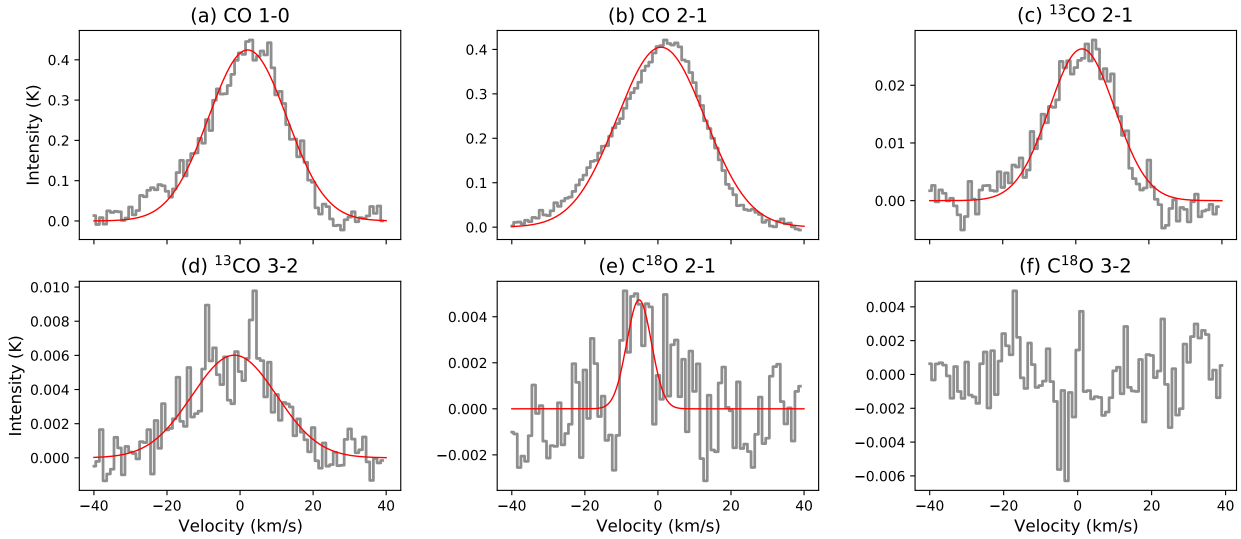

Figure 2.12. Shifted and averaged spectra over the inflow arms, overlaid with the best-fit Gaussian profiles. This stacking is used for the purpose of recovering faint emission from the arms and comparing with the pixel-based analysis. The integrated intensities of each line is estimated from the averaged spectra and then input to the multi-line modeling to determine the best-fit/1DMax solutions for environmental parameters and $\alpha_{\rm CO}$ in the arm regions. The results of the modeling are shown in Figure 2.13 and 2.14.

intensities. This is similar to the intensity-weighted mean $\alpha_{\rm CO}$ values derived from both our one- and two-component models. However, since they assumed a constant CO 2–1/1–0 ratio (R_{21}) of 0.7, they concluded a lower mean $\alpha_{\rm CO(1-0)}$ value of $0.7^{+0.27}_{-0.20}$ $\rm M_\odot$ (K km s^{-1} pc^2)$^{-1}$ appropriate for CO 1–0 intensities. While R_{21} = 0.7 may be a good approximation across galaxy disks (e.g., den Brok et al., 2021), studies on nearby galaxy centers have suggested higher R_{21} ($\gtrsim$0.9) in the central kpc region of disk galaxies (Israel, 2020; Yajima et al., 2021). As presented in Table 2.2, the mean R_{21} over our entire observed region is 1.0, and both our one- and two-component models predict a mean R_{21} higher than 0.9. Thus, if a higher R_{21} of $>$ 0.9 had been adopted by Sandstrom et al. (2013), their $\alpha_{\rm CO}$ estimates with CO 1–0 would be in good agreement with our modeling results.

2.5.2 $\alpha_{\rm CO}$ in the Inflow Arms

As pixel-based analyses in the arm regions may have higher uncertainties due to low S/N, we stack the spectra from inflow regions to recover low brightness emission applying

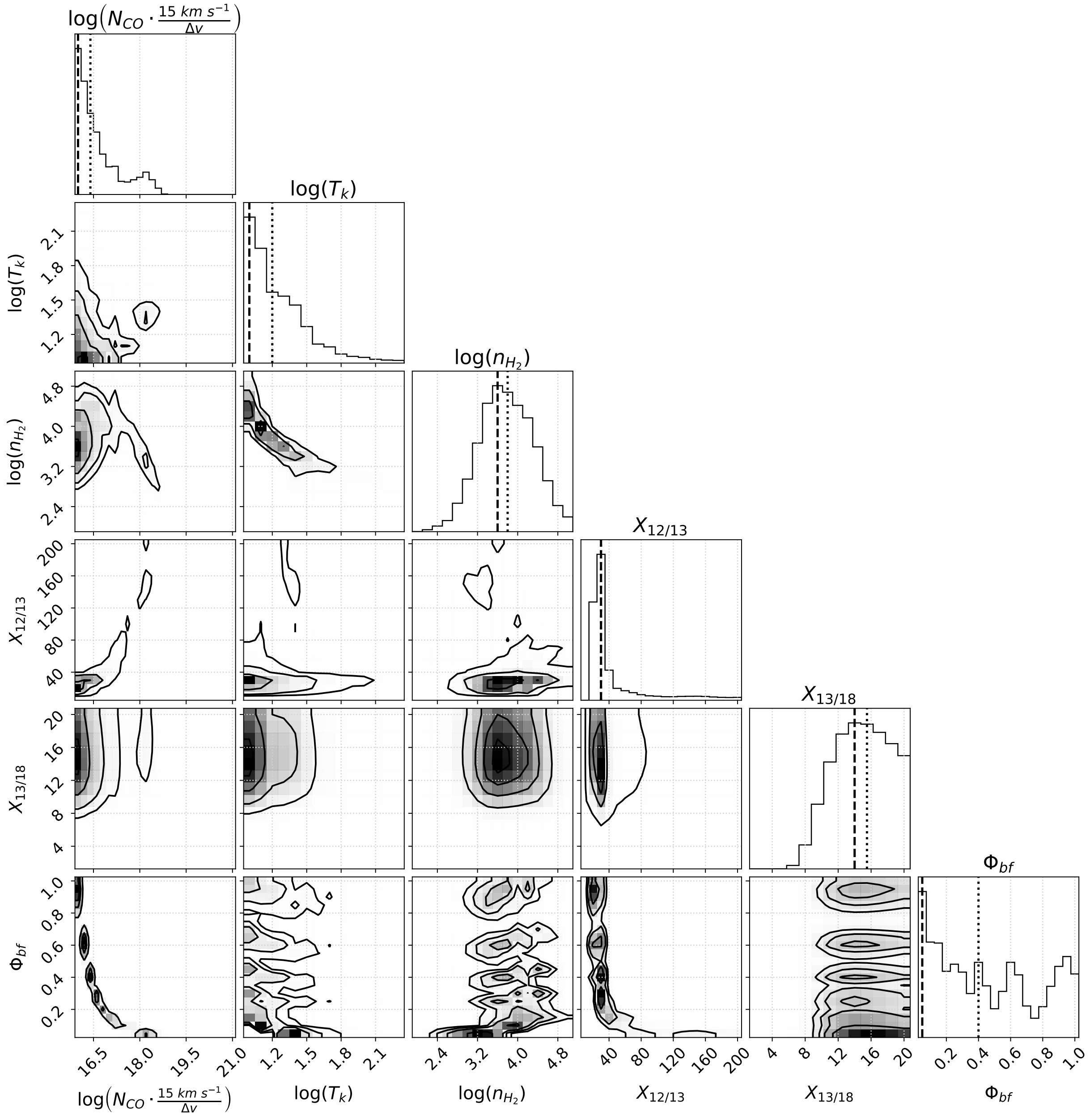

Figure 2.13. Marginalized 1D and 2D likelihood distributions of the stacked spectra from inflow arms. See the caption of Figure 2.5 for more information. Note that some of the parameters are less-constrained in these faint regions and thus pushing the solutions to the boundaries of the grid.

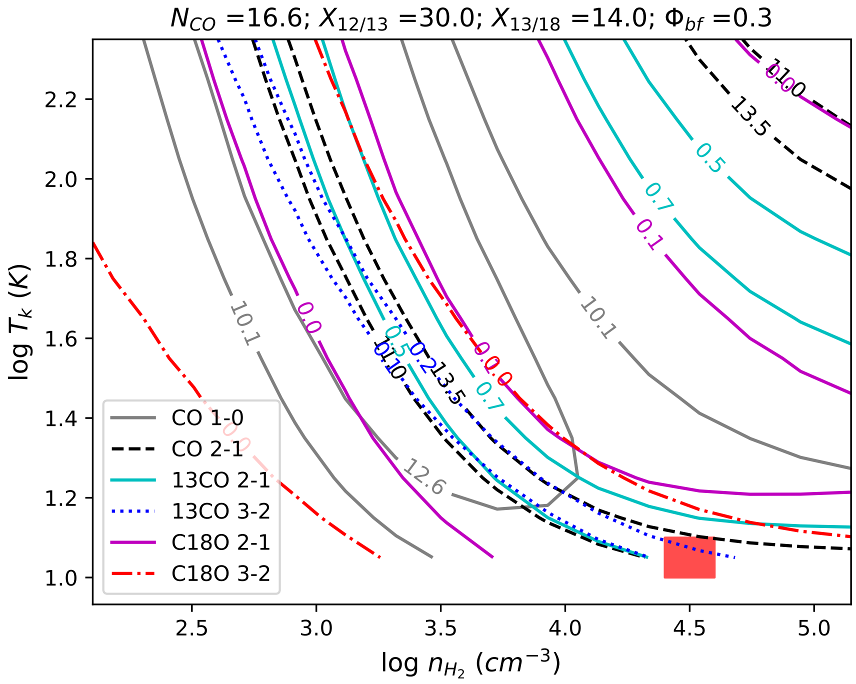

Figure 2.14. Constraints on the T_k–n_{H_2} slice where the best-fit parameter (red box) lies assuming a 10% flux uncertainty. See the caption of Figure 2.7 for more information.

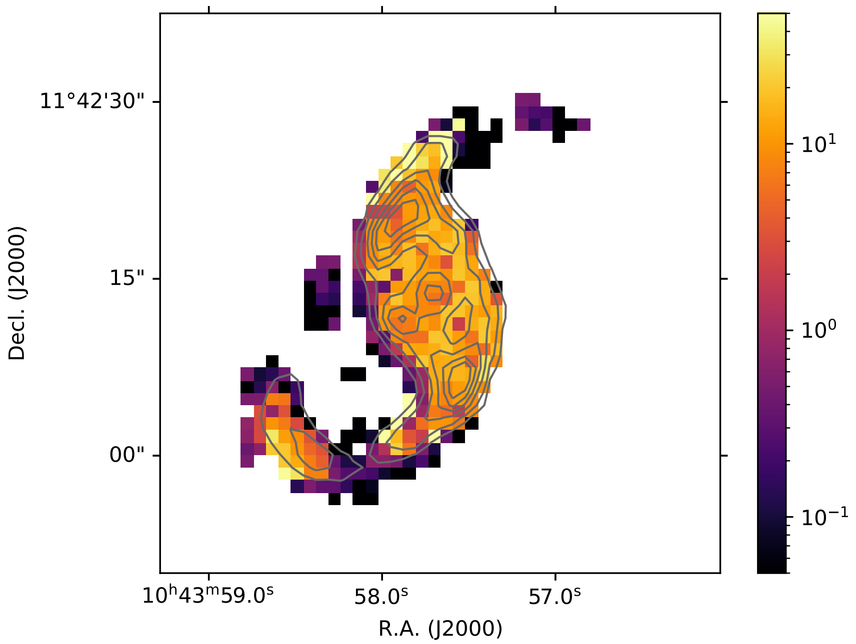

Figure 2.15. Optical depth (τ) map of CO 1–0 determined from the one-component 1DMax physical conditions. The arm regions have lower optical depths than the center, which may originate from higher velocity dispersions. The optically thin regions with $\tau < 1$ are found to have similar α_{CO} values to those predicted under LTE assumption (Bolatto et al., 2013).

the approach by Schruba et al. (2011). First, we set the moment 1 velocities of CO 2–1 as the reference velocity (i.e., $v = 0$) for each pixel and shift the spectra from all other lines to $v = 0$. Next, we extract the spectra in the $v = \pm 100$ km s^{-1} range and sum them up to obtain a stacked spectrum for each line. Figure 2.12 presents the shifted and stacked spectra over the arms (defined in Figure 2.2c), overlaid with the best-fit Gaussian function. The spectra of the ^{13}CO lines show much improvement in S/N after stacking. However, the spectrum of C^{18}O 3–2 is still noisy, as most pixels in the arms are below 1σ in C^{18}O 3–2 (see Figure 2.1) and therefore do not have reliable measurements even after stacking. Thus, we should be aware that C^{18}O 3–2 is not a significant detection in the stacked spectrum of inflow arms, and it is included in the fitting as an upper limit.

We measure the observed integrated flux of each line and use it as input to the multi-line modeling technique described in Section 2.4.2. Figures 2.13 and 2.14 show the likelihood distributions and the T_k–n_{H_2} slice where the best-fit parameter set lies. The 1DMax and best-fit physical conditions to the stacked spectra of inflow arms are found at $(N_{CO}/\Delta v, T_k, n_{H_2}, X_{12/13}, X_{13/18}, \Phi_{bf}) = (\frac{10^{16}}{15}$ cm^{-2} (km s^{-1})$^{-1}$, 10 K, $10^{3.6}$ cm^{-3}, 30, 14, 0.05) and ($\frac{10^{16.6}}{15}$ cm^{-2} (km s^{-1})$^{-1}$, 10 K, $10^{4.4}$ cm^{-3}, 30, 14, 0.3), respectively. Both solutions imply lower N_{CO}, lower T_k, and higher n_{H_2} in the arms compared with those in the central ~1 kpc. As shown in Figure 2.14, the constraints from five of the six lines have similar shapes, while CO 1–0 is the main constraint that pushes the solution to the lower-right corner. Therefore, even if we exclude the constraints from the C^{18}O lines that have low S/N in the arms, the best-fit solution would remain, which means that C^{18}O lines are not the key data in the arm regions. The line width determined by the best-fit Gaussian to the stacked CO 1–0 spectrum is $\Delta v_{FWHM} = 25.18 \pm 0.58$ km s^{-1}. By substituting the best-fit or 1DMax solutions of $N_{CO}/\Delta v$ and Φ_{bf}, and the fitted CO 1–0 line width into Equation 2.10, the α_{CO} of inflow arms is estimated to be 0.01–0.1 M$_\odot$ (K km s^{-1} pc^2)$^{-1}$. This matches our pixel-based estimation in the arms despite with lower S/N, and thus supports the idea that the inflow regions have substantially lower α_{CO} values than the center/ring.

From Figure 2.3d and e, we find that the CO/^{13}CO and CO/C^{18}O line ratios in the inflow arms are ~2× higher than in the center. This means that we observe more CO emission in the arms compared to the total molecular gas mass, which by definition indicates a lower $\alpha_{\rm CO}$ value. One possible scenario that could cause such high line ratios are high CO/^{13}CO and CO/C^{18}O abundance ratios. It is likely that the circumnuclear star formation activities have enriched ^{13}C or ^{18}O in the center but not in the inflows. This could lower the $X_{12/13}$ or $X_{13/18}$ abundances in the center and cause lower CO/^{13}CO and CO/C^{18}O line ratios than those in the arms. However, both the best-fit and 1DMax solutions based on the stacked spectra of inflow arms suggest $X_{12/13} \sim 30$ and $X_{13/18} \sim 10$, which are similar to those found in the center region as shown in Figure 2.8d and e. Note that the 1D likelihood of $X_{12/13}$ is very well-constrained for the arm regions with stacking (see Figure 2.13), which is different from the loosely constrained $X_{12/13}$ in the individual pixels of the center region. Even if the center pixels have higher $X_{12/13}$ (e.g., median $X_{12/13} \sim 90$ in Figure 2.5 and 2.6), this would contradict the expectation of star formation enrichment and would instead enhance CO/^{13}CO and CO/C^{18}O line ratios in the center. Therefore, changes in CO isotopologue abundances may not be the main reason that causes higher line ratios in the inflow regions.

The high line ratios observed in CO/^{13}CO and CO/C^{18}O 2–1 could also be explained if the optical depths of CO changes significantly. Figure 2.2b reveals a broader line width in the arms, which may indicate a more turbulent environment or the existence of shear in these bar-driven inflows. This could lead to lower optical depths in the gas inflows. As shown in Figure 2.15, the optical depths derived from the 1DMax physical conditions are found to be lower in the arms compared to the center, which is likely a combined effect of low $N_{\rm CO}$ and high Δv (see Equation 2.3). Since higher velocity dispersions and consequently lower optical depths allow a larger fraction of CO emission to escape, these may explain why $\alpha_{\rm CO}$ is low in the inflow arms.

In optically thin regions, the average $\alpha_{\rm CO}$ is $0.04^{+0.13}_{-0.03}$ $M_\odot$ (K km s^{-1} pc^2)$^{-1}$ based on the marginalized 1DMax $\alpha_{\rm CO}$ map shown in Figure 2.10a. The optically thin regions were determined by selecting pixels having $\tau < 1$ in Figure 2.15. Bolatto et al. (2013) derived an LTE equation to determine $\alpha_{\rm CO}$ as a function of the CO/H$_2$ abundance ($x_{\rm CO}$) and excitation temperature ($T_{\rm ex}$):

$$\alpha_{\rm CO} \approx \frac{1.6{\times}10^{19}}{4.5{\times}10^{19}} \frac{10^{-4}}{x_{\rm CO}} \frac{T_{\rm ex}}{30\,{\rm K}} \exp\left(\frac{5.53\,{\rm K}}{T_{\rm ex}} - 0.184\right) \tag{2.11}$$

where 4.5×10^{19} is the factor to convert $X_{\rm CO} = N_{\rm H_2}/I_{\rm CO(1-0)}$ cm^{-2} (K km s^{-1})$^{-1}$ to $\alpha_{\rm CO}$ (see Equation 2.10). By plugging our modeled $T_{\rm k}$ (Figure 2.8b) and the assumed $x_{\rm CO}$ of 3×10^{-4} into Equation 2.11, we get an average $\alpha_{\rm CO}$ of $0.12^{+0.16}_{-0.07}$ M$_\odot$ (K km s^{-1} pc^2)$^{-1}$ in the optically thin regions. This overlaps well with the average derived from our modeled $\alpha_{\rm CO}$ distribution, showing that the solutions from multi-line modeling are physically reasonable. We have also compared the excitation temperatures between CO and ^{13}CO predicted by the best-fit physical conditions of the averaged spectra in each region. In the arm regions, the predicted excitation temperatures of CO and ^{13}CO 2–1 lines are at 9.0 and 8.8 K, implying that the conditions in the arms are very close to LTE. On the other hand, the excitation temperatures of ^{13}CO in the center/ring are lower than those of CO by a factor of ∼1.5–2, indicating a clear departure from LTE that may originate from radiative trapping affecting the CO excitation. Radiative trapping lowers the effective critical density for the CO lines, leading to differences in the excitation for CO and ^{13}CO. We also note that temperature inhomogeneities in the gas will tend to bias CO lines to higher temperatures since warmer gas has a higher luminosity and, unlike ^{13}CO or optically thin tracers, not all CO emission from the full line-of-sight contributes to the measured integrated intensity due to optical depth effects. It is also important to note that our derived values of $\alpha_{\rm CO}$ vary inversely with $x_{\rm CO}$. Thus, any increase/decrease to the assumed $x_{\rm CO}$ of 3×10^{-4} would lower/raise the numerical values of $\alpha_{\rm CO}$.

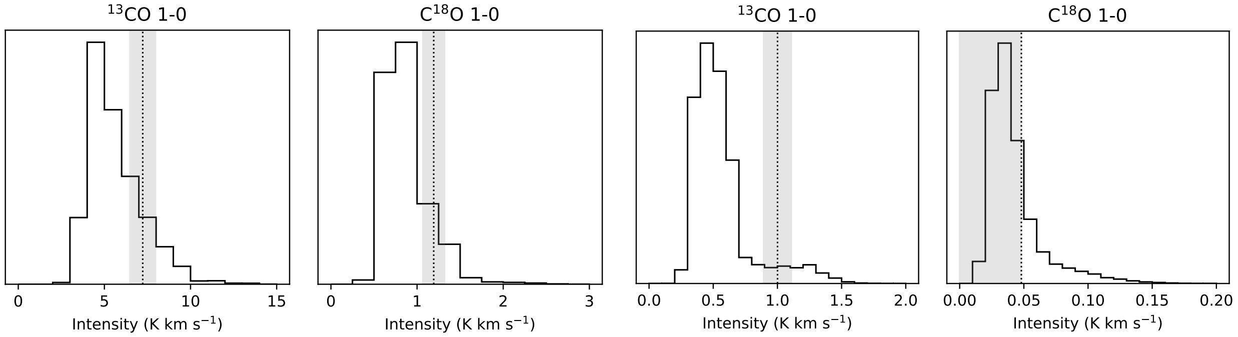

(a) (b)

Figure 2.16. Marginalized 1D likelihoods of the ^{13}CO and C^{18}O 1–0 intensities in the (a) center and (b) arms regions. The dotted lines mark the data measurements and the shaded regions show the $\pm 1\sigma$ uncertainties including the measurement uncertainty and a 10% calibration uncertainty. Since there is no detection of C^{18}O 1–0 in the arms, the dotted line in the far right panel marks the 1σ upper limit. Except for ^{13}CO 1–0 showing a factor of ~2 higher intensity than the predicted 1DMax value, the observed intensities of all the lines in other regions are within ~50% of the predicted 1DMax intensities.

2.5.3 Comparison with Other CO Isotopologue Transitions

To compare our modeling results with other observations, we also acquired ALMA data of ^{13}CO and C^{18}O 1–0 with an angular resolution of 8″ towards the center of NGC 3351. These data were analyzed in Jiménez-Donaire et al. (2017) and Gallagher et al. (2018). Since the resolution is lower than the matched 2.1″ resolution in our analysis, we only extract regional averages in the center, ring, and arms for comparison. First, we input the integrated intensities measured from the stacked spectra of each region (e.g., Figure 2.4) into the six-line modeling described in Section 2.4.2. This gives us a full probability grid for each region. Then, we generate the modeled intensity grids of ^{13}CO and C^{18}O 1–0 using RADEX, such that the modeled intensity at each grid point has an associated probability. Finally, we obtain the predicted 1D likelihoods for both lines using the method described in Section 2.4.4.

Figure 2.16a shows the predicted 1D likelihoods for the center region, covering an intensity range of 0 to 15 K km s^{-1} in steps of 1 K km s^{-1} for ^{13}CO 1–0 and 0 to 3 K km s^{-1} in steps of 0.25 K km s^{-1} for C^{18}O 1–0. The dotted lines mark measured intensities and the shaded regions show the $\pm 1\sigma$ uncertainties which include the measurement uncertainty and a 10% calibration uncertainty. Following Schruba et al. (2011), we estimate the measurement uncertainties using the signal-free part of the spectra and the fitted line widths. In the center region, both the observed intensities are within ~50% of the predicted 1DMax intensities. The 1D likelihoods and observed intensities for the ring region are similar to those in the center. On the other hand, Figure 2.16b shows that both the predicted and observed emission in the arms are fainter than the center/ring. For the arms, the 1D likelihoods range from 0 to 2 K km s^{-1} in steps of 0.1 K km s^{-1} for ^{13}CO and 0 to 0.2 K km s^{-1} in steps of 0.01 K km s^{-1} for C^{18}O. As there is no detection of C^{18}O 1–0 in the arms, the dotted line in the right panel of Figure 2.16b marks the 1σ upper limit, which is also within 50% of the 1DMax intensity. Notably, the observed ^{13}CO 1–0 intensity is a factor of ~2 higher than the prediction. This may indicate a more optically-thick CO or a lower $X_{12/13}$ abundance ratio in the arms compared with our modeling results. It could also imply that the excitation temperatures of ^{13}CO is underestimated in our models.

2.6 Discussion

Our multi-line modeling, either under the assumption of one- or two-component gas, results in similar distribution of environmental parameters. First, it reveals different physical conditions between the center (i.e., central ~1 kpc) of NGC 3351 and its adjacent inflow arms - the $N_{\rm CO}/\Delta v \sim 10^{18}/15$ cm^{-2} (km s^{-1})$^{-1}$ found in the center is much higher than $N_{\rm CO}/\Delta v \sim 2 \times 10^{16}/15$ cm^{-2} (km s^{-1})$^{-1}$ in the arms. Second, the temperature is ~30–60 K near the nucleus and both contact points, while other regions show lower temperatures of ~10–20 K (see Figure 2.8b). Third, the H$_2$ volume densities are $\sim 2\text{–}3 \times 10^3$ cm^{-3} across the whole region. The derived temperature and density ranges are consistent with those found in the Milky Way's CMZ (Longmore et al., 2013; Ginsburg et al., 2016; Krieger et al., 2017). Finally, the arm regions have lower optical depths than the center, which could originate from the broader line widths, shear, and bulk gas flows in the arms. The

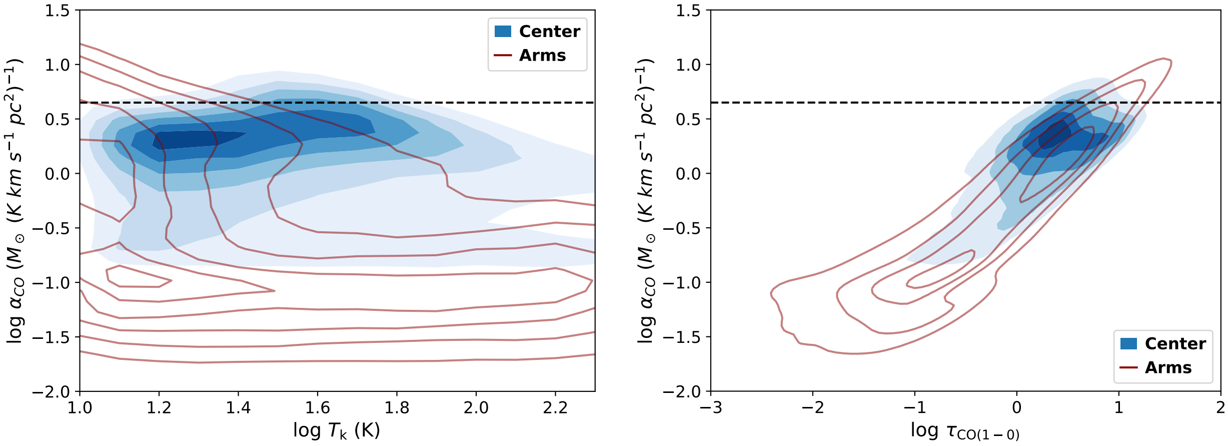

(a)

(b)

Figure 2.17. Relation between α_{CO} and (a) T_k or (b) $\tau_{CO(1-0)}$. The contours show density of points from 1000 likelihood-weighted random draws from the one-component model grids for all pixels in each region. The blue/red contours represent the pixels in the center/arms. The spread in the contours reflects both uncertainties and the relationship between the parameters. The dashed lines mark the Galactic α_{CO} value. There is no clear signs of correlation between α_{CO} and T_k, while α_{CO} and $\tau_{CO(1-0)}$ potentially shows a positive correlation.

lower optical depth in the arms allows more CO emission to escape and is possibly the reason why higher CO/^{13}CO and CO/C^{18}O ratios are observed in the arms (see Figure 2.3d and e). While a high $X_{12/13}$ value can also cause such high line ratios, this may not be the main reason as our modeling of the arm regions with stacking suggests a normal and well-constrained $X_{12/13}$ similar to the center. Observational studies of other barred galaxies have also found significantly higher CO/^{13}CO line ratio in their centers and shown that it is more likely to result from the dramatic change in optical depths or line widths than a high $X_{12/13}$ abundance (e.g., NGC 3627: Morokuma-Matsui et al., 2015; NGC 7465: Young et al., 2021). In addition, we think that turbulence and/or shear in the inflows is likely the cause of higher velocity dispersion in the arms, which is similar to the shear-driven inflows and turbulence in the CMZ of the Milky Way (e.g. Ginsburg et al., 2016; Kruijssen et al., 2019; Hatchfield et al., 2021).

Based on the one- and two-component models, the derived α_{CO} also differs significantly between the center and the arms. Assuming a x_{CO} of 3×10^{-4}, we find $\alpha_{CO} \sim$

0.5–2 $M_\odot$ (K km s^{-1} $pc^2)^{-1}$ in the center, which is lower than the Galactic value at 4.4 $M_\odot$ (K km s^{-1} $pc^2)^{-1}$. In the arms, the value of α_{CO} is even found to be approximately an order of magnitude lower than the center. The center and the arms altogether gives an intensity-weighted mean α_{CO} of ~1.5 $M_\odot$ (K km s^{-1} $pc^2)^{-1}$ over the entire observed region of ~2 kpc. Using the dust mass surface density derived from infrared SED modeling and lower resolution CO and H I observations, Sandstrom et al. (2013) found a similar α_{CO} value of $1.0^{+0.4}_{-0.3}$ $M_\odot$ (K km s^{-1} $pc^2)^{-1}$ in the central 1.7 kpc of NGC 3351 at 40″ scales. Their method assumes that the dust-to-gas ratio is constant across the center and finds the α_{CO} which best reproduces that result by minimizing scatter in dust-to-gas. Since the method used by Sandstrom et al. (2013) is completely independent of the multi-line modeling we use, the fact that both methods reach a similar α_{CO} value gives us more confidence in both results.

With the results of environmental conditions and α_{CO} summarized above, we conclude that the low α_{CO} in the central few kpc of NGC 3351 results from a combination of two factors. First, the central ring/nucleus has a slightly lower-than-Galactic α_{CO}. Secondly, the inflow arms have a substantially lower α_{CO}, because they consist mainly of optically-thin gas. Sun et al. (2018); Sun et al. (2020b) have analyzed cloud-scale molecular gas properties in nearby galaxy samples and clearly showed the increase of velocity dispersion and turbulent pressure toward barred galaxy centers. For the centers of barred galaxies, they reported a mass-weighted velocity dispersion that is ~5 times higher than the disk regions. This could be the cause for the ~2–9 times lower-than-Galactic α_{CO} in the central ~1 kpc of NGC 3351, as the Galactic α_{CO} value was based on molecular cloud measurements in the disk of the Milky Way.

Nevertheless, it is also possible given a different x_{CO}, that the central ~1 kpc of NGC 3351 has a Galactic α_{CO}, so that the significantly lower α_{CO} from the arms would become the main reason for a lower-than-Galactic α_{CO} observed over the central few kpc region. As mentioned in Section 2.5, the assumed x_{CO} value of 3×10^{-4} is appropriate for starburst regions, and thus it is higher than the common assumption of ~10^{-4}. If x_{CO} is in fact a factor of two or three lower than our assumption in the center, the derived value of α_{CO} would increase linearly and lead to a nearly-Galactic α_{CO} in this region. This resulting situation of a nearly-Galactic α_{CO} in the center and a significantly lower α_{CO} in the inflow arms would then be similar to that found in Papadopoulos et al. (2012a) and Leroy et al. (2015), where they reported a nearly-Galactic α_{CO} for GMCs and a much lower α_{CO} value for non-GMC associated gas.

Many explanations for low α_{CO} values have been proposed in the literature. From a theoretical perspective, Bolatto et al. (2013) have shown that enhanced temperatures may lead to lower α_{CO} for isolated and virialized GMCs. The magnetohydrodynamics simulation conducted by Gong et al. (2020) also showed that α_{CO} decreases with increasing heating from cosmic ray ionization. On the other hand, Papadopoulos et al. (2012a) showed the dependence of α_{CO} on optical depths for thermalized, optically thick emission. In such a case, α_{CO} is expected to be approximately proportional to $\tau/[1-\exp(-\tau)]$ if the excitation temperature is kept constant. To understand if the α_{CO} variations in the galaxy center of NGC 3351 are more related to increased temperature or to decreased optical depth, we investigate the correlation between the inferred α_{CO} and the kinetic temperatures or CO optical depths derived from the one-component modeling. For each pixel in the center and arms, we conduct 1000 likelihood-weighted random draws from the 6D full grids of the predicted T_{k}, $\tau_{\mathrm{CO(1-0)}}$ and α_{CO}. Figure 2.17 shows the density of the points from the random draw. The spread of these points reflects both the parameter uncertainties and the overall relationship between α_{CO} and T_{k} or $\tau_{\mathrm{CO(1-0)}}$. In Figure 2.17a, the center region spans a wide range in T_{k} and shows a roughly constant α_{CO} value. For the arms, there are two distinct regions with a higher or lower α_{CO} values, while the low-α_{CO} region extending to the highest temperatures indicates large T_{k} uncertainties in these pixels. Thus, we do not see clear correlation between α_{CO} and T_{k} in either the center or the arm regions. In contrast, Figure 2.17b clearly shows that α_{CO} and $\tau_{\mathrm{CO(1-0)}}$ are more correlated, with both the center and arm regions spanning a range in optical depths and $\alpha_{\rm CO}$. The distribution in Figure 2.17b suggests a positive correlation that is consistent with the thermalized $\alpha_{\rm CO}$ expression in Papadopoulos et al. (2012a), where $\alpha_{\rm CO}$ is expected to increase linearly with τ at $\tau \gg 1$ but barely rise at $\tau \ll 1$ if $T_{\rm ex}$ is constant. Furthermore, the data points from the center and arms are aligned in the $\alpha_{\rm CO}$-$\tau_{\rm CO(1-0)}$ parameter space, showing a continuous transition between the optically-thin and optically-thick regimes.

2.7 Conclusion

We present ALMA observations of multiple CO, ^{13}CO, and C^{18}O rotational lines at ~100 pc resolution toward the central ~2 kpc region of NGC 3351. We constrain the distributions of multiple environmental parameters using multi-line radiative transfer modeling and a Bayesian likelihood analysis along each sight line. With the probability distribution of physical parameters at each pixel, we derive the spatial variation of $\alpha_{\rm CO}$. We construct models with a one-component or two-component assumption on gas phases and compare the results. To recover faint emission from the inflow arms, we also conduct spectral stacking and compare with the pixel-based analysis. Our main results are summarized as follows:

1. All of the CO, ^{13}CO, and C^{18}O images resolve a compact nucleus at the galaxy center, a circumnuclear ring of star formation in the central ~1 kpc, and an emission-faint gap region inbetween. Except for C^{18}O 3–2, the images reveal two bar-driven inflow arms connected to the northern and southern part of the ring (i.e., contact points). The emission is brightest in all the lines at both contact points.

2. The 1DMax solutions from multi-line modeling show no clear variation in CO isotopologue abundance ratios. In the central ~1 kpc, we find $X_{12/13} \sim 20-30$ and $X_{13/18} \sim 6-10$, which are consistent with the values of the Galactic Center. However, we note that $X_{12/13}$ is the least well-constrained property with a broad 1D likelihood distribution in each pixel.

3. Both the one- and two-component modeling results suggest a dominant gas phase with $n_{\mathrm{H_2}} \sim 2$–3×10^3 cm^{-3} in the center and a higher T_{k} of ~30–60 K near the nucleus and contact points than in the rest of the regions. This density and temperature are consistent with those found in the Milky Way's Central Molecular Zone at pc resolutions.

4. The derived α_{CO} distributions based on the one- and two-component models reveal similar spatial variations: in the central 20″ (~1 kpc), α_{CO} ~0.5–2 $(3 \times 10^{-4}/x_{\mathrm{CO}})$ $\mathrm{M}_\odot$ (K km s^{-1} pc^2)$^{-1}$, which is a factor of 2–9 lower than the Galactic value, and it slowly decreases with increasing galactocentric radius; on the other hand, a substantially lower α_{CO} value of $\lesssim$0.1 $(3 \times 10^{-4}/x_{\mathrm{CO}})$ $\mathrm{M}_\odot$ (K km s^{-1} pc^2)$^{-1}$ is found in the inflow arms. We also derive similarly low α_{CO} values from a stacking analysis in the arms and using the LTE expression for α_{CO} in optically thin regions.

5. The substantially lower α_{CO} in the arms can be explained by lower optical depths which implies a higher escape probability for CO emission. The significantly higher CO/^{13}CO and CO/C^{18}O 2–1 ratios in the arms support this scenario, and the large velocity dispersions observed in the arms, likely due to turbulence or shear in the inflows, may be the reason behind such low optical depths.

6. The α_{CO} in the center/ring does not show correlation with temperature. The lower-than-Galactic α_{CO} in this region may be due to higher velocity dispersions in barred galaxy centers than in the disk of the Milky Way. Nevertheless, if our assumption of $x_{\mathrm{CO}} \sim 3\times10^{-4}$ is a factor of few higher than reality, the α_{CO} in the center/ring could have nearly Galactic α_{CO}.

7. We derive an intensity-weighted mean α_{CO} of 1.79 ± 0.10 and 1.11 ± 0.09 $(3 \times 10^{-4}/x_{\mathrm{CO}})$ $\mathrm{M}_\odot$ (K km s^{-1} pc^2)$^{-1}$ over the observed ~2 kpc region, based on one- and two-component models, respectively. This result is a combination of the central ~1 kpc region with a slightly lower-than-Galactic α_{CO} and the inflow arm regions with a significantly lower

α_{CO}. The derived values of the overall α_{CO} are similar to that determined by Sandstrom et al. (2013) using dust modeling at kpc scales.

Overall, our results suggest that dynamical effects and non-GMC associated gas can be important factors that cause α_{CO} variations. In the inflow arms of NGC 3351, α_{CO} is approximately an order of magnitude lower than in the center, possibly due to molecular gas with low optical depths resulting from broader line widths. Therefore, when using CO to trace molecular gas in galaxies with dynamical features that drive inflows (e.g., bars, ovals, interactions, mergers), it is important to account for α_{CO} variations originating from changes in the velocity dispersion and therefore optical depth in specific regions.

2.8 Acknowledgements

We thank the referee for helpful comments that improved the manuscript. Y.-H.T. thanks I-D. Chiang and J. Chastenet for helpful discussion at group meetings. Y.-H.T. and K.S. acknowledge funding support from NRAO Student Observing Support Grant SOSPADA-012 and from the National Science Foundation (NSF) under grant No. 2108081. The work of J.S. and A.K.L. is partially supported by the National Science Foundation (NSF) under Grants No. 1615105, 1615109, and 1653300. A.D.B. acknowledges partial support from grant NSF-AST210814. J.M.D.K. gratefully acknowledges funding from the Deutsche Forschungsgemeinschaft (DFG, German Research Foundation) through an Emmy Noether Research Group (grant number KR4801/1-1) and the DFG Sachbeihilfe (grant number KR4801/2-1), as well as from the European Research Council (ERC) under the European Union's Horizon 2020 research and innovation programme via the ERC Starting Grant MUSTANG (grant agreement number 714907). A.U. acknowledges support from the Spanish funding grants PGC2018-094671-B-I00 (MCIU/AEI/FEDER) and PID2019-108765GB-I00 (MICINN). A.T.B. and F.B. acknowledge funding from the European Research Council (ERC) under the European Union's Horizon 2020 research and innovation programme (grant agreement No. 726384/Empire). E.R. acknowledges the support of the Natural

Sciences and Engineering Research Council of Canada (NSERC), funding reference number RGPIN-2017-03987.

This paper makes use of the following ALMA data:
ADS/JAO.ALMA#2013.1.00634.S,
ADS/JAO.ALMA#2013.1.00885.S,
ADS/JAO.ALMA#2015.1.00956.S,
ADS/JAO.ALMA#2016.1.00972.S.
ALMA is a partnership of ESO (representing its member states), NSF (USA), and NINS (Japan), together with NRC (Canada), NSC and ASIAA (Taiwan), and KASI (Republic of Korea), in cooperation with the Republic of Chile. The Joint ALMA Observatory is operated by ESO, AUI/NRAO, and NAOJ. The National Radio Astronomy Observatory is a facility of the National Science Foundation operated under cooperative agreement by Associated Universities, Inc.

We acknowledge the usage of NASA's Astrophysics Data System (http://www.adsabs.harvard.edu) and `ds9`, a tool for data visualization supported by the Chandra X-ray Science Center (CXC) and the High Energy Astrophysics Science Archive Center (HEASARC) with support from the JWST Mission office at the Space Telescope Science Institute for 3D visualization.

*Facilities:*ALMA

Software:`CASA` (McMullin et al., 2007), `ds9` (Smithsonian Astrophysical Observatory, 2000; Joye and Mandel, 2003), `matplotlib` (Hunter, 2007), `numpy` (Harris et al., 2020), `scipy` (Virtanen et al., 2020), `astropy` (Astropy Collaboration et al., 2013; Astropy Collaboration et al., 2018), `RADEX` (van der Tak et al., 2007), `corner` (Foreman-Mackey, 2016) `spectral-cube` (Ginsburg et al., 2019)

* * *

This chapter, in full, is a reprint of the material as it appears in "Molecu-

lar Gas Properties and CO-to-H_2 Conversion Factors in the Central Kiloparsec of NGC 3351" by Yu-Hsuan Teng, Karin M. Sandstrom, Jiayi Sun, Adam K. Leroy, L. Clifton Johnson, Alberto D. Bolatto, J. M. Diederik Kruijssen, Andreas Schruba, Antonio Usero, Ashley T. Barnes, Frank Bigiel, Guillermo A. Blanc, Brent Groves, Frank P. Israel, Daizhong Liu, Erik Rosolowsky, Eva Schinnerer, J. D. Smith, and Fabian Walter, which was published in The Astrophysical Journal in 2022. The dissertation author was the primary investigator and author of this paper.

Chapter 3

The Physical Drivers and Observational Tracers of $\alpha_{\rm CO}$ Variations in Nearby Barred Galaxy Centers

Abstract

The CO-to-H_2 conversion factor ($\alpha_{\rm CO}$) is central to measuring the amount and properties of molecular gas. It is known to vary with environmental conditions, and previous studies have revealed lower $\alpha_{\rm CO}$ in the centers of some barred galaxies on kpc scales. To unveil the physical drivers of such variations, we obtained ALMA Band 3, 6, and 7 observations toward the inner ~2 kpc of NGC 3627 and NGC 4321 tracing ^{12}CO, ^{13}CO, and C^{18}O lines on ~100 pc scales. Our multi-line modeling and Bayesian likelihood analysis of these datasets reveal variations of molecular gas density, temperature, optical depth, and velocity dispersion, which are among the key drivers of $\alpha_{\rm CO}$. The central 300 pc nuclei in both galaxies show strong enhancement of temperature $T_{\rm k} \gtrsim 100$ K and density $n_{\rm H_2} > 10^3$ cm^{-3}. Assuming a CO-to-H_2 abundance of 3×10^{-4}, we derive 4–15 times lower $\alpha_{\rm CO}$ than the Galactic value across our maps, which agrees well with previous kpc-scale measurements. Combining the results with our previous work on NGC 3351, we find a strong correlation of $\alpha_{\rm CO}$ with low-J ^{12}CO optical depths ($\tau_{\rm CO}$), as well as an anti-correlation with T_k. The τ_CO correlation explains most of the α_CO variation in the three galaxy centers, whereas changes in T_k influence α_CO to second order. Overall, the observed line width and ^{12}CO/^{13}CO 2–1 line ratio correlate with τ_CO variation in these centers, and thus they are useful observational indicators for α_CO variation. We also test current simulation-based α_CO prescriptions and find a systematic overprediction, which likely originates from the mismatch of gas conditions between our data and the simulations.

3.1 Introduction

The cold and dense molecular gas in the interstellar medium (ISM) is the direct fuel for current and future star formation. Measuring the amount and properties of molecular gas is crucial for understanding star formation, the ISM, and their relations with galaxy evolution. While molecular hydrogen ($\mathrm{H_2}$) is the primary constituent of molecular gas, it is difficult to be directly observed in the cold ($T \lesssim 100$ K) phase where stars are formed (Tielens, 2010; Draine, 2011). Instead, molecular gas mass is often measured with the low-J rotational lines of carbon monoxide ($^{12}\mathrm{C}^{16}\mathrm{O}$, hereafter CO) by applying a CO-to-$\mathrm{H_2}$ conversion factor (Solomon et al., 1987; Bolatto et al., 2013). This conversion factor (α_CO) is often defined for the $J=1$–0 line as the ratio of total molecular gas mass (M_mol in $\mathrm{M_\odot}$) to the CO $J=1$–0 luminosity ($L_\mathrm{CO(1-0)}$ in K km s^{-1} pc^2), or equivalently, the ratio of molecular gas surface density (Σ_mol in $\mathrm{M_\odot}$ pc^{-2}) to the CO 1–0 intensity ($I_\mathrm{CO(1-0)}$ in K km s^{-1}):

$$\alpha_\mathrm{CO} = \frac{M_\mathrm{mol}}{L_\mathrm{CO(1-0)}} = \frac{\Sigma_\mathrm{mol}}{I_\mathrm{CO(1-0)}} \left[\frac{\mathrm{M_\odot}}{\mathrm{K\ km\ s^{-1}\ pc^2}}\right] . \tag{3.1}$$

Another common way to express the conversion factor is to quote the ratio between $\mathrm{H_2}$ column density and CO intensity, $X_\mathrm{CO} \equiv N_\mathrm{H_2}/I_\mathrm{CO(1-0)}$, which is related to α_CO via $X_\mathrm{CO}\left[\frac{\mathrm{cm^{-2}}}{\mathrm{K\ km\ s^{-1}}}\right] = 4.5\times10^{19}\ \alpha_\mathrm{CO}\left[\frac{\mathrm{M_\odot}}{\mathrm{K\ km\ s^{-1}\ pc^2}}\right]$, where the 4.5×10^{19} factor includes the mass contribution from Helium to M_mol.

$\alpha_{\rm CO}$ can be measured by estimating $M_{\rm mol}$ using virial methods, γ-ray emission, or optically-thin tracers like dust or CO isotopologues (e.g., Bolatto et al., 2008; Leroy et al., 2011; Ackermann et al., 2012b; Ackermann et al., 2012a; Sandstrom et al., 2013; Remy et al., 2017; Israel, 2020; Teng et al., 2022). Previous $\alpha_{\rm CO}$ measurements toward molecular clouds in the disks of the Milky Way or other nearby spiral galaxies have reported relatively consistent $\alpha_{\rm CO}$ values around 4.4 $M_\odot$ (K km s^{-1} $pc^2)^{-1}$ (or 2×10^{20} cm^{-2} (K km $s^{-1})^{-1}$ in $X_{\rm CO}$) within a factor of ~2 (see the review by Bolatto et al., 2013, and references therein). This also includes studies across various Galactic disk GMCs using CO and ^{13}CO observations together with radiative transfer modeling (Goldsmith et al., 2008; Liu et al., 2013; Nishimura et al., 2015), which is similar to the methodology we use in this paper. Therefore, many studies assume a constant, Galactic-like $\alpha_{\rm CO}$ value when inferring molecular gas mass from CO observations. However, recent theoretical studies have shown that $\alpha_{\rm CO}$ can vary by up to one or two orders of magnitude in different environments, and it is known to depend on gas properties including metallicity, temperature, column and volume densities, velocity dispersion, as well as the nature of excitation (e.g., Wolfire et al., 2010; Feldmann et al., 2012a; Glover and Clark, 2012; Narayanan et al., 2012; Kazandjian et al., 2012; Kazandjian et al., 2015; Bolatto et al., 2013; Renaud et al., 2019; Gong et al., 2020). Such environmental dependence can explain why $\alpha_{\rm CO}$ has been found in observations to deviate from the Galactic disk value in various galaxy centers (Israel, 2009a; Israel, 2009b; Israel, 2020; Sandstrom et al., 2013; Teng et al., 2022), (ultra-)luminous infrared galaxies (U/LIRGs; Downes and Solomon, 1998; Kamenetzky et al., 2014; Kamenetzky et al., 2017; Sliwa et al., 2014; Sliwa et al., 2017; Herrero-Illana et al., 2019), or low-metallicity galaxies (Israel, 1997; Israel, 2000; Papadopoulos et al., 2018; Madden et al., 2020).

The variation of $\alpha_{\rm CO}$ within and among galaxies has a direct impact on many important quantities and relations that are widely used in current studies, because of their dependence on molecular gas mass estimation. This includes the molecular gas depletion time (which depends on $M_{\rm mol}$ and star formation rate), the cloud free-fall time (which depends on $M_{\rm mol}$ and cloud size), the virial parameter and turbulent pressure (both of which depend on $M_{\rm mol}$, cloud size, and velocity dispersion), and the gas inflow rates in barred galaxy centers, to name only a few. For instance, Leroy et al. (2013) and den Brok et al. (2023) showed that the molecular cloud depletion time in galaxy centers will become significantly shorter if $\alpha_{\rm CO}$ depression is considered. Sun et al. (2020a); Sun et al. (2022) demonstrated how cloud virial parameter, turbulent pressure, and ISM dynamical equilibrium pressure would vary with different choices of $\alpha_{\rm CO}$. $\alpha_{\rm CO}$ is also the dominant source of uncertainty in estimating the bar-driven mass inflow rates in the Central Molecular Zone (Sormani and Barnes, 2019). Furthermore, $\alpha_{\rm CO}$ variation can change the slopes of star formation scaling relations (e.g., Feldmann et al., 2012b; Narayanan et al., 2012; Pessa et al., 2021; den Brok et al., 2023; Sun et al., 2023), such as the Kennicutt–Schmidt (Kennicutt, 1998; Schruba et al., 2011) and molecular gas main sequence relations (Lin et al., 2019). Therefore, it is critical to understand the physical drivers of $\alpha_{\rm CO}$ and establish how $\alpha_{\rm CO}$ behaves in different environmental regimes.

Recent years have seen progress on the development of a metallicity-dependent $\alpha_{\rm CO}$ prescription (Schruba et al., 2012; Amorín et al., 2016; Accurso et al., 2017b), which has been applied in several recent works (e.g., Sun et al., 2020a; Sun et al., 2020b; Pessa et al., 2021). In terms of the emissivity dependence, many studies adopt a bimodal $\alpha_{\rm CO}$ with ~0.8 $\rm M_\odot$ (K km $\rm s^{-1}$ $\rm pc^2)^{-1}$ in (U)LIRGs or starburst regions (Downes and Solomon, 1998) and the Galactic-like 4.4 $\rm M_\odot$ (K km $\rm s^{-1}$ $\rm pc^2)^{-1}$ elsewhere. However, recent theoretical studies and simulations suggest that $\alpha_{\rm CO}$ is not simply bimodal or metallicity dependent. Instead, it is likely to vary continuously with local environmental conditions in addition to metallicity (Narayanan et al., 2012; Bolatto et al., 2013). Theoretical and observational works have also shown that emissivity-related terms such as temperature, density, and opacity are important drivers of $\alpha_{\rm CO}$ variation, especially in actively star-forming galaxies including mergers and galaxy centers (Narayanan et al., 2011; Narayanan et al., 2012; Papadopoulos et al., 2012a; Cicone et al., 2018; Gong et al., 2020; Teng et al., 2022).

Therefore, a crucial next step would be to identify observational tracers and establish a robust prescription that can predict the effects of emissivity-related terms on $\alpha_{\rm CO}$.

Compared to observational studies, simulations can give direct $\alpha_{\rm CO}$ predictions from sophisticated modeling of gas dynamics, chemistry, and radiative transfer, allowing the development of prescriptions useful for observations. Thus, significant efforts have been made to investigate $\alpha_{\rm CO}$ variations using numerical simulations (Shetty et al., 2011a; Shetty et al., 2011b; Narayanan et al., 2011; Narayanan et al., 2012; Feldmann et al., 2012a; Bournaud et al., 2015; Duarte-Cabral et al., 2015; Peñaloza et al., 2018; Gong et al., 2018; Gong et al., 2020; Renaud et al., 2019; Seifried et al., 2020; Bisbas et al., 2021; Hu et al., 2022). In particular, Narayanan et al. (2012) proposed a functional prediction of $\alpha_{\rm CO}$ from metallicity and $I_{\rm CO(1-0)}$ based on low-redshift mergers and high-redshift disks in their simulation. Some studies focusing on starburst mergers also found correlations between $\alpha_{\rm CO}$ and star formation rate or molecular gas depletion time (Bournaud et al., 2015; Renaud et al., 2019). More recently, (magneto-)hydrodynamical simulations resolving down to pc scales further explored how $\alpha_{\rm CO}$ may vary with observational beam size (Gong et al., 2020; Hu et al., 2022). Both studies have suggested $\alpha_{\rm CO}$ dependence on $I_{\rm CO(1-0)}$, and Gong et al. (2020) also found $\alpha_{\rm CO}$ correlations with the CO 2–1/1–0 line ratio (R_{21}) and CO line peak temperature. While these simulations are limited to Galactic disk-like environments with much lower CO intensity (< 200 K km s^{-1}) and surface density (< 100 M$_\odot$ pc^{-2}) than in galaxy centers, it is important to test the simulation-based predictions and understand if and where they can accurately predict $\alpha_{\rm CO}$.

In this work, we study the spatial variations of molecular gas properties and $\alpha_{\rm CO}$ in nearby galaxy centers at 100 pc scales, using observations of multiple CO, ^{13}CO, and C^{18}O rotational transitions with the Atacama Large Millimeter/submillimeter Array (ALMA). We target nearby barred galaxies that were found by previous kpc-scale observations to have $\alpha_{\rm CO}$ depression in their central few kpc, including NGC 3351, NGC 3627, and NGC 4321 (Sandstrom et al., 2013; Morokuma-Matsui et al., 2015; Israel, 2020; Jiao et al., 2021).

Table 3.1. Source Information

Property	NGC 3627	NGC 4321	NGC 3351
R.A. (J2000)	$11^{\mathrm{h}}20^{\mathrm{m}}15\overset{\mathrm{s}}{.}0$	$12^{\mathrm{h}}22^{\mathrm{m}}54\overset{\mathrm{s}}{.}9$	$10^{\mathrm{h}}43^{\mathrm{m}}57\overset{\mathrm{s}}{.}8$
Decl. (J2000)	$+12^{\circ}59'29''$	$+15^{\circ}49'20''$	$+11^{\circ}42'13''$
Hubble Type	SABb	SABbc	SBb
Nuclear Type	LINER/AGN	H II/LINER	H II
Distance (Mpc)	11.32 ± 0.48	15.21 ± 0.49	9.96 ± 0.33
Linear Scale (pc/″)	54.9	73.7	48.3
Matched Beam (″)	2.0	1.7	2.1
Inclination (°)	57.3 ± 1.0	38.5 ± 2.4	45.1 ± 6.0
Position Angle (°)	173.1 ± 3.6	156.2 ± 1.7	192.7 ± 0.4
$\log_{10} M_*$ ($\mathrm{M}_\odot$)	10.84	10.75	10.37
SFR ($\mathrm{M}_\odot$/yr)	3.89	3.55	1.32

Positions, stellar masses, and star formation rates from Leroy et al. (2021b). Nuclear types suggested by Ho et al. (1997); Filho et al. (2000); Moustakas et al. (2010); Belfiore et al. (2022). Distances from Anand et al. (2021). Inclinations and position angles from Lang et al. (2020).

These galaxies were also found to have a near-solar gas-phase metallicity (Kreckel et al., 2019; Kreckel et al., 2020; Santoro et al., 2022; Williams et al., 2022). Following our previous work on the central kpc of NGC 3351 (Teng et al., 2022), here we present an extension towards the centers of NGC 3627 and NGC 4321. In this paper, we discuss the implications of the combined results for all three galaxy centers. The basic information for these galaxies is provided in Table 3.1.

This paper is structured as follows. Section 3.2 describes the observations and data reduction. Section 3.3 presents the results of integrated intensity, line ratios, and the regional statistics. Our multi-line modeling setup and results are presented in Section 3.4. In Section 3.5, we discuss implications from our modeling and α_{CO} solutions and compare with results from the literature. The conclusions are summarized in Section 3.6.

3.2 Observations and Data

We obtained ALMA observations of six low-J CO, ^{13}CO, and C^{18}O lines in Band 3, 6, and 7, covering at least the central $35'' \times 35''$ (1.5–2 kpc) area in NGC 3627 and NGC 4321. The achieved angular resolutions of 1–2″ (or $\lesssim$100 pc in physical scale) allow us to probe molecular gas conditions approaching typical giant molecular cloud (GMC) scales of a few tens of pc (e.g., Scoville et al., 1987). These observations were planned together with and set up similarly to those described in Teng et al. (2022, which cover the central ~30″ of NGC 3351). We briefly summarize the data characteristics below, and refer interested readers to Teng et al. (2022) for more details.

Our Band 3 observations (ALMA project IDs: 2015.1.00978.S and 2016.1.00972.S) captured the $J=1$–0 line of CO with the 12-m array in the C36-2/3 and C40-4 configurations for NGC 3627 and NGC 4321, respectively. The native beam sizes are accordingly $1.8'' \times 1.7''$ and $1.3'' \times 1.0''$. We use a three-pointing mosaic to cover the central $60'' \times 60''$ area in each galaxy. The rms noise level is 0.16 K (for NGC 3627) and 0.09 K (for NGC 4321) per 2.5 km s^{-1} velocity channel.

The Band 6 observations come from two separate projects and cover the $J=2$–1 transitions of CO, ^{13}CO, and C^{18}O in two distinct spectral tunings. Observations of the ^{13}CO and C^{18}O 2–1 (ALMA project ID: 2015.1.00978.S) were carried out in the C36-1 and C36-2/3 configurations for NGC 3627 and NGC 4321, respectively. We use a seven-pointing mosaic to cover the central $40'' \times 40''$ area for each target. The native beam size is $1.5'' \times 1.2''$ ($1.1'' \times 0.9''$) and the rms noise level is 15 mK (9 mK) per 2.5 km s^{-1} velocity channel for NGC 3627 (NGC 4321). The CO 2–1 data were instead obtained from the PHANGS–ALMA survey (project 2015.1.00956.S) and reach an angular resolution of ~1.6″ and an rms level of ~0.08 K (for more details, see Leroy et al. 2021b; Leroy et al. 2021a).

The Band 7 observations cover the $J=3$–2 lines of ^{13}CO and C^{18}O (ALMA project ID: 2016.1.00972.S) with a mixture of C40-1, C43-1, and C43-2 configurations for either target. The central $35'' \times 35''$ area in each galaxy is covered by a 14-pointing mosaic, and the achieved native beam sizes are $1.2'' \times 1.0''$ for NGC 3627 and $1.1'' \times 0.9''$ for NGC 4321. The rms noise level is 10 mK (7 mK) per 2.5 km s^{-1} velocity channel for NGC 3627 (NGC 4321).

We follow the same calibration and imaging process as described in full detail in Teng et al. (2022). In short, we calibrated the raw data with scripts provided by the observatory and imaged all the lines in a similar way adapting the PHANGS–ALMA pipeline (Leroy et al., 2021a). We then convolved all the data cubes to a matched round beam of 2.0″ (110 pc) for NGC 3627 and 1.7″ (125 pc) for NGC 4321, and produced a set of moment maps and effective line width (Δv) maps[1] for all six lines at the common resolution. The map creation scheme is also similar to that implemented in the PHANGS–ALMA pipeline, except that we start from a high confidence mask including at least two consecutive channels above 5σ, and then expand into a more inclusive mask with at least two consecutive channels above 2σ. Finally, we regridded all data products such that the pixel scale matches 1/2 the beam size (i.e., Nyquist sampling). These beam-matched, Nyquist-sampled data products include a set of moment maps and uncertainty maps for all the lines, where the uncertainty maps were derived from the noise measured in the data cubes propagated through the steps of creating the moment maps. The data products are used throughout this work, and many of the maps are presented in Section 3.3 and Appendix 3.C.1.

We note that most of the observations presented here only used the 12-m array, except for the CO 2–1 observations from PHANGS–ALMA (which combines ALMA 12-m, 7-m, and total-power observations to ensure flux recovery on all scales; see Leroy et al., 2021b). To minimize impacts from the lack of short-spacing data, we adopt the same method introduced in Teng et al. (2022). Namely, we estimate the flux recovery ratio by creating a new CO 2–1 image from only the PHANGS 12-m observations and measuring the (pixel-by-pixel) ratio of the moment 0 maps made from the 12-m only image and the combined 12-m+7-m+TP image. Then, we mask out all pixels with that ratio lower than 70% throughout our analysis. For NGC 3627 and NGC 4321, this results in ~1% and 12% of the number of pixels being masked, respectively, after applying the signal-to-noise (S/N) cuts described in Section 3.3. Thus, we expect individual line intensity errors due to incomplete u–v sampling to be less than 30%, assuming that CO 1–0 and 2–1 emission shows the same distribution. With the above procedure, we make sure that our analysis avoids regions where there can be significant missing flux due to the lack of short-spacing

---

[1] The effective line width is defined as $I_{\rm CO}/(\sqrt{2\pi}\,T_{\rm peak})$, which is identical to moment 2 for a Gaussian line profile. See Heyer et al. (2001) and Sun et al. (2018); Sun et al. (2020a) for more details.

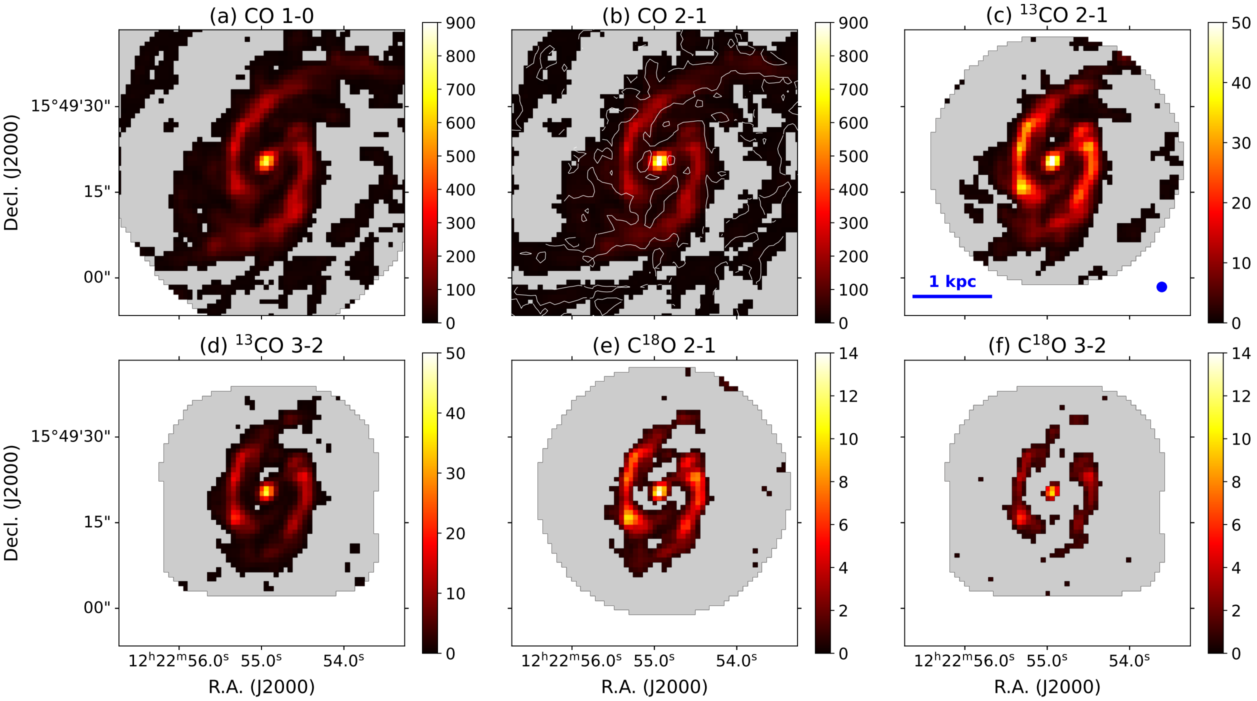

Figure 3.1. Integrated intensity maps of NGC 4321 (in units of K km s^{-1}). The white areas lie outside the field of view of ALMA observations, while the gray areas show the pixels with $< 3\sigma$ detection. The overlaid contour in panel (b) represents a 70% flux recovery rate (12-m/combined). The matched beam size of 1.7″ and a scale bar of 1 kpc are shown in panel (c). A bright nucleus and the inner spiral arms are securely detected in all six lines. The pixels in the gap between the nucleus and arms generally have low flux recovery rate with the 12-m array alone, and thus most of that region will be excluded from our analysis.

information.

3.3 Results

Figures 3.1 and 3.2 show the integrated intensity (moment 0) maps of the six observed lines for NGC 4321 and NGC 3627, respectively. In these figures, we mask out regions with S/N < 3 for the line integrated intensity based on the ratio of moment 0 map and its associated uncertainty map (Section 3.2). This masking is applied to the 2D moment maps and is distinct from the masking done on the 3D data cubes when creating the moment maps as described in Section 3.2.

In NGC 4321, the observations of all six lines capture a bright and compact (~300 pc) nucleus surrounded by two inner spiral arms or bar lanes at ~1 kpc galactocentric diameter.

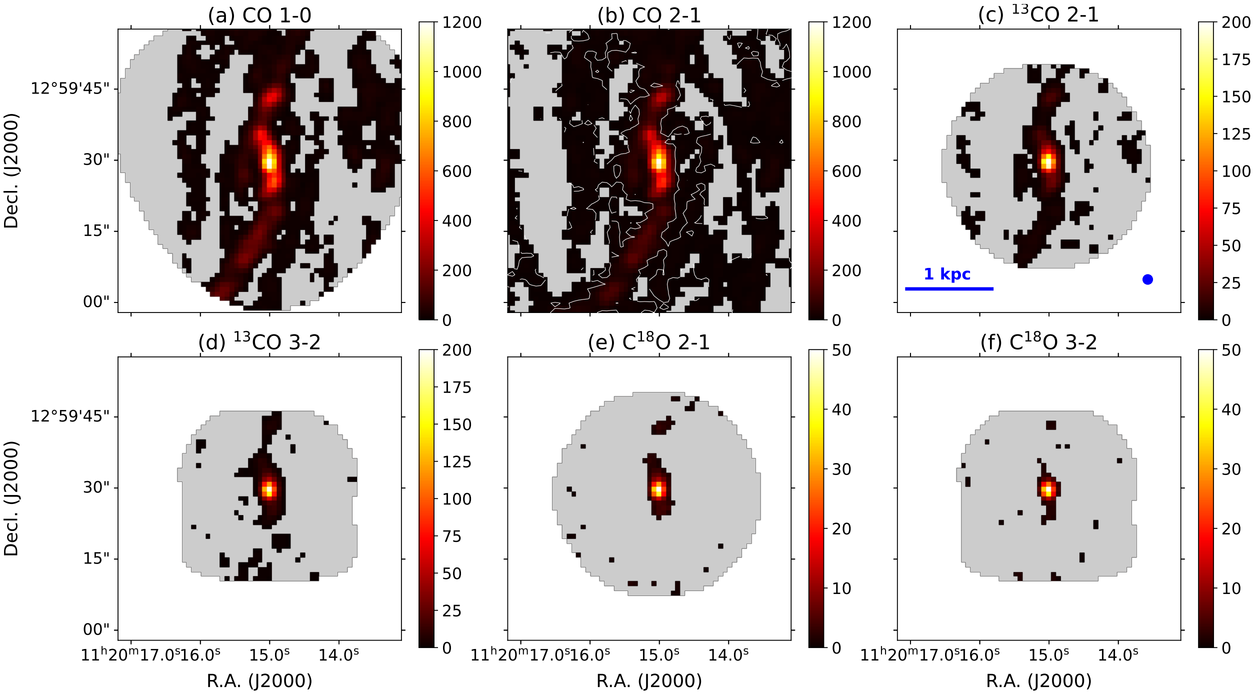

Figure 3.2. Same as Figure 3.1, but for NGC 3627. The matched beam size of 2.0″ and a scale bar of 1 kpc are shown in panel (c). The central nucleus with a size of ~300 pc is securely detected in all six lines, while the inner spiral arms are not bright enough to be detected in C^{18}O.

We note that the regions between the nucleus and the arms generally have < 70% flux recovery rate (based on CO 2–1), and thus they will be excluded from our analysis. The moment 0 images of NGC 3627 also reveal a ~300 pc nucleus as well as bar lanes connected to the center. The nucleus of NGC 3627 is over two times brighter than that of NGC 4321 and is detected in all six lines, while the outer lanes in NGC 3627 are not bright enough to be detected in C^{18}O. We note that the bar-ends of NGC 3627, which are known to have high star formation rate likely due to interactions between the spiral arms and the bar (Watanabe et al., 2011; Murphy et al., 2015; Beuther et al., 2017; Chevance et al., 2020; Bešlić et al., 2021), are just outside our common field of view but can be slightly seen near the south-east edge of Figure 3.2(b).

As shown in Figure 3.3, we define three different regions in both galaxies for further analysis. The "nucleus" is defined as the central 6″ (300–450 pc in diameter) region. The "inner arms" cover the inner 20″ region in galactocentric diameter but excludes the nucleus

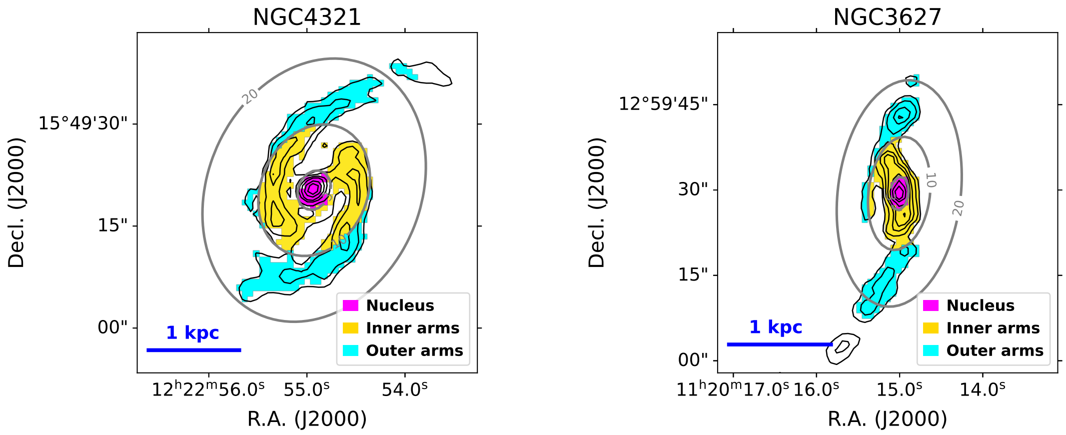

Figure 3.3. Definition of the nucleus, inner arms, and outer arms regions based on the galactocentric radius, which will be used for regional statistics and analysis. The black contours represent the CO 2–1 integrated intensity at 50, 100, 200, 300, 500, 700 (and 900 for NGC 3627) K km s^{-1}. The gray contours show the projected galactocentric radius of 3, 10, and 20″, respectively.

region, and the "outer arms" refer to pixels outside a diameter of 20″ that are connected to the inner arms[2]. All the pixels included in our analysis have S/N > 3 in ^{13}CO and a flux recovery rate of > 70%. To further ensure a reasonable uncertainty range for the parameters estimated from our modeling (Section 3.4), we only consider pixels with S/N $\gtrsim$5 and 50 in ^{13}CO and CO lines, respectively, which corresponds to $I_{\rm CO(2-1)} > 50$ K km s^{-1}. This intensity cutoff ensures a < 0.5 dex uncertainty in our $\alpha_{\rm CO}$ estimates for every included pixel, and it is applied in addition to the S/N > 3 criterion for ^{13}CO.

---

[2] The nomenclature of "arms" in this paper is simply based on gas morphology and has no implications on the dynamical driver of this feature. These regions are bar lanes or inner spiral arms within the main galactic bar, which are different from spiral arms seen in the outer disks.

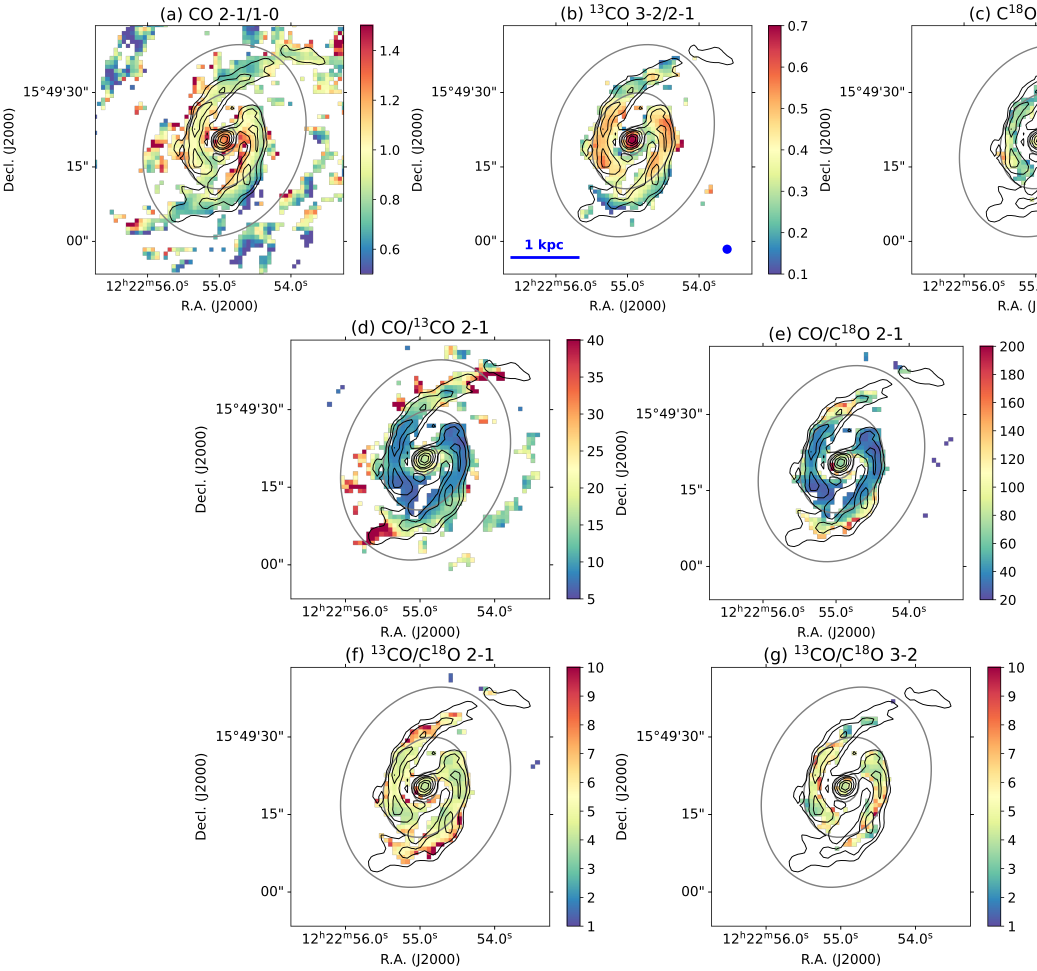

Figure 3.4. Line ratio maps of NGC 4321. Any region with < 70% flux recovered rate or < 3σ detection in either relevant line is masked out in each panel. The gray contours represent the projected galactocentric radii and the black contours show the CO 2–1 integrated intensity, both of which are the same as in Figure 3.3. (a)–(c) show the primarily temperature-sensitive line ratios, and (d)–(g) show the line ratios primarily sensitive to isotopologue abundances or optical depths.

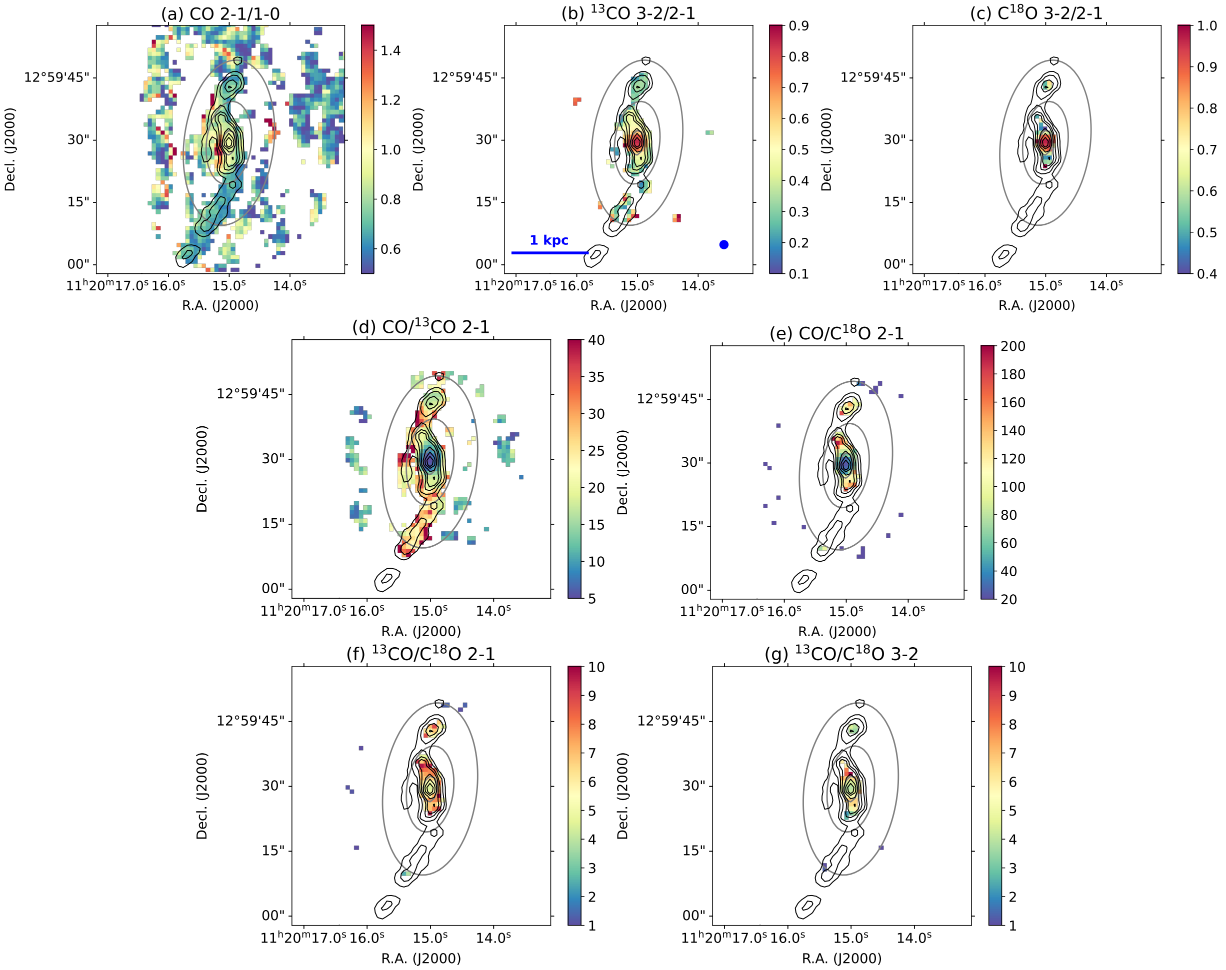

Figure 3.5. Line ratio maps of NGC 3627. Contour levels represent the CO 2–1 integrated intensity at $I_{\mathrm{CO}(2-1)} = 50, 100, 200, 300, 500, 700, 900$ K km s^{-1}. See the caption of Figure 3.4 for more information.

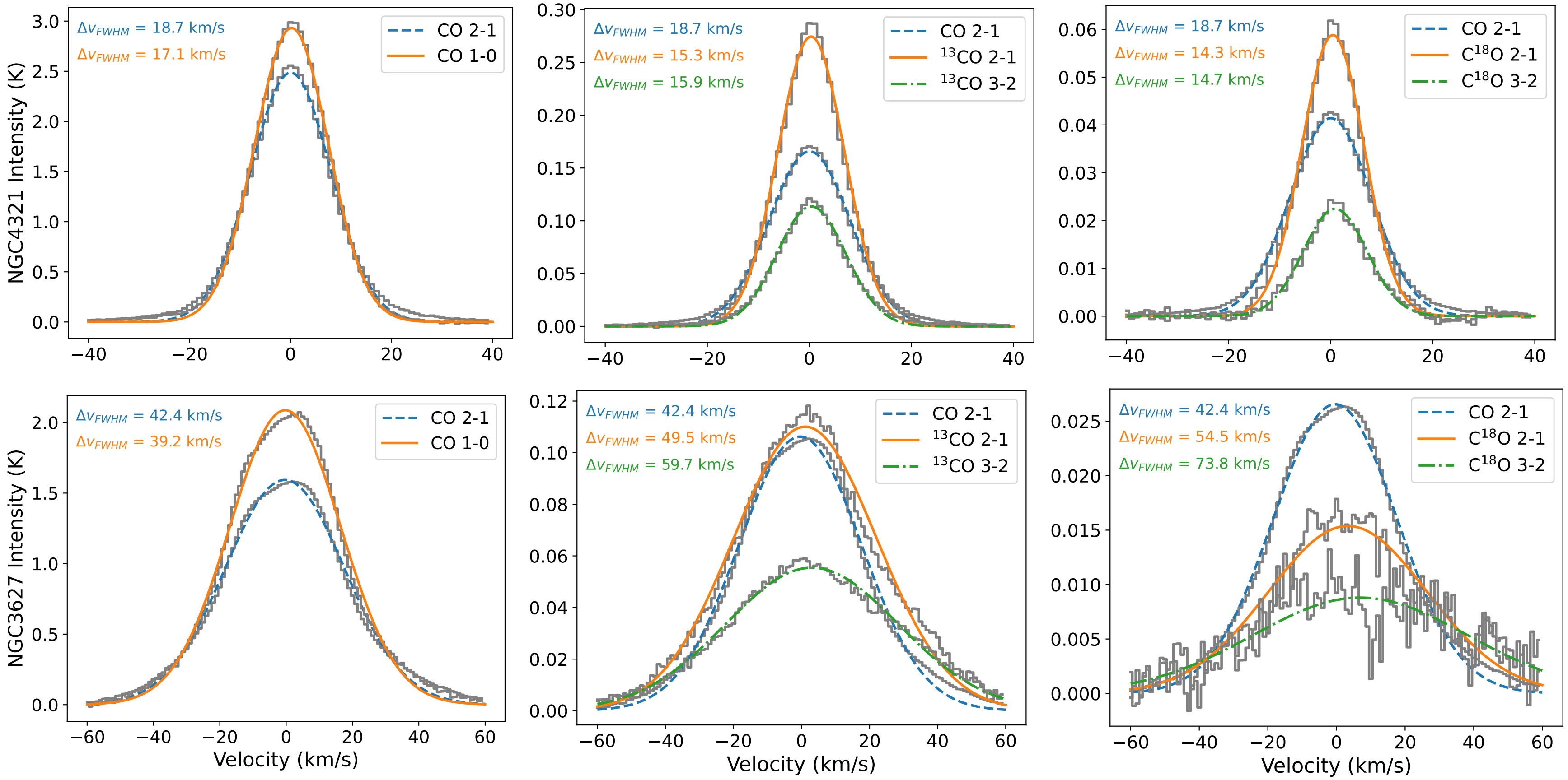

Figure 3.6. Shifted and averaged spectra over the whole kpc regions of NGC 4321 (top row) and NGC 3627 (bottom row), using the moment 1 of CO 2–1 as the fiducial velocity. The intensity of CO 2–1 is scaled down by a factor of 15 (60) in the middle (right) column. The best-fit Gaussian is overlaid, and the upper left corner of each panel lists the fitted FWHM line widths corresponding to the lines in the legend. In both galaxy centers, the overall line width agrees among all six lines within 30–40%.

Table 3.2. Regional Line Ratios and CO Line Width in NGC 4321.

Region		CO $\frac{2-1}{1-0}$	^{13}CO $\frac{3-2}{2-1}$	C^{18}O $\frac{3-2}{2-1}$	$\frac{\mathrm{CO}}{^{13}\mathrm{CO}}$ 2–1	$\frac{\mathrm{CO}}{\mathrm{C}^{18}\mathrm{O}}$ 2–1	$\frac{^{13}\mathrm{CO}}{\mathrm{C}^{18}\mathrm{O}}$ 2–1	$\frac{^{13}\mathrm{CO}}{\mathrm{C}^{18}\mathrm{O}}$ 3–2	Δv_{CO} [km s^{-1}]
Whole	Mean	0.92	0.38	0.46	16.97	62.53	5.46	5.00	17.7
	Std. Dev.	0.22	0.12	0.16	11.02	34.89	1.57	1.44	6.2
	Integrated Mean	0.92	0.43	0.46	11.51	49.93	4.80	4.69	—
Nucleus	Mean	1.22	0.51	0.58	18.97	101.86	5.43	5.25	34.4
	Std. Dev.	0.14	0.15	0.12	2.58	43.60	1.61	1.18	9.1
	Integrated Mean	1.22	0.61	0.61	17.95	81.38	4.58	4.68	—
Inner arms	Mean	0.99	0.44	0.44	9.16	43.67	4.82	5.17	17.2
	Std. Dev.	0.13	0.08	0.12	2.50	17.61	0.94	1.33	5.2
	Integrated Mean	0.96	0.46	0.44	8.51	37.72	4.47	4.77	—
Outer arms	Mean	0.82	0.29	—	18.56	92.01	6.68	—	16.2
	Std. Dev.	0.14	0.09	—	9.89	33.60	1.58	—	3.2
	Integrated Mean	0.81	0.31	—	14.60	80.39	6.18	—	—

Line ratios are calculated using the moment 0 maps in units of K km s^{-1}. The integrated means are calculated by first averaging the integrated intensities in each region and then dividing them to obtain the ratios, while the mean and standard deviation are for the individual pixels of the map. Δv_{CO} represents the effective line width[1] of CO, not the FWHM. All statistics only take into account the pixels selected for analysis (i.e., S/N > 3 in ^{13}CO, flux recovery rate > 70%, and $I_{\mathrm{CO}(2-1)} > 50$ K km s^{-1}). Due to poor detection of C^{18}O 3–2 in the outer arms, the statistics for C^{18}O 3–2/2–1 and ^{13}CO/C^{18}O 3–2 in that region are not provided.

Table 3.3. Regional Line Ratios and CO Line Width in NGC 3627.

Region		CO $\frac{2-1}{1-0}$	^{13}CO $\frac{3-2}{2-1}$	C^{18}O $\frac{3-2}{2-1}$	$\frac{\mathrm{CO}}{^{13}\mathrm{CO}}$ 2–1	$\frac{\mathrm{CO}}{\mathrm{C}^{18}\mathrm{O}}$ 2–1	$\frac{^{13}\mathrm{CO}}{\mathrm{C}^{18}\mathrm{O}}$ 2–1	$\frac{^{13}\mathrm{CO}}{\mathrm{C}^{18}\mathrm{O}}$ 3–2	Δv_{CO} [km s^{-1}]
Whole	Mean	0.75	0.46	0.73	19.88	87.84	6.13	5.16	34.1
	Std. Dev.	0.18	0.19	0.19	9.57	46.56	2.28	1.78	12.3
	Integrated Mean	0.81	0.63	0.85	12.55	55.51	5.67	4.60	—
Nucleus	Mean	0.93	0.74	0.86	7.51	44.75	5.69	4.94	60.9
	Std. Dev.	0.03	0.08	0.12	2.22	21.41	0.97	0.94	8.2
	Integrated Mean	0.93	0.78	0.91	6.65	34.29	5.16	4.40	—
Inner arms	Mean	0.85	0.43	0.65	21.06	109.64	7.29	5.86	38.9
	Std. Dev.	0.18	0.13	0.19	8.63	37.60	1.52	1.82	10.4
	Integrated Mean	0.84	0.49	0.64	15.78	98.93	7.12	5.89	—
Outer arms	Mean	0.72	0.35	—	27.20	—	—	—	26.2
	Std. Dev.	0.09	0.15	—	8.43	—	—	—	4.5
	Integrated Mean	0.70	0.32	—	23.15	—	—	—	—

Due to poor detection of both C^{18}O lines in the outer arms, the statistics for C^{18}O 3–2/2–1, CO/C^{18}O 2–1 and ^{13}CO/C^{18}O 2–1 and 3–2 in that region are not provided. See Table 3.2 notes for more information.

Figure 3.4 and 3.5 show the line ratio maps of CO 2–1/1–0, ^{13}CO 3–2/2–1, C^{18}O 3–2/2–1, CO/^{13}CO 2–1, CO/C^{18}O 2–1, ^{13}CO/C^{18}O 2–1, and ^{13}CO/C^{18}O 3–2, which are generated from the moment 0 maps in units of K km s^{-1}. These line ratio maps reveal clear variation among our defined regions. All the same-species ratios, which are primarily sensitive to temperature (panels (a)–(c) in Figures 3.4 and 3.5), show clear enhancement in the nucleus of NGC 4321 and 3627, suggesting warmer and/or denser gas toward both galactic nuclei. However, the two galaxies show different trends in the same-transition ratios which are mostly sensitive to abundance/opacity. In NGC 4321, the CO/^{13}CO and CO/C^{18}O ratios in the inner arms are ~2 times lower than in the nucleus, while the ^{13}CO/C^{18}O line ratios are similar between the arms and the nucleus. On the other hand, NGC 3627 shows that all four abundance/opacity sensitive ratios are lower in the nucleus than in the rest of the regions. This likely indicates different variations in optical depths and/or CO isotopologue abundances in these galaxy centers, which will be addressed via our modeling (Section 3.4).

The regional statistics of the observed line ratios are listed in Table 3.2 and 3.3. The means and standard deviations are calculated from the ensemble of pixel-by-pixel measurements in the relevant region, while the integrated means are determined by dividing between the regionally integrated intensities. Since the C^{18}O line(s) are not commonly detected in the outer arms, the relevant line ratios for those regions are not listed. The CO 2–1/1–0 ratio averaged over the whole field of view is 0.9 for NGC 4321 and 0.8 for NGC 3627, and it is even higher in their inner 300 pc nuclei. This is consistent with recent line ratio studies at kpc resolution (den Brok et al., 2021; Yajima et al., 2021; Leroy et al., 2022).

In Figure 3.6, we present the averaged spectra over the entire region defined in Figure 3.3 for all six lines. The spectra are obtained by applying the stacking technique (Schruba et al., 2011) and using the CO 2–1 moment 1 (see maps in Appendix 3.C.1) as the fiducial velocity centroid. Except for the poorly detected C^{18}O 3–2 line in NGC 3627,

Table 3.4. RADEX Input Parameters

Parameter	Range	Step Size
$\log(n_{\mathrm{H_2}}\ [\mathrm{cm^{-3}}])$	2.0–5.0	0.2 dex
$\log(T_{\mathrm{k}}\ [\mathrm{K}])$	1.0–2.7	0.1 dex
$\log(N_{\mathrm{CO}}\ [\mathrm{cm^{-2}}])$	15.0–20.0	0.2 dex
$X_{12/13}$	10–200	10
$X_{13/18}$	2–20	1
$\log(\Phi_{\mathrm{bf}})$	−1.3–0	0.1 dex
$\Delta v\ [\mathrm{km\ s^{-1}}]$	15.0	—

The fixed Δv of 15 km $\mathrm{s^{-1}}$ is only a fiducial value for the model grid. The parameter of interest is $N_{\mathrm{CO}}/\Delta v$.

the averaged spectra of all the lines in each galaxy show similar line widths within 30–40%. This means that the velocity dispersion among different observed lines are overall in good agreement, and we also see agreement on pixel-by-pixel scales via a thorough check of each individual line of sight (e.g., Appendix 3.A). Comparing to NGC 4321, we notice that the averaged spectra for NGC 3627 show some level of discrepancy with the best-fit Gaussian function. The discrepancy is possibly due to a larger fraction of area in NGC 3627 having multi-component gas along the same lines of sight, and this will be further discussed in Appendix 3.A. The regional statistics of the CO 2–1 effective line widths are also listed in Table 3.2 and 3.3, and their maps can be found in Appendix 3.C.1. The line widths in CO 1–0 are consistent with CO 2–1 within 10%.

To investigate the physical implications of these line ratio and line width variations, we determine the gas physical conditions pixel by pixel in these galaxy centers in Section 3.4, using multi-line radiative transfer modeling without assuming local thermodynamic equilibrium (LTE).

3.4 Multi-line Bayesian Modeling

3.4.1 Modeling Setup

To constrain the physical conditions and $\alpha_{\rm CO}$ in different sub-regions of the galaxy centers, we run a non-LTE radiative transfer code, RADEX (van der Tak et al., 2007), to construct a one-component model and fit it with our observations at ~100 pc scales. RADEX assumes a homogeneous medium and uses radiative transfer equations based on the escape probability formalism to find a converged solution for the excitation temperature and level population. On a pixel-by-pixel basis, we model the integrated intensities of the six CO, ^{13}CO, and C^{18}O lines under various combinations of H_2 volume density ($n_{\rm H_2}$), kinetic temperature ($T_{\rm k}$), CO column density per line width ($N_{\rm CO}/\Delta v$), CO/^{13}CO ($X_{12/13}$) and ^{13}CO/C^{18}O ($X_{13/18}$) abundance ratios, and the beam-filling factor ($\Phi_{\rm bf}$).

This model assumes the same beam-filling factor for all six observed lines. We note that earlier studies on some barred galaxy centers found high CO/^{13}CO line ratios in bar regions, which may be explained by the existence of diffuse molecular components that lead to differences in the beam-filling factor of CO and ^{13}CO lines (Hüttemeister et al., 2000; Watanabe et al., 2011). However, those studies worked at near-kpc resolutions, and the near-GMC resolution used in this work should reduce the possible beam-filling factor mismatch. While $\Phi_{\rm bf}$ could still be lower for emission from higher transitions or less abundant isotopologues, investigating how much $\Phi_{\rm bf}$ differs between the lines in each region requires more sophisticated modeling or simulation that includes $\Phi_{\rm bf}$ as a variable. We briefly describe the modeling setup below and note that the modeling approach is the same as that adopted in Teng et al. (2022), where readers can find more details about our RADEX implementation and model construction. We also release all the source code and parameters in a GitHub repository[3].

We build a six-dimensional RADEX model grid with $\log(n_{\rm H_2}\ [{\rm cm^{-3}}])$ varied from 2

---

[3] https://github.com/ElthaTeng/multiline-bayesian-modeling

to 5 in steps of 0.2 dex, T_k from 10 to 500 K in steps of 0.1 dex, $N_{CO}/\Delta v$ from $10^{15}/15$ to $10^{20}/15$ cm^{-2} (km s^{-1})$^{-1}$ in steps of 0.2 dex, $X_{12/13}$ from 10 to 200 in steps of 10, $X_{13/18}$ from 2 to 20 in steps of 1, and $\log(\Phi_{bf})$ from −1.3 to 0 in steps of 0.1 dex (see Table 3.4). While the N_{CO} and Δv = 15km s^{-1} listed in Table 3.4 are input separately to RADEX[4], it is important to note that the radiative transfer calculation in RADEX depends only on their ratio $N_{CO}/\Delta v$ (van der Tak et al., 2007; see also Kamenetzky et al., 2012; Teng and Hirano, 2020; Teng et al., 2022). This means that we are essentially fitting $N_{CO}/\Delta v$, and thus variation of Δv across the observed regions would not affect our results as long as we ensure that $N_{CO}/\Delta v$ is unchanged when we derive N_{CO} using the observed Δv. We set the upper limit of T_k to ∼500 K due to low reliability to distinguish a higher T_k with J=3–2 as the highest transition in our setting. The parameter ranges were determined by ensuring well-covered probability density functions (PDFs) in representative nucleus and arm regions. We note that RADEX fails to converge at several grid points where $T_k > 200$ K and $N_{CO}/\Delta v \geq 10^{19}/15$ cm^{-2} (km s^{-1})$^{-1}$, and thus we exclude those solutions in our modeling. We will show that such conditions tend to result in unreasonably large line-of-sight path length which will also be excluded by our line-of-sight prior, so the lack of these models does not impact our analysis.

Following Teng et al. (2022), we study pixel by pixel the marginalized PDFs of each parameter using a Bayesian likelihood analysis. With the marginalized 1D PDFs, we will determine the peak parameter values as the “1DMax” solutions and the 50th percentile values as the “median” solutions. The “best-fit” solution which corresponds to the global minimum χ^2 value of the full 6D grid is also derived. In contrast to a single best-fit solution representing the gas physical properties, the PDFs are descriptive of the local variations over the full parameter space, and the 1DMax/median solutions from the PDFs reflect a more complete characterization of the parameter distributions. Therefore, we will focus on the 1DMax/median solutions throughout our analysis, while we also show that 1DMax,

---

[4] In RADEX calculation, the line width should be input in FWHM, and thus we converted our effective line width Δv to FWHM by a factor of 2.35 in this step.

median, and best-fit solutions agree well in many cases. In our χ^2 calculation, we include the measurement uncertainty and an estimated flux calibration uncertainty of 10% for Band 3 and 20% for Band 6 or 7, respectively (Sliwa et al., 2017; Bonato et al., 2019). For regions with $C^{18}O$ detection $< 3\sigma$ (e.g., outer arms), we still include the $C^{18}O$ intensity with its (higher) associated uncertainty in our modeling. However, those lines are excluded from our fitting if the pixel has negative $C^{18}O$ integrated intensity below 1σ. Thus, the solutions for some pixels can be constrained by less than six lines, although this situation only occurs in the outer arms of NGC 3627.

To avoid solutions that result in unrealistically large line-of-sight path lengths ($\ell_{\rm los}$), we also set a prior by requiring

$$\ell_{\rm los} = N_{\rm CO}(\sqrt{\Phi_{\rm bf}}\, n_{\rm H_2}\, x_{\rm CO})^{-1} < 200 \text{ pc}. \tag{3.2}$$

where $x_{\rm CO}$ is the $\mathrm{CO/H_2}$ abundance ratio that is normally found or adopted as 3×10^{-4} in active star-forming regions (Lacy et al., 1994; Ward et al., 2003; Sliwa et al., 2014). This 200 pc constraint considers the typical molecular gas scale height of ~100 pc for our Galaxy and nearby disk galaxies (Yim et al., 2014; Heyer and Dame, 2015), as well as a tolerance of a factor-of-two increase due to galaxy inclination. Since $n_{\rm H_2}$ and $\Phi_{\rm bf}$ are both our modeled parameters, and $N_{\rm CO}$ can be obtained by multiplying the modeled $N_{\rm CO}/\Delta v$ with the observed line width, this line-of-sight prior can be easily implemented by excluding all the grid points (i.e., parameter combinations) that give $\ell_{\rm los} > 200$ pc and setting their probability to zero. As shown by Equation 3.2, the prior tends to rule out solutions with high column densities of $> 10^{19}/15$ cm^{-2} (km s^{-1})$^{-1}$ and low volume densities of < 300 cm^{-3}. This also means that most of the conditions where RADEX fails to converge are excluded by the line-of-sight constraint due to high CO column densities.

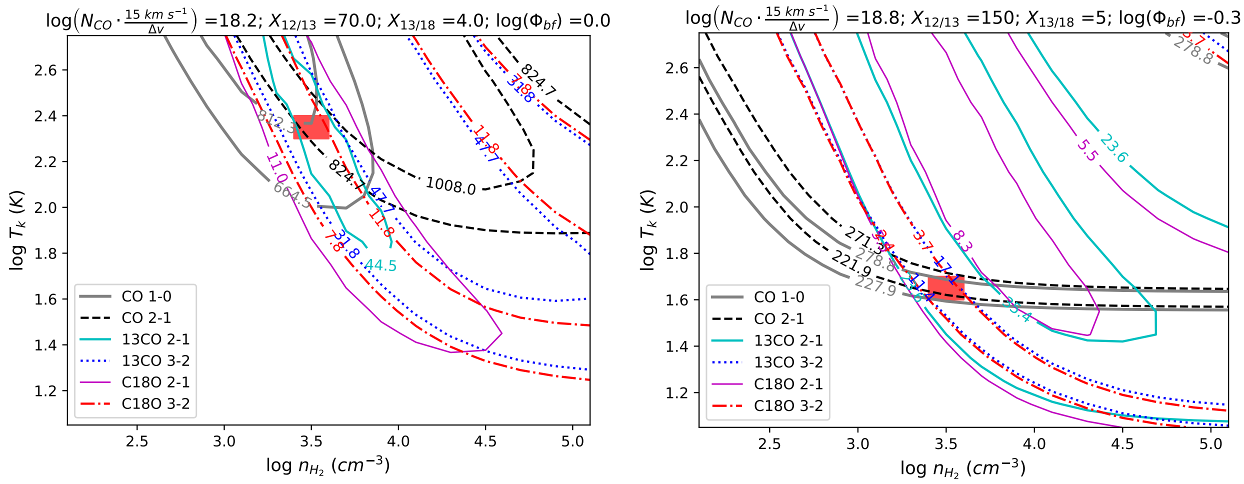

(a)

(b)

Figure 3.7. Best-fit (i.e. lowest χ^2) constraints from the six observed line fluxes at (a) the central pixel and (b) a pixel in the northern, inner arm of NGC 4321. Contours show the ranges of observed line intensities $\pm 1\sigma$ uncertainties, including the measurement and calibration uncertainties. Red boxes represent the best-fit solutions. Note that these are the solutions with the lowest χ^2 value in the full grid, not the 1DMax solutions based on the marginalized PDFs, and thus the $X_{12/13}$ values here may deviate from the lower $X_{12/13}$ suggested by 1DMax solutions. Except for $X_{12/13}$, other parameters are similar to the 1DMax solutions as their 1D likelihoods are single-peaked and well-constrained (see Figure 3.8 and related discussion).

3.4.2 Molecular Gas Physical Conditions

By fitting the line observations with the constructed RADEX models at each pixel, we obtain well-constrained solutions for most of the physical parameters. Figure 3.7 demonstrates how the best-fit solutions are constrained by the six observed line intensities ($\pm 1\sigma$, including measurement and calibration uncertainties) at the central pixel and another pixel in the inner arm region of NGC 4321. In general, we find the best-fit solution of each pixel well within the constraints given by all the observed lines, although the number or species of lines that give crucial constraints varies from pixel to pixel (see Section 3.5.5 for further discussion).

Overall, we find the marginalized PDFs for each parameter to be single-peaked and well-covered by the parameter space. However, we notice that the PDFs of $X_{12/13}$ tend to be broader than other parameters, implying that the $X_{12/13}$ abundance ratio is generally less constrained by the model based on the observed lines. This was also seen in similar

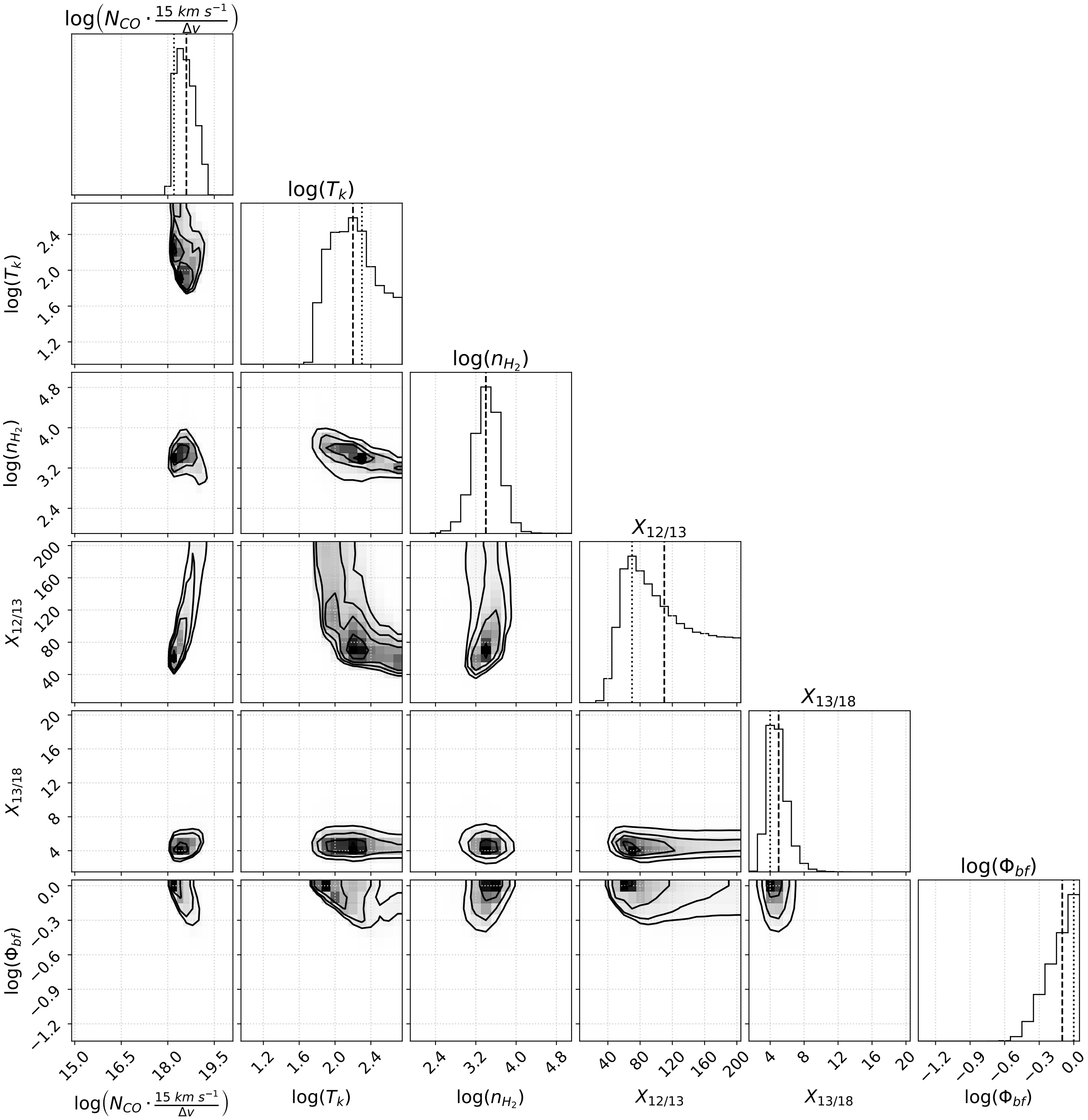

Figure 3.8. Marginalized 1D and 2D probability distributions of the central pixel of NGC 4321. In the panels of 1D PDFs (on the diagonal), the dashed lines represent the 50th percentile (i.e., median) values of the cumulative 1D PDFs, and the dotted lines label the best-fit solution as in Figure 3.7(a). Except for the PDF of $X_{12/13}$ which is less constrained, the median values of other parameters are closely aligned with the best-fit and 1DMax solutions.

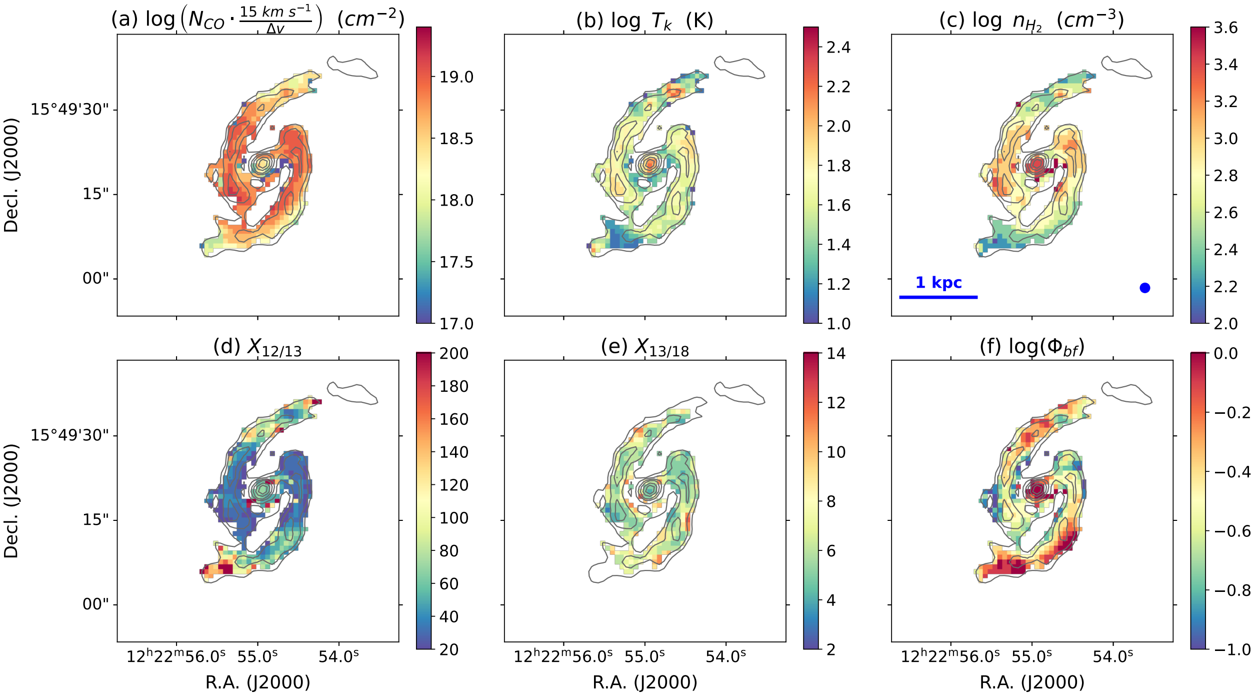

Figure 3.9. Maps of the 1DMax physical conditions derived from the modeling for NGC 4321. Panel (a) shows log($N_{\rm CO}$) normalized to a fiducial line width of 15 km s^{-1} over the whole region. Contours represent the CO 2–1 emission shown in Figure 3.1(b). A 3σ mask of the C^{18}O 2–1 image is applied to (e).

modeling toward other galaxy centers or (U)LIRGs (Sliwa et al., 2014; Sliwa et al., 2017; Teng et al., 2022). In Figure 3.8, we show the marginalized 1D and 2D PDFs for the central pixel of NGC 4321. The vertical dashed lines on the 1D PDFs represent the 50th percentile values (median), which generally agree with the 1D PDF peaks (1DMax) as well as the best-fit solutions shown in Figure 3.7(a). In this pixel, the 1DMax solution of $X_{12/13}$ matches the best-fit solution, but it is inconsistent with the median due to the broader and asymmetric PDF of $X_{12/13}$. More examples of the PDFs and/or best-fit solutions for other pixels in NGC 4321 and NGC 3627 are presented in Appendix 3.C.2. Over the entire observed regions, we find that the best-fit and 1DMax solutions of $N_{\rm CO}/\Delta v$, $n_{\rm H_2}$, $T_{\rm k}$, $X_{13/18}$ and $\Phi_{\rm bf}$ are mostly consistent, while the 1DMax $X_{12/13}$ can deviate from the best-fit or median solutions in some regions due to less constrained PDFs.

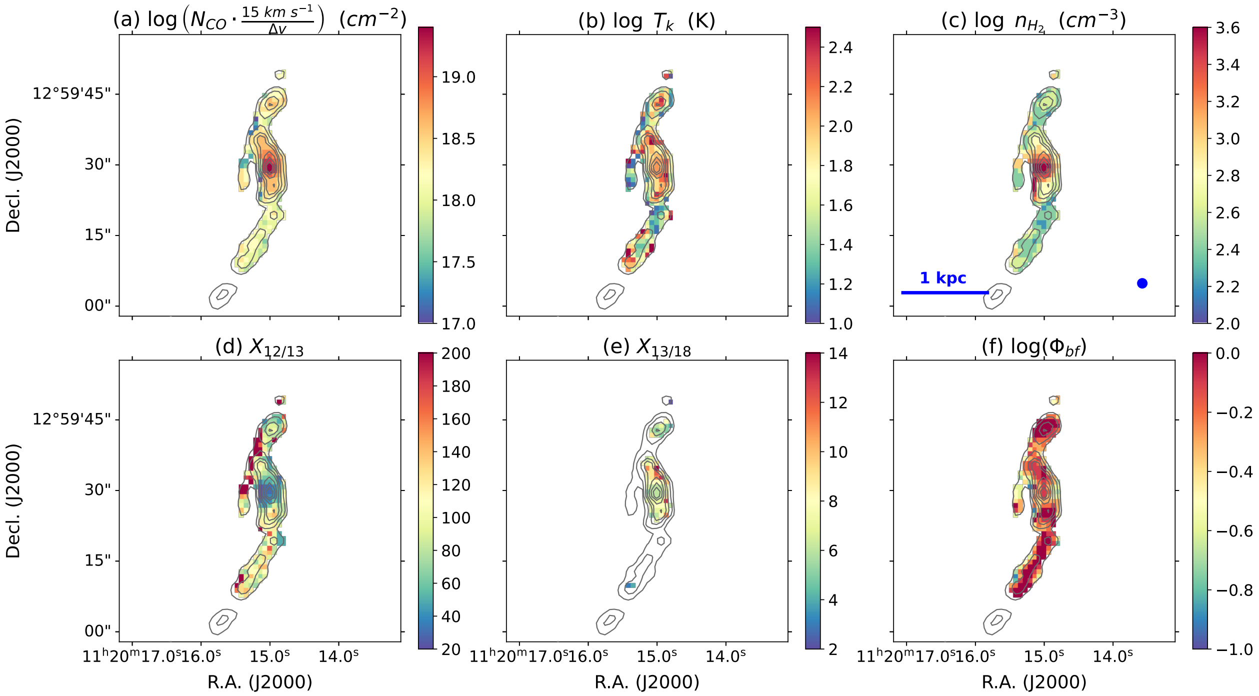

Figure 3.10. Same as Figure 3.9 but for NGC 3627.

Table 3.5. Regional Averages and Standard Deviations of the 1D PDF Solutions

Region		$\log\left(N_{\mathrm{CO}}\,\frac{15\ \mathrm{km\ s^{-1}}}{\Delta v}\right)$ ($\mathrm{cm^{-2}}$)	$\log T_{\mathrm{k}}$ (K)	$\log n_{\mathrm{H_2}}$ ($\mathrm{cm^{-3}}$)	$X_{12/13}$	$X_{13/18}$	$\log\ \Phi_{\mathrm{bf}}$
NGC 4321							
Whole	1DMax	18.60 ± 0.47	1.57 ± 0.24	2.78 ± 0.31	60.95 ± 44.77	6.43 ± 1.71	−0.46 ± 0.27
($N_{\mathrm{pix}} = 412$)	Median	18.33 ± 0.35	1.60 ± 0.19	2.86 ± 0.28	91.58 ± 22.87	6.84 ± 2.06	−0.49 ± 0.20
Nucleus	1DMax	18.16 ± 0.62	1.69 ± 0.31	3.19 ± 0.36	76.96 ± 46.94	6.78 ± 2.30	−0.13 ± 0.16
($N_{\mathrm{pix}} = 23$)	Median	18.05 ± 0.47	1.79 ± 0.24	3.21 ± 0.27	95.51 ± 18.71	7.06 ± 2.63	−0.27 ± 0.10
Inner arms	1DMax	18.79 ± 0.43	1.63 ± 0.19	2.95 ± 0.19	37.88 ± 28.18	6.02 ± 1.49	−0.59 ± 0.21
($N_{\mathrm{pix}} = 203$)	Median	18.49 ± 0.32	1.63 ± 0.13	3.00 ± 0.20	81.12 ± 16.03	6.25 ± 1.76	−0.59 ± 0.15
Outer arms	1DMax	18.44 ± 0.38	1.48 ± 0.25	2.55 ± 0.24	84.14 ± 46.37	7.07 ± 1.74	−0.35 ± 0.25
($N_{\mathrm{pix}} = 186$)	Median	18.20 ± 0.28	1.54 ± 0.21	2.66 ± 0.21	102.50 ± 24.37	7.78 ± 2.07	−0.40 ± 0.19
NGC 3627							
Whole	1DMax	18.24 ± 0.41	1.75 ± 0.40	2.70 ± 0.36	100.51 ± 47.23	7.31 ± 2.18	−0.23 ± 0.22
($N_{\mathrm{pix}} = 214$)	Median	18.07 ± 0.35	1.78 ± 0.26	2.71 ± 0.32	110.52 ± 23.94	7.84 ± 2.17	−0.32 ± 0.16
Nucleus	1DMax	19.07 ± 0.23	2.05 ± 0.07	3.43 ± 0.14	41.33 ± 10.87	6.60 ± 0.80	−0.23 ± 0.09
($N_{\mathrm{pix}} = 15$)	Median	18.88 ± 0.19	2.06 ± 0.05	3.32 ± 0.12	89.69 ± 9.26	6.66 ± 0.86	−0.27 ± 0.06
Inner arms	1DMax	18.27 ± 0.38	1.76 ± 0.37	2.79 ± 0.34	93.37 ± 42.43	8.24 ± 2.11	−0.27 ± 0.22
($N_{\mathrm{pix}} = 92$)	Median	18.09 ± 0.31	1.82 ± 0.24	2.82 ± 0.32	106.62 ± 25.46	8.81 ± 2.06	−0.35 ± 0.16
Outer arms	1DMax	18.10 ± 0.29	1.69 ± 0.44	2.51 ± 0.19	114.95 ± 46.41	5.40 ± 1.74	−0.19 ± 0.23
($N_{\mathrm{pix}} = 107$)	Median	17.95 ± 0.20	1.72 ± 0.26	2.54 ± 0.16	116.79 ± 21.54	6.30 ± 1.91	−0.31 ± 0.17

The averages are determined from the ensemble of 1DMax and median solutions from the 1D PDFs. The listed uncertainties represent the standard deviations across pixels in each region, while the deviations between 1DMax and medians can reflect the uncertainties in individual PDFs. N_{pix} indicates the number of pixels used for each region.

We present the 1DMax solution maps for each parameter in Figures 3.9 and 3.10. The regional statistics of the 1DMax and median solutions are listed in Table 3.5. Both NGC 4321 and NGC 3627 show clear trends of increasing T_k and n_{H_2} from the outer arms to the nucleus. $N_\mathrm{CO}/\Delta v$, which reflects the optical depth, also increases toward the centers, except in the nucleus of NGC 4321. Despite having a 0.2–0.5 dex lower $N_\mathrm{CO}/\Delta v$, the nucleus of NGC 4321 has similar N_CO as the arm regions. This is because the line width at the NGC 4321 nucleus is > 30 km s^{-1}, which is larger than the $10-20$ km s^{-1} line widths in the inner/outer arms by more than a factor of two (see Table 3.2). We note that the line width at the nucleus of NGC 3627 is also $> 2\times$ larger than that in its arm regions, and thus the central enhancement of N_CO is even more dramatic than that shown by the $N_\mathrm{CO}/\Delta v$ enhancement in Table 3.5. With a typical line width of ~60 km s^{-1}, the mean N_CO in the NGC 3627 nucleus exceeds 3×10^{19} cm^{-2}.

High temperature and volume density are also found in the nucleus of NGC 3627, with mean T_k and n_{H_2} reaching > 100 K and 3×10^{3} cm^{-3}, respectively. The nucleus of NGC 4321 also shows T_k ~100 K and $n_{\mathrm{H}_2} > 10^{3}$ cm^{-3}, higher than the average conditions of the arm regions in both galaxies. We note that the nuclear type of NGC 4321 is mostly classified as a low-ionization nuclear emission region (LINER) and NGC 3627 as either a LINER or a Seyfert 2 AGN (Ho et al., 1997; Filho et al., 2000; Moustakas et al., 2010; Belfiore et al., 2022). As the inner ~300 pc regions may be impacted by nuclear activity, it is reasonable to find much more excited gas conditions in these regions.

From Figures 3.9 and 3.10, we find a consistent 1DMax solution of $X_{12/13}$ ~40 across the inner arms of NGC 4321 and the nucleus of NGC 3627, though the median solutions imply higher $X_{12/13}$ of 80–90 (see Table 3.5 and Appendix 3.C.2). On the other hand, the 1DMax and medians in the inner/outer arms of NGC 3627 agree well, suggesting $X_{12/13}$ ~100. Both the 1DMax and median solutions in the nucleus and outer arms of NGC 4321 also imply higher $X_{12/13}$ of 80–100. Similar to the $X_{12/13}$ distribution, we also derive the lowest $X_{13/18}$ (~6) in the inner arms of NGC 4321 and the nucleus of NGC 3627.

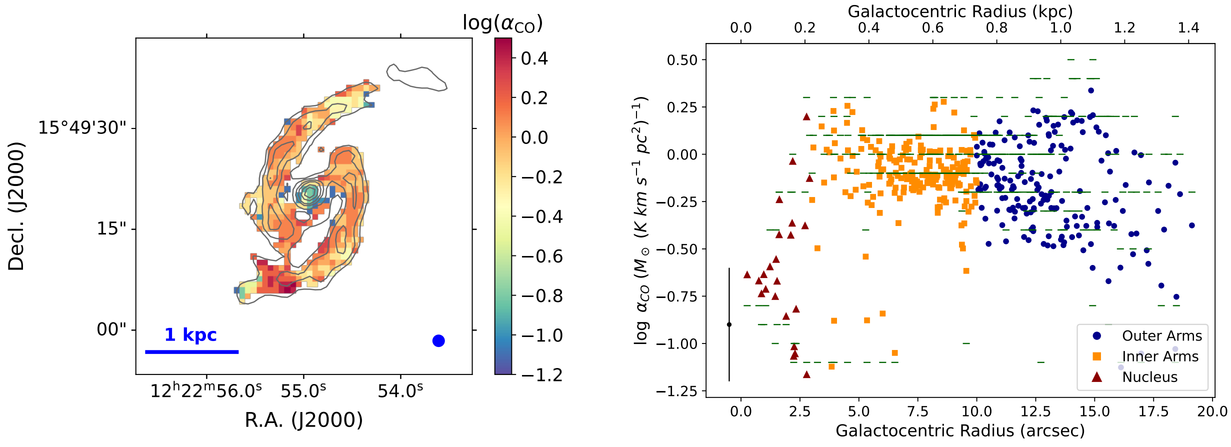

(a)

(b)

Figure 3.11. Spatial variation of α_{CO} in NGC 4321. (a) 1DMax log(α_{CO}) map in units of $M_\odot$ (K km s^{-1} pc^2)$^{-1}$; the contours represent the moment 0 of CO 2–1. (b) Relation between the modeled α_{CO} and galactocentric radius. The colored points correspond to the median α_{CO} in different regions, and the green horizontal lines present the 1DMax solutions which are similar to the medians. A typical error bar of $\sigma = \pm 0.3$ dex is shown in the lower left corner. All α_{CO} values are below the Galactic disk average of log(α_{CO}) = 0.64 or α_{CO} = 4.4 $M_\odot$ (K km s^{-1} pc^2)$^{-1}$. In the nucleus, α_{CO} is a factor of 3–5 lower than in the arms. Furthermore, α_{CO} in the outer arms shows a decreasing trend with galactocentric radius (see Section 3.5.1 for further discussion).

The decrease of both $X_{12/13}$ and $X_{13/18}$ in those regions may indicate ^{13}C and ^{18}O enrichment from enhanced star formation. We note that the derived $X_{13/18}$ across both galaxy centers are well-constrained at a range of 6–8 which is similar to the Galactic Center value (Areal et al., 2018). On the other hand, our derived $X_{12/13}$ values are higher than $X_{12/13}$ ~25 found in our Galactic Center (Wilson and Rood, 1994; Milam et al., 2005; Yan et al., 2023) as well as the central kpc of NGC 3351 (Teng et al., 2022). This is in line with the higher $X_{12/13}$ values varying from ~40 to >100 that have been commonly found in other starburst galaxy centers or (U)LIRGs, likely due to higher inflow rates and/or stellar nucleosynthesis enrichment (Henkel et al., 2014; Sliwa et al., 2014; Sliwa et al., 2017; Tang et al., 2019).

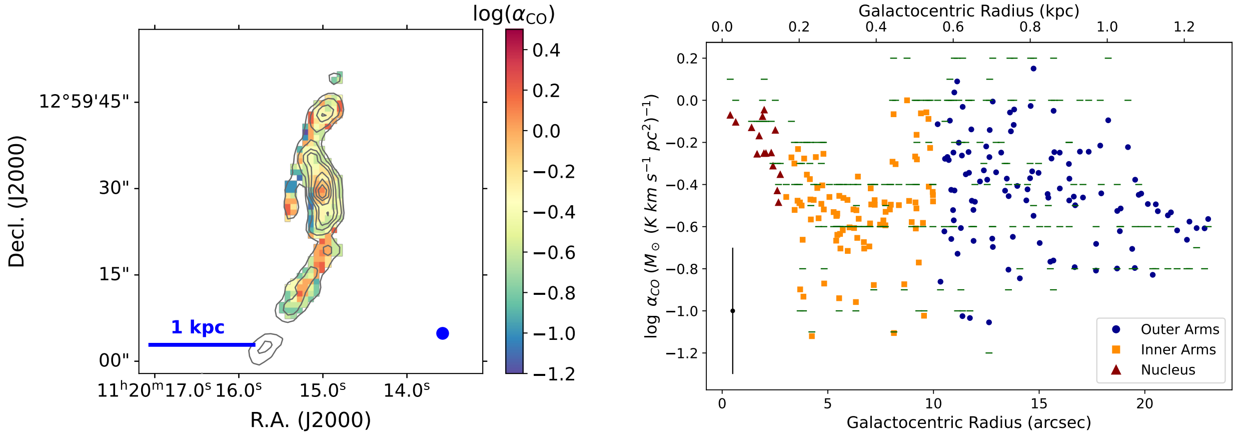

(a)

(b)

Figure 3.12. Spatial variation of $\alpha_{\rm CO}$ in NGC 3627. See the caption of Figure 3.11 for more information. The derived $\alpha_{\rm CO}$ values are generally lower than NGC 4321 and substantially lower than the Galactic disk average. $\alpha_{\rm CO}$ decreases sharply from the nucleus to the inner arms, while the outer arms show a larger scatter likely due to limited constraints from the ^{13}CO 3–2 and C^{18}O observations.

3.4.3 CO-to-H$_2$ Conversion Factors

The CO-to-H$_2$ conversion factor (see Equation 3.1 for definition) can be expressed as a function of $N_{\rm CO}$, $\Phi_{\rm bf}$, and the CO 1–0 intensity $I_{\rm CO(1-0)}$:

$$\begin{aligned}\alpha_{\rm CO} &= \frac{M_{\rm mol}}{L_{\rm CO(1-0)}}\left[\frac{\rm M_\odot}{\rm K\ km\ s^{-1}\ pc^2}\right]\\ &= \frac{1.36\, m_{\rm H_2}\,[{\rm M_\odot}]\, N_{\rm CO}\,[{\rm cm^{-2}}]\, A\,[{\rm cm^2}]\,\Phi_{\rm bf}}{x_{\rm CO}\, I_{\rm CO(1-0)}\,[{\rm K\ km\ s^{-1}}]\, A\,[{\rm pc^2}]}\\ &= \frac{1}{4.5\times10^{19}}\cdot\frac{N_{\rm CO}\,[{\rm cm^{-2}}]\,\Phi_{\rm bf}}{x_{\rm CO}\, I_{\rm CO(1-0)}\,[{\rm K\ km\ s^{-1}}]}\,,\end{aligned} \tag{3.3}$$

where $x_{\rm CO}$ is the CO/H$_2$ abundance ratio. In the second step of the above equation, the factor of 1.36 is to include the mass contribution from helium, $m_{\rm H_2}$ is the mass of a hydrogen molecule, and A is the area relevant to the conversion between $I_{\rm CO}$ and $L_{\rm CO}$. All of these factors are reduced to the constant in the final step of Equation 3.3. We note that galaxy inclinations do not affect the result of $\alpha_{\rm CO}$, because the inclination correction on $N_{\rm CO}$ and $I_{\rm CO(1-0)}$ (which includes Δv) would cancel out in Equation 3.3.

Since our modeling directly constrains $N_{\rm CO}$ and $\Phi_{\rm bf}$ and provides a prediction of the $I_{\rm CO(1-0)}$ values that matches the observed one, we can derive the spatial distribution of $\alpha_{\rm CO}$ from the modeling with an assumption of $x_{\rm CO}$. While $N_{\rm CO}$ can be determined by multiplying $N_{\rm CO}/\Delta v$ with Δv, we caution that the Δv should be consistent with the line width of the observed $I_{\rm CO(1-0)}$. This is different from the $\alpha_{\rm CO}$ calculation in Teng et al. (2022), where the line widths were not consistent. As we will compare their result on NGC 3351 with ours in Section 3.5, we list the updated $\alpha_{\rm CO}$ values of NGC 3351 in Appendix 3.B for self-consistency. We note that the key conclusions in Teng et al. (2022) are unchanged, but the updated $\alpha_{\rm CO}$ values are overall lowered by a factor of two to three (see Appendix 3.B for more details).

Throughout our analysis, we assume $x_{\rm CO} = 3 \times 10^{-4}$, which is supported by measurements of warm/dense star-forming clouds (e.g., Lacy et al., 1994; Sofia et al., 2004; Sheffer et al., 2008) and commonly adopted in various starburst regions (e.g., Kamenetzky et al., 2012; Kamenetzky et al., 2014; Sliwa et al., 2014; Sliwa et al., 2017). As this value assumes that most carbon is in the form of CO, which is not necessarily true in some galaxy centers (e.g., Liu et al., 2022; Liu et al., 2023), the uncertainty in our $\alpha_{\rm CO}$ values could be at the factor of 2–3 level because of this assumption. In addition, while we do not expect that elemental abundance variations of C and O are large enough to drive $x_{\rm CO}$ variations on sub-kpc scales, there are other mechanisms which may destroy the CO molecule and lower the CO/H_2 abundance, such as photodissociation by FUV radiation and cosmic rays in starburst or AGN environments (Gong et al., 2018; Bisbas et al., 2021; Liu et al., 2022). The effect of photodissociation is the strongest in optically thin and CO-faint regions where the shielding of FUV radiation is weak, such as interarm and outer galaxy regions. However, we emphasize that a better prediction of the $x_{\rm CO}$ value is not feasible with current dataset and analysis. Thus, it is important to note that our derived $\alpha_{\rm CO}$ values depend inversely on $x_{\rm CO}$, i.e., $\alpha_{\rm CO}^{\rm true} = \alpha_{\rm CO}^{\rm derived} \times (3 \times 10^{-4}/x_{\rm CO})$.

With Equation 3.3 and following the procedure described in Teng et al. (2022, Section 4.4), we create a grid of $\log(\alpha_{\rm CO})$ from -2.5 to 2.5 with a step size of 0.1 and obtain marginalized PDFs of $\alpha_{\rm CO}$ for each pixel. Then, we extract the 1DMax/median $\alpha_{\rm CO}$ solutions from the PDFs. With this method, the derived $\alpha_{\rm CO}$ does not depend on the best-fit/1DMax/median solutions of $N_{\rm CO}$ and $\Phi_{\rm bf}$ determined in Section 3.4.2, since those parameters are fit simultaneously within the full grid before marginalization. We refer readers to Teng et al. (2022) for more details.

Figures 3.11 and 3.12 show the spatial variations of $\alpha_{\rm CO}$ across the observed regions. The 1DMax and median $\alpha_{\rm CO}$ solutions are similar and have consistent trends with the galactocentric radius. We will mainly present the median solutions hereafter due to their continuity across the $\alpha_{\rm CO}$ parameter space resulting from interpolation. As shown in Figure 3.11(b), the arm regions of NGC 4321 have a roughly constant $\log(\alpha_{\rm CO})$ around -0.1 (i.e., $\alpha_{\rm CO} \approx 0.8$ $M_\odot$ (K km s^{-1} $pc^2)^{-1}$), and there is a decreasing trend toward the outer arms. On the other hand, the nucleus region shows $\log(\alpha_{\rm CO}) \approx -0.7$ (or $\alpha_{\rm CO} \approx$ 0.2 $M_\odot$ (K km s^{-1} $pc^2)^{-1}$), which is a factor of 3–5 lower than in the arms. In NGC 3627, the general $\alpha_{\rm CO}$ values are even a factor of 2–3 lower than in NGC 4321. Furthermore, Figure 3.12(b) shows that $\alpha_{\rm CO}$ decreases sharply from the nucleus to the inner arms, while the outer arms show a large scatter of $\alpha_{\rm CO}$ which likely results from the lower S/N of ^{13}CO 3–2 and C^{18}O data in this region.

We note that trends of decreasing $\alpha_{\rm CO}$ with radius are seen in the inner/outer arm regions of both NGC 3627 and NGC 4321. We will discuss these $\alpha_{\rm CO}$ trends seen in barred galaxy centers in Section 3.5.1. Moreover, our modeling results show that all pixels across the observed regions in both galaxy centers have $\alpha_{\rm CO}$ that is 4–15 times below the Galactic disk average of 4.4 $M_\odot$ (K km s^{-1} $pc^2)^{-1}$. This range of lower $\alpha_{\rm CO}$ is consistent with previous kpc-scale estimations toward galaxy centers using independent techniques (Strong et al., 2004; Sandstrom et al., 2013; Israel, 2020; den Brok et al., 2023). In Section 3.5.2, we will compare our kpc-averaged $\alpha_{\rm CO}$ with those studies which included NGC 3627 and NGC 4321.

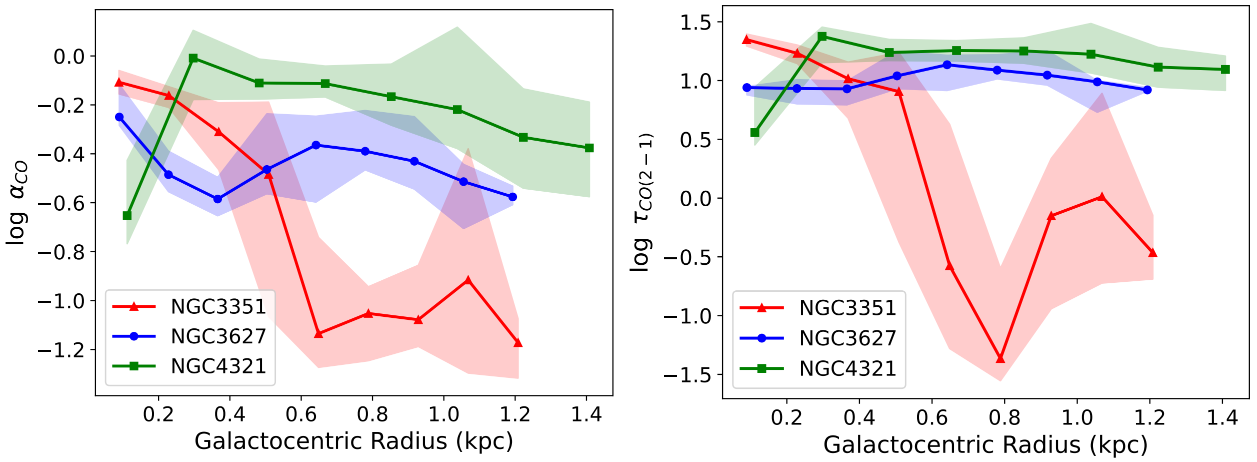

(a) (b)

Figure 3.13. Medians of the modeled (a) $\alpha_{\rm CO}$ in units of $\rm M_\odot$ (K km s^{-1} pc^2)$^{-1}$ and (b) line center $\tau_{\rm CO(2-1)}$ within ~100 pc galactocentric radii bins in the centers of NGC 3351 (red), NGC 3627 (blue), and NGC 4321 (green). Shaded areas span the 25th and 75th percentile ranges. All regions show $\alpha_{\rm CO}$ at least a factor of four lower than the Galactic value of $\log(\alpha_{\rm CO}) = 0.64$. The radial trend of $\alpha_{\rm CO}$ is mostly consistent with that of $\tau_{\rm CO(2-1)}$ in all three galaxy centers except in NGC 3627's nucleus.

3.5 Discussion

3.5.1 $\alpha_{\rm CO}$ Distribution and Environmental Dependence

To study the spatial variation of $\alpha_{\rm CO}$ at ~100 pc scales in barred, star-forming galaxy centers, we present a cross comparison among the results from Teng et al. (2022) on NGC 3351 and this work on NGC 3627 and NGC 4321. As the non-LTE radiative transfer modeling also predicts the optical depth for each line, we derive full PDFs of the CO optical depths (in both 1–0 and 2–1) as well as $\sqrt{n_{\rm H_2}}/T_{\rm k}$, using the same technique for determining the $\alpha_{\rm CO}$ solutions in Section 3.4.3. It is interesting to compare our $\alpha_{\rm CO}$ with CO optical depth ($\tau_{\rm CO}$) and gas temperature ($T_{\rm k}$), as they together determine the amount of escaped CO emission that can change $\alpha_{\rm CO}$ (Papadopoulos et al., 2012a; Teng et al., 2022). We also derive $\sqrt{n_{\rm H_2}}/T_{\rm k}$ because $\alpha_{\rm CO}$ is expected to be approximately proportional to this quantity for isolated and virialized clouds when CO lines are optically thick and thermalized (Bolatto et al., 2013; Gong et al., 2020). The grids for both $\log(\tau_{\rm CO})$ and $\log(\sqrt{n_{\rm H_2}}/T_{\rm k})$ range from -2 to 2 with a step size of 0.1.

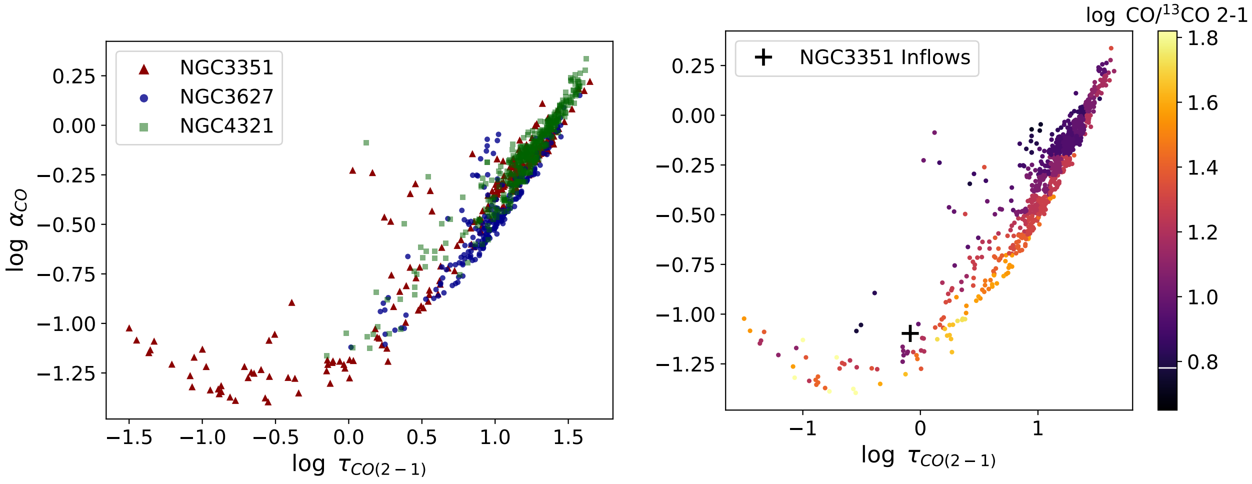

(a) (b)

Figure 3.14. Modeled $\alpha_{\rm CO}$ and $\tau_{\rm CO(2-1)}$, color-coded by (a) three galaxies and (b) 2D-binned medians of the observed CO/^{13}CO 2–1 ratios. In panel (b), the black cross sign represents spectral stacking result of the NGC 3351 inflows (see Teng et al. 2022 and Appendix 3.B), and the white line on the color bar indicates the typical ratio found in the disks of Milky Way or other nearby galaxies. In the optically thick regime ($\tau_{\rm CO} > 1$), a positive correlation of $\alpha_{\rm CO}$ with $\tau_{\rm CO}$ is constantly seen in the three galaxy centers, and the CO/^{13}CO 2–1 ratio generally reflects the $\tau_{\rm CO}$ variation in optically thick regions.

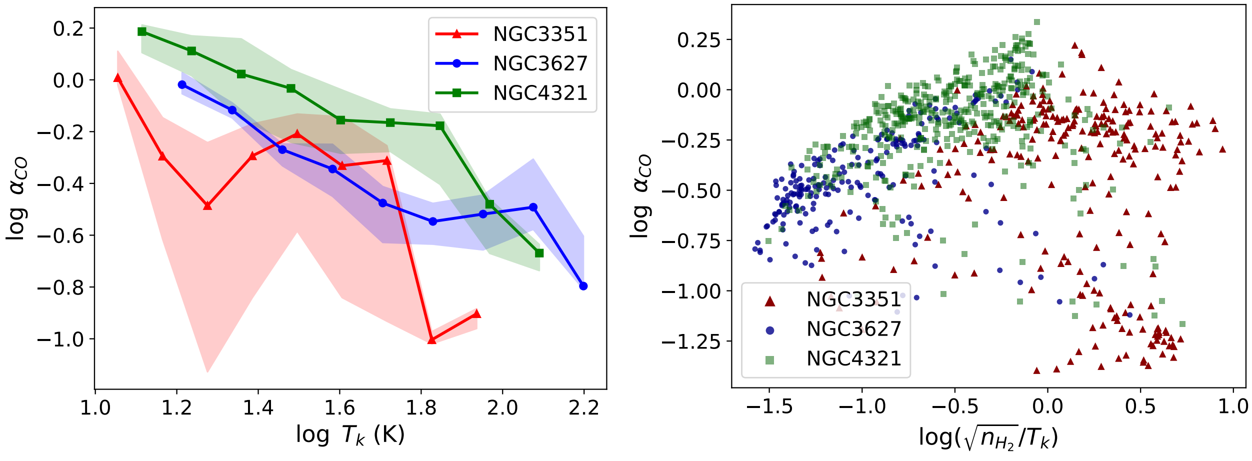

(a) (b)

Figure 3.15. Relation of the modeled $\log(\alpha_{\rm CO})$ with (a) $\log(T_{\rm k})$ and (b) $\log(\sqrt{n_{\rm H_2}}/T_{\rm k})$ for NGC 3351 (red), NGC 3627 (blue), and NGC 4321 (green). Both NGC 3627 and NGC 4321 show clear correlations of $\alpha_{\rm CO}$ decreasing with $T_{\rm k}$ and increasing with $\sqrt{n_{\rm H_2}}/T_{\rm k}$. In NGC 3351, there is no strong dependence on $T_{\rm k}$, and its lower $\alpha_{\rm CO}$ than the virial balance assumed $\sqrt{n_{\rm H_2}}/T_{\rm k}$ trend may indicate super-virial gas in the center of NGC 3351.

Figure 3.13(a) shows the radially-binned medians and the 25–75th percentile ranges of the median $\alpha_{\rm CO}$ solutions presented in Figure 3.11(b) and 3.12(b), together with the NGC 3351 results (see Appendix 3.B). The bin size is ~150 pc in galactocentric radius. A similar plot showing the median solutions of $\tau_{\rm CO(2-1)}$ is provided in Figure 3.13(b). It is clear that all regions in the three galaxy centers have $\alpha_{\rm CO}$ at least four times lower than the Galactic value of $\log(\alpha_{\rm CO})$ ~0.64. In addition, all three galaxies show a globally decreasing $\alpha_{\rm CO}$ trend until a radius of ~1.5 kpc, and $\alpha_{\rm CO}$ in NGC 3351 inflow regions (i.e., beyond a radius of ~0.5 kpc; Teng et al., 2022) drops substantially. Excluding the NGC 3351 inflow regions, $\alpha_{\rm CO}$ in the three galaxy centers vary between 0.2–1.5 $\rm M_\odot$ (K km $\rm s^{-1}$ $\rm pc^2)^{-1}$. By comparing between Figure 3.13(a) and (b), it is clear that for each galaxy the radial variation of $\alpha_{\rm CO}$ and $\tau_{\rm CO(2-1)}$ are overall similar. We note that the spatial variations are consistent between $\tau_{\rm CO(2-1)}$ and $\tau_{\rm CO(1-0)}$, except that the values of $\tau_{\rm CO(2-1)}$ are generally higher than $\tau_{\rm CO(1-0)}$. The higher $\tau_{\rm CO(2-1)}$ than $\tau_{\rm CO(1-0)}$ in our galaxy centers is likely caused by the higher density/temperature that efficiently excites CO to upper-J and thus depopulates the lower-J levels, and it is consistent with theoretical predictions for gas with $N_{\rm CO} \gtrsim 10^{17}$ $\rm cm^{-2}$ (e.g., Hu et al., 2022).

Motivated by the resemblance of Figure 3.13(a) and (b), we further investigate the correlation between $\alpha_{\rm CO}$ and $\tau_{\rm CO}$. Figure 3.14 presents the pixel-based median solutions of $\alpha_{\rm CO}$ and $\tau_{\rm CO(2-1)}$ from all three galaxies, where we can see a tight, positive trend between $\alpha_{\rm CO}$ and $\tau_{\rm CO}$ in optically thick regions. On the other hand, the optically thin gas from the bar-driven inflows of NGC 3351 show substantially lower $\alpha_{\rm CO}$ with little dependence on $\tau_{\rm CO}$, which matches the expectation for relatively diffuse ($n_{\rm H_2} < 300$ $\rm cm^{-2}$) gas in simulations (Gong et al., 2018; Gong et al., 2020). The positive correlation between $\alpha_{\rm CO}$ and $\tau_{\rm CO}$ agrees well with theoretical predictions for thermalized emission, where $\alpha_{\rm CO} \propto \tau/[1-\exp(-\tau)] \approx \tau$ is expected for optically thick emission with $\tau \gg 1$ (Papadopoulos et al., 2012a). Since $\tau_{\rm CO}$ is by definition proportional to $N_{\rm CO}$ and Δv, this means that gas concentration toward galaxy centers (which increases $N_{\rm CO}$) and turbulence/shear effects (which changes Δv) play important roles in setting $\alpha_{\rm CO}$ in the central kpc of these barred galaxies. It is thus possible that the overall higher velocity dispersion in galaxy centers can lower the optical depth and lead to systematically lower $\alpha_{\rm CO}$ than the Galactic disk value across our maps (see Section 3.5.3 for further discussion).

While there is a strong $\alpha_{\rm CO}$ dependence on $\tau_{\rm CO}$, we also notice diverging $\alpha_{\rm CO}$ toward the nucleus ($r \lesssim 300$ pc) of NGC 3627, where $\alpha_{\rm CO}$ is increasing while $\tau_{\rm CO(2-1)}$ remains unchanged. This means that the $\alpha_{\rm CO}$ variation cannot be solely explained by $\tau_{\rm CO}$, and thus there must be additional factors at play. Theoretical studies have suggested that $\alpha_{\rm CO}$ may decrease with temperature as the optically thick CO 1–0 intensity increases with temperature (Narayanan et al., 2012; Bolatto et al., 2013; Hu et al., 2022). We present the relation between our modeled $\log(\alpha_{\rm CO})$ and $\log(T_{\rm k})$ in Figure 3.15(a). While NGC 3351 does not show strong evidence for $\alpha_{\rm CO}$ varying with $T_{\rm k}$ (see also Teng et al., 2022), we find a clear decrease of $\alpha_{\rm CO}$ with $T_{\rm k}$ in NGC 3627 and NGC 4321. Notably, the local peak of $\alpha_{\rm CO}$ for NGC 3627 (blue curve) near $\log(T_{\rm k}) = 2.1$ corresponds to the $\alpha_{\rm CO}$ increase in NGC 3627's nucleus, and $\alpha_{\rm CO}$ continues to drop in regions with even higher temperature. Though the nucleus in NGC 3627 already has high $T_{\rm k} \gtrsim 100$ K, the highest $T_{\rm k}$ actually occurs in regions surrounding the nucleus (see Figure 3.10(b)). This temperature drop toward the nucleus could explain why $\alpha_{\rm CO}$ rises while $\tau_{\rm CO}$ stays flat in Figure 3.13.

Based on NGC 3627 and NGC 4321, the 25th–75th percentile scatter of $\alpha_{\rm CO}$ in the $\alpha_{\rm CO}$–$T_{\rm k}$ relation is ~0.4 dex, which is larger than the ~0.1 dex scatter in the $\alpha_{\rm CO}$–$\tau_{\rm CO}$ relation shown in Figure 3.14. This suggests that optical depth and gas temperature effects contribute ~80% and 20% of the change in the derived $\alpha_{\rm CO}$, respectively, assuming they are independent and no other factors are at play. In that case, $\tau_{\rm CO}$ is likely the main driver of $\alpha_{\rm CO}$ variation in these galaxy centers, while $T_{\rm k}$ plays a secondary role in changing $\alpha_{\rm CO}$. Using the results from all three galaxies but excluding the optically thin inflow regions of

NGC 3351, we fit the $\alpha_{\rm CO}$, $\tau_{\rm CO}$, and $T_{\rm k}$ relation with a power law and obtain

$$\begin{aligned}\log \frac{\alpha_{\rm CO}}{\rm M_\odot\ (K\ km\ s^{-1}\ pc^2)^{-1}} \\ = 0.78\ \log \tau_{\rm CO(2-1)} - 0.18\ \log \frac{T_{\rm k}}{\rm K} - 0.84\ .\end{aligned} \tag{3.4}$$

By performing bootstrapping and refitting 1000 times, we determine an uncertainty of ± 0.03 for the slopes with respect to either log $\tau_{\rm CO(2-1)}$ or log $T_{\rm k}$, and ± 0.08 for the intercept.

Figure 3.16 illustrates how the ratio of $\alpha_{\rm CO}$ measured from our modeling and predicted by Equation 3.4 varies with $\tau_{\rm CO}$ and $T_{\rm k}$. In the optically thick regime, the 25–75th percentile scatter is 0.12 dex, which is similar to that seen in the $\alpha_{\rm CO}$–$\tau_{\rm CO}$ relation (see Figure 3.14). A rough inverse trend can be seen between $\tau_{\rm CO}$ and $T_{\rm k}$, which is expected as higher temperature can increase level population in high-J transitions and decrease the optical depth of low-J line emission. It is also clear that the power-law fit underestimates $\alpha_{\rm CO}$ in the optically-thin inflow regions of NGC 3351. Therefore, we emphasize that Equation 3.4 should only be applied to optically thick regions.

We further remind readers that this paper focuses on disentangling the emissivity-related drivers of $\alpha_{\rm CO}$, and thus $x_{\rm CO}$ is assumed constant at a starburst value of 3×10^{-4} over the entire region. This means that Equation 3.4 should either be limited to starburst-like environments with higher $x_{\rm CO}$, or be adjusted by multiplying a factor of $3 \times 10^{-4}/x_{\rm CO}$. For instance, molecular clouds in the Milky Way disk can have $\gtrsim 3$ times higher $\alpha_{\rm CO}$ values than that predicted by Equation 3.4, as they normally have $x_{\rm CO} \lesssim 10^{-4}$ (Frerking et al., 1982; Blake et al., 1987; Kulesa, 2002; Sheffer et al., 2008; Pitts et al., 2019).

The spatial variation of $x_{\rm CO}$ may also affect the derived $\alpha_{\rm CO}$ variation. If $x_{\rm CO}$ in the arms is lower than in the nucleus, as expected from increasing CO-dark H_2 fraction with galactocentric radius due to decreasing gas surface density (e.g., Smith et al., 2014), then $\alpha_{\rm CO}$ in the arms of NGC 3627 would become similar to the nucleus having higher $\alpha_{\rm CO}$ values. Alternatively, increasing $x_{\rm CO}$ in the NGC 3627 nucleus is also possible via the enrichment of ^{12}C through stellar nucleosynthesis from intermediate or high-mass stars. While it is typically expected that stronger cosmic ray ionization would decrease x_{CO} in starburst or AGN-host galaxy centers (Gong et al., 2020; Bisbas et al., 2021; Liu et al., 2022), exceptions have been found in places reaching high gas temperature of ~100 K due to the trigger of OH formation that further increases x_{CO} (Bisbas et al., 2017). Therefore, with the modeled $T_{\mathrm{k}} > 100$ K near the nucleus of NGC 3627, the potential rise of x_{CO} could also lead us to overestimate α_{CO}, implying that α_{CO} in the nucleus may not be distinctly higher than the arm regions. However, we emphasize again that our modeling cannot constrain the absolute x_{CO} values, and thus the net change of x_{CO} is still to be studied in more detail with the comprehensive effects mentioned above.

To investigate whether the theoretical expectation of $\alpha_{\mathrm{CO}} \propto \sqrt{n_{\mathrm{H_2}}}/T_{\mathrm{k}}$ under the virial assumption also holds in the three galaxy centers, Figure 3.15(b) shows the relation between the modeled $\log(\alpha_{\mathrm{CO}})$ and $\log(\sqrt{n_{\mathrm{H_2}}}/T_{\mathrm{k}})$. It is clear that both NGC 3627 and NGC 4321 show a positive correlation of α_{CO} with $\sqrt{n_{\mathrm{H_2}}}/T_{\mathrm{k}}$, which may indicate that the molecular clouds are overall close to virial balance or have a similar virial parameter. However, a similarly high virial parameter should be more likely in our case, given that previous studies already reported high virial parameters of 2–10 for GMCs in both galaxy centers assuming a Galactic-like or metallicity-dependent α_{CO} (Pan and Kuno, 2017; Rosolowsky et al., 2021). The high virial parameter in these galaxy centers may indicate unbound molecular clouds that could suppress star formation (e.g., Sorai et al., 2012; Nimori et al., 2013). On the other hand, NGC 3351 shows the highest $\sqrt{n_{\mathrm{H_2}}}/T_{\mathrm{k}}$ values due to generally lower T_{k} and higher $n_{\mathrm{H_2}}$, and the NGC 3351 inflows (data points in the bottom-right corner) are strong dynamical feature with optically thin CO emission (Teng et al., 2022) and thus do not match the assumption for $\sqrt{n_{\mathrm{H_2}}}/T_{\mathrm{k}}$ dependence (Bolatto et al., 2013; Gong et al., 2020). We do not see a clear correlation in the center of NGC 3351, which shows a roughly constant α_{CO} that is lower than the positive trend formed by the other two galaxies. This lower α_{CO} could be explained by the increased turbulence and shear near the NGC 3351 inflows, making the clouds there super-virial.

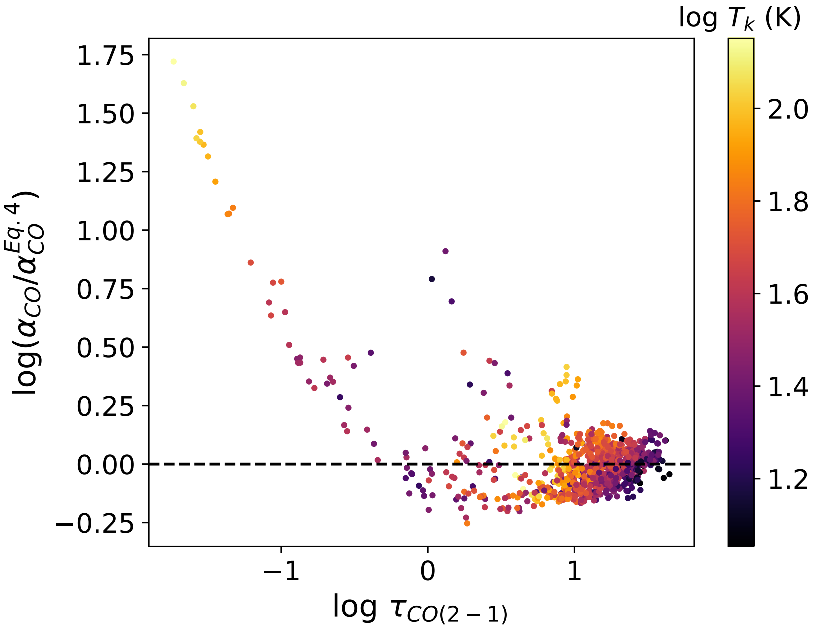

Figure 3.16. Ratio of the modeled and fitting-predicted α_{CO} (by Equation 3.4) versus the CO optical depth, colorcoded by the modeled gas temperature. The dashed line indicates perfect agreement between the modeled and predicted α_{CO}. The fitted Equation 3.4 should be limited to optically thick regions, where the 25–75th percentile scatter along the y-axis is 0.12 dex.

In summary, we find a strong, positive α_{CO} dependence on τ_{CO} after combining the modeling results of the central kpc of NGC 3351, NGC 3627, and NGC 4321. This correlation is in line with theoretical expectations for thermalized and optically thick clouds, and it can explain most of the α_{CO} variations found in the three galaxy centers. Additionally, an anti-correlation between α_{CO} and T_{k} is clearly seen in NGC 3627 and 4321, suggesting T_{k} as a secondary driver of α_{CO} variation after τ_{CO}. The α_{CO} in NGC 3627 and 4321 also shows a positive but weaker correlation with $\sqrt{n_{\mathrm{H_2}}}/T_{\mathrm{k}}$, which suggests that the molecular clouds in those regions have similar (likely high) virial parameters.

3.5.2 Comparison to α_{CO} Measurements in Literature

To compare our α_{CO} results with previous measurements on kpc scales (Sandstrom et al., 2013; Israel, 2020), we calculate the intensity-weighted mean α_{CO} over the observed regions. Based on Equation 3.3, we compute the average and standard deviation of 2000 likelihood-weighted random draws of N_{CO}, Φ_{bf}, and I_{CO} from the full model grid for each pixel. The procedure is described in Teng et al. (2022, Section 5.1) in greater detail. Since the $\alpha_{\rm CO}$ values in Sandstrom et al. (2013) were derived from CO 2–1 intensities assuming a constant R_{21} of 0.7, we will directly compare the $\alpha_{\rm CO(2-1)}$ values to avoid uncertainties originating from R_{21}. This means that $I_{\rm CO(1-0)}$ in Equation 3.3 will be replaced with $I_{\rm CO(2-1)}$ when we derive the intensity-weighted $\alpha_{\rm CO}$ for comparison to the dust-based results.

The intensity-weighted mean $\alpha_{\rm CO(2-1)}$ is 0.93±0.04 and 0.62±0.04 $\rm M_\odot$ (K km s^{-1} pc^2)$^{-1}$ over the central ~kpc of NGC 4321 and NGC 3627 included in our analysis. Using dust modeling and CO 2–1 observations, Sandstrom et al. (2013) derived $\alpha_{\rm CO(2-1)} = 0.9^{+0.4}_{-0.3}$ and $0.8^{+0.3}_{-0.1}$ $\rm M_\odot$ (K km s^{-1} pc^2)$^{-1}$ in the central 2.6 kpc and 1.7 kpc region of NGC 4321 and NGC 3627, respectively. For NGC 4321, our $\alpha_{\rm CO(2-1)}$ value is consistent with their dust-based estimate, as well as the carbon budget-based estimate of $\alpha_{\rm CO(2-1)}$ ~0.96 by Israel (2020) towards the central 22″ region after applying our integrated mean $R_{21} = 0.92$ in Table 3.2. We note that Israel (2020) also reported $T_{\rm k} > 100$ K with $X_{12/13} = 80$ for the center of NGC 4321 using a two-component model. Over the central kpc region of NGC 3351, the mean $\alpha_{\rm CO(2-1)}$ of 0.75 is also consistent with the Sandstrom et al. (2013) estimate of $1.0^{+0.4}_{-0.3}$ (see Appendix 3.B).

For NGC 3627, our derived mean $\alpha_{\rm CO(2-1)}$ of 0.62 is slightly lower than 0.8 from Sandstrom et al. (2013), while it is higher than $\alpha_{\rm CO(2-1)}$ ~0.43 determined by Israel (2020) applying our integrated mean R_{21} of 0.81 in Table 3.3. With assumptions on dust-to-gas ratios and applying our $R_{21} = 0.81$, a recent work by Jiao et al. (2021) also suggests $\alpha_{\rm CO(2-1)} = 0.99 \pm 0.37$, which overlaps with the solutions from this work and Sandstrom et al. (2013). One potential explanation for the discrepancy between Sandstrom et al. (2013) and our result is a calibration issue of the HERACLES CO 2–1 data used by Sandstrom et al. (2013). As shown in den Brok et al. (2021, Appendix C), the HERACLES data of NGC 3627 has been found to have significant calibration uncertainties with up to a factor of two lower intensity than the PHANGS–ALMA data we use. This implies that the $\alpha_{\rm CO}$ solution determined by Sandstrom et al. (2013) could be overestimated using the HERACLES data with fainter CO emission.

Moreover, it is also possible that our modeling overestimates α_{CO} in NGC 3627 due to the underestimation of T_{k}. Figure 3.10(b) shows that many regions in NGC 3627 have high T_{k} that exceed few hundreds K, potentially due to the AGN in its nucleus. Since our modeled lines only include transitions up to J=3–2, such line combination may not be sufficient to reveal temperatures above a few hundred K. We have also tested regions with $T_{\mathrm{k}} > 100$ K using the two-component model constructed by Teng et al. (2022), and still find $\gtrsim$100 K for the dominant component. Additionally, we have checked the spectral line energy distribution (SLED) of CO in all three galaxy centers using Herschel SPIRE/FTS data at 40″ resolution covering up to CO J=9–8 (A. Crocker, private communication). We find that the SLED of NGC 3627 is peaked in higher-J lines than the other two galaxy centers, which also supports the scenario of higher T_{k} in the center of NGC 3627. Thus, our modeling could have underestimated T_{k} in NGC 3627, and higher-J CO lines may be needed to accurately constrain such high T_{k}. If the center of NGC 3627 in fact has higher T_{k} than what we derived, this could lead to overestimation of α_{CO} as long as $n_{\mathrm{H_2}}$ does not deviate much from our modeling result (Papadopoulos et al., 2012a; Bolatto et al., 2013). The α_{CO} estimate from Israel (2020) also has the issue of lacking high-J CO lines, and the author reported $T_{\mathrm{k}} \lesssim 60$ K in the center of NGC 3627 which is even lower than our results and inconsistent with the bright emission seen in high-J transitions.

We conclude that the overall α_{CO} in the central kpc of NGC 3627 is likely a factor of 5–10 lower than the Galactic α_{CO}, while the actual value is still uncertain as seen from the inconsistency among Sandstrom et al. (2013), Israel (2020), Jiao et al. (2021), and this work. High-resolution observations toward high-J CO transitions will be essential to securely measure the environmental conditions and α_{CO} in this region. On the other hand, the α_{CO} values in the center of NGC 4321 match perfectly well among these studies using independent methods, which increases the reliability of the NGC 4321 results.

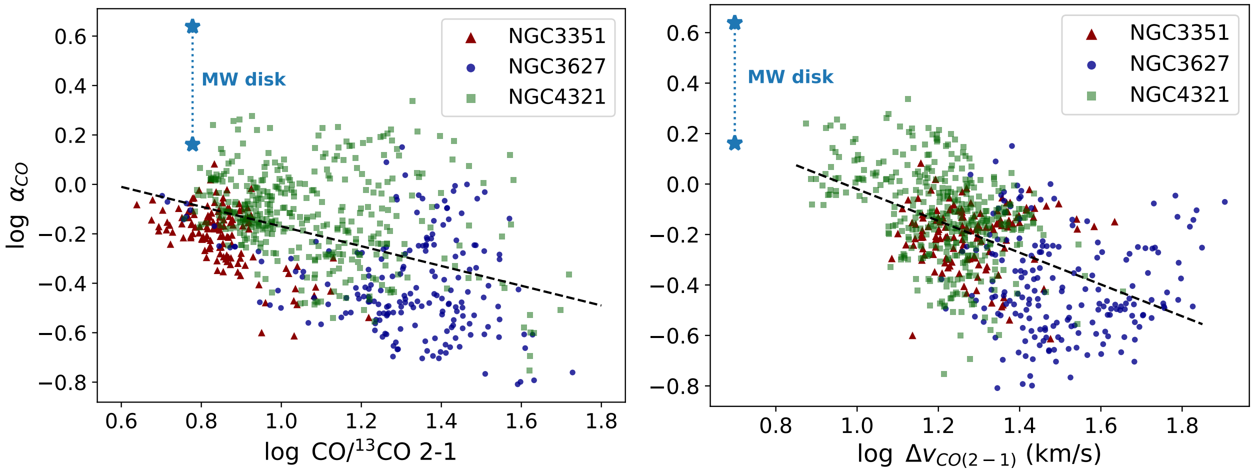

(a)

(b)

Figure 3.17. Relation of the modeled log($\alpha_{\rm CO}$) with the observed (a) CO/^{13}CO 2–1 line ratio and (b) CO 2–1 effective line width in optically thick regions with $\tau_{\rm CO(2-1)} > 5$. The dashed lines represent the best-fit power law relations (Equations 3.5 and 3.6). The typical Milky Way disk values with $x_{\rm CO}$ ranging from ~10^{-4} (higher $\alpha_{\rm CO}$) to 3×10^{-4} (lower $\alpha_{\rm CO}$) are labeled by the blue stars. The data points cover all regions except the inflow regions of NGC 3351. Despite a ~0.4 dex scatter in both relations, there is a clear trend of $\alpha_{\rm CO}$ decreasing with the line ratio and CO line width, suggesting these observable properties as potential tracers for $\alpha_{\rm CO}$ variations in galaxy centers.

3.5.3 Observational Tracers for $\alpha_{\rm CO}$ Variations

The CO/^{13}CO Line Ratios

As shown in Figure 3.14, all three galaxy centers show a clear correlation between $\alpha_{\rm CO}$ and $\tau_{\rm CO}$. In Figure 3.14(b), the colors represent the median CO/^{13}CO 2–1 ratios within each (two-dimensional) bin of $\alpha_{\rm CO}$ and $\tau_{\rm CO}$. The adopted bin size is 0.1 in both log($\alpha_{\rm CO}$) and log($\tau_{\rm CO}$) dimensions, which is consistent with the bin size we adopted when deriving the PDFs and solutions for log($\alpha_{\rm CO}$) and log($\tau_{\rm CO}$). The median-filtered line ratios shown by the color gradient is a visualization choice to emphasize the overall trend of the line ratio with $\tau_{\rm CO}$ or $\alpha_{\rm CO}$. We find that the color-coded CO/^{13}CO 2–1 ratios form a gradient across the parameter space when $\tau_{\rm CO} > 1$, suggesting an anti-correlation of the line ratio with $\tau_{\rm CO}$ or $\alpha_{\rm CO}$. It is also clear that the CO/^{13}CO ratio in these galaxy centers is higher than the Galactic disk-like ratio of ~6 (Aalto et al., 1995; Roman-Duval et al., 2016), which is consistent with the finding of elevated CO/^{13}CO ratios in LIRGs or central starburst regions

(Aalto et al., 1995; Aalto et al., 2010; Sliwa et al., 2012; Sliwa et al., 2014; Sliwa et al., 2017).

The inverse relation between $\alpha_{\rm CO}$ and the CO/^{13}CO 2–1 ratio is also clearly demonstrated by Figure 3.17(a). Here we only include optically thick regions with $\tau_{\rm CO(2-1)} > 5$, where $\alpha_{\rm CO}$ strongly depends on $\tau_{\rm CO}$. With $\tau_{\rm CO} < 30$ and $X_{12/13} > 40$ across our measurements, we obtain ^{13}CO optical depth that is solidly in the optically thin regime. Therefore, the correlations suggested by Figures 3.14(b) and 3.17(a) agree with the interpretation that the observed CO/^{13}CO 2–1 ratio is generally tracing $\tau_{\rm CO(2-1)}$ variations inversely in the three galaxy centers. This is because the decrease of $\tau_{\rm CO}$ can lead to more escaped CO emission and thus increasing the CO/^{13}CO ratio when CO is optically thick and ^{13}CO is optically thin. Since there is also a strong correlation between $\alpha_{\rm CO}$ and $\tau_{\rm CO}$, this implies that the CO/^{13}CO ratio may be used as an observational tracer for $\alpha_{\rm CO}$ variation. As indicated by the dashed line on Figure 3.17(a), we conduct a power law fit to the data points and find

$$\log \frac{\alpha_{\rm CO}}{\rm M_\odot\ (K\ km\ s^{-1}\ pc^2)^{-1}} = -0.40\ \log R_{12/13} + 0.23\ , \qquad (3.5)$$

where $R_{12/13}$ is the observed CO/^{13}CO 2–1 line ratio, and both the fitted slope and intercept have an uncertainty of ± 0.03. Similar to Equation 3.4, this fitted relation is only appropriate for starburst-like regions with a higher CO abundance $x_{\rm CO}$, unless the predicted value is further scaled by a factor of $3 \times 10^{-4}/x_{\rm CO}$. This scaling of $x_{\rm CO}$ can explain the factor of 3–4 discrepancy between the fit (with $x_{\rm CO} = 3 \times 10^{-4}$) and the typical Galactic disk $\alpha_{\rm CO}$ value (with $x_{\rm CO} \lesssim 10^{-4}$) as shown in Figure 3.17(a). There is a dispersion of $\sigma \sim 0.2$ dex between the modeled and fitting-predicted $\alpha_{\rm CO}$, which likely originates from the uncertainty in $X_{12/13}$ variation as well as the exclusion of temperature effects.

The CO/^{13}CO ratio should also vary with the molecular abundance $X_{12/13}$, which is one of our directly modeled parameters. As presented in Section 3.4.2, most regions show 1DMax $X_{12/13}$ solutions consistent with the best-fit solutions at $X_{12/13}$ ~80–100 (e.g., compare Figure 3.7(a) with Figure 3.8). Even in several regions with 1DMax $X_{12/13}$~40, their median $X_{12/13}$ also show higher $X_{12/13}$ ~ 80–100 that is similar to their best-fit solutions. Thus, even though the $X_{12/13}$ PDFs are generally not as well constrained as other parameters, it is likely that most regions have $X_{12/13}$ ~80–100 based on the match between the 1DMax/median and best-fit solutions. Moreover, the $X_{13/18}$ abundances are roughly constant and well-constrained at 6–8 over both galaxies, which implies that significant spatial variations in $X_{12/13}$ is unlikely from a nucleosynthesis perspective as enrichment of both ^{12}C and ^{18}O would be expected from massive stars. Therefore, $X_{12/13}$ may not be the main driver of the CO/^{13}CO line ratio variations. The roughly constant $X_{12/13}$ and varying CO optical depths in these galaxy centers can explain why the CO/^{13}CO 2–1 line ratio is overall reflecting $\tau_{\rm CO}$ variations in Figures 3.14(b) and 3.17(a).

In Teng et al. (2022), the bar-driven inflows of NGC 3351 shows enhanced CO/^{13}CO 2–1 ratio with nearly optically thin CO emission, which also suggests the inverse relation between $\tau_{\rm CO}$ and CO/^{13}CO line ratio. Notably, their stacking result for the inflow regions revealed well-constrained $X_{12/13}$ PDFs showing 1DMax and median $X_{12/13}$ ~30. Since the value is similar to that found in the central regions of NGC 3351, it provided evidence for $\tau_{\rm CO}$ being the main driver of the CO/^{13}CO line ratio. Furthermore, Cormier et al. (2018) also reported anti-correlations of $\alpha_{\rm CO}$ with CO/^{13}CO 1–0 ratio across the disks of several galaxies, using dust-based $\alpha_{\rm CO}$ (from Sandstrom et al. 2013) with single-dish CO observations at ~1.5 kpc resolutions. Interestingly, such an anti-correlation was only seen in the three galaxies hosting starburst-dominated nuclei in their sample, but not in the other five normal star-forming galaxies. This can be explained by the increased optical depth variation in starburst environments. Similarly, barred galaxy centers tend to have variable gas dynamics and conditions due to higher excitation, turbulence, shear, and gas concentration, which altogether can lead to even more significant $\tau_{\rm CO}$ variations. Within the three barred galaxy centers presented in this work, we find that $\alpha_{\rm CO}$ is positively correlated with $\tau_{\rm CO}$, and that the CO/^{13}CO 2–1 line ratio mainly traces the $\tau_{\rm CO}$ variation. These results suggest that the

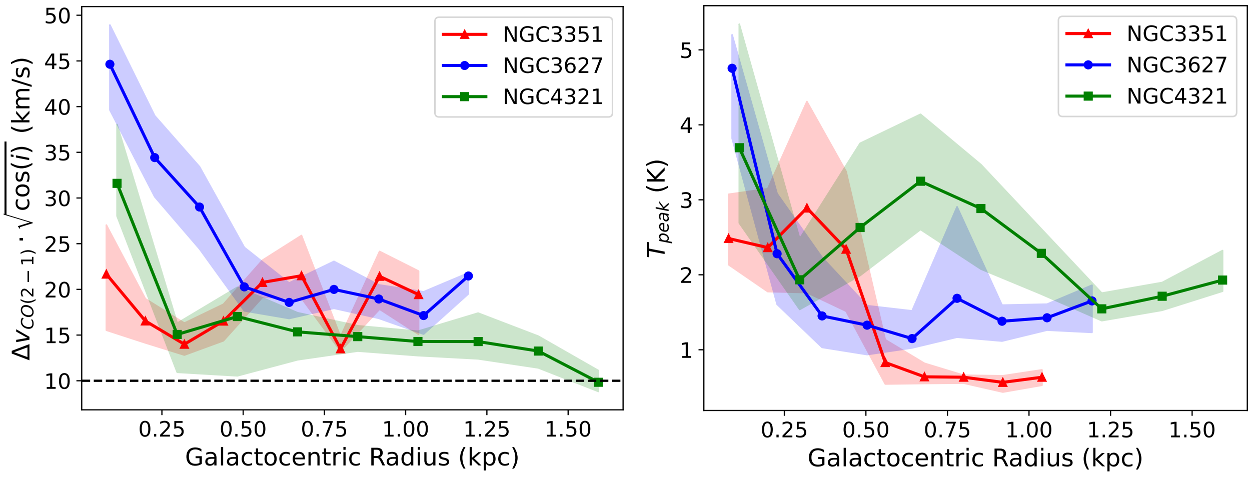

(a) (b)

Figure 3.18. Galactocentric radial profiles of the CO 2–1 (a) effective line widths with a $\sqrt{\cos(i)}$ inclination correction and (b) spectral peak intensities for NGC 3351 (red), NGC 3627 (blue), and NGC 4321 (green). Colored lines show the radial-binned medians and shaded areas show the 25th and 75th percentile ranges. The horizontal dashed line represents an approximate boundary of velocity dispersion that distinguishes between gas in barred centers and in disks or unbarred centers (Sun et al., 2020b).

CO/^{13}CO ratio can be a useful observational tracer for α_{CO} variation, particularly in galaxy centers where optical depth is generally high and spans a wide dynamic range.

Spectral Line Widths and Peak Temperatures

With spectroscopic observations, the line width (Δv) and brightness temperature at the line peak (T_{peak}) provide two direct observables that may contain information about gas properties. For optically thick lines like CO, T_{peak} can be a probe of the excitation temperature (T_{ex}) if the beam-filling factor is known or fixed. On the other hand, line width represents the one-dimensional velocity dispersion, which is indicative of turbulent motions. Since the line center optical depth is a function of surface density and velocity dispersion, variations in line widths may also provide hints for optical depth changes.

As we have already shown the strong α_{CO} dependence on τ_{CO}, it is likely that the observed Δv can also trace the α_{CO} variations. Figure 3.17(b) presents a scatter plot of the modeled α_{CO} versus the observed CO 2–1 line width for regions with $\tau_{\mathrm{CO(2-1)}} > 5$. It is clear that α_{CO} decreases with Δv, consistent with the expectation of α_{CO} increasing with τ_{CO}. The power law fit is presented by the dashed line, indicating

$$\log \frac{\alpha_{\mathrm{CO}}}{\mathrm{M}_{\odot}\ (\mathrm{K\ km\ s^{-1}\ pc^{2}})^{-1}} = -0.63\ \log \frac{\Delta v_{\mathrm{CO}}}{\mathrm{km\ s^{-1}}} + 0.61\ , \tag{3.6}$$

where the uncertainty is ± 0.04 and ± 0.05 for the fitted slope and intercept, respectively. The dispersion with respect to this prediction is $\sigma \sim 0.2$ dex, which is reasonable as the surface density term in the optical depth and the temperature are also included as parameters in our modeled α_{CO}. The stars in Figure 3.17(b) indicate the Galactic α_{CO} values at $\Delta v = 5$ km s^{-1}, which is typical for Galactic disk clouds with size of ~100 pc (e.g., Heyer and Dame, 2015). We emphasize that the line-of-sight Δv is what relates directly to τ_{CO}, and thus there is no need to correct Δv for inclination effects among different galaxies.

Figure 3.18 shows the radial profiles of the observed CO 2–1 line width and T_{peak} in NGC 3351, NGC 3627, and NGC 4321. Here we multiply the observed line width by a $\sqrt{\cos(i)}$ factor to eliminate the line width dependency on galaxy inclination, following the empirical correction found by Sun et al. (2022) based on data with similar resolution of 150 pc. This correction is only applied here to bring out the line width effects from small-scale turbulence or large-scale dynamical processes, ensuring a fair comparison among different galaxies. With the inclination correction, Δv in the three galaxies becomes roughly aligned at radii beyond 500 pc. We find a significant increase in line width toward the nuclei ($r \lesssim 200$ pc) of NGC 3627 and NGC 4321, which is consistent with increased velocity dispersion being the cause of lower optical depths seen in Figure 3.13(b). The increase of line width in the inflow regions of NGC 3351 ($r \gtrsim 500$ pc) is also notable, reaching comparable values to its central nucleus and being higher than in the other two galaxies. Contrary to most situations where T_{peak} dominates the integrated intensity variation (e.g., Egusa et al., 2022), T_{peak} is consistently low in the NGC 3351 inflows, and thus the enhanced velocity dispersion plays a more important role in the observed CO emission of this region.

Interestingly, all the mentioned regions with enhanced velocity dispersion are places where abrupt changes in α_{CO} are found (see Figure 3.13(a)). Furthermore, Sun et al. (2020b) found that molecular gas in barred galaxy centers tends to have higher velocity dispersion than in galaxy disks or non-barred galaxy centers, and they can be distinguished by an approximate boundary of $\Delta v = 10$ km/s (without inclination correction). As shown in Figure 3.18(a), almost all pixels in the three galaxy centers have $\Delta v > 10$ km/s even after inclination correction. The average line width in our galaxy centers (see Tables 3.2 and 3.3) are also 3–5 times higher than that of the galaxy disk sample in Sun et al. (2020b). Such higher velocity dispersion can lead to lower optical depths in galaxy centers, and may explain the overall lower-than-disk α_{CO} across the whole central kpc regions (Sandstrom et al., 2013). Notably, this scenario of higher velocity dispersion lowering α_{CO} in galaxy centers is compatible with the kpc-scale α_{CO} dependence on stellar mass surface density found by Bolatto et al. (2013) and I-D. Chiang et al. (in preparation). This is because the stellar mass surface density can track additional external pressure from the ISM that sets the high velocity dispersion in galaxy centers. Therefore, in addition to the CO/^{13}CO line ratio, the observed line width may also be useful in predicting α_{CO} changes due to its relation with optical depth.

Another potential observational tracer for α_{CO} is T_{peak}, which can be indicative of the excitation temperature T_{ex} as well as the total integrated intensity when CO is optically thick. However, we do not find the observed T_{peak} tracking the modeled α_{CO}, even though α_{CO} is found to anti-correlate with T_{k} (see Section 3.5.1). This means that T_{peak} is not a good indicator of T_{k} in our case, which can be due to deviation from LTE in most regions as we generally find $T_{\mathrm{ex}} < T_{\mathrm{k}}$. As shown in Figure 3.18(b), the radial variation of the observed T_{peak} differs from that of α_{CO} in Figure 3.13(a). The relation between α_{CO} and the observed T_{peak} is presented in Figure 3.19(b) in Section 3.5.4.

In this work, we find that the sub-kpc scale α_{CO} variation in galaxy centers is dominated by τ_{CO} variations, which can be reflected by the observed CO/^{13}CO line ratio as well as the CO line width. While we also find a secondary effect of T_{k} on α_{CO}, the observed

$T_{\rm peak}$ do not trace the $\alpha_{\rm CO}$ variation well given the non-LTE conditions as well as density or optical depth variations in barred galaxy centers. In Section 3.5.4, we will show that simulations also predict only a mild $\alpha_{\rm CO}$ dependence on $T_{\rm peak}$, and that dependence can be washed out if observed with a ~100 pc beam size.

3.5.4 Comparison with Existing $\alpha_{\rm CO}$ Prescriptions

Recent simulation studies have developed predictions for $\alpha_{\rm CO}$ in terms of metallicity, CO line ratios, and/or CO integrated intensities (Narayanan et al., 2012; Accurso et al., 2017a; Accurso et al., 2017b; Gong et al., 2020; Hu et al., 2022). Such predictions have the potential to greatly improve the assessment of molecular gas content in galaxies, and therefore testing them is critical. However, most simulations focus on low-metallicity or Galactic disk-like environments, which do not capture the dense, turbulent conditions or gas inflows that are common in galaxy centers. To test if the current $\alpha_{\rm CO}$ predictions can be applied to star-forming galaxy centers, we compare our $\alpha_{\rm CO}$ results with the established prescriptions and discuss the consistency/discrepancy.

Based on magneto-hydrodynamic simulations of the ISM on kpc-sized chunks of galactic disks down to 2 pc resolution, Gong et al. (2020) proposed three different $\alpha_{\rm CO}$ prescriptions as a function of metallicity, beam size, as well as CO line related properties: R_{21}, $T_{\rm peak}$, and CO integrated intensity $I_{\rm CO(1-0)}$, respectively. The prescriptions are cautioned to be only applicable to disk-like environment with $I_{\rm CO(1-0)} < 200$ K km s^{-1}, which is the maximum intensity of their simulated data at 2 pc resolution. Their native 2 pc resolution data also span a range of $2 > R_{21} > 0.1$ and $20 > T_{\rm peak} > 0.1$ K. Figure 3.19 compares our modeled $\alpha_{\rm CO}$ with the Gong et al. (2020) simulated data (brown curves) and prescriptions (black dashed lines) at solar metallicity and a ~100 pc beam size. We also show their simulated data at 2 pc resolution (gray curves), which seems to extend to denser/hotter regions that are more consistent with the main sample of our observations. However, we note that their 2-pc data should be resolving individual molecular clouds, while our results at ~100 pc resolutions are sampling beam-averaged, unresolved gas.

Overall, it is clear that our observational data have higher R_{21}, $T_{\rm peak}$, and $I_{\rm CO(1-0)}$ than the simulated data at $\gtrsim$100 pc scales, and that our $\alpha_{\rm CO}$ results are systematically lower than the extrapolated predictions. The R_{21}-dependent prediction has the most potential to match our data within a factor of three discrepancy, while the $T_{\rm peak}$- and $I_{\rm CO(1-0)}$-dependent predictions show deviations with a factor of 3–10. This is in line with the suggestion by Gong et al. (2020) to adopt the R_{21} prescription for larger ($>$ 100 pc) beam sizes, as R_{21} can better reflect CO excitation and suffers less from beam dilution. As shown in Figure 3.19, the predicted $\alpha_{\rm CO}$ correlations with $T_{\rm peak}$ and $I_{\rm CO(1-0)}$ are fairly weak, likely due to significant beam-averaging over temperature and density at $\gtrsim$100 pc resolutions.

In addition, we find that the $\gtrsim$100 pc simulated data have some overlap with all three galaxies in the dynamic range of $T_{\rm peak}$ but almost no overlap in that of $I_{\rm CO(1-0)}$, implying that the line width is generally broader in our case (see also Section 3.5.3). This can be a vital reason for the discrepancy on $\alpha_{\rm CO}$ between the simulations and observations, as the enhanced velocity dispersion due to strong dynamical effects in these galaxy centers cannot be captured by such simulations, where gas inflows and central starbursts were not taken into account. Another possible reason for the difference with simulations is our assumption of constant CO abundance, $x_{\rm CO}$. This could be important in some regions with low $T_{\rm peak}$ and $I_{\rm CO}$, where the optical depth is low and the photodissociation may lower $x_{\rm CO}$, leading to possible underestimation of $\alpha_{\rm CO}$ in our modeling. However, the difference in $x_{\rm CO}$ cannot explain the overall lower $\alpha_{\rm CO}$ seen in the majority of our observed data with $n_{\rm H_2} > 300$ cm^{-3}, since most of the simulated data from Gong et al. (2020) in this regime reaches their maximum $x_{\rm CO}$ of 3.2×10^{-4}, which is similar to our assumption.

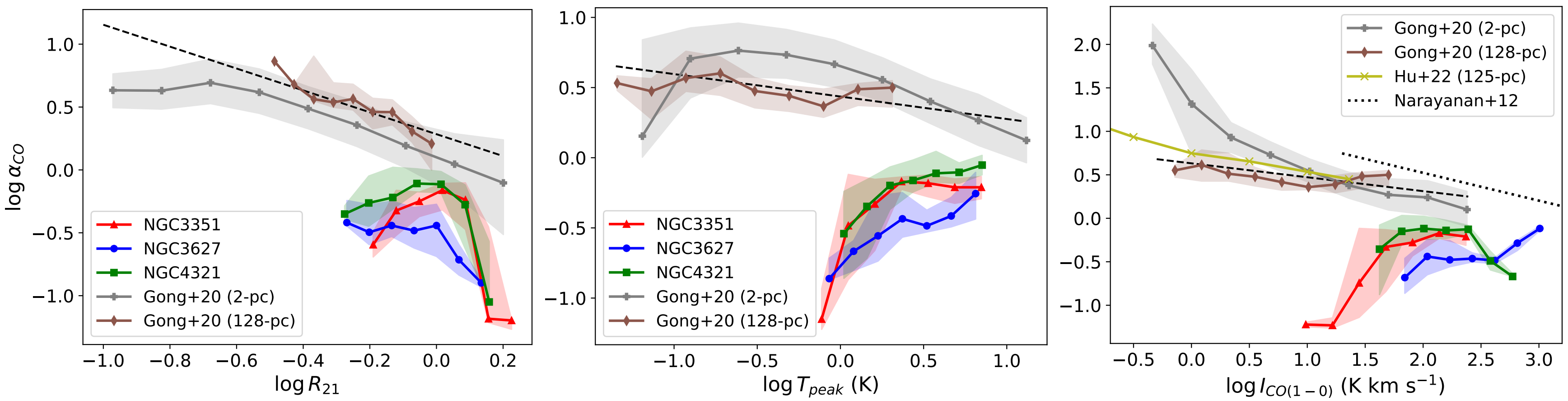

(a) (b) (c)

Figure 3.19. $\alpha_{\rm CO}$ relations with the observed (a) CO 2–1/1–0 ratio, (b) peak temperature of CO 1–0, and (c) CO 1–0 integrated intensity, comparing our observations (colored lines as before) with the simulations. The solid lines and shaded areas indicate the binned medians and 25th/75th percentile ranges. The brown (gray), solid lines show the simulated data at 128-pc (2-pc) resolution from Gong et al. (2020), and the dashed lines represent their suggested prescriptions with a 100 pc beam size. In panel (c), the dotted line and the yellow line show the simulation-based predictions suggested by Narayanan et al. (2012) and Hu et al. (2022), respectively. The mismatch of gas conditions such as CO excitation and velocity dispersion between the observation and simulations may explain why $\alpha_{\rm CO}$ values in the galaxy centers are lower than that predicted by simulations probing Galactic disk-like environments.

It is important to note that the simulation by Gong et al. (2020) represents a different regime of physical conditions than our measurements, as nearly half of the simulated data are optically thin and sub-thermally excited. However, they have also explored $\alpha_{\rm CO}$ dependence in the optically thick and thermally excited regime, which is closer to the conditions of our data and may explain the $\tau_{\rm CO}$ correlation we observe. Compared to Gong et al. (2020), our three galaxy centers lie beyond the "high-density" regime ($n_{\rm H_2} \gtrsim 300$ cm^{-3}) where they found saturated CO emission with growing $N_{\rm H_2}$ due to increased optical depths. This saturated level corresponds to $N_{\rm H_2} \gtrsim 5 \times 10^{21}$ cm^{-2} or $N_{\rm CO} \gtrsim 1.5 \times 10^{18}$ cm^{-2} (assuming consistent $x_{\rm CO}$ of 3×10^{-4}), the value of which agrees with our $N_{\rm CO}$ solutions. In the sub-thermal regime where CO intensity is not yet saturated, Gong et al. (2020) reported decreasing $\alpha_{\rm CO}$ with $n_{\rm H_2}$, which can be explained by increasing excitation temperature and CO abundance. Meanwhile, they also found that $\alpha_{\rm CO}$ starts to increase with $n_{\rm H_2}$ when entering the thermal regime where CO becomes fully optically thick. This "turnover" trend of $\alpha_{\rm CO}$ suggests that the impact from optical depth effects can take over in dense, optically thick regions like galaxy centers, which potentially explains why optical depth effects dominate the $\alpha_{\rm CO}$ trend in our results (see Section 3.5.1 and 3.5.3).

In addition to Gong et al. (2020), other hydrodynamic simulations also suggested $\alpha_{\rm CO}$ as a multivariate function of metallicity, CO integrated intensity, and/or beam size (Narayanan et al., 2012; Hu et al., 2022). As shown in Figure 3.19(c), the prediction by Narayanan et al. (2012) is within 0.2 dex higher than that by Gong et al. (2020) at $I_{\rm CO(1-0)} \gtrsim 30$ K km s^{-1} and solar metallicity. We also overplot the simulated data at 125-pc resolution from a recent study by Hu et al. (2022), which predicts a similar $\alpha_{\rm CO}$ trend to Gong et al. (2020) and reaches a maximum $x_{\rm CO}$ of 2.8×10^{-4}. We find our modeled $N_{\rm CO}$ generally higher than the predicted relations between CO optical depth and column density at solar metallicity in Hu et al. (2022).

By assembling previous observations at >kpc scales including nearby disks (Sandstrom et al., 2013) and (U)LIRGs (Downes and Solomon, 1998; Papadopoulos et al., 2012a), Bolatto et al. (2013) also suggested a prescription of α_{CO} as a function of metallicity (Z', normalized to the solar value), characteristic giant molecular cloud surface density (Σ_{GMC}), and the total (gas + star) surface density (Σ_{tot}):

$$\alpha_{\mathrm{CO}} = 2.9 \exp\left(\frac{40}{Z'\ \Sigma_{\mathrm{GMC}}}\right)\left(\frac{\Sigma_{\mathrm{tot}}}{100\ \mathrm{M_\odot\ pc^{-2}}}\right)^{-\gamma} \tag{3.7}$$

$\mathrm{M_\odot}$ (K km s^{-1} pc^2)$^{-1}$, where $\gamma = 0.5$ if $\Sigma_{\mathrm{tot}} > 100\ \mathrm{M_\odot\ pc^{-2}}$ or $\gamma = 0$ otherwise. To compare our results with this kpc-based prescription, we calculate the stellar mass surface densities Σ_* using the PHANGS–MUSE data at a native resolution of ~1.5″ (Emsellem et al., 2022). We weight the Σ_* with our observed $I_{\mathrm{CO(1-0)}}$ and then average over the entire region covered in our analysis. Similarly, we derive the average molecular gas mass surface density (Σ_{mol}) by multiplying the $I_{\mathrm{CO(1-0)}}$ maps with our modeled α_{CO} and then calculating the intensity-weighted mean across the maps.

The resulting Σ_* (Σ_{mol}) for the centers of NGC 3351, 3627, and 4321 are approximately 5000 (63), 4500 (115), and 2100 (94) $\mathrm{M_\odot\ pc^{-2}}$. It is clear that Σ_{tot} is dominated by Σ_* in all three galaxy centers, and the derived Σ_{mol} is similar to the $\Sigma_{\mathrm{GMC}} = 100\ \mathrm{M_\odot\ pc^{-2}}$ adopted in Bolatto et al. (2013). Finally, we correct the derived surface densities with their galaxy inclinations by a cosine factor and then substitute into Equation 3.7, assuming $\Sigma_{\mathrm{GMC}} = 100\ \mathrm{M_\odot\ pc^{-2}}$ at solar metallicity [5].

With the corrected surface density, Equation 3.7 predicts log(α_{CO}) of -0.22, -0.20, and -0.04 $\mathrm{M_\odot}$ (K km s^{-1} pc^2)$^{-1}$ over the centers of NGC 3351, 3627, and 4321, respectively. Our modeled α_{CO} distributions show log(α_{CO}) of $-0.22^{+0.12}_{-0.39}$, $-0.46^{+0.24}_{-0.21}$, and $-0.14^{+0.17}_{-0.24}$ $\mathrm{M_\odot}$ (K km s^{-1} pc^2)$^{-1}$ in the central $r < 20''$ of these galaxies. The intensity-weighted mean $\alpha_{\mathrm{CO(2-1)}}$ derived in Section 3.5.2 is equivalent to log(α_{CO}) of -0.12, -0.30, and -0.07 $\mathrm{M_\odot}$ (K km s^{-1} pc^2)$^{-1}$ if we convert the CO 2–1 intensity back to CO 1–0 via the integrated

---

[5] For the Bolatto et al. (2013) prescription, the solar metallicity condition is suggested to be paired with a fixed GMC surface density of 100 $\mathrm{M_\odot\ pc^{-2}}$. This is because the exponential term (see Equation 3.7) can easily lead to unrealistic α_{CO} values even with small variations in the adopted GMC surface density (see also Sun et al., 2023). We therefore use the suggested value of 100 $\mathrm{M_\odot\ pc^{-2}}$ here to avoid such issues, and we also show that the intensity-weighted Σ_{mol} at kpc scales for our galaxy centers roughly agrees with that value.

mean R_{21} (see Tables 3.2, 3.3, and Table 2 of Teng et al., 2022). Both results overlap well with the predicted values from Equation 3.7, assuming a reasonable 0.2 dex uncertainty of the prediction. Notably, the range of our $\Sigma_{\rm tot}$ (dominated by Σ_*) is also similar to the (U)LIRG samples used in Bolatto et al. (2013) to develop the prescription.

We conclude that on kpc scales, our $\alpha_{\rm CO}$ results are compatible with the Bolatto et al. (2013) prescription. On sub-kpc scales, the existing simulation-based prescriptions may overestimate $\alpha_{\rm CO}$ when being applied to galaxy centers with higher surface density, CO intensity, and velocity dispersion. Future simulations capturing gas inflows and local turbulence will be needed to develop a better $\alpha_{\rm CO}$ prescription appropriate for galaxy centers or other extreme environments.

3.5.5 Multi-line Constraints in the Modeling

Our multi-line modeling jointly analyzes six low-J transitions of CO, ^{13}CO, and C^{18}O. In this subsection, we discuss how modeling solutions would change if different subsets of lines were used. We will compare our solutions from the six-line modeling (Section 3.4.2) to those determined from various combinations of lines, and identify the most critical measurements that enable good constraints on the parameters. In addition to the modeling of NGC 3627 and NGC 4321, we will also include the modeling results of NGC 3351 from Teng et al. (2022) as the observed lines and modeling approach are the same.

From Figure 3.7, we find that the constraints given by the ^{13}CO 2–1 and C^{18}O 2–1 are almost identical, and the same applies to ^{13}CO 3–2 and C^{18}O 3–2 (see also Figure 3.25 in the Appendix). This means that the best-fit solutions would remain the same even if we remove the constraints from both C^{18}O lines. Teng et al. (2022) also reported that the C^{18}O line constraints are not critical to the results for the inflow regions in NGC 3351, though they did not further examine other regions. To test how the removal of C^{18}O would affect the modeling solutions, we present in the left column of Figure 3.20 the pixel-by-pixel solutions of $T_{\rm k}$, $n_{\rm H_2}$, and $N_{\rm CO}/\Delta v$ modeled with and without the two C^{18}O lines on the

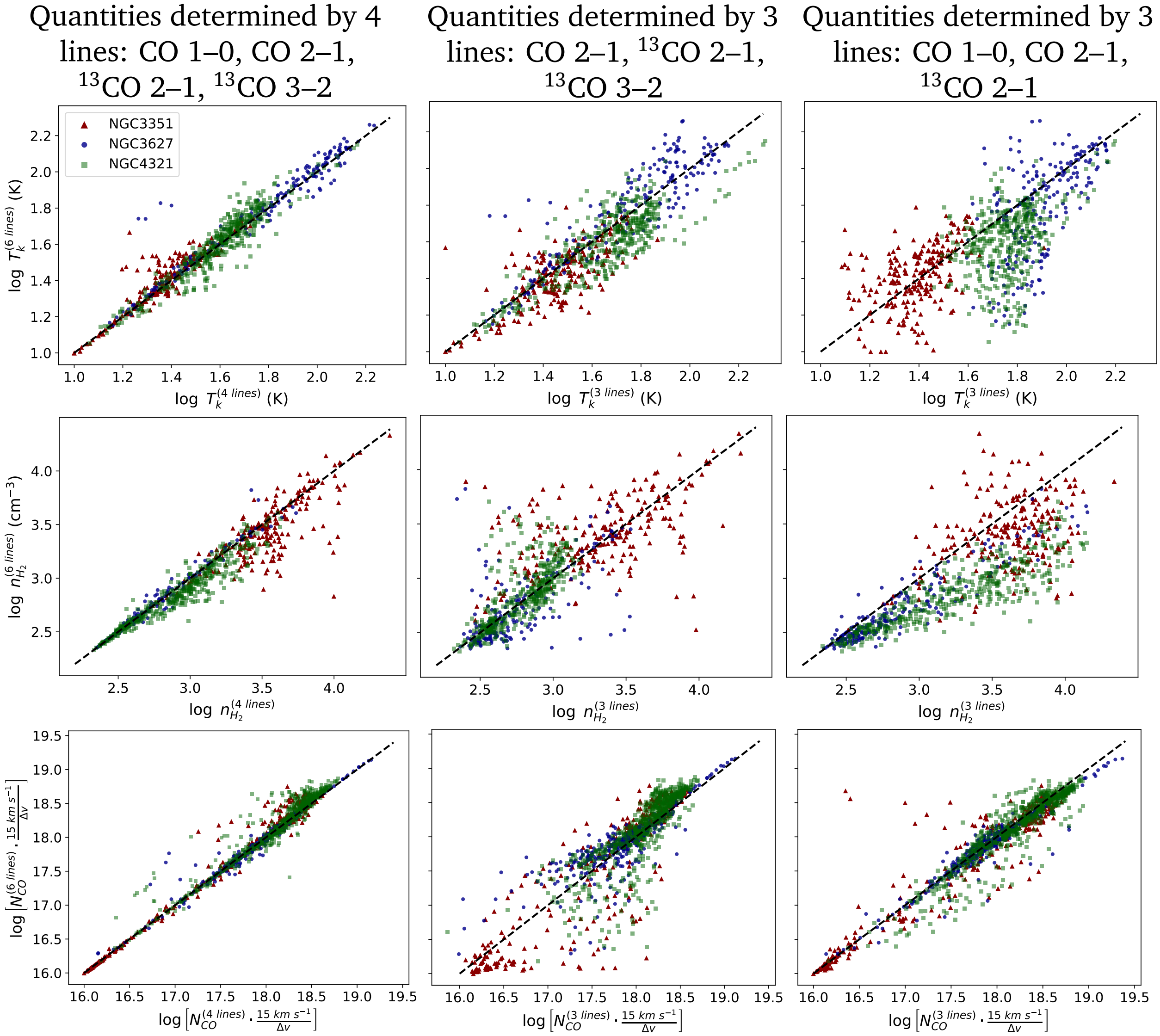

Figure 3.20. Median solutions of T_k (first row), n_{H_2} (middle row), and $N_\mathrm{CO}/\Delta v$ (bottom row) determined by multi-line modeling with different sets of emission lines in the central kpc regions of NGC 3351 (red), NGC 3627 (blue), and NGC 4321 (green). The y-axes represent the environmental parameters constrained by all six lines, which are compared to the x-axes showing those constrained by only a subset of lines. *Left column:* removing the two C^{18}O lines still reproduce consistent solutions with those determined by the six-line modeling. *Middle column:* CO 2–1, ^{13}CO 2–1, and ^{13}CO 3–2 are key constraints, while the addition of CO 1–0 (left column) is crucial for reducing the scatter and constraining $N_\mathrm{CO}/\Delta v$. *Right column:* without the high-J constraint from ^{13}CO 3–2, the derived T_k and n_{H_2} would deviate from the six-line modeling results.

y-axes and x-axes, respectively. It is clear that solutions obtained from both scenarios are consistent with only a ~0.2 dex scatter for all quantities. We note that $C^{18}O$ emission is weak in the arms of NGC 3627, but it is well detected in NGC 4321 and the central ~kpc of NGC 3351, so the low S/N of the $C^{18}O$ measurements is not the main reason for such consistency. We conclude that the combination of CO 1–0, CO 2–1, ^{13}CO 2–1, and ^{13}CO 3–2 can already provide strong constraints on the gas properties, while $C^{18}O$ 2–1 and 3–2 tend to give constraints similar to ^{13}CO and thus do not provide much additional information.

The middle and right columns of Figure 3.20 compare the six-line modeling solutions with the solutions determined by only three of the lines. In the middle column panels, we present the case with CO 2–1, ^{13}CO 2–1, and ^{13}CO 3–2, and the rightmost panels show the case with CO 1–0, CO 2–1, and ^{13}CO 2–1. We include CO 2–1 and ^{13}CO 2–1 in both cases because the detection of these lines were used to define our analyzed regions (i.e., CO 2–1 flux recovery > 70% and ^{13}CO 2–1 S/N > 3). We find that the inclusion of ^{13}CO 3–2 (middle panels) is critical to obtaining accurate solutions for T_k and n_{H_2}, as removing that line leads to much larger scatter and/or bias in the reconstructed T_k and n_{H_2} even with the inclusion of CO 1–0 (right panels). This is likely because ^{13}CO 3–2 is the only high-J transition in the set of lines, and thus it provides critical constraints on density and temperature in addition to the lower-J 1–0 or 2–1 transitions. On the other hand, including both CO 1–0 and 2–1 can significantly reduce the scatter in $N_\mathrm{CO}/\Delta v$ since the ^{12}CO emission is highly dependent on optical depth (see bottom panels of Figure 3.20).

In summary, CO 2–1, ^{13}CO 2–1, and ^{13}CO 3–2 can be an efficient combination to measure gas temperature and volume density via multi-line modeling, while the addition of CO 1–0 would be important to obtain more reliable and precise estimates for optical depth. Since ^{13}CO has a slightly higher effective critical density and much lower optical depth than CO, the inclusion of a ^{13}CO line ratio can better constrain regions with higher volume/surface density or optical depth such as galaxy centers. Notably, the $C^{18}O$ lines give degenerate but lower quality information to the ^{13}CO lines. Since it is observationally expensive to securely detect the faint C^{18}O lines, this result may help reduce observing time for similar studies in the future or over larger area. However, we emphasize that the conclusion is simply drawn from the modeling results toward the central kpc of NGC 3351, NGC 3627, and NGC 4321, which are all barred centers with starburst or AGN signatures. It is likely that different transitions or species are needed to constrain regions such as galaxy disks or unbarred galaxy centers.

3.6 Conclusions

We present ALMA observations of six low-J CO, ^{13}CO, and C^{18}O lines toward the inner 2–3 kpc regions of NGC 3627 and NGC 4321 at ~100 pc resolution. Using non-LTE radiative transfer modeling with Bayesian likelihood analysis, we constrain molecular gas properties including density, temperature, and CO isotopologue abundances on a pixel-by-pixel basis. With the modeling, we further derive $\alpha_{\rm CO}$ and correlate with parameters such as optical depth, temperature, velocity dispersion, and line ratios to discuss the physical drivers and observational tracers of $\alpha_{\rm CO}$ variations in barred galaxy centers. The results on NGC 3351 from Teng et al. (2022) are incorporated in our discussion for a more comprehensive view. We also compare the results with existing $\alpha_{\rm CO}$ estimates and predictions. Our main findings and conclusions are as follows:

1. The moment 0 images of all six lines reveal a bright nucleus with size of ~300 pc in diameter in both NGC 3627 and NGC 4321. The nuclei are connected with inner spiral arms or bar lanes, which are observed in all the lines for NGC 4321 but not securely detected in C^{18}O for NGC 3627. The temperature sensitive line ratios are significantly higher in both nuclei with an integrated mean R_{21} of 0.9 for NGC 3627 and 1.2 for NGC 4321, suggesting high excitation and thermalized gas. The integrated mean R_{21} over the entire central region of NGC 3627 and 4321 is 0.8 and 0.9, respectively, which are consistent with previous observations on kpc scales.

2. Our modeling results in well-constrained solutions for most physical parameters. Both galaxies show increasing kinetic temperature (T_k) and H_2 volume density (n_{H_2}) trends toward the centers, with both nuclei reaching $T_\mathrm{k} \gtrsim 100$ K and $n_{\mathrm{H}_2} > 10^3$ cm^{-3}. We find that the ^{13}CO/C^{18}O abundance ratio ($X_{13/18}$) varies in the range 6–8, which is similar to the Galactic Center values. The ^{12}CO/^{13}CO abundance ratio ($X_{12/13}$) ranges from 80–100 for most regions, despite being less constrained than other parameters.

3. Assuming the CO/H_2 abundance ratio $x_\mathrm{CO} = 3 \times 10^{-4}$, all the pixels in both galaxy centers show lower CO conversion factor (α_CO) than the standard Galactic value by a factor of 4 to 15. We find that most regions have $\alpha_\mathrm{CO} < 1\,(3 \times 10^{-4}/x_\mathrm{CO})$ M$_\odot$ (K km s^{-1} pc^2)$^{-1}$, and it generally decreases with galactocentric radius till a radius of 1.5 kpc. This decreasing α_CO trend with similar values was also seen within the inner 1 kpc nuclear ring of NGC 3351 (Teng et al., 2022).

4. We derive intensity-weighted mean $\alpha_\mathrm{CO(2-1)}$ of 0.62 ± 0.04 and 0.93 ± 0.04 over the central ~2 kpc regions for NGC 3627 and NGC 4321, respectively. The result for NGC 4321 matches well with previous dust-based and carbon budget-based studies at lower resolutions (Sandstrom et al., 2013; Israel, 2020). However, our α_CO value for NGC 3627 is in between those studies with a ~0.2 dex discrepancy. The disagreement may be related to calibration issues for NGC 3627 in previous CO mapping. Another possibility may be that the high temperatures in NGC 3627 are not well measured in our observations with lines only up to J=3–2 .

5. Based on the modeling results on three barred galaxy centers (including NGC 3351), we find a strong, positive α_CO dependence with CO optical depth (τ_CO) that is responsible for ~80% of the changes in α_CO. The rest of the α_CO variation is driven by T_k, which varies inversely with α_CO and can explain the α_CO variation in local regions where the α_CO and τ_CO trends do not match. This suggests that emissivity-related terms are critical in driving α_CO in barred galaxy centers, and that optical depth is likely a more dominant driver of

$\alpha_{\rm CO}$ than gas temperature in this regime.

6. The observed ^{12}CO/^{13}CO 2–1 ratio and line width generally trace the $\tau_{\rm CO}$ variation inversely in all three galaxy centers. With the tight correlation seen in $\alpha_{\rm CO}$ and $\tau_{\rm CO}$, this indicates that both the line ratio and line width can be good observational tracers for predicting $\alpha_{\rm CO}$ variations in galaxy centers, where optical depth effects are dominant. We find the velocity dispersion in the centers of the barred galaxies studied here is higher than the typical values in galaxy disks or non-barred centers by a factor of 3–5, which may explain the overall lower-than-Galactic disk $\alpha_{\rm CO}$.

7. We have tested current $\alpha_{\rm CO}$ prescriptions based on observations and simulations. The Bolatto et al. (2013) prescription matches our average $\alpha_{\rm CO}$ values across the three galaxy centers, given the high total surface density of gas and stars. On the other hand, current simulation-based prescriptions do not probe similar physical conditions to our galaxy centers, and their extrapolation into this regime tends to overpredict $\alpha_{\rm CO}$. Future simulations that capture gas inflows and local turbulence have the potential to provide better $\alpha_{\rm CO}$ predictions for more extreme environments such as in galaxy centers or (U)LIRGs.

8. We also test our multi-line modeling by varying input combinations of observed molecular lines and comparing the solutions with those from modeling all six lines (i.e., CO 1–0 and 2–1, ^{13}CO 2–1 and 3–2, and C^{18}O 2–1 and 3–2). Combining the results of three galaxy centers, we find that CO 2–1, ^{13}CO 2–1, and ^{13}CO 3–2 are the most essential constraints that lead to the six-line solutions, while CO 1–0 also plays a significant role in constraining the CO column density per line width ($N_{\rm CO}/\Delta v$). The addition of both C^{18}O lines is not crucial as they often duplicate the constraints provided by the ^{13}CO lines. However, the well-determined $X_{13/18}$ abundances derived from the C^{18}O lines can be useful information in particular when the $X_{12/13}$ solutions are uncertain.

In general, our results suggest that CO optical depth is the dominant driver for

α_{CO} variations in the central kpc of barred galaxy centers, which can cover a compact nucleus and its surrounding bar lanes or inner spiral arms. To the second order, the increase/decrease of gas temperature in local regions can further lower/raise the α_{CO} values. The lower-than-Galactic disk α_{CO} in these barred centers can be explained by the overall enhanced velocity dispersion that lowers the opacity. As we find the CO/^{13}CO 2–1 ratio and CO line width mainly reflecting the changes of CO optical depth, these observables may be useful in predicting α_{CO} variation in other galaxy centers or similar environments.

3.7 Acknowledgements

We thank the referee for insightful comments that helped improve the manuscript. Y.-H.T. and K.S. acknowledge funding support from NRAO Student Observing Support Grant SOSPADA-012 and from the National Science Foundation (NSF) under grant No. 2108081. J.S. acknowledges support by the Natural Sciences and Engineering Research Council of Canada (NSERC) through a Canadian Institute for Theoretical Astrophysics (CITA) National Fellowship. HAP acknowledges support by the National Science and Technology Council of Taiwan under grant 110-2112-M-032-020-MY3. MQ acknowledges support from the Spanish grant PID2019-106027GA-C44, funded by MCIN/AEI/10.13039/501100011033. AU acknowledges support from the Spanish grants PGC2018-094671-B-I00, funded by MCIN/AEI/10.13039/501100011033 and by "ERDF A way of making Europe", and PID2019-108765GB-I00, funded by MCIN/AEI/10.13039/501100011033. RSK and SCOG acknowledge support from the Deutsche Forschungsgemeinschaft (DFG) in the Collaborative Research Centre (SFB 881, ID 138713538) "The Milky Way System" (subprojects A1, B1, B2, and B8) and from the Heidelberg Cluster of Excellence (EXC 2181, ID 390900948) "STRUCTURES", funded by the German Excellence Strategy. RSK also thanks for funding form the European Research Council in the ERC Synergy Grant "ECOGAL" (ID 855130). RSK and SCOG also benefit from computing resources provided by the State of Baden-Württemberg through bwHPC and DFG through grant INST 35/1134-1 FUGG, and from the data storage facility SDS@hd supported through grant INST 35/1314-1 FUGG. FB acknowledges funding from the European Research Council (ERC) under the European Union's Horizon 2020 research and innovation programme (grant agreement No.726384/Empire). ES acknowledges funding from the European Research Council (ERC) under the European Union's Horizon 2020 research and innovation programme (grant agreement No. 694343). MCS acknowledges financial support from the Royal Society (URF\R1\221118).

This work was carried out as part of the PHANGS collaboration. This paper makes use of the following ALMA data:
ADS/JAO.ALMA#2013.1.00885.S,
ADS/JAO.ALMA#2015.1.00956.S,
ADS/JAO.ALMA#2015.1.00978.S,
ADS/JAO.ALMA#2016.1.00972.S.
ALMA is a partnership of ESO (representing its member states), NSF (USA), and NINS (Japan), together with NRC (Canada), NSC and ASIAA (Taiwan), and KASI (Republic of Korea), in cooperation with the Republic of Chile. The Joint ALMA Observatory is operated by ESO, AUI/NRAO, and NAOJ. The National Radio Astronomy Observatory is a facility of the National Science Foundation operated under cooperative agreement by Associated Universities, Inc.

We acknowledge the usage of NASA's Astrophysics Data System (http://www.adsabs.harvard.edu) and `ds9`, a tool for data visualization supported by the Chandra X-ray Science Center (CXC) and the High Energy Astrophysics Science Archive Center (HEASARC) with support from the JWST Mission office at the Space Telescope Science Institute for 3D visualization.

*Facilities:*ALMA

Software:`CASA` (CASA Team et al., 2022), `ds9` (Smithsonian Astrophysical Observatory, 2000; Joye and Mandel, 2003), `matplotlib` (Hunter, 2007), `numpy` (Harris et al., 2020), `scipy` (Virtanen et al., 2020), `astropy` (Astropy Collaboration et al., 2013; Astropy

Collaboration et al., 2018), `RADEX` (van der Tak et al., 2007), `corner` (Foreman-Mackey, 2016)

* * *

This chapter, in full, is a reprint of the material as it appears in "The Physical Drivers and Observational Tracers of CO-to-H_2 Conversion Factor Variations in Nearby Barred Galaxy Centers" by Yu-Hsuan Teng, Karin M. Sandstrom, Jiayi Sun, Munan Gong, Alberto D. Bolatto, I-Da Chiang, Adam K. Leroy, Antonio Usero, Simon C. O. Glover, Ralf S. Klessen, Daizhong Liu, Miguel Querejeta, Eva Schinnerer, Frank Bigiel, Yixian Cao, M ´elanie Chevance, Cosima Eibensteiner, Kathryn Grasha, Frank P. Israel, Eric J. Murphy, Lukas Neumann, Hsi-An Pan, Francesca Pinna, Mattia C. Sormani, J. D. T. Smith, Fabian Walter, and Thomas G. Williams, which was published in The Astrophysical Journal in 2023. The dissertation author was the primary investigator and author of this paper.

Appendices

3.A Effects of Multiple Velocity Components

While our modeling and analysis assume one-component gas structure along each sightline, it is likely that a few regions have multi-component gas along the same sightlines. To investigate whether there is multi-component gas present, we check each individual spectrum in the cube.

By inspecting the spectra of all the pixels included in our analysis, we find that ~8% (28%) of sightlines in NGC 4321 (NGC 3627) shows double-peaked line profiles. The higher fraction of multi-component sightlines in NGC 3627 may be partially due to the higher inclination of NGC 3627 compared to NGC 4321, and it is also consistent with previous studies which identified more overlapping giant molecular clouds/associations in the center of NGC 3627 than in NGC 4321 (Pan and Kuno, 2017; Rosolowsky et al., 2021). In Figure 3.21, we present an example of double-peaked spectra in CO 2–1 and ^{13}CO 2–1 and show how their intensity ratio varies with velocity. The lower/upper limit of the velocity range in the right panels of Figure 3.21 corresponds to the FWHM line width of the lower/higher velocity component.

For NGC 4321, multi-component sightlines are mostly found around the middle along both inner arms at similar declinations to the nucleus. As shown by the top-right panel of Figure 3.21, we find that the double-peaked spectra in NGC 4321 generally have consistent CO/^{13}CO ratios in both components, and the ratio is also similar to the integrated line ratio observed from the moment 0 map. In this case, the emissivity properties of both components would agree with what we derived using the single-component model, even if there were separate components along the sightline.

On the other hand, double/multi-peaked line profiles are scattered in both the inner and outer arms of NGC 3627, and the CO/^{13}CO ratios can vary between components along the same sightlines. The bottom row of Figure 3.21 presents an extreme case found in NGC 3627 where the two spectral peaks clearly show opposite trends in their relative intensities. We find that the CO/^{13}CO ratio in this case can differ by almost a factor of two between both components, and the integrated line ratio only agrees with the dominant component, which has a broader line width. This implies that the optical depth and $\alpha_{\rm CO}$ values derived from our one-component modeling could be biased toward one of the components in such regions, and the observed line width of that component would also be overestimated (e.g., $\sim$50 km s^{-1} instead of 67 km s^{-1} for the showcased pixel in NGC 3627).

With the extreme case in NGC 3627, we have tested how the results would change by modeling the two components separately using the integrated intensity per Gaussian component for all six lines. We find that the component with a broader line width (which dominates the integrated intensity) has similar gas conditions ($<$ 0.2 dex difference in all the modeled parameters) and the same $\alpha_{\rm CO}$ as what we obtained with the one-component modeling. On the contrary, the other component shows a different gas condition with higher temperature and lower density, optical depth, and $X_{12/13}$ abundance ratio, which altogether leads to the lower CO/^{13}CO line ratio seen in the bottom-right panel of Figure 3.21. We note that the relations in Figure 3.19 and Equations 3.5 and 3.6 would remain the same even if the difference in CO/^{13}CO line ratio (a factor of two at most) solely reflects optical depth changes, as the scatter in those $\alpha_{\rm CO}$ correlations are larger than a factor of two. In addition, the scatter of the line width correlation could even be reduced, since many of the high Δv points (from NGC 3627) seen in Figure 3.19(b) were overestimated due to the one-component assumption.

To summarize, our one-component assumption throughout this work should only impact our parameter estimation in a minority of regions. We find that the center of NGC 4321 is dominated by single velocity components, and the impact on radiative transfer calculation is likely small even in the few sightlines with evidence of multiple velocity components. For the center of NGC 3627, the majority of sightlines also show single-component spectra, while our one-component modeling could be biased toward one of the components in some multi-component sightlines. A more comprehensive modeling that covers different components along the same sightline would require a careful channel-by-channel analysis across all the regions. For NGC 3627, this can be done in future works with the support of SCOUSE (Henshaw et al., 2016) and existing GMC catalogues (e.g., Rosolowsky et al., 2021).

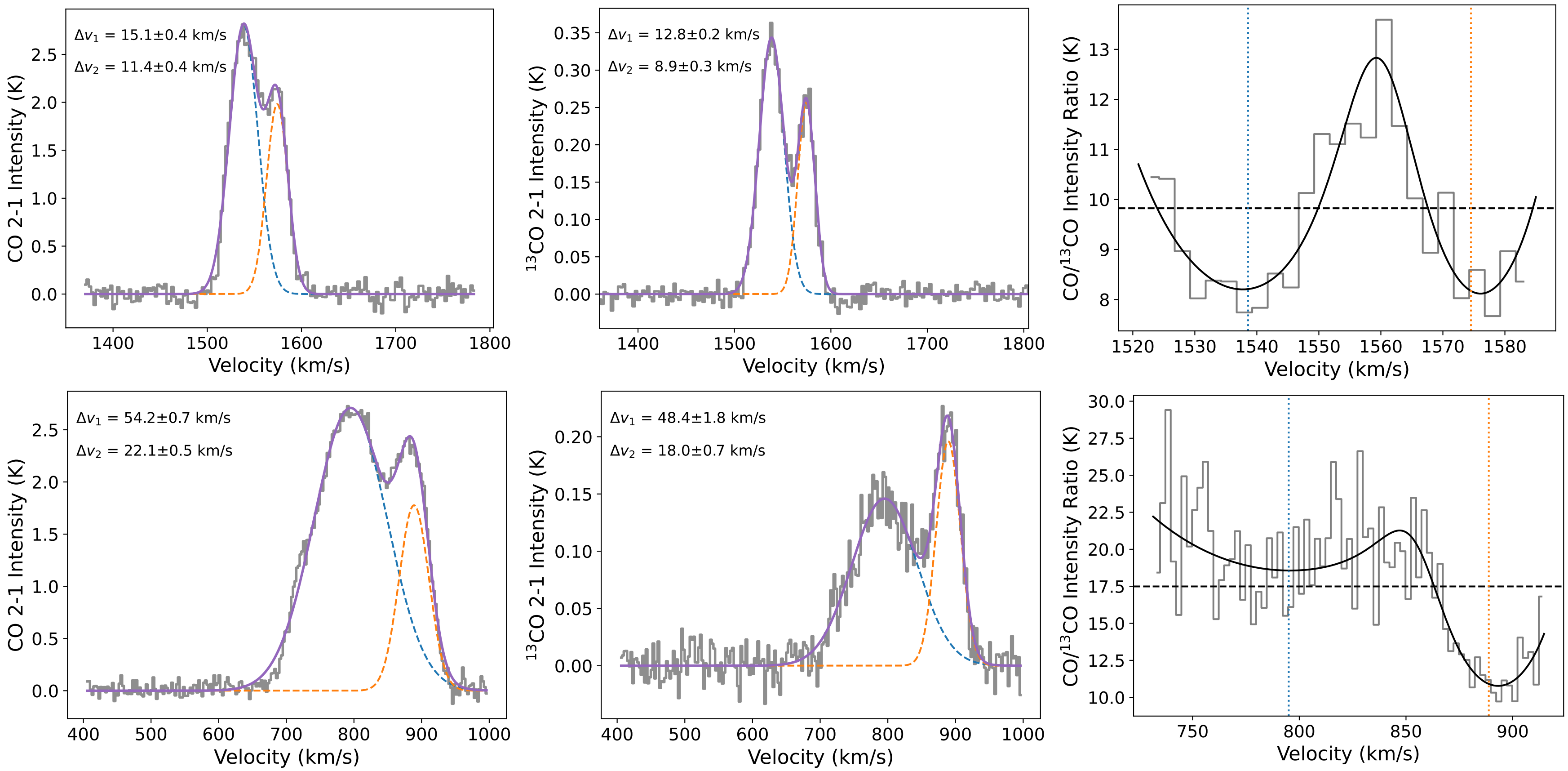

Figure 3.21. Example of double-peaked line profiles in CO 2–1 (left column) and ^{13}CO 2–1 (middle column), together with their intensity ratios (right column). The top and bottom rows showcase pixels from the western inner arm of NGC 4321 and the southern inner arm of NGC 3627, respectively. The line profiles can be well described by the sum (solid, purple lines) of two Gaussian functions (dashed lines), and the fitted line widths for both components are shown in the upper left corners. In the right column, the horizontal dashed line represents the integrated line intensity ratio, and the vertical dotted lines label the peak velocities of the two Gaussian fits. The bottom row demonstrates an extreme case with opposite trends of relative intensities in the two components, which leads to almost a factor of two difference in the CO/^{13}CO line ratio.

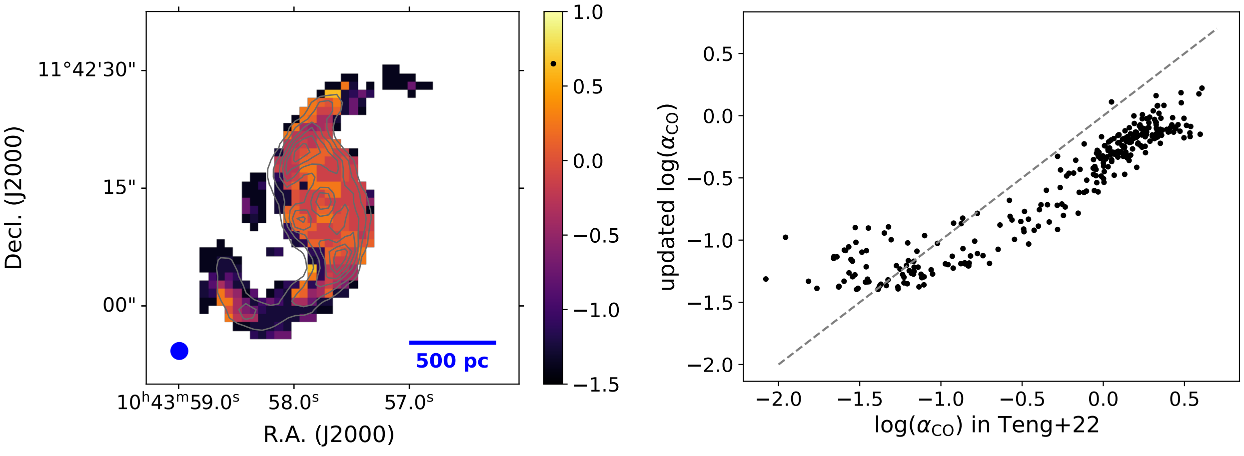

(a) (b)

Figure 3.22. (a) The updated 1DMax α_{CO} map of NGC 3351 as a direct comparison to Figure 10(a) in Teng et al. (2022). The black dot on the color bar indicates the MW disk α_{CO} value, and the contours represent CO 1–0 integrated intensity. The α_{CO} distribution is qualitatively unchanged. (b) Relation of the updated α_{CO} with those in Teng et al. (2022). The dashed line indicates equality. The α_{CO} values are overall lowered by a factor of two to three.

3.B Updates of the NGC 3351 α_{CO} Values

As mentioned in Section 3.4.3, the α_{CO} solutions for NGC 3351 in Teng et al. (2022) should be a factor of 2–3 lower if consistent line widths were adopted when computing the α_{CO} model grid. This factor of 2–3 overestimation comes from the observed line width in NGC 3351 being overall 2–3 times higher than the FWHM line width of 15 km s^{-1} assumed in RADEX. Here we recalculate and update the α_{CO} values for NGC 3351 which are used in this work for a self-consistent comparison. We emphasize that this does not change the qualitative results and main findings in Teng et al. (2022).

Figure 3.22(a) presents the updated 1DMax α_{CO} map of NGC 3351. The color bar and scale are set to be the same as Teng et al. (2022, Figure 10a) for easier comparison. We find no major change in α_{CO} in the inflow regions as their observed FWHM line width is close to the RADEX-assumed 15 km s^{-1}. It is also clear that α_{CO} in the inflow regions remain substantially lower than the central nuclear ring, even though α_{CO} within the nuclear ring becomes 2–3 times lower. The pixel-by-pixel relation between the pre- and post-updated

$\alpha_{\rm CO}$ values is shown in Figure 3.22(a).

We also report changes in the intensity-weighted mean $\alpha_{\rm CO}$ over the entire kpc region ($\langle\alpha_{\rm CO}\rangle_{\rm kpc}$), as well as the spectrally-stacked $\alpha_{\rm CO}$ value of the inflow regions. After correction, $\langle\alpha_{\rm CO}\rangle_{\rm kpc} = 0.75 \pm 0.04$ $M_\odot$ (K km s^{-1} pc^2)$^{-1}$, which is 2.4 times lower than 1.79 ± 0.10 in Teng et al. (2022). In addition, the spectrally-stacked $\alpha_{\rm CO}$ over the inflow arms based on the best-fit solution becomes 0.08 $M_\odot$ (K km s^{-1} pc^2)$^{-1}$, which is still within the range of 0.01–0.1 $M_\odot$ (K km s^{-1} pc^2)$^{-1}$ reported in Teng et al. (2022).

3.C Additional Figures on the Data and Modeling

3.C.1 Maps of Moment 1 and Effective Line Width

While this work do not focus on the molecular gas dynamics, we provide here the moment 1 and effective line width maps toward our targets as a reference for future studies. Figures 3.23 and 3.24 show the CO 2–1 maps for NGC 4321 and NGC 3627, respectively. The moment 1 maps for both galaxies reveal clear signature of counter-clockwise gas rotation, and the effective line widths are highest in the nuclei possibly due to unresolved gas motion within the central beam.

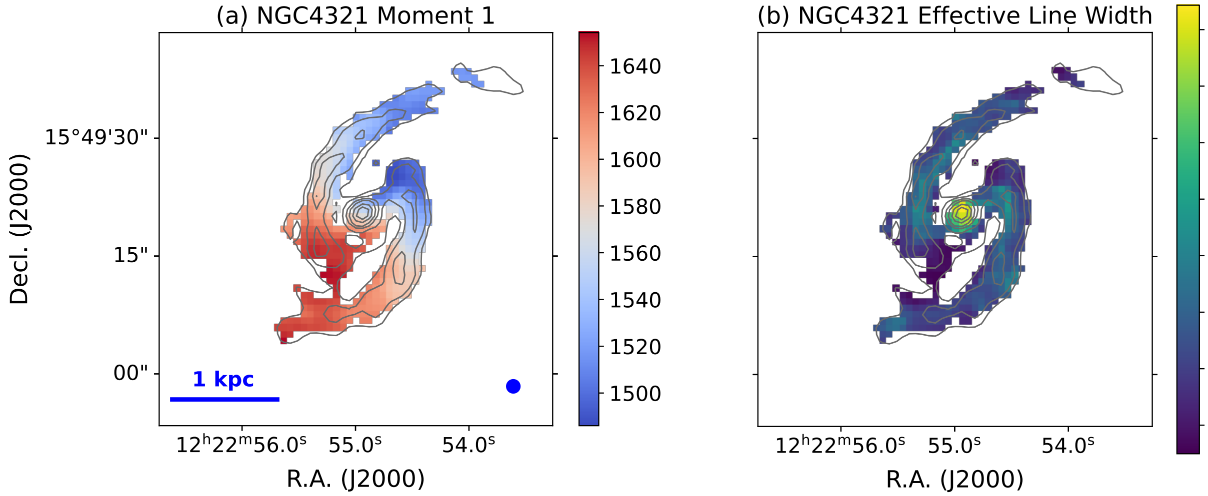

Figure 3.23. Maps of the CO 2–1 (a) moment 1 and (b) effective line width for NGC 4321, both in units of km s^{-1}.

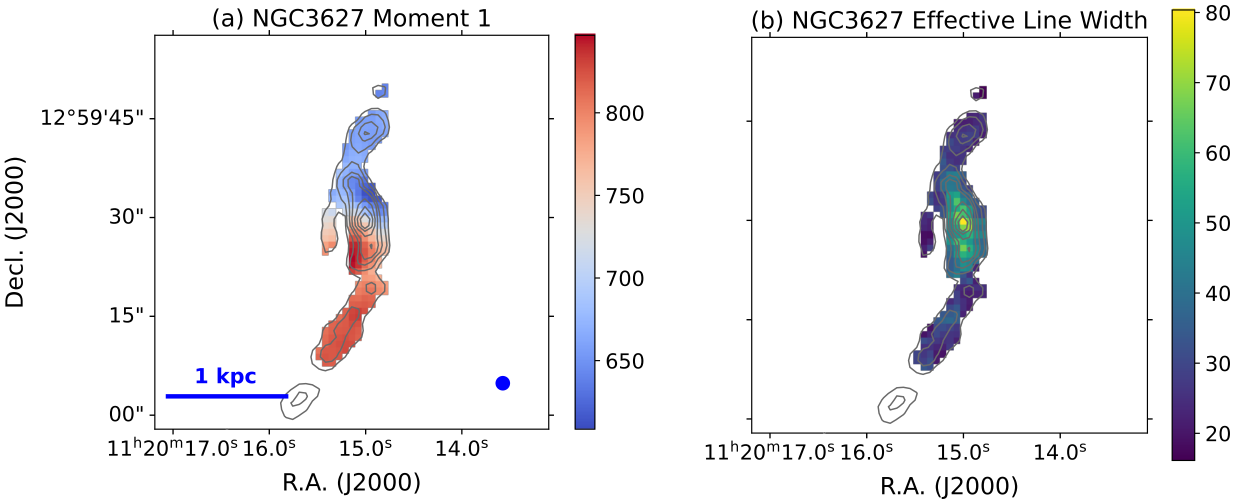

Figure 3.24. Same as Figure 3.23 but for NGC 3627.

3.C.2 Line Constraints and Modeled Probability Distributions

Besides the line constraints and modeled PDFs for the NGC 4321 nucleus presented in Figures 3.7 and 3.8, here we include additional figures for other representative regions. Figure 3.25 shows the line constraints and best-fit solutions for the nucleus and inner arms of NGC 3627. Figures 3.26, 3.27, and 3.28 demonstrate the PDFs for the inner arms of NGC 4321, the nucleus of NGC 3627, and the inner arms of NGC 3627, respectively.

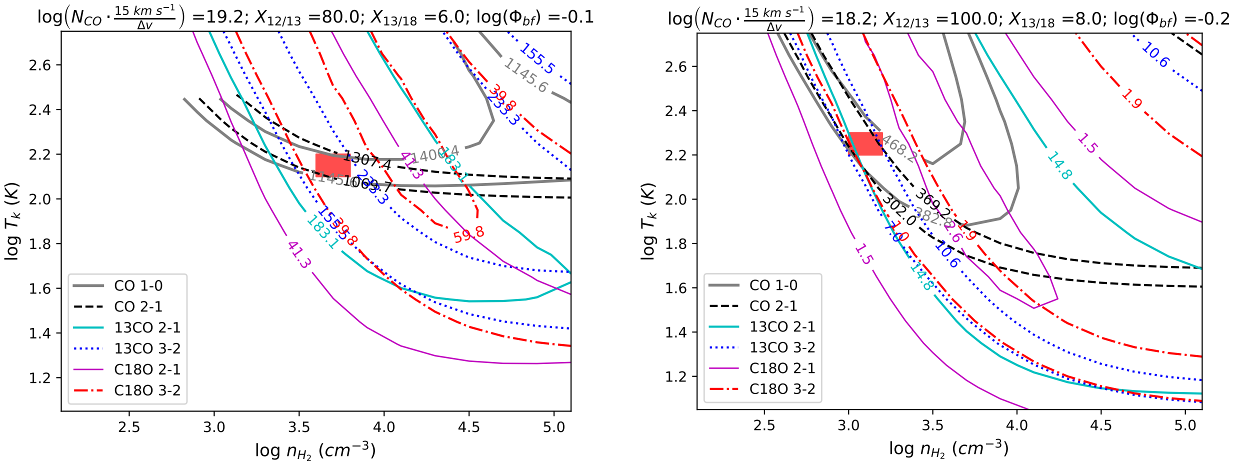

(a)

(b)

Figure 3.25. Same as Figure 3.7 but for (a) the central pixel of NGC 3627 and (b) a pixel in the northern inner arm of NGC 3627. The low-density and high-temperature part in panel (a) is excluded due to violation of the $\ell_{\rm los} < 200$ pc constraint.

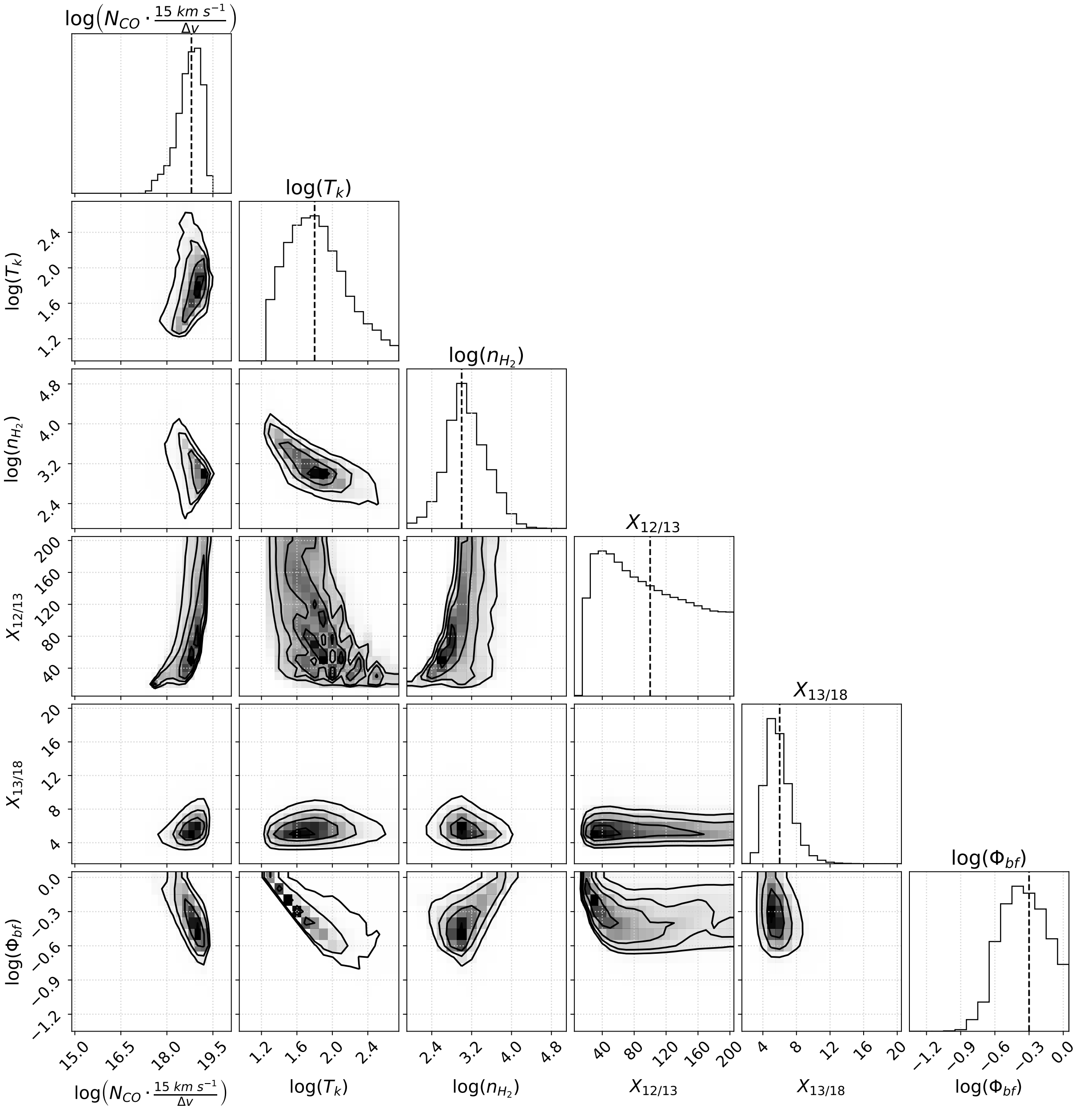

Figure 3.26. Marginalized 1D and 2D likelihood distributions of a pixel in the northern arm of NGC 4321, which is also the same pixel as shown in Figure 3.7(b). See the caption of Figure 3.8 for more information.

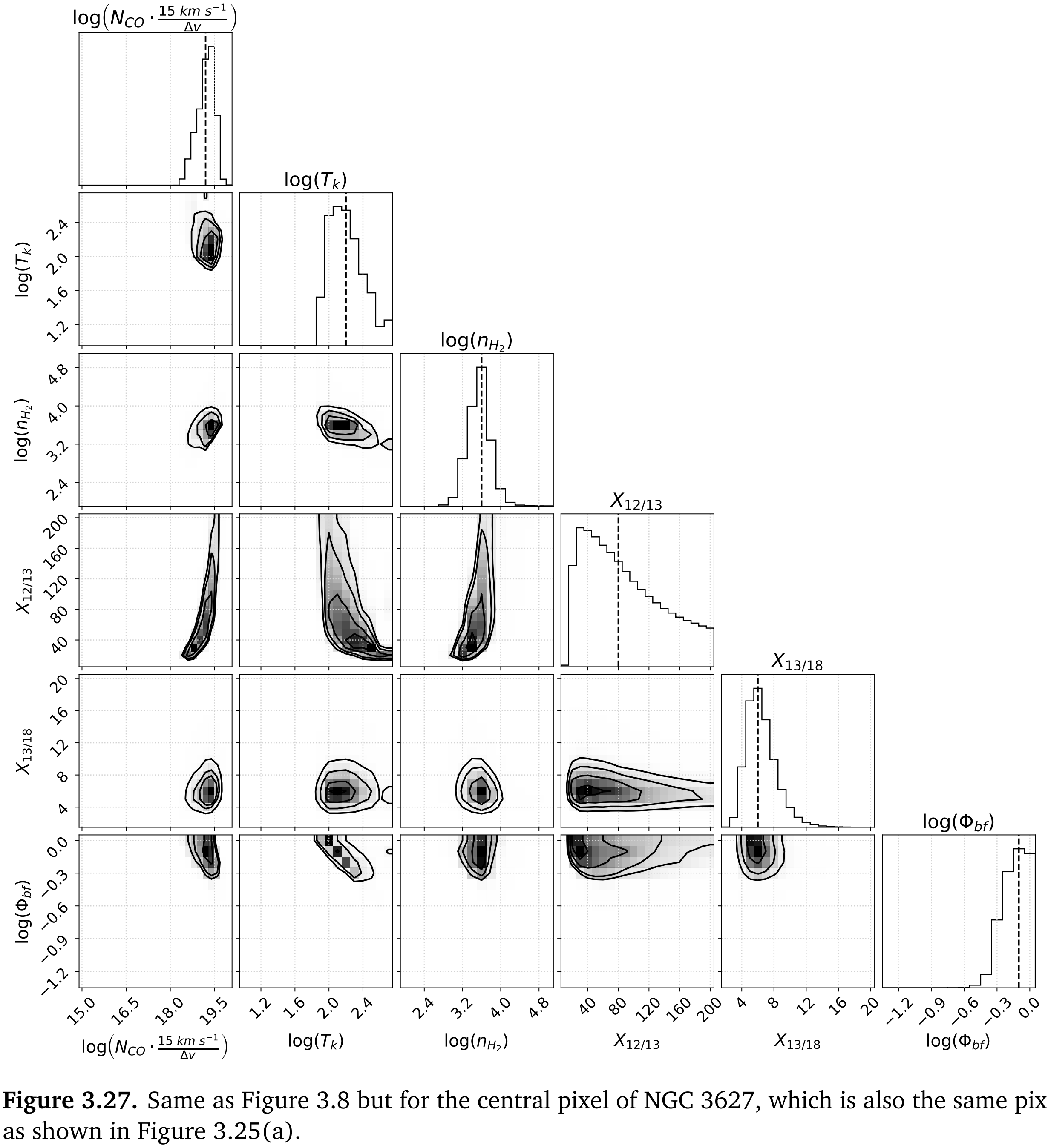

Figure 3.27. Same as Figure 3.8 but for the central pixel of NGC 3627, which is also the same pixel as shown in Figure 3.25(a).

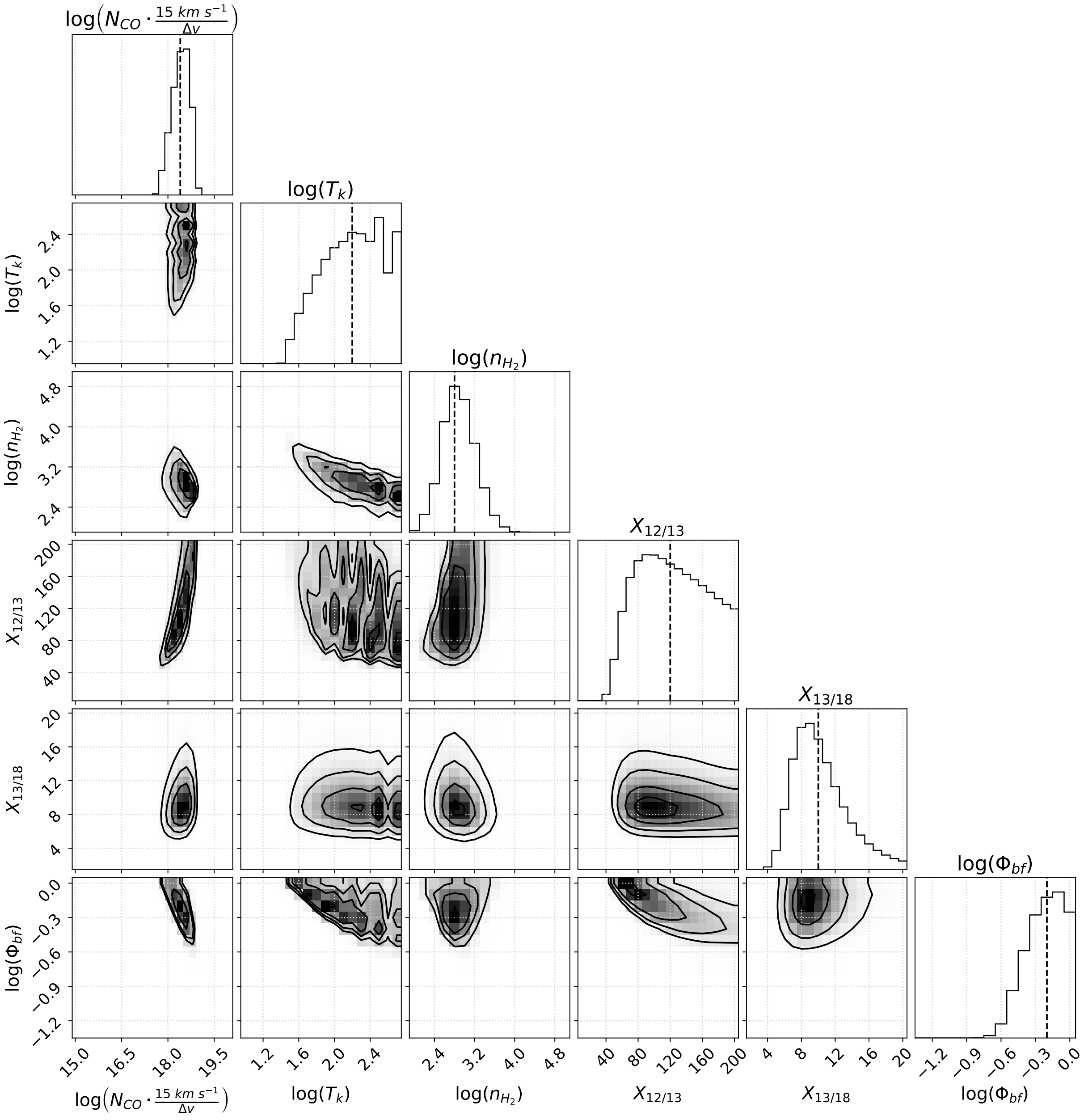

Figure 3.28. Same as Figure 3.8 but for a pixel in the northern inner arm of NGC 3627, which is also the same pixel as shown in Figure 3.25(b).

Chapter 4

Star Formation Efficiency in Nearby Galaxies Revealed with a New α_{CO} Prescription

Abstract

Determining how galactic environment, especially the high gas densities and complex dynamics in bar-fed galaxy centers, alters the star formation efficiency (SFE) of molecular gas is critical to understanding galaxy evolution. However, these same physical or dynamical effects also alter the emissivity properties of CO, leading to variations in the CO-to-H_2 conversion factor (α_{CO}) that impact the assessment of the gas column densities and thus of the SFE. To address such issues, we investigate the dependence of α_{CO} on local CO velocity dispersion at 150 pc scales using a new set of dust-based α_{CO} measurements, and propose a new α_{CO} prescription that accounts for CO emissivity variations across galaxies. Based on this prescription, we estimate the SFE in a sample of 65 galaxies from the PHANGS–ALMA survey. We find increasing SFE towards high surface density regions like galaxy centers, while using a constant or metallicity-based α_{CO} results in a more homogeneous SFE throughout the centers and disks. Our prescription further reveals a mean molecular gas depletion time of 700 Myr in the centers of barred galaxies,

which is overall 3–4 times shorter than in non-barred galaxy centers or the disks. Across the galaxy disks, the depletion time is consistently around 2–3 Gyr regardless of the choice of α_{CO} prescription. All together, our results suggest that the high level of star formation activity in barred centers is not simply due to an increased amount of molecular gas but also an enhanced SFE compared to non-barred centers or disk regions.

4.1 Introduction

Star formation in galaxies is governed by the amount of molecular gas and the efficiency with which that gas is converted into stars. To understand the evolutionary process of star formation activity within galaxies, it is critical to measure the molecular gas star formation efficiency (SFE; defined as the ratio between star formation rate, SFR, and molecular gas mass, M_{mol}), or molecular gas depletion time ($t_{\mathrm{dep}} = 1/\mathrm{SFE}$) (see review by Saintonge and Catinella, 2022). Previous studies have found that SFR and molecular gas surface densities are highly correlated (i.e., the molecular Kennicutt-Schmidt relation, or mKS relation; Kennicutt, 1998) and that t_{dep} is usually at 1–4 Gyr across nearby star-forming galaxies (e.g., Bigiel et al., 2008; Leroy et al., 2008; Saintonge et al., 2011; Schruba et al., 2011; Utomo et al., 2017; Sun et al., 2023). Despite the minor variation in general, t_{dep} is also found to vary systematically with local and global host galaxy properties, which could be driven by environmental and/or dynamical effects from e.g., metallicity, molecular cloud structure, bar instabilities, active galactic nuclei, or galaxy interactions (Saintonge et al., 2011; Saintonge et al., 2012; Schruba et al., 2019; Ellison et al., 2021a; Ellison et al., 2021b; Querejeta et al., 2021; Lu et al., 2022; Villanueva et al., 2022; Jiménez-Donaire et al., 2023; Maeda et al., 2023).

The assessment of molecular gas SFE relies heavily on the CO-to-H_2 conversion factor (α_{CO})[1]:

$$\alpha_{\mathrm{CO}} = \frac{M_{\mathrm{mol}}}{L'_{\mathrm{CO(1-0)}}} = \frac{\Sigma_{\mathrm{mol}}}{I_{\mathrm{CO(1-0)}}} \left[\frac{\mathrm{M}_\odot}{\mathrm{K\ km\ s^{-1}\ pc^2}}\right] , \tag{4.1}$$

where M_{mol} (Σ_{mol}) is the total molecular gas mass (surface density) and $L'_{\mathrm{CO(1-0)}}$ ($I_{\mathrm{CO(1-0)}}$) is the line luminosity (intensity) of CO J=1–0. α_{CO} is known to vary with molecular gas conditions such as density, temperature, and dynamical state (see review by Bolatto et al., 2013; hereafter B13), which are the same conditions that could also alter the intrinsic SFE of the molecular gas. Due to the lack of a widely-agreed prescription that can accurately predict α_{CO}, many studies could only assume a constant α_{CO} referencing the Milky Way (MW) disk average (e.g., B13) to convert CO observations to molecular gas mass. This has made α_{CO} variation one of the dominant sources of uncertainty in current molecular gas and SFE studies (see discussions in Ellison et al., 2020b; Maeda et al., 2023; Sun et al., 2023).

The impacts of α_{CO} variations on both SFE and cloud evolutionary timescale estimates are particularly critical in galaxy centers (Leroy et al., 2013; Utomo et al., 2017; Muraoka et al., 2019; Ellison et al., 2020b; Pessa et al., 2021; Maeda et al., 2023; Sun et al., 2023). In those environments, α_{CO} can be 5–15 times lower than the Galactic disk value (Ackermann et al., 2012a; Sandstrom et al., 2013; Israel, 2020; Teng et al., 2022; Teng et al., 2023; den Brok et al., 2023). The lower α_{CO} in galaxy centers is likely driven by CO emissivity variations due to higher excitation and/or stronger dynamical effects such as turbulence or inflowing gas (Narayanan et al., 2012; Papadopoulos et al., 2012a; Bolatto et al., 2013; Gong et al., 2020; Teng et al., 2023). These effects may also explain the low α_{CO} seen in mergers or (ultra-)luminous infrared galaxies (U/LIRGs) (Downes and Solomon, 1998; Krieger et al., 2017; Sliwa et al., 2017; Cicone et al., 2018; Herrero-Illana et al., 2019).

Reducing the uncertainty in molecular gas and SFE studies, and thereby improving our understanding in star formation and galaxy evolution, requires a robust α_{CO} prescription

---

[1] α_{CO} is defined for the CO $J = 1-0$ line in most literature, but it can also be evaluated for other transitions. In this work, when we refer to α_{CO}, we mean $\alpha_{\mathrm{CO(1-0)}}$ unless otherwise specified.

that can be systematically applied to large samples of galaxies with diverse environments. Recent studies have proposed various types of α_{CO} prescription depending on metallicity, stellar mass surface density, SFR, SFE, and/or CO line-related properties (Genzel et al., 2012; Narayanan et al., 2012; Bolatto et al., 2013; Hunt et al., 2015; Amorín et al., 2016; Accurso et al., 2017a; Renaud et al., 2019; Gong et al., 2020; Madden et al., 2020; Ramambason et al., 2023). However, establishing a reliable α_{CO} calibration remains a challenge because it requires α_{CO} measurements covering a sufficient sample of galaxies spanning a broad range of molecular gas physical and dynamical conditions, and the two most realistic ways to measure α_{CO} in nearby galaxies are via dust emission (which is typically restricted to kpc resolutions; Israel 1997; Leroy et al. 2011; Sandstrom et al. 2013; Schruba et al. 2017; Pitts and Barnes 2021; den Brok et al. 2023; Yasuda et al. 2023; Chiang et al. 2024) or multi-CO isotopologue observations (which is expensive at cloud scales; Sliwa et al. 2017; Cormier et al. 2018; Israel 2020; Sharda et al. 2022; Teng et al. 2022; Teng et al. 2023).

Thanks to the high resolution and sensitivity of the Atacama Large Millimeter/submillimeter Array (ALMA), CO (isotopologue) observations are now routinely possible at cloud scales in nearby galaxies (e.g., Leroy et al., 2021b; Davis et al., 2022; Koda et al., 2023; Williams et al., 2023). In particular, recent studies modeling multi-CO isotopologues in nearby galaxy centers have revealed that CO opacity is the dominant driver of α_{CO} variations (Israel, 2020; Teng et al., 2022; Teng et al., 2023). This strong dependence of α_{CO} on CO opacity further leads to a clear anti-correlation between α_{CO} and the observed line width at ~100 pc scales in barred galaxy centers (Teng et al., 2023; hereafter T23).

Motivated by these latest measurements of α_{CO}, we will test if the correlation found in T23 also applies to the 12 galaxies (labeled with * in Table 4.1, including 8 barred and 4 non-barred) which have dust-inferred α_{CO} values at kpc scales (from Chiang et al. 2024; hereafter C24) and molecular gas velocity dispersion measured at 150-pc scales (from the PHANGS–ALMA survey; Leroy et al., 2021b; Sun et al., 2022). The results of this comparison lead us to a new $\alpha_{\rm CO}$ prescription capturing CO emissivity effects in star-forming galaxies. In this paper, we present this prescription, discuss its physical implications, and study its impact on SFE across a sizable sample of galaxy centers and disks with diverse properties.

4.2 Data and Measurements

4.2.1 PHANGS Datasets

Our analysis is based on various molecular gas and star formation properties, leveraging a database developed by Sun et al. (2022) which assembled multi-wavelength measurements of 80 galaxies from the PHANGS–ALMA survey (Leroy et al., 2021b). From this database, we extract multiple physical quantities in matched hexagonal apertures with fixed sizes of 1.5 kpc. The quantities used in this work include: intensity-weighted mean molecular gas velocity dispersion measured at 150-pc scale ($\langle \Delta v \rangle_{\rm 150pc}$), area-weighted mean CO(2–1) line integrated intensity ($I_{\rm CO(2-1)}$), stellar mass surface density ($\Sigma_{\rm star}$), SFR surface density ($\Sigma_{\rm SFR}$), and gas-phase metallicity (Z', normalized to the solar value [$12+\log({\rm O/H})_\odot = 8.69$] and calibrated based on Pettini and Pagel 2004). All these quantities are corrected for the effects of galaxy inclination and data sensitivity limits (see Sun et al. 2022 for more details).

To further explore trends in galaxies with or without stellar bars, we adopt the classification of stellar bars for PHANGS galaxies (Querejeta et al., 2021). Table 4.1 lists the 65 galaxies included in our analysis, which is the overlap between Querejeta et al. (2021) and Sun et al. (2022). This sample from PHANGS has high-resolution CO(2–1) data with beam sizes of 150 pc or smaller. Columns (6–10) in Table 4.1 show the measurements extracted from Sun et al. (2022) for the central 1.5 kpc regions of those galaxies.

Table 4.1. Galaxy Sample and Properties in the Central 1.5 kpc Regions

Galaxy (1)	Bar (2)	Dist. [Mpc] (3)	Incl. [deg] (4)	P.A. [deg] (5)	Z' [$Z_\odot$] (6)	$\log(\Sigma_{\rm SFR})$ $\left[\frac{M_\odot}{\rm yr\ kpc^2}\right]$ (7)	$I_{\rm CO(2-1)}$ [K km s^{-1}] (8)	$\log(\Sigma_{\rm star})$ [$M_\odot$ pc^{-2}] (9)	$\langle\Delta v\rangle_{\rm 150pc}$ [km s^{-1}] (10)	$\log(\alpha_{\rm CO}^{\rm Eq.4.2})$ $\left[\frac{M_\odot\ s}{\rm K\ km\ pc^2}\right]$ (11)	$\log(t_{\rm dep})$ [yr] (12)
IC1954	1	12.8	57.1	63.4	1.10	-1.67	7.5	2.51	7.1	0.36	9.08
IC5273	1	14.2	52.0	234.1	1.12	-1.59	4.7	2.48	7.4	0.34	8.78
NGC0253*	1	3.7	75.0	52.5	1.33	0.3166	198.2	990.2	28.5	-0.15	8.88
NGC0628*	0	9.8	8.9	20.7	1.29	-1.82	6.3	3.03	5.4	0.45	9.26
NGC0685	1	19.9	23.0	100.9	1.23	-2.15	2.8	2.42	6.8	0.37	9.15
NGC1087	1	15.8	42.9	359.1	1.19	-1.12	24.7	2.68	13.4	0.12	8.82
NGC1097	1	13.6	48.6	122.4	1.34	-0.29	196.0	3.61	33.1	-0.20	8.57
NGC1300	1	19.0	31.8	278.0	1.33	-1.57	44.6	3.25	23.2	-0.07	9.33
NGC1317	1	19.1	23.2	221.5	1.33	-1.45	25.2	3.64	18.0	0.02	9.06
NGC1365	1	19.6	55.4	201.1	1.36	0.04	462.4	3.80	25.6	-0.11	8.70
NGC1385	0	17.2	44.0	181.3	1.21	-1.00	15.0	2.78	9.5	0.25	8.60
NGC1433	1	18.6	28.6	199.7	1.35	-1.46	44.6	3.63	17.3	0.03	9.33
NGC1511	0	15.3	72.7	297.0	1.18	-1.17	12.4	2.60	7.5	0.33	8.79
NGC1512	1	18.8	42.5	261.9	1.34	-1.36	31.9	3.41	11.3	0.19	9.24

Continued on next page

Table 4.1. Galaxy Sample and Properties in the Central 1.5 kpc Regions

Galaxy (1)	Bar (2)	Dist. [Mpc] (3)	Incl. [deg] (4)	P.A. [deg] (5)	Z' $[\mathrm{Z}_\odot]$ (6)	$\log(\Sigma_{\mathrm{SFR}})$ $\left[\frac{\mathrm{M}_\odot}{\mathrm{yr\ kpc}^2}\right]$ (7)	$I_{\mathrm{CO(2-1)}}$ $[\mathrm{K\ km\ s^{-1}}]$ (8)	$\log(\Sigma_{\mathrm{star}})$ $[\mathrm{M}_\odot\ \mathrm{pc}^{-2}]$ (9)	$\langle\Delta v\rangle_{150\mathrm{pc}}$ $[\mathrm{km\ s^{-1}}]$ (10)	$\log(\alpha_{\mathrm{CO}}^{\mathrm{Eq.4.2}})$ $\left[\frac{\mathrm{M}_\odot\ \mathrm{s}}{\mathrm{K\ km\ pc}^2}\right]$ (11)	$\log(t_{\mathrm{dep}})$ [yr] (12)
NGC1546	0	17.7	70.3	147.8	1.29	-1.52	45.0	3.08	7.9	0.31	9.67
NGC1559	1	19.4	65.4	244.5	1.29	-1.47	10.5	2.77	6.6	0.38	9.06
NGC1566	1	17.7	29.5	214.7	1.34	-0.97	55.7	3.63	28.7	-0.15	8.76
NGC1637	1	11.7	31.1	20.6	1.20	-0.82	12.2	2.57	22.8	-0.07	8.03
NGC1792	0	16.2	65.1	318.9	1.33	-1.35	52.0	3.08	10.7	0.21	9.46
NGC1809	0	20.0	57.6	138.2	1.14	-1.71	2.2	2.19	3.1	0.65	8.88
NGC2090	0	11.8	64.5	192.5	1.22	-2.19	4.5	2.79	4.2	0.54	9.57
NGC2283	1	13.7	43.7	-4.1	1.18	-1.93	3.0	2.31	5.1	0.47	9.07
NGC2566	1	23.4	48.5	312.0	1.34	-0.05	265.0	3.16	26.5	-0.12	8.53
NGC2835	1	12.2	41.3	1.0	1.21	-2.23	2.2	2.47	4.3	0.53	9.30
NGC2903	1	10.0	66.8	203.7	1.33	-0.81	55.8	3.15	19.7	-0.01	8.73
NGC2997	0	14.1	33.0	108.1	1.34	-0.95	68.5	3.21	16.2	0.06	9.03
NGC3059	1	20.2	29.4	-14.8	1.29	-0.84	23.1	2.68	11.4	0.18	8.58
NGC3137	0	16.4	70.3	-0.3	1.18	-2.53	3.0	2.19	3.2	0.64	9.85

Continued on next page

Table 4.1. Galaxy Sample and Properties in the Central 1.5 kpc Regions

Galaxy	Bar	Dist.	Incl.	P.A.	Z'	$\log(\Sigma_{\rm SFR})$	$I_{\rm CO(2-1)}$	$\log(\Sigma_{\rm star})$	$\langle\Delta v\rangle_{\rm 150pc}$	$\log(\alpha_{\rm CO}^{\rm Eq.4.2})$	$\log(t_{\rm dep})$
		[Mpc]	[deg]	[deg]	[$Z_\odot$]	$\left[\frac{\rm M_\odot}{\rm yr\ kpc^2}\right]$	[K km s^{-1}]	[M$_\odot$ pc^{-2}]	[km s^{-1}]	$\left[\frac{\rm M_\odot\ s}{\rm K\ km\ pc^2}\right]$	[yr]
(1)	(2)	(3)	(4)	(5)	(6)	(7)	(8)	(9)	(10)	(11)	(12)
NGC3351*	1	10.0	45.1	193.2	1.29	-0.71	34.4	3.18	19.2	-0.01	8.43
NGC3507	1	23.6	21.7	55.8	1.30	-1.57	17.3	3.16	23.4	-0.08	8.91
NGC3511	1	13.9	75.1	256.8	1.22	-1.94	17.2	2.50	6.6	0.38	9.74
NGC3521*	0	13.2	68.8	343.0	1.36	-1.66	14.8	3.50	6.7	0.37	9.40
NGC3596	0	11.3	25.1	78.4	1.10	-1.55	6.3	2.68	7.0	0.36	8.90
NGC3621	0	7.1	65.8	343.8	1.23	-1.86	8.4	2.66	5.2	0.46	9.44
NGC3626	1	20.0	46.6	165.2	1.31	-1.40	11.2	3.52	13.5	0.12	8.76
NGC3627*	1	11.3	57.3	173.1	1.35	-1.19	64.9	3.53	34.6	-0.22	8.98
NGC4254*	0	13.1	34.4	68.1	1.30	-1.10	35.7	3.27	10.3	0.22	9.06
NGC4293	1	15.8	65.0	48.3	1.31	-1.11	45.0	2.92	27.4	-0.13	8.82
NGC4298	0	14.9	59.2	313.9	1.22	-1.79	14.3	2.69	9.7	0.24	9.38
NGC4303	1	17.0	23.5	312.4	1.32	-0.83	70.8	3.52	16.9	0.04	8.91
NGC4321*	1	15.2	38.5	156.2	1.34	-0.78	101.0	3.35	19.5	-0.01	8.96
NGC4457	1	15.1	17.4	78.7	1.30	-1.15	38.7	3.69	29.0	-0.15	8.77

Continued on next page

Table 4.1. Galaxy Sample and Properties in the Central 1.5 kpc Regions

Galaxy	Bar	Dist. [Mpc]	Incl. [deg]	P.A. [deg]	Z' [$Z_\odot$]	$\log(\Sigma_{\rm SFR})$ $\left[\frac{M_\odot}{\rm yr\ kpc^2}\right]$	$I_{\rm CO(2-1)}$ [K km s^{-1}]	$\log(\Sigma_{\rm star})$ [$M_\odot$ pc^{-2}]	$\langle\Delta v\rangle_{\rm 150pc}$ [km s^{-1}]	$\log(\alpha_{\rm CO}^{\rm Eq.4.2})$ $\left[\frac{M_\odot\ \rm s}{\rm K\ km\ pc^2}\right]$	$\log(t_{\rm dep})$ [yr]
(1)	(2)	(3)	(4)	(5)	(6)	(7)	(8)	(9)	(10)	(11)	(12)
NGC4496A	1	14.9	53.8	51.1	1.04	-2.21	1.6	2.17	2.8	0.69	9.29
NGC4535	1	15.8	44.7	179.7	1.32	-1.03	43.1	2.78	20.1	-0.02	8.83
NGC4536*	1	16.2	66.0	305.6	1.30	-0.56	110.3	3.30	21.0	-0.04	8.76
NGC4540	1	15.8	28.7	12.8	1.14	-1.90	3.9	2.65	6.3	0.40	9.07
NGC4548	1	16.2	38.3	138.0	1.34	-1.96	9.7	3.38	24.8	-0.10	9.03
NGC4569*	1	15.8	70.0	18.0	1.35	-1.13	112.1	3.24	27.6	-0.14	9.23
NGC4571	0	14.9	32.7	217.5	1.23	-2.36	2.5	2.63	2.7	0.70	9.63
NGC4689*	0	15.0	38.7	164.1	1.26	-1.81	9.2	2.61	5.6	0.44	9.40
NGC4731	1	13.3	64.0	255.4	1.02	-1.97	1.6	1.99	5.1	0.47	8.85
NGC4781	1	11.3	59.0	290.0	1.09	-1.76	9.1	2.59	8.2	0.30	9.20
NGC4826	0	4.4	59.1	293.6	1.27	-1.43	27.9	3.26	21.8	-0.05	9.01
NGC4941*	1	15.0	53.4	202.2	1.25	-1.31	6.9	3.00	18.7	0.00	8.34
NGC4951	0	15.0	70.2	91.2	1.15	-1.77	10.0	2.67	11.4	0.18	9.14
NGC5042	0	16.8	49.4	190.6	1.18	-2.15	2.2	2.52	5.3	0.46	9.14

Continued on next page

Table 4.1. Galaxy Sample and Properties in the Central 1.5 kpc Regions

Galaxy (1)	Bar (2)	Dist. [Mpc] (3)	Incl. [deg] (4)	P.A. [deg] (5)	Z' [$Z_\odot$] (6)	$\log(\Sigma_{\rm SFR})$ $\left[\frac{\rm M_\odot}{\rm yr\ kpc^2}\right]$ (7)	$I_{\rm CO(2-1)}$ [K km s^{-1}] (8)	$\log(\Sigma_{\rm star})$ [M$_\odot$ pc^{-2}] (9)	$\langle \Delta v \rangle_{\rm 150pc}$ [km s^{-1}] (10)	$\log(\alpha_{\rm CO}^{\rm Eq.4.2})$ $\left[\frac{\rm M_\odot\ s}{\rm K\ km\ pc^2}\right]$ (11)	$\log(t_{\rm dep})$ [yr] (12)
NGC5068	1	5.2	35.7	342.4	0.98	-2.01	1.0	2.33	3.6	0.60	8.79
NGC5128	0	3.7	45.3	32.2	1.36	-0.78	45.3	3.70	22.7	-0.07	8.56
NGC5134	1	19.9	22.7	311.6	1.30	-1.94	4.9	3.33	11.4	0.18	9.00
NGC5248*	1	14.9	47.4	109.2	1.30	-0.97	72.6	3.35	15.7	0.07	9.08
NGC5530	0	12.3	61.9	305.4	1.23	-2.02	6.4	3.00	4.8	0.50	9.51
NGC5643	1	12.7	29.9	318.7	1.29	-0.29	42.0	2.88	26.7	-0.12	7.98
NGC6300	1	11.6	49.6	105.4	1.31	-0.55	41.1	2.85	36.2	-0.23	8.11
NGC7456	0	15.7	67.3	16.0	1.09	-2.70	0.9	1.99	2.7	0.70	9.56
NGC7496	1	18.7	35.9	193.7	1.21	-0.43	46.2	2.72	23.7	-0.08	8.20

Note. (1) Galaxies with an asterisk are those with $\alpha_{\rm CO}$ measurements (see Section 4.2.2); (2) bar classification (Querejeta et al., 2021); (3) distance (Anand et al., 2021); (4–5) inclination and position angles (Lang et al., 2020); (6–10) the central 1.5 kpc measurements of gas-phase metallicity (PP04-based), kpc-averaged SFR surface density, kpc-averaged CO(2-1) integrated intensity, kpc-averaged stellar mass surface density, and CO intensity-weighted mean velocity dispersion at 150-pc scale (Sun et al., 2022); (11) $\log(\alpha_{\rm CO})$ derived from (10) using Equation 4.2; (12) molecular gas depletion time derived from (7), (8), and (11) using Equation 4.6.

4.2.2 Dust-based α_{CO} Measurements

We obtain spatially resolved α_{CO} from C24, where α_{CO} is measured at 2 kpc resolution across 41 nearby ($\leq$ 20 Mpc) and moderately-inclined (Incl. $\leq 80^{\circ}$) spiral galaxies with resolved measurements of CO integrated intensity (including PHANGS-ALMA) and atomic gas. The authors assumed a constant dust-to-metals ratio to constrain the total gas mass with dust and metallicity measurements. In their sample, eight barred and four non-barred galaxies from PHANGS have dust-based α_{CO} measurements (those with an * in Table 4.1). These measurements typically cover out to a galactocentric radius of $\sim$10 kpc, including $\sim$2000 Nyquist-sampled data points. It is based on these data that we examine scaling relations of α_{CO} and develop an α_{CO} prescription in Section 4.3.1.

The α_{CO} measurements in C24 were derived based on the PHANGS CO(2–1) data, and we directly use their $\alpha_{\mathrm{CO(2-1)}}$ measurements to ensure methodological consistency when we derive molecular gas surface density and SFE (see Sections 4.3.3 and 4.3.4). To compare with most α_{CO} literature using $\alpha_{\mathrm{CO(1-0)}}$, however, we convert the measured $\alpha_{\mathrm{CO(2-1)}}$ to $\alpha_{\mathrm{CO(1-0)}}$ by assuming a CO(2–1)/(1–0) ratio (R_{21}) of 0.65. Such results can be easily reverted to $\alpha_{\mathrm{CO(2-1)}}$ via a linear scaling with 0.65. We note that C24 also provided $\alpha_{\mathrm{CO(1-0)}}$ measurements assuming a SFR-dependent R_{21}, and we have checked that using such α_{CO} does not change any of our results qualitatively (see Section 4.3.1).

We also note that the metallicity adopted by C24 for computing α_{CO} is based on the S-calibration in Pilyugin and Grebel (2016, hereafter PG16S), which is different from the O3N2 calibration used for the PHANGS dataset based on Pettini and Pagel (2004, hereafter PP04). Recent studies suggest that PG16S is a more reliable metallicity prescription than PP04 (e.g., Kreckel et al., 2019). With the data on 12 galaxies, we find that PP04 estimates result in $\sim$0.2 dex higher Z' than PG16S (see also De Vis et al., 2019), which might be due to the mismatch in the adopted solar oxygen abundance value under different calibration schemes (e.g., $12+\log(\mathrm{O/H})_{\odot} = 8.50$ or 8.69; see discussion in Esteban et al., 2022). Throughout this work, we adopt PG16S-based Z' from C24 for analyses restricted to these 12 galaxies. However, due to the lack of PG16S-based measurements on all 65 PHANGS galaxies, we use the PP04-based Z' when implementing metallicity-dependent $\alpha_{\rm CO}$ prescriptions across the full sample for consistency.

To evaluate the credibility of the observed $\alpha_{\rm CO}$ trends with our parameters of interest (i.e., $\langle\Delta v\rangle_{\rm 150pc}$ and Z'), we calculate for each parameter bin the number of pixels with reliable $\alpha_{\rm CO}$ measurements divided by the number of pixels with measured Δv or Z'. For Δv, we find the fraction of reliable pixels to be 70–100% for bins with $\langle\Delta v\rangle_{\rm 150pc} \gtrsim 3$ km s^{-1}, while it drops significantly to $< 50\%$ in lower velocity dispersion bins[2]. This means that our $\alpha_{\rm CO}$ data coverage is insufficient to accurately represent regions with $\Delta v \lesssim 3$ km s^{-1}. As for Z', the corresponding completeness of $\alpha_{\rm CO}$ is above 60% across regions with $Z' \gtrsim 0.6$, while it drops below 40% at lower metallicities (where the PHANGS-ALMA dataset has poorer coverage). These "incomplete" regimes will be excluded by our fitting and analysis in Section 4.3.1, where we present the new $\alpha_{\rm CO}$ prescription.

4.3 Results

4.3.1 A Velocity Dispersion-based $\alpha_{\rm CO}$ Prescription

To investigate how the dust-based $\alpha_{\rm CO}$ varies with local velocity dispersion, we use nearest-neighbor matching to relate the $\alpha_{\rm CO}$ measurements at 2-kpc scales with the velocity dispersion which is measured at 150-pc scale and then averaged over 1.5-kpc-sized apertures via intensity weighting ($\langle\Delta v\rangle_{\rm 150pc}$). As shown in Figure 4.1(a), the data clearly follow an inverse power-law relation, which is in close agreement with the fit by T23 on three barred galaxy centers at ~100 pc scales (i.e., dash-dotted orange line, assuming a CO/H_2 abundance of 1.5×10^{-4}). The central regions of the 12 galaxies (vertical, gray bars in Figure 4.1(a)) align well with the overall trend, showing that velocity dispersion

---

[2] This is likely due to a large amount of low S/N measurements clustering around ~2.5 km/s, which is the velocity resolution of the PHANGS CO data

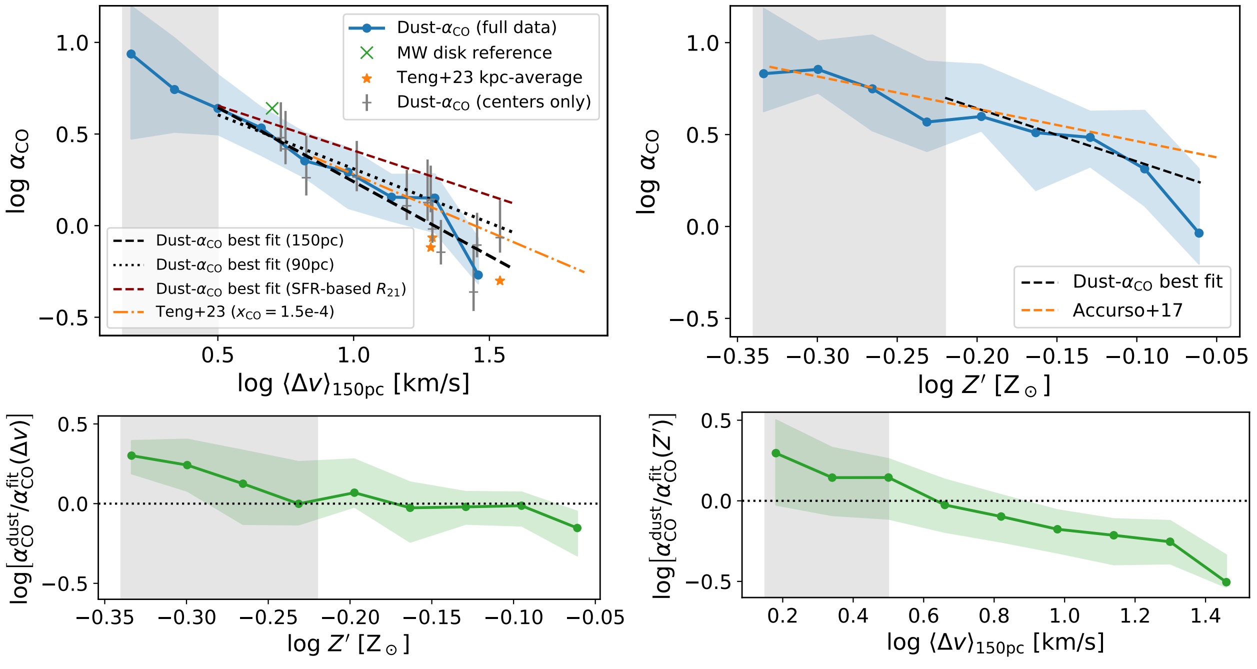

(a) (b)

Figure 4.1. Column (a): Dust-based α_{CO} measurements show a strong anti-correlation with the intensity-weighted average of 150-pc scale molecular gas velocity dispersion (top), consistent with the result from T23 on barred galaxy centers (orange line, with an assumed CO/H_2 abundance $x_{CO} = 1.5 \times 10^{-4}$); the blue lines and shaded area represent the binned medians and 16th–84th percentile of the measured α_{CO}; the gray shaded area indicates low-confidence regime where α_{CO} sampling is incomplete; the black dashed/dotted lines show the best fit power-law relations with $\langle\Delta v\rangle$ at 150/90 pc resolutions, and the red dashed line represents the best fit relation when α_{CO} is derived by assuming a SFR-dependent R_{21} (C24). The residuals of the fit (bottom) do not correlate with Z' in the data-complete regime, suggesting that the observed α_{CO} variations can be fully captured by our Δv-based prescription, without requiring an additional metallicity dependence. Column (b): Similar to (a), but the measured α_{CO} is correlated with metallicity (top), and the residuals are correlated with $\langle\Delta v\rangle_{150pc}$ (bottom); the orange dashed line marks the prediction from Accurso et al. (2017a), which agrees with the overall data but shows a larger scatter.

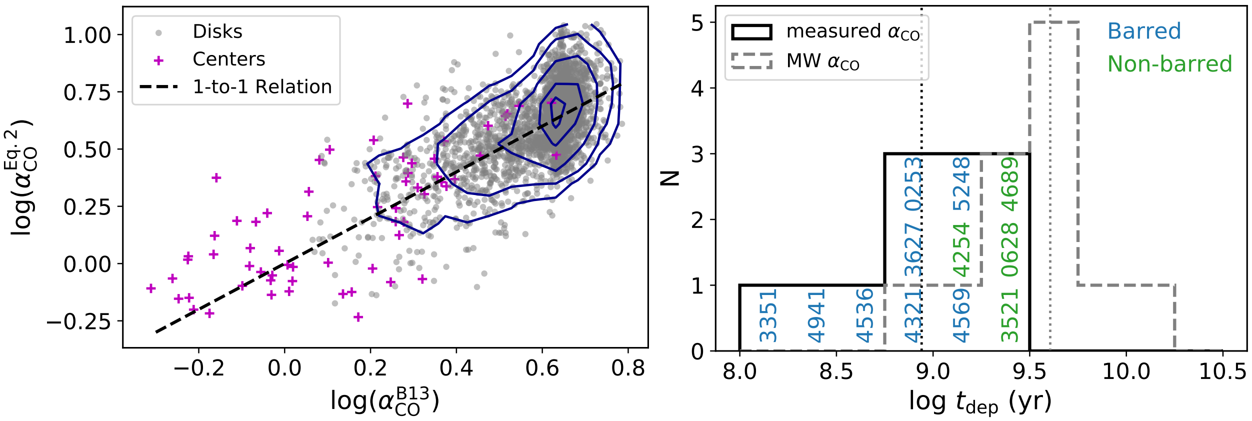

(a) (b)

Figure 4.2. (a) Comparison of the derived $\alpha_{\rm CO}$ using our Δv-based prescription (Equation 4.2) and the Z' plus $\Sigma_{\rm star}$-based prescription (Equation 4.3; B13), applied to 65 galaxies. The overlaid contours indicate 16%, 50%, 84%, 95%, and 98% data inclusion of the disk regions. The two prescriptions show a general 1-to-1 agreement (dashed line), which supports the credibility of our prescription. (b) Molecular gas depletion time ($t_{\rm dep}$) of 12 galaxy centers (with their NGC names shown on the histogram) determined by the measured $\alpha_{\rm CO}$ (solid line) and the MW $\alpha_{\rm CO}$ (dashed line). The median $t_{\rm dep}$ using measured or MW $\alpha_{\rm CO}$ are indicated by the vertical dotted lines. Overall, $t_{\rm dep}$ is lower using the measured $\alpha_{\rm CO}$, and a clear separation is found between barred and non-barred galaxies, suggesting high star formation efficiency in barred galaxy centers.

can trace $\alpha_{\rm CO}$ variations in both the centers and disks[3]. The green cross sign marks the typical MW disk values of $\alpha_{\rm CO}{\sim}4.35$ M$_\odot$ (K km s^{-1} pc^2)$^{-1}$ and Δv = 5 km s^{-1}, which also agrees with the overall trend. The shaded area in Figure 4.1(a) indicates the regime where $\alpha_{\rm CO}$ data is incomplete (see Section 4.2.2).

Excluding the incomplete regime, we conduct a least-squares fitting in log-log space based on the remaining ~1600 data points, using the `curve_fit` function in `scipy.optimize`. The best-fit power-law relation to these data from 12 galaxies is represented by

$$\log \alpha_{\rm CO} = -0.81\ \log\langle \Delta v\rangle_{\rm 150pc} + 1.05\ , \tag{4.2}$$

where $\alpha_{\rm CO}$ and $\langle \Delta v\rangle_{\rm 150pc}$ are in units of M$_\odot$ (K km s^{-1} pc^2)$^{-1}$ and km s^{-1}, respectively. The best-fit relation is shown by the black dashed line in the top panel of Figure 4.1(a) and is consistent with the trend of the binned $\alpha_{\rm CO}$ medians. The dispersion of data with respect to

---

[3] In this paper, *center* refers to the central ~2 kpc-sized aperture at $R_{\rm gal}$=0, and *disks* represents the rest of the measurements.

Equation 4.2 is $\sigma \sim 0.12$ dex, and the standard deviation error returned by `curve_fit` is ± 0.02 for both the fitted slope and intercept. We remind readers that the $\alpha_{\rm CO}$ data here are converted from $\alpha_{\rm CO(2-1)}$ assuming $R_{21} = 0.65$, and thus it should be scaled by $R_{21}/0.65$ if R_{21} is known. If a SFR-dependent R_{21} is used following C24, the trend of $\alpha_{\rm CO}$ in Figure 4.1(a) could be shallower by 30–40%, as indicated by the red dashed line.

While the functional fit in Equation 4.2 is based on Δv measured at 150-pc scale, we also find a similar best-fit relation (dotted line) for six of those galaxies where $\langle \Delta v \rangle_{\rm 90pc}$ is available. Because Δv does not vary strongly between 90 and 150 pc scales (see also Sun et al., 2022), we would not expect this to change our results, and thus Equation 4.2 should be applicable with Δv measurements around 100-pc resolutions. We note that the evaluation of Δv can also be affected by the number of gas components overlapping along the same sightlines, which could increase Δv in barred galaxy centers. However, such effect is found to be mild (see T23, Appendix A), and we expect it to be even milder in our case, as $\langle \Delta v \rangle_{\rm 150pc}$ is averaged over kpc-sized regions.

4.3.2 Comparison to Previous Literature

We compare our Δv-based prescription with existing $\alpha_{\rm CO}$ prescriptions in the literature, including those based on metallicity (Accurso et al., 2017a; Sun et al., 2020a) or combining metallicity and stellar mass surface density (B13). First, we investigate if metallicity alone could trace the observed $\alpha_{\rm CO}$ variations. Figure 4.1(b) relates the measured $\alpha_{\rm CO}$ with metallicity, using the same metallicity as those used in C24 to calculate $\alpha_{\rm CO}$ (see Section 4.2.2). The data and the power-law fit (black dashed line) overall agrees with the purely metallicity-dependent $\alpha_{\rm CO}$ prescription from Accurso et al. (2017a) (orange dashed line)[4], although the data scatter is larger than the trend with velocity dispersion. In the regime where our dataset is complete, the scatter of the observed $\alpha_{\rm CO}$ is $\sigma \sim 0.1$ dex with

---

[4] The Z' in the original prescription [$\alpha_{\rm CO} = 4.35(Z')^{-1.6}$] was based on the PP04 calibration. Here we convert their prescription to the same (PG16S-based) metallicity scale as we adopt, using an approximate conversion based on De Vis et al. (2019).

$\langle \Delta v \rangle_{150\mathrm{pc}}$ and 0.3 dex with Z'. This shows a significant improvement in predicting α_{CO} with our Δv-based prescription, compared to current metallicity-dependent prescriptions.

In the bottom panels of Figures 4.1(a) and (b), we relate the residuals of each α_{CO} fit with Z' or $\langle \Delta v \rangle_{150\mathrm{pc}}$, in order to check if metallicity effects can explain any residual variation of α_{CO} around the Δv trend, or the opposite. Above the completeness limit, we find no trend between the residuals from the Δv prescription and metallicity. On the other hand, the residuals from the metallicity fit clearly decrease with Δv above the completeness threshold. This suggests that Δv is crucial for tracing the α_{CO} changes, even without including metallicity effects. We have checked that the α_{CO} correlation with Z' seen in this regime may come from the correlation between Z' and Δv, as both variables decrease with the galactocentric radius.

Taking both metallicity and emissivity effects into account, B13 also suggested a tentative prescription[5] based on α_{CO} measurements in nearby disks and (U)LIRGs:

$$\alpha_{\mathrm{CO}} \approx 2.9\ \exp\left(\frac{0.4}{Z'}\right)\left(\frac{\Sigma_{\mathrm{star}} + \Sigma_{\mathrm{mol}}}{100\ \mathrm{M}_{\odot}\ \mathrm{pc}^{-2}}\right)^{-\gamma}\ , \tag{4.3}$$

where $\gamma = 0.5$ if $\Sigma_{\mathrm{star}} + \Sigma_{\mathrm{mol}} > 100\ \mathrm{M}_{\odot}\ \mathrm{pc}^{-2}$ or $\gamma = 0$ otherwise. To compare the derived α_{CO} from our proposed prescription (Equation 4.2) with that from B13, we apply both prescriptions to galaxies in the PHANGS sample (see Table 4.1) using kpc-scale Z' and Σ_{star}. As we find $\Sigma_{\mathrm{mol}} \ll \Sigma_{\mathrm{star}}$ even with a (likely-overestimated) Galactic α_{CO} (Sun et al., 2022), we neglect Σ_{mol} in Equation 4.3. We note that C24 also reported a similar α_{CO} relation that scales with $\Sigma_{\mathrm{star}}^{-0.5}$.

Figure 4.2(a) compares the α_{CO} values predicted by Equations 4.2 and 4.3. Excluding the regime of $\log(\alpha_{\mathrm{CO}}) \gtrsim 0.65$ where B13 enforces a MW-like α_{CO} value with $\gamma = 0$ (which also corresponds to the low-confidence regime of our Δv-based prescription), the two prescriptions show an overall match with a $\sim$0.5 dex scatter. Despite a significant scatter,

---

[5] The original prescription included a molecular cloud surface density term which was assumed at $100\ \mathrm{M}_{\odot}\ \mathrm{pc}^{-2}$. Here we adopt the same value and note that this helps avoid unrealistic α_{CO} values in low surface density regions (Sun et al. 2023, T23).

this general agreement may indicate that Δv and $\Sigma_{\rm star}$ are tracing the same physical process that drives $\alpha_{\rm CO}$ variations. A likely scenario is that Δv is set by the additional gravitational potential from stellar components, which can thus be tracked by $\Sigma_{\rm star}$ (see B13 and C24). It is also possible that Δv is a proxy of molecular gas surface densities and/or local CO intensities which could also reflect opacity and $\alpha_{\rm CO}$ changes, as previous studies have found good correlations between these properties (Sun et al., 2022, see also Section 4.4 for further discussion).

The B13 prescription was mostly based on $\alpha_{\rm CO}$ measurements that were independent from ours and included several U/LIRGs in their sample, and the ~0.5 dex scatter with our prescription is also consistent with the uncertainty estimated by B13. Therefore, the rough agreement seen in Figure 4.2(a) may also provide additional evidence for the validity of our proposed prescription. Compared to a $\Sigma_{\rm star}$-based prescription, one advantage of using a Δv-based prescription is that Δv straightforwardly traces the optical depth change (Teng et al., 2022; Teng et al., 2023), making it closer to the underlying physics that could control $\alpha_{\rm CO}$ variations. Another advantage is that Δv can be directly obtained from the CO data. Thus, no ancillary multi-band data are needed to estimate $\alpha_{\rm CO}$, which circumvents uncertainties in translating observations into $\Sigma_{\rm star}$. We remind readers that our prescription is calibrated to $\langle \Delta v \rangle_{\rm 150pc}$ in CO (2–1), which is typically consistent with $\langle \Delta v \rangle_{\rm 150pc}$ in CO (1–0) but may be different from that measured in higher-J CO lines (Yuan et al., 2020; Teng et al., 2022; Teng et al., 2023). We also point out that systematic measurements of Δv at 150-pc resolutions can be difficult across more extreme starbursts like U/LIRGs (e.g., Wilson et al., 2019), which are usually more distant and/or more morphologically-disturbed than the galaxies in our sample.

We note that the scaling of $\alpha_{\rm CO}$ with Δv in Equation 4.2 is similar to what would be predicted by simple theoretical arguments. As shown by Equation 8 in Gong et al. (2020) (see also related derivations in Chapter 19 of Draine, 2011 and Chapter 8 of Krumholz, 2015), the excitation temperature ($T_{\rm ex}$) under Large Velocity Gradient approximation with assumptions of a two-level optically-thick system can be written as

$$T_{\rm ex} \propto \rho_{\rm mol} \sqrt{\frac{L_{\rm mol} \cdot x_{\rm CO}}{\Delta v}} \,, \tag{4.4}$$

where $\rho_{\rm mol}$ and $L_{\rm mol}$ are the density and size of a CO-emitting molecular cloud, respectively. To first order, we also have $I_{\rm CO} \sim T_{\rm ex} \cdot \Delta v$ from the cloud. Thus, combining Equation 4.1 with Equation 4.4, we obtain

$$\alpha_{\rm CO} = \frac{\Sigma_{\rm mol}}{I_{\rm CO}} \sim \frac{\rho_{\rm mol} \cdot L_{\rm mol}}{T_{\rm ex} \cdot \Delta v} \propto \sqrt{\frac{L_{\rm mol}}{x_{\rm CO} \cdot \Delta v}} \,. \tag{4.5}$$

The resulting $\alpha_{\rm CO}$ dependence on the inverse square root of Δv is similar to the fits in Figure 4.1. While the fitted slope for $\langle \Delta v \rangle_{\rm 150pc}$ (Equation 4.2) is slightly steeper than -0.5, we emphasize that the above calculation is highly simplified and is only for providing an intuitive check with theoretical expectations.

4.3.3 Star Formation Efficiency in Galaxy Centers

As $\alpha_{\rm CO}$ determines the total molecular gas surface density ($\Sigma_{\rm mol}$, in units of $\rm M_\odot\ pc^{-2}$), the variation of $\alpha_{\rm CO}$ directly affects the estimation of molecular gas depletion time ($t_{\rm dep}$) or SFE ($= 1/t_{\rm dep}$):

$$t_{\rm dep} = \Sigma_{\rm mol} \;/\; \Sigma_{\rm SFR} = \alpha_{\rm CO} \cdot I_{\rm CO} \;/\; \Sigma_{\rm SFR} \,. \tag{4.6}$$

While we examine only the SFE in this work, we note that the impact of $\alpha_{\rm CO}$ on estimating the SFE per molecular cloud free-fall time is even more significant, as $\alpha_{\rm CO}$ also affects the assessment of cloud density which changes the free-fall time (e.g., Querejeta et al., 2023; Sun et al., 2023). Motivated by the clear trend of galaxy centers having lower $\alpha_{\rm CO}$ values (Figures 4.1(a) and 4.2(a)), we derive $t_{\rm dep}$ for the 12 galaxy centers with $\alpha_{\rm CO}$ measurements (C24; T23), using kpc-scale $\Sigma_{\rm SFR}$ and $I_{\rm CO(2-1)}$ (see Table 4.1). Then, we examine how $t_{\rm dep}$ in galaxy centers derived from the measured $\alpha_{\rm CO}$ would differ from that using the standard MW $\alpha_{\rm CO}$ of 4.35 (or 6.7 in terms of $\alpha_{\rm CO(2-1)}$) $\rm M_\odot\ (K\ km\ s^{-1}\ pc^2)^{-1}$.

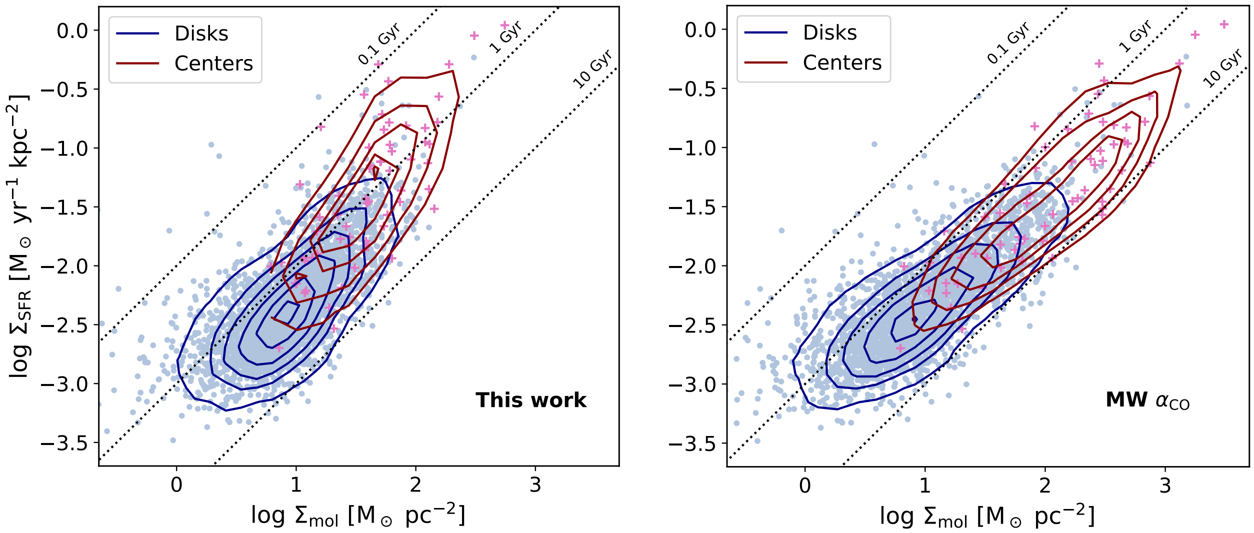

(a)

(b)

Figure 4.3. The molecular Kennicutt-Schmidt (mKS) relation across 65 PHANGS galaxies, where the α_{CO} used to derive Σ_{mol} is based on (a) Equation 4.2 or (b) the MW value. The thin dotted lines represent constant molecular gas depletion times (t_{dep}) of 0.1, 1, and 10 Gyr. With our α_{CO} prescription, the galaxy centers clearly show a steeper trend than the disks, indicating shorter t_{dep} towards higher Σ_{mol}. Adopting the MW α_{CO} instead results in a roughly constant t_{dep} for both centers and disks.

Figure 4.2(b) presents histograms of t_{dep} for the 12 galaxy centers. For the histogram using the measured α_{CO}, we separate barred and non-barred galaxies with different colors. We find that the median t_{dep} with the MW α_{CO} is 4–5 times longer than that with the measured α_{CO}. Furthermore, adopting the MW α_{CO} results in a similar t_{dep} of ~3 Gyr between barred and non-barred centers. In contrast, if the measured α_{CO} is used, the median t_{dep} of barred and non-barred centers becomes 0.6 Gyr and 2.0 Gyr, respectively, differing by more than a factor of three. This suggests that SFE in barred galaxy centers tend to be higher than non-barred galaxy centers, and that using a constant α_{CO} can obscure such a trend.

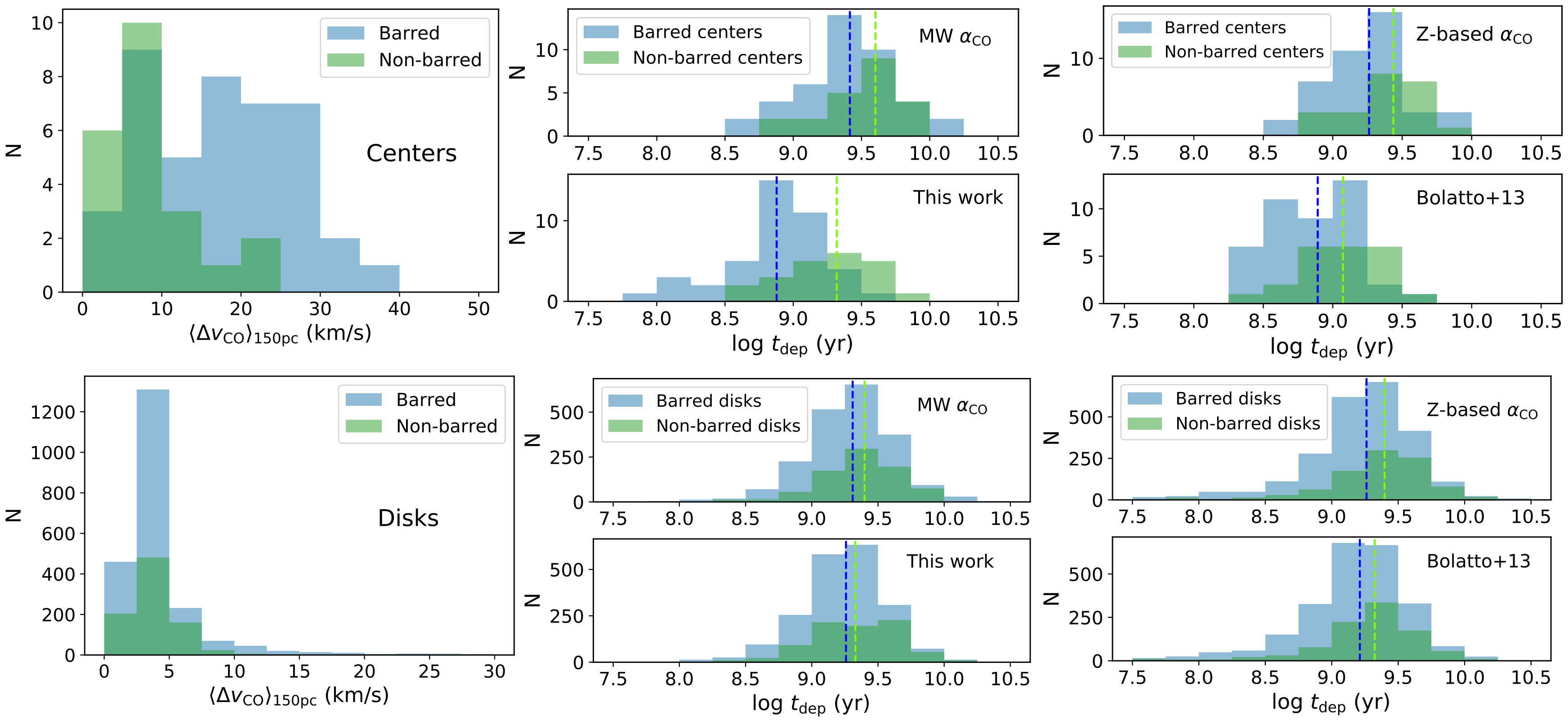

Figure 4.4. Molecular gas velocity dispersion and the derived depletion time of PHANGS galaxies using four different $\alpha_{\rm CO}$ prescriptions. The upper/lower panels show the centers/disks regions. The medians of the barred/non-barred distributions are indicated by the blue/green dashed lines. Our prescription reveals that barred centers tend to have higher star formation efficiency than non-barred centers due to a generally higher velocity dispersion, but such trend is easily obscured using other prescriptions. Contrary to the centers, the disk regions show consistent distribution of velocity dispersion and depletion time between barred and non-barred galaxies, regardless of which prescription is used.

4.3.4 Systematic Impact on Star Formation Efficiency

With the PHANGS sample (Table 4.1), we investigate the impact of different $\alpha_{\rm CO}$ prescriptions on SFE or $t_{\rm dep}$ in the centers and disks of barred and non-barred galaxies. Figure 4.3 shows the molecular Kennicutt-Schmidt (mKS) relation across all 65 galaxies measured at the 1.5-kpc scale, comparing $\Sigma_{\rm mol}$ determined from our $\alpha_{\rm CO}$ prescription (Equation 4.2) with that determined using a MW $\alpha_{\rm CO}$. It is clear that adopting the MW $\alpha_{\rm CO}$ results in a wider range of $\Sigma_{\rm mol}$ with values reaching > 1000 M$_\odot$ pc^{-2} in galaxy centers, while our prescription suggests $\Sigma_{\rm mol} < 200$ M$_\odot$ pc^{-2} in general. Furthermore, our prescription reveals a trend of higher SFE towards higher $\Sigma_{\rm mol}$, which steepens the mKS relation for galaxy centers and other high-$\Sigma_{\rm mol}$ regions. With the MW $\alpha_{\rm CO}$, however, both galaxy centers and disks exhibit a roughly constant SFE. These results show that $\alpha_{\rm CO}$ and $\Sigma_{\rm mol}$ in galaxy centers may overall be overestimated by a factor of 5 with the MW $\alpha_{\rm CO}$, and that the choice of $\alpha_{\rm CO}$ greatly affects our understanding of galactic-scale star formation.

Figure 4.4 presents histograms of velocity dispersion and $t_{\rm dep}$ across the PHANGS sample, separating centers (upper panels) and disks (lower panels) for barred (blue) and non-barred (green) galaxies. In non-barred galaxy centers, $\langle\Delta v\rangle_{\rm 150pc}$ is typically < 10 km s^{-1}, while barred centers span a significantly wider range up to ~40 km s^{-1}. On the other hand, barred and non-barred disks show consistent velocity dispersion, with $\langle\Delta v\rangle_{\rm 150pc}$ typically below 5 km s^{-1} but reaching up to 10 km s^{-1}. These distributions agree with Sun et al. (2020b), who reported similar Δv between galaxy disks and non-barred centers but an overall ~5 times higher Δv in barred centers.

We then examine the distribution of $t_{\rm dep}$ derived with different $\alpha_{\rm CO}$ prescriptions. Using our Δv-based prescription, we find distinctly different $t_{\rm dep}$ between barred and non-barred centers, with the mean/median of $t_{\rm dep}$ in barred galaxy centers (~700 Myr) being 3 times shorter than in non-barred centers (~2.1 Gyr). The 16th–84th percentile ranges for $t_{\rm dep}$ in barred and non-barred centers is 0.3–1.6 and 0.8–3.6 Gyr, respectively. In contrast, all other prescriptions result in < 0.2 dex difference between the median $t_{\rm dep}$ of the two types of systems. Such a small difference between barred and non-barred centers is even true for the B13 prescription which shows similarly short $t_{\rm dep}$ for all galaxy centers that generally matches our results. Particularly, the MW $\alpha_{\rm CO}$ leads to two completely overlapping $t_{\rm dep}$ distributions, overestimating the overall $t_{\rm dep}$ in barred galaxy centers by a factor of 3–4 if compared to our results. As for the disks, the median of $t_{\rm dep}$ remains consistent at 2–3 Gyr across all four prescriptions, while it is found to be systematically lower in barred galaxies than in non-barred galaxies by ~0.1 dex.

Notably, our prescription reveals short $t_{\rm dep}$ down to $\lesssim$100 Myr in some barred galaxy centers, which is not seen with other prescriptions. Such a short time scale is supported by recent simulations of galaxy centers including effects from bar-driven inflows (e.g., Armillotta et al., 2019; Sormani et al., 2020; Moon et al., 2021). In addition, we note that the overall $t_{\rm dep}$ for galaxy centers is similar between our result and B13's, both suggesting $t_{\rm dep}$ ~1 Gyr which is shorter than the disks value of ~3 Gyr. This factor-of-three difference between centers and disks is consistent with recent simulations (e.g., Tress et al., 2020a). However, using the MW or Z-based $\alpha_{\rm CO}$ for galaxy centers obscures such difference and leads to similar $t_{\rm dep}$ across entire galaxies.

4.4 Discussion

The correlation of $\alpha_{\rm CO}$ with ~100-pc scale velocity dispersion with only a $\sigma \sim 0.1$ dex scatter (see Section 4.3.1), contrary to ~0.3 dex or larger scatter using Z- and/or $\Sigma_{\rm star}$-based prescriptions, shows that velocity dispersion is an excellent observational tracer for $\alpha_{\rm CO}$ variations in star-forming galaxies. The rationale behind such a strong relation may be that Δv directly traces the optical depth changes that are the dominant effect responsible for altering $\alpha_{\rm CO}$ across these galaxies, as it has been shown that opacity variation is the primary driver of $\alpha_{\rm CO}$ in various galaxy centers (Israel, 2020; Teng et al., 2022; Teng et al., 2023). However, effects of CO-dark gas and CO excitation can also be important to explain $\alpha_{\rm CO}$ variations across the galaxy disks, which have therefore motivated previous

$\alpha_{\rm CO}$ prescriptions based on metallicity and/or CO integrated intensity (e.g., Narayanan et al., 2012; Hunt et al., 2015; Amorín et al., 2016; Accurso et al., 2017a; Gong et al., 2020).

As discussed in Section 4.3.2, the correlation of $\alpha_{\rm CO}$ with metallicity (Z') is indirectly included in the dependence with Δv because both Z' and Δv vary with galactocentric radius and are thus correlated. Furthermore, statistical studies on molecular cloud properties have shown that velocity dispersion also correlates well with molecular gas surface density and the CO integrated intensity across galaxy disks (Heyer et al., 2009; Sun et al., 2020b; Sun et al., 2022; Rosolowsky et al., 2021). Therefore, it is likely that our Δv-based prescription contains opacity variations and metallicity gradients as well as the physics of the $\alpha_{\rm CO}$–$I_{\rm CO}$ correlation suggested by simulation studies (Narayanan et al., 2012; Gong et al., 2020; Hu et al., 2022). This means that the proposed prescription (Equation 4.2) may incorporate more than one piece of physics into a single scaling relation, which could explain why the trend holds across different galactic environments. We also note that metallicity effects on $\alpha_{\rm CO}$ should be more drastic in low-metallicity dwarf galaxies due to the lack of dust shielding that can prevent CO from dissociation, and thus metallicity variations being included in our Δv-based prescription might only be true in the context of MW-like star-forming disk galaxies as represented by the PHANGS sample.

In Sections 4.3.3 and 4.3.4, our prescription (based on the dust $\alpha_{\rm CO}$ measurements) suggests lower $\alpha_{\rm CO}$ in barred galaxy centers that lead to higher SFE than non-barred centers and the disks. This low $\alpha_{\rm CO}$ and high SFE in barred centers imply that the amount of molecular gas can be overestimated by previous studies due to inaccurate $\alpha_{\rm CO}$ or the assumption of a constant SFE. By comparing the derived $\Sigma_{\rm mol}$ under different $\alpha_{\rm CO}$ assumptions for all galaxies in Table 4.1, we find that the median $\Sigma_{\rm mol}$ of barred centers is 3 times higher than that of non-barred centers if using a MW-like $\alpha_{\rm CO}$. On the other hand, our $\alpha_{\rm CO}$ prescription results in only 1.3 times higher $\Sigma_{\rm mol}$ in barred centers. Therefore, it is likely that the enhanced SFE is a more important factor causing high SFR observed in barred galaxy centers, compared to an increased amount of molecular gas driven inwards by bars.

Recent studies using $\alpha_{\rm CO}$ prescriptions from Narayanan et al. (2012) or B13 also show that barred galaxies tend to have higher central gas concentration than non-barred galaxies, although the degree of concentration is not as significant as using a constant $\alpha_{\rm CO}$ (Sakamoto et al., 1999; Sheth et al., 2005; Schinnerer et al., 2006; Kuno et al., 2007). Such accumulation of gas towards the centers can increase SFR in barred centers, and it is consistent with the theoretical expectation that non-axisymmetric gravitational potential from bars can induce gas inflows and transport more gas into galaxy centers (e.g., Wada and Habe, 1995; Regan and Teuben, 2004; Kim et al., 2012; Tress et al., 2020b). Bars thus influence the secular evolution of galaxies by redistributing molecular gas mass and angular momentum (see review by Kormendy and Kennicutt, 2004).

Studies have also shown that if $\alpha_{\rm CO}$ changes were treated properly, starbursts in galaxy centers and variations of SFRs across nearby galaxies are primarily driven by higher SFE rather than increased molecular gas fraction (Leroy et al., 2013; Ellison et al., 2020b; Ellison et al., 2020a; den Brok et al., 2023). This is contrary to studies using constant, Z-based, or $\Sigma_{\rm star}$-based $\alpha_{\rm CO}$, which resulted in similar SFE between barred and non-barred galaxies (e.g., Saintonge et al., 2012; Querejeta et al., 2021, see also Section 4.3.4). With our proposed $\alpha_{\rm CO}$ prescription, we find enhanced SFE in barred centers, which could originate from variations in molecular gas distribution, density structure, or dynamical effects of turbulence and shocks powered by stellar feedback (e.g., Kainulainen et al., 2009; Renaud et al., 2012; Liu et al., 2023). However, these factors driving SFE variations are the same ones that can alter CO emissivity and $\alpha_{\rm CO}$. Therefore, only with accurate $\alpha_{\rm CO}$ values can we disentangle SFE from $\alpha_{\rm CO}$ and unravel the physical drivers of SFR. Using the latest and best possible measurements of $\alpha_{\rm CO}$ and molecular gas properties across a sample of nearby galaxies, our work lays a foundation for benchmarking $\alpha_{\rm CO}$ calibration in star-forming galaxies (including starbursting galaxy centers) and allows for further investigation on SFE, SFE per cloud free-fall time, or other related properties that can improve our knowledge of galaxy evolution.

4.5 Conclusions

We construct a new $\alpha_{\rm CO}$ prescription applicable to star-forming galaxies, where CO emissivity variations are critical in altering $\alpha_{\rm CO}$. The prescription is a major step towards precise calibration of $\alpha_{\rm CO}$ across galaxies, and it reveals unprecedented trends in star formation properties which may have been obscured by previous $\alpha_{\rm CO}$ prescriptions. Our key results are summarized as follows:

1. The strong anti-correlation between measured $\alpha_{\rm CO}$ and CO velocity dispersion (Δv) at $\sim$100-pc scales shows that Δv is useful for predicting $\alpha_{\rm CO}$, and it suggests that CO opacity altered by Δv changes or other correlated properties of the molecular gas across the entire galaxies are primary drivers of $\alpha_{\rm CO}$ in star-forming galaxies.

2. The proposed $\alpha_{\rm CO}$ prescription (Equation 4.2) is applicable to regions with metallicity above 0.6 $Z_\odot$ and $\langle \Delta v \rangle_{\rm 150pc} \gtrsim 3$ km s^{-1}. The expected scatter in $\alpha_{\rm CO}$ is $\sigma \sim 0.1$ dex, which is a substantial improvement over existing $\alpha_{\rm CO}$ prescriptions. Our Δv-based prescription has the advantage of connecting directly to the physical causes of $\alpha_{\rm CO}$ change (e.g., CO opacity) as well as requiring only the CO observations which is most relevant to tracing molecular gas.

3. With the measured $\alpha_{\rm CO}$, we find distinctly shorter molecular gas depletion time ($t_{\rm dep}$) in barred galaxy centers than non-barred galaxy centers, as well as a generally shorter $t_{\rm dep}$ in galaxy centers than the disks. In contrast, assuming a constant MW $\alpha_{\rm CO}$ results in $t_{\rm dep} \sim 3$ Gyr for all regions, which underestimates the star formation efficiency (SFE) in galaxy centers and also obscures the difference between barred and non-barred galaxies.

4. Our prescription reveals short $t_{\rm dep}$ down to 100 Myr in barred galaxy centers, with the median $t_{\rm dep}$ ($0.7^{+0.9}_{-0.4}$ Gyr) being 3 times shorter than in non-barred galaxy centers

($2.1^{+1.5}_{-1.3}$ Gyr). However, all other prescriptions (MW, metallicity-based, and B13) show < 0.2 dex difference between the two regions, even if B13 results in an overall shorter $t_{\rm dep}$ for galaxy centers which aligns better with our results. Thus, SFE in barred galaxy centers may be underestimated by a factor of three or more in previous studies due to $\alpha_{\rm CO}$ uncertainties.

5. All four prescriptions tested in this work show similar $t_{\rm dep}$ of 2–3 Gyr in the disk regions and non-barred galaxy centers across the PHANGS sample, which is in good agreement with previous literature (e.g., Leroy et al., 2008; Saintonge et al., 2011; Sun et al., 2023).

4.6 Acknowledgments

This work was carried out as part of the PHANGS collaboration. Y.-H.T. and K.S. acknowledge funding support from NRAO Student Observing Support Grant SOSPADA-012 and from the National Science Foundation (NSF) under grant No. 2108081. Y.-H.T. also acknowledges support by the Ministry of Education of Taiwan through Government Scholarship to Study Abroad. J.S. acknowledges support by the Natural Sciences and Engineering Research Council of Canada (NSERC) through a Canadian Institute for Theoretical Astrophysics (CITA) National Fellowship. KG is supported by the Australian Research Council through the Discovery Early Career Researcher Award (DECRA) Fellowship (project number DE220100766) funded by the Australian Government. KG is supported by the Australian Research Council Centre of Excellence for All Sky Astrophysics in 3 Dimensions (ASTRO 3D), through project number CE170100013. HAP acknowledges support by the National Science and Technology Council of Taiwan under grant 110-2112-M-032-020-MY3. MB gratefully acknowledges support from the ANID BASAL project FB210003 and from the FONDECYT regular grant 1211000. IC thanks the National Science and Technology Council for support through grant 111-2112-M-001-038-MY3, and the Academia Sinica for Investigator Award AS-IA-109-M02. JC acknowledges funding from the Belgian Science Policy Office (BELSPO) through the PRODEX project "JWST/MIRI Science exploitation" (C4000142239).

MC gratefully acknowledges funding from the DFG through an Emmy Noether Research Group (grant number CH2137/1-1). COOL Research DAO is a Decentralized Autonomous Organization supporting research in astrophysics aimed at uncovering our cosmic origins. SKS acknowledges financial support from the German Research Foundation (DFG) via Sino-German research grant SCHI 536/11-1. AU acknowledges support from the Spanish grant PID2019-108765GB-I00, funded by MCIN/AEI/10.13039/501100011033. J. D. H. gratefully acknowledges financial support from the Royal Society (University Research Fellowship; URF/R1/221620).

This paper makes use of the following ALMA data:
ADS/JAO.ALMA#2012.1.00650.S,
ADS/JAO.ALMA#2013.1.00803.S,
ADS/JAO.ALMA#2013.1.01161.S,
ADS/JAO.ALMA#2015.1.00925.S,
ADS/JAO.ALMA#2015.1.00956.S,
ADS/JAO.ALMA#2017.1.00392.S,
ADS/JAO.ALMA#2017.1.00766.S,
ADS/JAO.ALMA#2017.1.00886.L,
ADS/JAO.ALMA#2018.1.01321.S,
ADS/JAO.ALMA#2018.1.01651.S.
ADS/JAO.ALMA#2018.A.00062.S.
ALMA is a partnership of ESO (representing its member states), NSF (USA), and NINS (Japan), together with NRC (Canada), NSC and ASIAA (Taiwan), and KASI (Republic of Korea), in cooperation with the Republic of Chile. The Joint ALMA Observatory is operated by ESO, AUI/NRAO, and NAOJ. The National Radio Astronomy Observatory is a facility of the National Science Foundation operated under cooperative agreement by Associated Universities, Inc. This work is based in part on data products from the Wide-field Infrared Survey Explorer(Wright et al., 2010), which is a joint project of the University of California,

Los Angeles, and the Jet Propulsion Laboratory/California Institute of Technology, funded by the National Aeronautics and Space Administration. We acknowledge the usage of the SAO/NASA Astrophysics Data System.

*Facilities:*ALMA, WISE, Herschel, VLA

Software:`matplotlib` (Hunter, 2007), `numpy` (Harris et al., 2020), `scipy` (Virtanen et al., 2020), `astropy` (Astropy Collaboration et al., 2013; Astropy Collaboration et al., 2018), `ipython` (Pérez and Granger, 2007)

* * *

This chapter, in full, is a reprint of the material as it appears in "Star Formation Efficiency in Nearby Galaxies Revealed with a New CO-to-H_2 Conversion Factor Prescription" by Yu-Hsuan Teng, I-Da Chiang, Karin M. Sandstrom, Jiayi Sun, Adam K. Leroy, Alberto D. Bolatto, Antonio Usero, Eve C. Ostriker, Miguel Querejeta, Jeremy Chastenet, Frank Bigiel, Mederic Boquien, Jakob den Brok, Yixian Cao, Melanie Chevance, Ryan Chown, Dario Colombo, Cosima Eibensteiner, Simon C. O. Glover, Kathryn Grasha, Jonathan D. Henshaw, Marıa J. Jimenez-Donaire, Daizhong Liu, Eric J. Murphy, Hsi-An Pan, Sophia K. Stuber, & Thomas G. Williams, which was published in The Astrophysical Journal in 2024. The dissertation author was the primary investigator and author of this paper.

Chapter 5

Conclusion

In this dissertation, I have presented my research on molecular gas and star formation in nearby galaxies, with a significant focus on galaxy centers. The overarching goal is to break through the current limitation in understanding molecular gas and star formation in galaxies via reducing the uncertainty in CO-to-H_2 conversion factor ($\alpha_{\rm CO}$) and addressing its entanglement with star formation efficiency (SFE) measurements. In a broader context, this also helps us understand how molecular gas properties and its distribution within galaxies shape the star formation processes and impact the secular evolution of galaxies.

5.1 Summary

Chapters 2 and 3 describes two papers I led (Teng et al., 2022; Teng et al., 2023) to study the variation of $\alpha_{\rm CO}$ and its relation to gas physical conditions in barred galaxy centers, where $\alpha_{\rm CO}$ was suspected to be low by previous low-resolution measurements. Using non-LTE radiative transfer calculations and multi-line Bayesian modeling, I published a Python pipeline (Teng, 2024) to model gas density, temperature, opacity, isotopologue abundance ratios, and $\alpha_{\rm CO}$. Based on the developed methodology in Chapter 2, I have produced the first resolved and precise measurements of $\alpha_{\rm CO}$ and molecular gas properties in three nearby galaxy centers, using ALMA observations of low-J ^{12}CO, ^{13}CO, and C^{18}O lines at giant molecular cloud ($\sim$100 pc) scales.

In Chapter 3, I also disentangled multiple physical drivers of $\alpha_{\rm CO}$ based on the cloud-scale measurements of gas properties and $\alpha_{\rm CO}$. I found that CO opacity change is the primary driver of $\alpha_{\rm CO}$ across the observed barred galaxy centers. Even more, my work revealed strong evidence that observables like the velocity dispersion and ^{12}CO/^{13}CO line intensity ratio can be useful tracers for predicting $\alpha_{\rm CO}$. I also found that current simulations tend to overpredict $\alpha_{\rm CO}$ in galaxy centers, as they do not capture gas inflows and large-scale turbulence which are the key drivers for CO opacity and $\alpha_{\rm CO}$ variations.

To further unravel the variations of SFE in nearby galaxies, I led a study (Chapter 4; Teng et al., 2024) investigating the dependence of $\alpha_{\rm CO}$ on local CO velocity dispersion and proposed a new $\alpha_{\rm CO}$ prescription that accounts for CO emissivity variations across galaxies. The prescription is calibrated using a new set of $\alpha_{\rm CO}$ measurements via dust and HI observations (Chiang et al., 2024), and it is consistent with the relation I found in Chapter 3 for barred galaxy centers. Based on the proposed prescription, I estimated SFE in a sample of 65 galaxies from the PHANGS–ALMA survey (Leroy et al., 2021b) and found enhanced SFE towards galaxy centers. The result indicates a smooth but non-linear extension of the mKS relation towards high surface density regions.

Moreover, my prescription reveals significantly higher SFE and shorter gas depletion time in barred galaxy centers than in the disks or non-barred galaxy centers, and such trends can be obscured using a constant Galactic $\alpha_{\rm CO}$ or other existing $\alpha_{\rm CO}$ prescriptions. These findings using the new $\alpha_{\rm CO}$ prescription have important implications for galactic-scale star formation, suggesting that SFE is not constant throughout galaxies, and that the high level of star formation activity in barred galaxy centers may be due to an enhanced SFE rather than a significant molecular gas concentration towards the central regions of galaxies.

5.2 Future Directions

This dissertation, mostly in the framework of understanding $\alpha_{\rm CO}$ variation and its impact on star formation in galaxies, has also opened up exciting new directions in molecular gas research. For instance, we have started to take the next critical steps to achieve a cutting-edge, accurate α_{CO} prescription covering an even wider range of galactic environments (e.g., starburst mergers; He et al., 2024). We can also incorporate dynamical effects and chemical network into numerical simulations, to compare with measurements of molecular gas properties and α_{CO} in regimes with dense and turbulent gas. In this section, I list three potential directions, connecting theoretical and observational efforts, to further improve our knowledge of α_{CO} and molecular clouds across galaxies.

(i) α_{CO} calibration based on observed line ratios: In Chapters 3 and 4, I have verified a strong correlation between α_{CO} and cloud-scale velocity dispersion (Δv), which can be used to accurately predict α_{CO} in star-forming galaxies. Now, a key next step is to examine the α_{CO} correlation with observed CO line intensity ratios that could also be α_{CO} indicators, including the CO/^{13}CO line ratio (tracing CO opacity; Teng et al., 2023) and the CO 2–1/1–0 ratio (tracing CO excitation; Gong et al., 2020). This not only provides new pathways for calibrating α_{CO}, but also allows a solid test of whether CO opacity is the key driver that alters α_{CO} across entire galaxies. To this end, I have been leading several ALMA proposals on measuring α_{CO} and mapping ^{13}CO (2–1) lines in a diverse sample of galaxies. These observations will bridge the gap of α_{CO} prescriptions between normal and extreme environments, leading to a universal prescription applicable to a variety of galaxies.

(ii) Incorporating dynamics and chemistry into numerical simulations: While current simulations can include sophisticated chemistry and radiative transfer models to predict molecular line emission and provide α_{CO} estimates (e.g., Gong et al., 2020; Hu et al., 2022), they are found to overestimate α_{CO} in dense and turbulent regions like galaxy centers (Teng et al., 2023). However, simulations incorporating nuclear gas inflows or large-scale turbulence do exist (Brucy et al., 2020; Moon et al., 2021), and combining such simulations with the established chemical network may be the key to produce reliable α_{CO} prediction that agrees with observations. This experiment, together with (i), are critical to achieving a robust α_{CO} prescription appropriate for diverse galactic environments.

(iii) Updating molecular cloud and star formation properties: While I have examined the effects of α_{CO} on SFE variations in Chapter 4, α_{CO} also impacts the estimation of other important quantities, including molecular cloud free-fall time, virial parameter, turbulent pressure, ISM dynamical equilibrium pressure, and various star formation scaling relations (Wilson et al., 2019; Pessa et al., 2021; den Brok et al., 2023; Sun et al., 2023; Querejeta et al., 2023). With newly developed α_{CO} prescriptions (e.g., Chiang et al., 2024; Teng et al., 2024), we can revisit all these quantities with updated α_{CO} and gain new insights on how molecular cloud and star formation evolve in galaxies. These updated quantities and relations also form a bridge to simulation studies (Orr et al., 2018; Brucy et al., 2020; Ostriker and Kim, 2022), providing a consistency check with experiment (ii).

In this dissertation, I have established the modeling and techniques for measuring molecular gas properties and α_{CO} with multi-line CO isotopologue observations (Teng et al., 2022), revealed the physical drivers and key observables for tracing α_{CO} variations in barred galaxy centers (Teng et al., 2023), and constructed a new α_{CO} prescription that can be applied across large galaxy samples for future molecular gas studies (Teng et al., 2024). Using the latest and best possible measurements of α_{CO} and molecular gas properties across a variety of galaxies, this dissertation reveals new trends in SFE variations and lays the foundation for benchmarking α_{CO} calibration in nearby galaxies.

The most beautiful thing we can experience is the mysterious.
It is the source of all true art and science.
—Albert Einstein

Acronyms

(U)LIRGs	(ultra)-luminous infrared galaxies.
AGN	active galactic nucleus.
ALMA	Atacama Large Millimeter/submillimeter Array.
CMZ	Central Molecular Zone.
CO	carbon monoxide.
FUV	far ultra-violet.
FWHM	full width half maximum.
GMC	giant molecular cloud.
HERACLES	HERA CO-Line Extragalactic Survey.
ISM	interstellar medium.
KS	Kennicutt-Schmidt.
LAS	largest angular structure.
LINER	low-ionization nuclear emission region.
LTE	local thermodynamic equilibrium.
LVG	Large Velocity Gradient.
MW	Milky Way.
PDF	probability density function.
PHANGS	Physics at High Angular resolution in Nearby GalaxieS.
rms	root-mean-square.
S/N	signal-to-noise ratio.
SED	spectral energy distribution.
SFE	star formation efficiency.
SFR	star formation rate.
SLED	spectral line energy distribution.
TP	total-power.

Bibliography

S. Aalto, R. Beswick, and E. Jütte (2010). "^{13}CO 1-0 imaging of the Medusa merger, NGC 4194. Large scale variations in molecular cloud properties." In: *A&A* 522, A59, A59. DOI: 10.1051/0004-6361/200913511 (cited on page 106).

S. Aalto, R. S. Booth, J. H. Black, and L. E. B. Johansson (1995). "Molecular gas in starburst galaxies: line intensities and physical conditions." In: *A&A* 300, p. 369 (cited on pages 105, 106).

A. A. Abdo et al. (2010). "Fermi Observations of Cassiopeia and Cepheus: Diffuse Gamma-ray Emission in the Outer Galaxy." In: *ApJ* 710.1, pp. 133–149. DOI: 10.1088/0004-637X/710/1/133. arXiv: 0912.3618 `[astro-ph.HE]` (cited on page 12).

G. Accurso, A. Saintonge, T. G. Bisbas, and S. Viti (2017a). "Radiative transfer meets Bayesian statistics: where does a galaxy's [C II] emission come from?" In: *MNRAS* 464.3, pp. 3315–3330. DOI: 10.1093/mnras/stw2580. arXiv: 1607.03488 `[astro-ph.GA]` (cited on pages 111, 138, 147, 149, 157).

G. Accurso, A. Saintonge, B. Catinella, L. Cortese, R. Davé, S. H. Dunsheath, R. Genzel, J. Gracia-Carpio, T. M. Heckman, Jimmy, C. Kramer, Cheng Li, K. Lutz, D. Schiminovich, K. Schuster, A. Sternberg, E. Sturm, L. J. Tacconi, K. V. Tran, and J. Wang (2017b). "Deriving a multivariate α_{CO} conversion function using the [C II]/CO (1-0) ratio and its application to molecular gas scaling relations." In: *MNRAS* 470.4, pp. 4750–4766. DOI: 10.1093/mnras/stx1556. arXiv: 1702.03888 `[astro-ph.GA]` (cited on pages 8, 12, 68, 111).

M. Ackermann et al. (2012a). "Fermi-LAT Observations of the Diffuse γ-Ray Emission: Implications for Cosmic Rays and the Interstellar Medium." In: *ApJ* 750.1, 3, p. 3. DOI: 10.1088/0004-637X/750/1/3. arXiv: 1202.4039 `[astro-ph.HE]` (cited on pages 13, 67, 137).

M. Ackermann et al. (2012b). "The cosmic-ray and gas content of the Cygnus region as measured in γ-rays by the Fermi Large Area Telescope." In: *A&A* 538, A71, A71. DOI: 10.1051/0004-6361/201117539. arXiv: 1110.6123 `[astro-ph.HE]` (cited on pages 12, 67).

D. Alloin and J. -L. Nieto (1982). "On the inner ring of HII regions in NGC 3351." In: *A&AS* 50, pp. 491–504 (cited on page 14).

R. Amorín, C. Muñoz-Tuñón, J. A. L. Aguerri, and P. Planesas (2016). "Molecular gas in low-metallicity starburst galaxies:. Scaling relations and the CO-to-H_2 conversion factor." In: *A&A* 588, A23, A23. DOI: 10.1051/0004-6361/201526397. arXiv: 1512.06153 `[astro-ph.GA]` (cited on pages 68, 138, 157).

Gagandeep S. Anand, Janice C. Lee, Schuyler D. Van Dyk, Adam K. Leroy, Erik Rosolowsky, Eva Schinnerer, Kirsten Larson, Ehsan Kourkchi, Kathryn Kreckel, Fabian Scheuermann, Luca Rizzi, David Thilker, R. Brent Tully, Frank Bigiel, Guillermo A. Blanc, Médéric Boquien, Rupali Chandar, Daniel Dale, Eric Emsellem, Sinan Deger, Simon C. O. Glover, Kathryn Grasha, Brent Groves, Ralf S. Klessen, J. M. Diederik Kruijssen, Miguel Querejeta, Patricia Sánchez-Blázquez, Andreas Schruba, Jordan Turner, Leonardo Ubeda, Thomas G. Williams, and Brad Whitmore (2021). "Distances to PHANGS galaxies: New tip of the red giant branch measurements and adopted distances." In: *MNRAS* 501.3, pp. 3621–3639. DOI: 10.1093/mnras/staa3668. arXiv: 2012.00757 `[astro-ph.GA]` (cited on pages 14, 70, 144).

M. B. Areal, S. Paron, M. Celis Peña, and M. E. Ortega (2018). "Exploring the $^{13}CO/C^{18}O$ abundance ratio towards Galactic young stellar objects and HII regions." In: *A&A* 612, A117, A117. DOI: 10.1051/0004-6361/201732067. arXiv: 1712.09578 `[astro-ph.GA]` (cited on pages 5, 14, 37, 92).

Lucia Armillotta, Mark R. Krumholz, Enrico M. Di Teodoro, and N. M. McClure-Griffiths (2019). "The life cycle of the Central Molecular Zone - I. Inflow, star formation, and winds." In: *MNRAS* 490.3, pp. 4401–4418. DOI: 10.1093/mnras/stz2880. arXiv: 1905.01309 `[astro-ph.GA]` (cited on page 156).

Astropy Collaboration, T. P. Robitaille, E. J. Tollerud, P. Greenfield, M. Droettboom, E. Bray, T. Aldcroft, M. Davis, A. Ginsburg, A. M. Price-Whelan, W. E. Kerzendorf, A. Conley, N. Crighton, K. Barbary, D. Muna, H. Ferguson, F. Grollier, M. M. Parikh, P. H. Nair, H. M. Unther, C. Deil, J. Woillez, S. Conseil, R. Kramer, J. E. H. Turner, L. Singer, R. Fox, B. A. Weaver, V. Zabalza, Z. I. Edwards, K. Azalee Bostroem, D. J. Burke, A. R. Casey, S. M. Crawford, N. Dencheva, J. Ely, T. Jenness, K. Labrie, P. L. Lim, F. Pierfederici, A. Pontzen, A. Ptak, B. Refsdal, M. Servillat, and O. Streicher (2013). "Astropy: A community Python package for astronomy." In: *A&A* 558, A33, A33. DOI: 10.1051/0004-6361/201322068. arXiv: 1307.6212 `[astro-ph.IM]` (cited on pages 63, 123, 162).

Astropy Collaboration et al. (2018). "The Astropy Project: Building an Open-science Project and Status of the v2.0 Core Package." In: *AJ* 156, 123, p. 123. DOI: 10.3847/1538-3881/aabc4f. arXiv: 1801.02634 `[astro-ph.IM]` (cited on pages 63, 123, 162).

A. T. Barnes, J. Kauffmann, F. Bigiel, N. Brinkmann, D. Colombo, A. E. Guzmán, W. J. Kim, L. Szűcs, V. Wakelam, S. Aalto, T. Albertsson, N. J. Evans, S. C. O. Glover, P. F.

Goldsmith, C. Kramer, K. Menten, Y. Nishimura, S. Viti, Y. Watanabe, A. Weiss, M. Wienen, H. Wiesemeyer, and F. Wyrowski (2020). "LEGO - II. A 3 mm molecular line study covering 100 pc of one of the most actively star-forming portions within the Milky Way disc." In: *MNRAS* 497.2, pp. 1972–2001. DOI: 10.1093/mnras/staa1814. arXiv: 2007.11005 `[astro-ph.GA]` (cited on page 14).

A. T. Barnes, S. N. Longmore, C. Battersby, J. Bally, J. M. D. Kruijssen, J. D. Henshaw, and D. L. Walker (2017). "Star formation rates and efficiencies in the Galactic Centre." In: *MNRAS* 469.2, pp. 2263–2285. DOI: 10.1093/mnras/stx941. arXiv: 1704.03572 `[astro-ph.GA]` (cited on page 39).

F. Belfiore, F. Santoro, B. Groves, E. Schinnerer, K. Kreckel, S. C. O. Glover, R. S. Klessen, E. Emsellem, G. A. Blanc, E. Congiu, A. T. Barnes, M. Boquien, M. Chevance, D. A. Dale, J. M. Diederik Kruijssen, A. K. Leroy, H. -A. Pan, I. Pessa, A. Schruba, and T. G. Williams (2022). "A tale of two DIGs: The relative role of H II regions and low-mass hot evolved stars in powering the diffuse ionised gas (DIG) in PHANGS-MUSE galaxies." In: *A&A* 659, A26, A26. DOI: 10.1051/0004-6361/202141859. arXiv: 2111.14876 `[astro-ph.GA]` (cited on pages 70, 91).

I. Bešlić, A. T. Barnes, F. Bigiel, J. Puschnig, J. Pety, C. Herrera Contreras, A. K. Leroy, A. Usero, E. Schinnerer, S. E. Meidt, E. Emsellem, A. Hughes, C. Faesi, K. Kreckel, F. M. C. Belfiore, M. Chevance, J. S. den Brok, C. Eibensteiner, S. C. O. Glover, K. Grasha, M. J. Jimenez-Donaire, R. S. Klessen, J. M. D. Kruijssen, D. Liu, I. Pessa, M. Querejeta, E. Rosolowsky, T. Saito, F. Santoro, A. Schruba, M. C. Sormani, and T. G. Williams (2021). "Dense molecular gas properties on 100 pc scales across the disc of NGC 3627." In: *MNRAS* 506.1, pp. 963–988. DOI: 10.1093/mnras/stab1776. arXiv: 2106.09742 `[astro-ph.GA]` (cited on page 74).

H. Beuther, S. Meidt, E. Schinnerer, R. Paladino, and A. Leroy (2017). "Interactions of the Galactic bar and spiral arm in NGC 3627." In: *A&A* 597, A85, A85. DOI: 10.1051/0004-6361/201526749. arXiv: 1609.06448 `[astro-ph.GA]` (cited on page 74).

F. Bigiel, I. de Looze, A. Krabbe, D. Cormier, A. T. Barnes, C. Fischer, A. D. Bolatto, A. Bryant, S. Colditz, N. Geis, R. Herrera-Camus, C. Iserlohe, R. Klein, A. K. Leroy, H. Linz, L. W. Looney, S. C. Madden, A. Poglitsch, J. Stutzki, and W. D. Vacca (2020). "SOFIA/FIFI-LS Full-disk [C II] Mapping and CO-dark Molecular Gas across the Nearby Spiral Galaxy NGC 6946." In: *ApJ* 903.1, 30, p. 30. DOI: 10.3847/1538-4357/abb677. arXiv: 2011.02498 `[astro-ph.GA]` (cited on page 12).

F. Bigiel, A. Leroy, F. Walter, E. Brinks, W. J. G. de Blok, B. Madore, and M. D. Thornley (2008). "The Star Formation Law in Nearby Galaxies on Sub-Kpc Scales." In: *AJ* 136.6, pp. 2846–2871. DOI: 10.1088/0004-6256/136/6/2846. arXiv: 0810.2541 `[astro-ph]` (cited on pages 2, 136).

Thomas G. Bisbas, Andreas Schruba, and Ewine F. van Dishoeck (2019). "Simulating the atomic and molecular content of molecular clouds using probability distributions of physical parameters.” In: *MNRAS* 485.3, pp. 3097–3111. DOI: 10.1093/mnras/stz405. arXiv: 1901.11306 `[astro-ph.GA]` (cited on page 39).

Thomas G. Bisbas, Jonathan C. Tan, and Kei E. I. Tanaka (2021). “Photodissociation region diagnostics across galactic environments.” In: *MNRAS* 502.2, pp. 2701–2732. DOI: 10.1093/mnras/stab121. arXiv: 2012.06773 `[astro-ph.GA]` (cited on pages 69, 94, 101).

Thomas G. Bisbas, Ewine F. van Dishoeck, Padelis P. Papadopoulos, László Szűcs, Shmuel Bialy, and Zhi-Yu Zhang (2017). “Cosmic-ray Induced Destruction of CO in Star-forming Galaxies.” In: *ApJ* 839.2, 90, p. 90. DOI: 10.3847/1538-4357/aa696d. arXiv: 1703.08598 `[astro-ph.GA]` (cited on page 101).

John H. Black, Ewine F. van Dishoeck, Steven P. Willner, and R. Claude Woods (1990). “Interstellar Absorption Lines toward NGC 2264 and AFGL 2591: Abundances of H 2, H + 3, and CO.” In: *ApJ* 358, p. 459. DOI: 10.1086/168999 (cited on page 44).

Geoffrey A. Blake, E. C. Sutton, C. R. Masson, and T. G. Phillips (1987). “Molecular Abundances in OMC-1: The Chemical Composition of Interstellar Molecular Clouds and the Influence of Massive Star Formation.” In: *ApJ* 315, p. 621. DOI: 10.1086/165165 (cited on page 100).

Guillermo A. Blanc, Andreas Schruba, II Evans Neal J., Shardha Jogee, Alberto Bolatto, Adam K. Leroy, Mimi Song, Remco C. E. van den Bosch, Niv Drory, Maximilian Fabricius, David Fisher, Karl Gebhardt, Amanda Heiderman, Irina Marinova, Stuart Vogel, and Tim Weinzirl (2013). “The VIRUS-P Exploration of Nearby Galaxies (VENGA): The X $_{CO}$ Gradient in NGC 628.” In: *ApJ* 764.2, 117, p. 117. DOI: 10.1088/0004-637X/764/2/117. arXiv: 1212.4152 `[astro-ph.GA]` (cited on pages 8, 12, 13).

L. Blitz, J. B. G. M. Bloemen, W. Hermsen, and T. M. Bania (1985). “The gamma-ray deficit toward the Galactic Center.” In: *A&A* 143, pp. 267–273 (cited on page 13).

Alberto D. Bolatto, Adam K. Leroy, Erik Rosolowsky, Fabian Walter, and Leo Blitz (2008). “The Resolved Properties of Extragalactic Giant Molecular Clouds.” In: *ApJ* 686.2, pp. 948–965. DOI: 10.1086/591513. arXiv: 0807.0009 `[astro-ph]` (cited on pages 12, 67).

Alberto D. Bolatto, Mark Wolfire, and Adam K. Leroy (2013). “The CO-to-H_2 Conversion Factor.” In: *ARA&A* 51.1, pp. 207–268. DOI: 10.1146/annurev-astro-082812-140944. arXiv: 1301.3498 `[astro-ph.GA]` (cited on pages 1, 7, 8, 11, 12, 44, 51, 54, 59, 66–68, 96, 99, 101, 104, 110, 115, 116, 121, 137, 138, 148–151, 156, 158, 160).

M. Bonato, E. Liuzzo, A. Giannetti, M. Massardi, G. De Zotti, S. Burkutean, V. Galluzzi, M. Negrello, I. Baronchelli, J. Brand, M. A. Zwaan, K. L. J. Rygl, N. Marchili, A. Klitsch, and I. Oteo (2018). “ALMACAL IV: a catalogue of ALMA calibrator continuum observations.” In: *MNRAS* 478.2, pp. 1512–1519. DOI: 10.1093/mnras/sty1173. arXiv: 1805.00024 [astro-ph.GA] (cited on page 29).

M. Bonato, E. Liuzzo, D. Herranz, J. González-Nuevo, L. Bonavera, M. Tucci, M. Massardi, G. De Zotti, M. Negrello, and M. A. Zwaan (2019). “ALMA photometry of extragalactic radio sources.” In: *MNRAS* 485.1, pp. 1188–1195. DOI: 10.1093/mnras/stz465. arXiv: 1901.08976 [astro-ph.GA] (cited on pages 29, 85).

F. Bournaud, E. Daddi, A. Weiß, F. Renaud, C. Mastropietro, and R. Teyssier (2015). “Modeling CO emission from hydrodynamic simulations of nearby spirals, starbursting mergers, and high-redshift galaxies.” In: *A&A* 575, A56, A56. DOI: 10.1051/0004-6361/201425078. arXiv: 1409.8157 [astro-ph.GA] (cited on page 69).

Noé Brucy, Patrick Hennebelle, Frédéric Bournaud, and Cédric Colling (2020). “Large-scale Turbulent Driving Regulates Star Formation in High-redshift Gas-rich Galaxies.” In: *ApJL* 896.2, L34, p. L34. DOI: 10.3847/2041-8213/ab9830. arXiv: 2006.02084 [astro-ph.GA] (cited on pages 165, 166).

Daniel Callanan, Steven N. Longmore, J. M. Diederik Kruijssen, Andreas Schruba, Adam Ginsburg, Mark R. Krumholz, Nate Bastian, João Alves, Jonathan D. Henshaw, Johan H. Knapen, and Mélanie Chevance (2021). “The centres of M83 and the Milky Way: opposite extremes of a common star formation cycle.” In: *MNRAS* 505.3, pp. 4310–4337. DOI: 10.1093/mnras/stab1527. arXiv: 2105.09761 [astro-ph.GA] (cited on page 13).

Daniela Calzetti, Andrew J. Battisti, Irene Shivaei, Matteo Messa, Michele Cignoni, Angela Adamo, Daniel A. Dale, John S. Gallagher, Kathryn Grasha, Eva K. Grebel, Robert C. Kennicutt, Sean T. Linden, Göran Östlin, Elena Sabbi, Linda J. Smith, Monica Tosi, and Aida Wofford (2021). “Revisiting Attenuation Curves: The Case of NGC 3351.” In: *ApJ* 913.1, 37, p. 37. DOI: 10.3847/1538-4357/abf118. arXiv: 2103.12117 [astro-ph.GA] (cited on pages 14, 15, 37).

CASA Team, Ben Bean, Sanjay Bhatnagar, Sandra Castro, Jennifer Donovan Meyer, Bjorn Emonts, Enrique Garcia, Robert Garwood, Kumar Golap, Justo Gonzalez Villalba, Pamela Harris, Yohei Hayashi, Josh Hoskins, Mingyu Hsieh, Preshanth Jagannathan, Wataru Kawasaki, Aard Keimpema, Mark Kettenis, Jorge Lopez, Joshua Marvil, Joseph Masters, Andrew McNichols, David Mehringer, Renaud Miel, George Moellenbrock, Federico Montesino, Takeshi Nakazato, Juergen Ott, Dirk Petry, Martin Pokorny, Ryan Raba, Urvashi Rau, Darrell Schiebel, Neal Schweighart, Srikrishna Sekhar, Kazuhiko Shimada, Des Small, Jan-Willem Steeb, Kanako Sugimoto, Ville Suoranta, Takahiro Tsutsumi, Ilse M. van Bemmel, Marjolein Verkouter, Akeem Wells, Wei Xiong, Arpad Szomoru, Morgan Griffith, Brian Glendenning, and Jeff Kern (2022). “CASA, the Common Astronomy Software Applications for Radio Astronomy.” In: *PASP* 134.1041, 114501, p. 114501. DOI: 10.1088/1538-3873/ac9642. arXiv: 2210.02276 [astro-ph.IM] (cited on page 123).

Mélanie Chevance, J. M. Diederik Kruijssen, Alexander P. S. Hygate, Andreas Schruba, Steven N. Longmore, Brent Groves, Jonathan D. Henshaw, Cinthya N. Herrera, Annie Hughes, Sarah M. R. Jeffreson, Philipp Lang, Adam K. Leroy, Sharon E. Meidt, Jérôme Pety, Alessandro Razza, Erik Rosolowsky, Eva Schinnerer, Frank Bigiel, Guillermo A. Blanc, Eric Emsellem, Christopher M. Faesi, Simon C. O. Glover, Daniel T. Haydon, I. -Ting Ho, Kathryn Kreckel, Janice C. Lee, Daizhong Liu, Miguel Querejeta, Toshiki Saito, Jiayi Sun, Antonio Usero, and Dyas Utomo (2020). "The lifecycle of molecular clouds in nearby star-forming disc galaxies." In: *MNRAS* 493.2, pp. 2872–2909. DOI: 10.1093/mnras/stz3525. arXiv: 1911.03479 `[astro-ph.GA]` (cited on page 74).

I-Da Chiang, Karin M. Sandstrom, Jérémy Chastenet, Alberto D. Bolatto, Eric W. Koch, Adam K. Leroy, Jiayi Sun, Yu-Hsuan Teng, and Thomas G. Williams (2024). "Resolved Measurements of the CO-to-H_2 Conversion Factor in 37 Nearby Galaxies." In: *ApJ* 964.1, 18, p. 18. DOI: 10.3847/1538-4357/ad23ed. arXiv: 2311.00407 `[astro-ph.GA]` (cited on pages 138, 145, 147, 149–152, 164, 166).

Claudia Cicone, Paola Severgnini, Padelis P. Papadopoulos, Roberto Maiolino, Chiara Feruglio, Ezequiel Treister, George C. Privon, Zhi-yu Zhang, Roberto Della Ceca, Fabrizio Fiore, Kevin Schawinski, and Jeff Wagg (2018). "ALMA [C I]^3 P $_1$-^{3} P $_0$ Observations of NGC 6240: A Puzzling Molecular Outflow, and the Role of Outflows in the Global α $_{CO}$ Factor of (U)LIRGs." In: *ApJ* 863.2, 143, p. 143. DOI: 10.3847/1538-4357/aad32a. arXiv: 1807.06015 `[astro-ph.GA]` (cited on pages 68, 137).

Luis Colina, María Luisa García Vargas, J. Miguel Mas-Hesse, A. Alberdi, and A. Krabbe (1997). "Nuclear Spiral and Ring Star-forming Structures and the Starburst–Active Galactic Nucleus Connection in Barred Spirals NGC 3351 and NGC 4303." In: *ApJL* 484.1, pp. L41–L45. DOI: 10.1086/310766 (cited on pages 14, 37).

D. Cormier, F. Bigiel, M. J. Jiménez-Donaire, A. K. Leroy, M. Gallagher, A. Usero, K. Sandstrom, A. Bolatto, A. Hughes, C. Kramer, M. R. Krumholz, D. S. Meier, E. J. Murphy, J. Pety, E. Rosolowsky, E. Schinnerer, A. Schruba, K. Sliwa, and F. Walter (2018). "Full-disc ^{13}CO(1-0) mapping across nearby galaxies of the EMPIRE survey and the CO-to-H_2 conversion factor." In: *MNRAS* 475.3, pp. 3909–3933. DOI: 10.1093/mnras/sty059. arXiv: 1801.03105 `[astro-ph.GA]` (cited on pages 8, 12, 107, 138).

R. I. Davies, F. Müller Sánchez, R. Genzel, L. J. Tacconi, E. K. S. Hicks, S. Friedrich, and A. Sternberg (2007). "A Close Look at Star Formation around Active Galactic Nuclei." In: *ApJ* 671.2, pp. 1388–1412. DOI: 10.1086/523032. arXiv: 0704.1374 `[astro-ph]` (cited on page 13).

Timothy A. Davis, Jindra Gensior, Martin Bureau, Michele Cappellari, Woorak Choi, Jacob S. Elford, J. M. Diederik Kruijssen, Federico Lelli, Fu-Heng Liang, Lijie Liu, Ilaria Ruffa, Toshiki Saito, Marc Sarzi, Andreas Schruba, and Thomas G. Williams (2022). "WISDOM Project - X. The morphology of the molecular ISM in galaxy centres and its dependence on galaxy structure." In: *MNRAS* 512.1, pp. 1522–1540. DOI: 10.1093/mnras/stac600. arXiv: 2203.01358 [astro-ph.GA] (cited on page 138).

P. De Vis, A. Jones, S. Viaene, V. Casasola, C. J. R. Clark, M. Baes, S. Bianchi, L. P. Cassara, J. I. Davies, I. De Looze, M. Galametz, F. Galliano, S. Lianou, S. Madden, A. Manilla-Robles, A. V. Mosenkov, A. Nersesian, S. Roychowdhury, E. M. Xilouris, and N. Ysard (2019). "A systematic metallicity study of DustPedia galaxies reveals evolution in the dust-to-metal ratios." In: *A&A* 623, A5, A5. DOI: 10.1051/0004-6361/201834444. arXiv: 1901.09040 [astro-ph.GA] (cited on pages 145, 149).

J. S. den Brok, D. Chatzigiannakis, F. Bigiel, J. Puschnig, A. T. Barnes, A. K. Leroy, M. J. Jiménez-Donaire, A. Usero, E. Schinnerer, E. Rosolowsky, C. M. Faesi, K. Grasha, A. Hughes, J. M. D. Kruijssen, D. Liu, L. Neumann, J. Pety, M. Querejeta, T. Saito, A. Schruba, and S. Stuber (2021). "New constraints on the ^{12}CO(2-1)/(1-0) line ratio across nearby disc galaxies." In: *MNRAS* 504.3, pp. 3221–3245. DOI: 10.1093/mnras/stab859. arXiv: 2103.10442 [astro-ph.GA] (cited on pages 49, 81, 103).

Jakob S. den Brok, Frank Bigiel, Jérémy Chastenet, Karin Sandstrom, Adam Leroy, Antonio Usero, Eva Schinnerer, Erik W. Rosolowsky, Eric W. Koch, I-Da Chiang, Ashley T. Barnes, Johannes Puschnig, Toshiki Saito, Ivana Bešlić, Melanie Chevance, Daniel A. Dale, Cosima Eibensteiner, Simon Glover, María J. Jiménez-Donaire, Yu-Hsuan Teng, and Thomas G. Williams (2023). "Wide-field CO isotopologue emission and the CO-to-H_2 factor across the nearby spiral galaxy M101." In: *A&A* 676, A93, A93. DOI: 10.1051/0004-6361/202245718. arXiv: 2302.03044 [astro-ph.GA] (cited on pages 1, 68, 95, 137, 138, 158, 166).

R. L. Dickman, Ronald L. Snell, and F. Peter Schloerb (1986). "Carbon Monoxide as an Extragalactic Mass Tracer." In: *ApJ* 309, p. 326. DOI: 10.1086/164604 (cited on page 44).

Jennifer Donovan Meyer, Jin Koda, Rieko Momose, Thomas Mooney, Fumi Egusa, Misty Carty, Robert Kennicutt, Nario Kuno, David Rebolledo, Tsuyoshi Sawada, Nick Scoville, and Tony Wong (2013). "Resolved Giant Molecular Clouds in Nearby Spiral Galaxies: Insights from the CANON CO (1-0) Survey." In: *ApJ* 772.2, 107, p. 107. DOI: 10.1088/0004-637X/772/2/107. arXiv: 1305.5275 [astro-ph.GA] (cited on pages 8, 12).

D. Downes and P. M. Solomon (1998). "Rotating Nuclear Rings and Extreme Starbursts in Ultraluminous Galaxies." In: *ApJ* 507.2, pp. 615–654. DOI: 10.1086/306339. arXiv: astro-ph/9806377 [astro-ph] (cited on pages 8, 13, 44, 67, 68, 114, 137).

Bruce T. Draine (2011). *Physics of the Interstellar and Intergalactic Medium* (cited on pages 6, 66, 151).

A. Duarte-Cabral, D. M. Acreman, C. L. Dobbs, J. C. Mottram, S. J. Gibson, C. M. Brunt, and K. A. Douglas (2015). "Synthetic CO, H_2 and H I surveys of the second galactic quadrant, and the properties of molecular gas." In: *MNRAS* 447.3, pp. 2144–2158. DOI: 10.1093/mnras/stu2586. arXiv: 1412.2785 `[astro-ph.GA]` (cited on page 69).

A. Eckart, D. Downes, R. Genzel, A. I. Harris, D. T. Jaffe, and W. Wild (1990). "Warm Gas and Spatial Variations of Molecular Excitation in the Nuclear Region of IC 342." In: *ApJ* 348, p. 434. DOI: 10.1086/168252 (cited on pages 5, 14).

Fumi Egusa, Yulong Gao, Kana Morokuma-Matsui, Guilin Liu, and Fumiya Maeda (2022). "CO Excitation and its Connection to Star Formation at 200 pc in NGC 1365." In: *ApJ* 935.2, 64, p. 64. DOI: 10.3847/1538-4357/ac8050. arXiv: 2207.05910 `[astro-ph.GA]` (cited on page 109).

Sara L. Ellison, Lihwai Lin, Mallory D. Thorp, Hsi-An Pan, Jillian M. Scudder, Sebastian F. Sánchez, Asa F. L. Bluck, and Roberto Maiolino (2021a). "The ALMaQUEST Survey - V. The non-universality of kpc-scale star formation relations and the factors that drive them." In: *MNRAS* 501.4, pp. 4777–4797. DOI: 10.1093/mnras/staa3822. arXiv: 2012.04771 `[astro-ph.GA]` (cited on page 136).

Sara L. Ellison, Mallory D. Thorp, Lihwai Lin, Hsi-An Pan, Asa F. L. Bluck, Jillian M. Scudder, Hossen Teimoorinia, Sebastian F. Sánchez, and Mark Sargent (2020a). "The ALMaQUEST survey - III. Scatter in the resolved star-forming main sequence is primarily due to variations in star formation efficiency." In: *MNRAS* 493.1, pp. L39–L43. DOI: 10.1093/mnrasl/slz179. arXiv: 1911.11887 `[astro-ph.GA]` (cited on page 158).

Sara L. Ellison, Mallory D. Thorp, Hsi-An Pan, Lihwai Lin, Jillian M. Scudder, Asa F. L. Bluck, Sebastian F. Sánchez, and Mark Sargent (2020b). "The ALMaQUEST Survey - II. What drives central starbursts at z ∼ 0?" In: *MNRAS* 492.4, pp. 6027–6041. DOI: 10.1093/mnras/staa001. arXiv: 2001.05003 `[astro-ph.GA]` (cited on pages 3, 137, 158).

Sara L. Ellison, Tony Wong, Sebastian F. Sánchez, Dario Colombo, Alberto Bolatto, Jorge Barrera-Ballesteros, Rubén García-Benito, Veselina Kalinova, Yufeng Luo, Monica Rubio, and Stuart N. Vogel (2021b). "The EDGE-CALIFA survey: central molecular gas depletion in AGN host galaxies - a smoking gun for quenching?" In: *MNRAS* 505.1, pp. L46–L51. DOI: 10.1093/mnrasl/slab047. arXiv: 2105.02916 `[astro-ph.GA]` (cited on page 136).

Debra Meloy Elmegreen, Frederick R. Chromey, Michael Santos, and Daniel Marshall (1997). "Near-Infrared Observations of Circumnuclear Star Formation in NGC 3351, NGC 3504, and NGC 5248." In: *AJ* 114, p. 1850. DOI: 10.1086/118610 (cited on page 15).

Eric Emsellem, Eva Schinnerer, Francesco Santoro, Francesco Belfiore, Ismael Pessa, Rebecca McElroy, Guillermo A. Blanc, Enrico Congiu, Brent Groves, I. -Ting Ho, Kathryn Kreckel, Alessandro Razza, Patricia Sanchez-Blazquez, Oleg Egorov, Chris Faesi, Ralf S. Klessen, Adam K. Leroy, Sharon Meidt, Miguel Querejeta, Erik Rosolowsky, Fabian Scheuermann, Gagandeep S. Anand, Ashley T. Barnes, Ivana Bešlić, Frank Bigiel, Médéric Boquien, Yixian Cao, Mélanie Chevance, Daniel A. Dale, Cosima Eibensteiner, Simon C. O. Glover, Kathryn Grasha, Jonathan D. Henshaw, Annie Hughes, Eric W. Koch, J. M. Diederik Kruijssen, Janice Lee, Daizhong Liu, Hsi-An Pan, Jérôme Pety, Toshiki Saito, Karin M. Sandstrom, Andreas Schruba, Jiayi Sun, David A. Thilker, Antonio Usero, Elizabeth J. Watkins, and Thomas G. Williams (2022). "The PHANGS-MUSE survey. Probing the chemo-dynamical evolution of disc galaxies." In: *A&A* 659, A191, A191. DOI: 10.1051/0004-6361/202141727. arXiv: 2110.03708 `[astro-ph.GA]` (cited on page 115).

C. Esteban, J. E. Méndez-Delgado, J. García-Rojas, and K. Z. Arellano-Córdova (2022). "About Metallicity Variations in the Local Galactic Interstellar Medium." In: *ApJ* 931.2, 92, p. 92. DOI: 10.3847/1538-4357/ac6b38. arXiv: 2204.12258 `[astro-ph.GA]` (cited on page 145).

Robert Feldmann, Nickolay Y. Gnedin, and Andrey V. Kravtsov (2012a). "The X-factor in Galaxies. I. Dependence on Environment and Scale." In: *ApJ* 747.2, 124, p. 124. DOI: 10.1088/0004-637X/747/2/124. arXiv: 1112.1732 `[astro-ph.CO]` (cited on pages 12, 67, 69).

Robert Feldmann, Nickolay Y. Gnedin, and Andrey V. Kravtsov (2012b). "The X-factor in Galaxies. II. The Molecular-hydrogen-Star-formation Relation." In: *ApJ* 758.2, 127, p. 127. DOI: 10.1088/0004-637X/758/2/127. arXiv: 1204.3910 `[astro-ph.CO]` (cited on pages 3, 68).

Mercedes E. Filho, Peter D. Barthel, and Luis C. Ho (2000). "The Nature of Composite LINER/H II Galaxies as Revealed from High-Resolution VLA Observations." In: *ApJS* 129.1, pp. 93–110. DOI: 10.1086/313412. arXiv: astro-ph/0002404 `[astro-ph]` (cited on pages 70, 91).

Daniel Foreman-Mackey (2016). "corner.py: Scatterplot matrices in Python." In: *Journal of Open Source Software* 1.2, p. 24. DOI: 10.21105/joss.00024. URL: https://doi.org/10.21105/joss.00024 (cited on pages 36, 63, 124).

M. A. Frerking, W. D. Langer, and R. W. Wilson (1982). "The relationship between carbon monoxide abundance and visual extinction in interstellar clouds." In: *ApJ* 262, pp. 590–605. DOI: 10.1086/160451 (cited on pages 44, 100).

Dimitri A. Gadotti, Patricia Sánchez-Blázquez, Jesús Falcón-Barroso, Bernd Husemann, Marja K. Seidel, Isabel Pérez, Adriana de Lorenzo-Cáceres, Inma Martinez-Valpuesta, Francesca Fragkoudi, Gigi Leung, Glenn van de Ven, Ryan Leaman, Paula Coelho, Marie Martig, Taehyun Kim, Justus Neumann, and Miguel Querejeta (2019). "Time Inference with MUSE in Extragalactic Rings (TIMER): properties of the survey and high-level data products." In: *MNRAS* 482.1, pp. 506–529. DOI: 10.1093/mnras/sty2666. arXiv: 1810.01425 `[astro-ph.GA]` (cited on page 15).

Molly J. Gallagher, Adam K. Leroy, Frank Bigiel, Diane Cormier, María J. Jiménez-Donaire, Eve Ostriker, Antonio Usero, Alberto D. Bolatto, Santiago García-Burillo, Annie Hughes, Amanda A. Kepley, Mark Krumholz, Sharon E. Meidt, David S. Meier, Eric J. Murphy, Jérôme Pety, Erik Rosolowsky, Eva Schinnerer, Andreas Schruba, and Fabian Walter (2018). "Dense Gas, Dynamical Equilibrium Pressure, and Star Formation in Nearby Star-forming Galaxies." In: *ApJ* 858.2, 90, p. 90. DOI: 10.3847/1538-4357/aabad8. arXiv: 1803.10785 `[astro-ph.GA]` (cited on page 55).

R. Genzel, L. J. Tacconi, F. Combes, A. Bolatto, R. Neri, A. Sternberg, M. C. Cooper, N. Bouché, F. Bournaud, A. Burkert, J. Comerford, P. Cox, M. Davis, N. M. Förster Schreiber, S. Garcia-Burillo, J. Gracia-Carpio, D. Lutz, T. Naab, S. Newman, A. Saintonge, K. Shapiro, A. Shapley, and B. Weiner (2012). "The Metallicity Dependence of the CO $\rightarrow$ H_2 Conversion Factor in z $>=$ 1 Star-forming Galaxies." In: *ApJ* 746.1, 69, p. 69. DOI: 10.1088/0004-637X/746/1/69. arXiv: 1106.2098 `[astro-ph.CO]` (cited on page 138).

Adam Ginsburg, Christian Henkel, Yiping Ao, Denise Riquelme, Jens Kauffmann, Thushara Pillai, Elisabeth A. C. Mills, Miguel A. Requena-Torres, Katharina Immer, Leonardo Testi, Juergen Ott, John Bally, Cara Battersby, Jeremy Darling, Susanne Aalto, Thomas Stanke, Sarah Kendrew, J. M. Diederik Kruijssen, Steven Longmore, James Dale, Rolf Guesten, and Karl M. Menten (2016). "Dense gas in the Galactic central molecular zone is warm and heated by turbulence." In: *A&A* 586, A50, A50. DOI: 10.1051/0004-6361/201526100. arXiv: 1509.01583 `[astro-ph.GA]` (cited on pages 37, 39, 56, 57).

Adam Ginsburg, Eric Koch, Thomas Robitaille, Chris Beaumont, Adamginsburg, Brigitta Sipőcz, John ZuHone, Sushobhana Patra, Craig Jones, P. L. Lim, Kris Stern, Erik Rosolowsky, Nicholas Earl, Miguel De Val-Borro, Jrobbfed, Shuokong, Amanda Kepley, Vlas Sokolov, The Gitter Badger, Sébastien Maret, Julián Garrido, Joseph Booker, and Erik Tollerud (2019). *radio-astro-tools/spectral-cube: Release v0.4.5*. Version v0.4.5. DOI: 10.5281/zenodo.3558614 (cited on page 63).

Simon C. O. Glover and Paul C. Clark (2012). "Star formation in metal-poor gas clouds." In: *MNRAS* 426.1, pp. 377–388. DOI: 10.1111/j.1365-2966.2012.21737.x. arXiv: 1203.4251 `[astro-ph.GA]` (cited on page 67).

Paul F. Goldsmith, Mark Heyer, Gopal Narayanan, Ronald Snell, Di Li, and Chris Brunt (2008). "Large-Scale Structure of the Molecular Gas in Taurus Revealed by High Linear Dynamic Range Spectral Line Mapping." In: *ApJ* 680.1, pp. 428–445. DOI: 10.1086/587166. arXiv: 0802.2206 `[astro-ph]` (cited on page 67).

Munan Gong, Eve C. Ostriker, and Chang-Goo Kim (2018). "The X_{CO} Conversion Factor from Galactic Multiphase ISM Simulations." In: *ApJ* 858.1, 16, p. 16. DOI: 10.3847/1538-4357/aab9af. arXiv: 1803.09822 `[astro-ph.GA]` (cited on pages 69, 94, 98).

Munan Gong, Eve C. Ostriker, Chang-Goo Kim, and Jeong-Gyu Kim (2020). “The Environmental Dependence of the X_{CO} Conversion Factor.” In: *ApJ* 903.2, 142, p. 142. DOI: 10.3847/1538-4357/abbdab. arXiv: 2009.14631 [astro-ph.GA] (cited on pages 8, 12, 59, 67–69, 96, 98, 101, 111–114, 137, 138, 151, 157, 165).

Karl D. Gordon, Julia Roman-Duval, Caroline Bot, Margaret Meixner, Brian Babler, Jean-Philippe Bernard, Alberto Bolatto, Martha L. Boyer, Geoffrey C. Clayton, Charles Engelbracht, Yasuo Fukui, Maud Galametz, Frederic Galliano, Sacha Hony, Annie Hughes, Remy Indebetouw, Frank P. Israel, Katherine Jameson, Akiko Kawamura, Vianney Lebouteiller, Aigen Li, Suzanne C. Madden, Mikako Matsuura, Karl Misselt, Edward Montiel, K. Okumura, Toshikazu Onishi, Pasquale Panuzzo, Deborah Paradis, Monica Rubio, Karin Sandstrom, Marc Sauvage, Jonathan Seale, Marta Sewiło, Kirill Tchernyshyov, and Ramin Skibba (2014). “Dust and Gas in the Magellanic Clouds from the HERITAGE Herschel Key Project. I. Dust Properties and Insights into the Origin of the Submillimeter Excess Emission.” In: *ApJ* 797.2, 85, p. 85. DOI: 10.1088/0004-637X/797/2/85. arXiv: 1406.6066 [astro-ph.GA] (cited on page 48).

A. D. Goulding and D. M. Alexander (2009). “Towards a complete census of AGN in nearby Galaxies: a large population of optically unidentified AGN.” In: *MNRAS* 398.3, pp. 1165–1193. DOI: 10.1111/j.1365-2966.2009.15194.x. arXiv: 0906.0772 [astro-ph.CO] (cited on page 15).

C. J. Grier, S. Mathur, H. Ghosh, and L. Ferrarese (2011). “Discovery of Nuclear X-ray Sources in Sings Galaxies.” In: *ApJ* 731.1, 60, p. 60. DOI: 10.1088/0004-637X/731/1/60. arXiv: 1011.4295 [astro-ph.GA] (cited on page 15).

Guillermo F. Hägele, Ángeles I. Díaz, Mónica V. Cardaci, Elena Terlevich, and Roberto Terlevich (2007). “Kinematics of gas and stars in the circumnuclear star-forming ring of NGC3351.” In: *MNRAS* 378.1, pp. 163–178. DOI: 10.1111/j.1365-2966.2007.11751.x. arXiv: astro-ph/0703140 [astro-ph] (cited on pages 14, 37).

Charles R. Harris, K. Jarrod Millman, St’efan J. van der Walt, Ralf Gommers, Pauli Virtanen, David Cournapeau, Eric Wieser, Julian Taylor, Sebastian Berg, Nathaniel J. Smith, Robert Kern, Matti Picus, Stephan Hoyer, Marten H. van Kerkwijk, Matthew Brett, Allan Haldane, Jaime Fern’andez del R’ıo, Mark Wiebe, Pearu Peterson, Pierre G’erard-Marchant, Kevin Sheppard, Tyler Reddy, Warren Weckesser, Hameer Abbasi, Christoph Gohlke, and Travis E. Oliphant (2020). “Array programming with NumPy.” In: *Nature* 585.7825, pp. 357–362. DOI: 10.1038/s41586-020-2649-2. URL: https://doi.org/10.1038/s41586-020-2649-2 (cited on pages 63, 123, 162).

H Perry Hatchfield, Mattia C. Sormani, Robin G. Tress, Cara Battersby, Rowan J. Smith, Simon C. O. Glover, and Ralf S. Klessen (2021). “Dynamically Driven Inflow onto the Galactic Center and its Effect upon Molecular Clouds.” In: *arXiv e-prints*, arXiv:2106.08461, arXiv:2106.08461. arXiv: 2106.08461 [astro-ph.GA] (cited on page 57).

Hao He, Christine Wilson, Jiayi Sun, Yu-Hsuan Teng, and Erik Rosolowsky (2024). “Unraveling the Mystery of the Low CO-to-H_2 Conversion Factor in Starburst Galaxies: RADEX Modeling of the Antennae.” In: *arXiv e-prints*, arXiv:2401.16476, arXiv:2401.16476. DOI: 10.48550/arXiv.2401.16476. arXiv: 2401.16476 [astro-ph.GA] (cited on pages 7, 165).

Tamara T. Helfer and Leo Blitz (1995). “High-Resolution Berkeley-Illinois-Maryland Association Observations of CO, HCN, and 13CO in NGC 1068.” In: *ApJ* 450, p. 90. DOI: 10.1086/176122 (cited on page 14).

C. Henkel, H. Asiri, Y. Ao, S. Aalto, A. L. R. Danielson, P. P. Papadopoulos, S. García-Burillo, R. Aladro, C. M. V. Impellizzeri, R. Mauersberger, S. Martín, and N. Harada (2014). “Carbon and oxygen isotope ratios in starburst galaxies: New data from NGC 253 and Mrk 231 and their implications.” In: *A&A* 565, A3, A3. DOI: 10.1051/0004-6361/201322962. arXiv: 1403.3974 [astro-ph.GA] (cited on page 92).

J. D. Henshaw, S. N. Longmore, J. M. D. Kruijssen, B. Davies, J. Bally, A. Barnes, C. Battersby, M. Burton, M. R. Cunningham, J. E. Dale, A. Ginsburg, K. Immer, P. A. Jones, S. Kendrew, E. A. C. Mills, S. Molinari, T. J. T. Moore, J. Ott, T. Pillai, J. Rathborne, P. Schilke, A. Schmiedeke, L. Testi, D. Walker, A. Walsh, and Q. Zhang (2016). *SCOUSE: Semi-automated multi-COmponent Universal Spectral-line fitting Engine*. Astrophysics Source Code Library, record ascl:1601.003. ascl: 1601.003 (cited on page 127).

R. Herrero-Illana, G. C. Privon, A. S. Evans, T. Díaz-Santos, M. Á. Pérez-Torres, V. U, A. Alberdi, K. Iwasawa, L. Armus, S. Aalto, J. Mazzarella, J. Chu, D. B. Sanders, L. Barcos-Muñoz, V. Charmandaris, S. T. Linden, I. Yoon, D. T. Frayer, H. Inami, D. -C. Kim, H. J. Borish, J. Conway, E. J. Murphy, Y. Song, S. Stierwalt, and J. Surace (2019). “Molecular gas and dust properties of galaxies from the Great Observatories All-sky LIRG Survey.” In: *A&A* 628, A71, A71. DOI: 10.1051/0004-6361/201834088. arXiv: 1907.03854 [astro-ph.GA] (cited on pages 67, 137).

Mark Heyer and T. M. Dame (2015). “Molecular Clouds in the Milky Way.” In: *ARA&A* 53, pp. 583–629. DOI: 10.1146/annurev-astro-082214-122324 (cited on pages 35, 85, 109).

Mark Heyer, Coleman Krawczyk, Julia Duval, and James M. Jackson (2009). “Re-Examining Larson’s Scaling Relationships in Galactic Molecular Clouds.” In: *ApJ* 699.2, pp. 1092–1103. DOI: 10.1088/0004-637X/699/2/1092. arXiv: 0809.1397 [astro-ph] (cited on pages 4, 157).

Mark H. Heyer, John M. Carpenter, and Ronald L. Snell (2001). “The Equilibrium State of Molecular Regions in the Outer Galaxy.” In: *ApJ* 551.2, pp. 852–866. DOI: 10.1086/320218. arXiv: astro-ph/0101133 [astro-ph] (cited on pages 21, 72).

Luis C. Ho, Alexei V. Filippenko, and Wallace L. W. Sargent (1997). “A Search for “Dwarf” Seyfert Nuclei. III. Spectroscopic Parameters and Properties of the Host Galaxies.”

In: *ApJS* 112.2, pp. 315–390. DOI: 10.1086/313041. arXiv: astro-ph/9704107 `[astro-ph]` (cited on pages 70, 91).

Chia-Yu Hu, Andreas Schruba, Amiel Sternberg, and Ewine F. van Dishoeck (2022). "Dependence of X $_{CO}$ on Metallicity, Intensity, and Spatial Scale in a Self-regulated Interstellar Medium." In: *ApJ* 931.1, 28, p. 28. DOI: 10.3847/1538-4357/ac65fd. arXiv: 2201.03885 `[astro-ph.GA]` (cited on pages 69, 98, 99, 111, 113, 114, 157, 165).

S. Huettemeister, T. L. Wilson, T. M. Bania, and J. Martin-Pintado (1993). "Kinetic temperatures in Galactic Center molecular clouds." In: *A&A* 280, pp. 255–267 (cited on page 42).

L. K. Hunt, S. García-Burillo, V. Casasola, P. Caselli, F. Combes, C. Henkel, A. Lundgren, R. Maiolino, K. M. Menten, L. Testi, and A. Weiss (2015). "Molecular depletion times and the CO-to-H_2 conversion factor in metal-poor galaxies." In: *A&A* 583, A114, A114. DOI: 10.1051/0004-6361/201526553. arXiv: 1509.04870 `[astro-ph.GA]` (cited on pages 138, 157).

J. D. Hunter (2007). "Matplotlib: A 2D graphics environment." In: *Computing In Science & Engineering* 9.3, pp. 90–95 (cited on pages 63, 123, 162).

S. Hüttemeister, S. Aalto, M. Das, and W. F. Wall (2000). "Changing molecular gas properties in the bar and center of NGC 7479." In: *A&A* 363, pp. 93–107 (cited on page 83).

Masatoshi Imanishi, Kouichiro Nakanishi, and Takuma Izumi (2018). "ALMA Multiple-transition Observations of High-density Molecular Tracers in Ultraluminous Infrared Galaxies." In: *ApJ* 856.2, 143, p. 143. DOI: 10.3847/1538-4357/aab42f. arXiv: 1803.02408 `[astro-ph.GA]` (cited on page 39).

N. Imara (2015). "Rethinking a Mysterious Molecular Cloud." In: *ApJ* 803.1, 38, p. 38. DOI: 10.1088/0004-637X/803/1/38. arXiv: 1503.02542 `[astro-ph.SR]` (cited on page 12).

F. Israel (2000). "Extragalactic H_2 and its Variable Relation to CO." In: *Molecular Hydrogen in Space*. Ed. by F. Combes and G. Pineau Des Forets, p. 293. arXiv: astro-ph/0001250 `[astro-ph]` (cited on page 67).

F. P. Israel (1997). "H_2 and its relation to CO in the LMC and other magellanic irregular galaxies." In: *A&A* 328, pp. 471–482. arXiv: astro-ph/9709194 `[astro-ph]` (cited on pages 67, 138).

F. P. Israel (2009a). "CI and CO in nearby galaxy centers. The bright galaxies NGC 1068 (M 77), NGC 2146, NGC 3079, NGC 4826 (M 64), and NGC 7469." In: *A&A* 493.2, pp. 525–538. DOI: 10.1051/0004-6361:200810655. arXiv: 0811.4058 `[astro-ph]` (cited on page 67).

F. P. Israel (2009b). “CI and CO in nearby galaxy centers. The star-burst galaxies NGC 278, NGC 660, NGC 3628 NGC 4631, and NGC 4666.” In: *A&A* 506.2, pp. 689–702. DOI: 10.1051/0004-6361/200811586. arXiv: 0908.3586 [astro-ph.CO] (cited on pages 5, 8, 13, 14, 67).

F. P. Israel (2020). “Central molecular zones in galaxies: ^{12}CO-to-^{13}CO ratios, carbon budget, and X factors.” In: *A&A* 635, A131, A131. DOI: 10.1051/0004-6361/201834198. arXiv: 2001.04975 [astro-ph.GA] (cited on pages 2, 5, 8, 13, 14, 39, 49, 67, 69, 95, 102–104, 120, 137, 138, 156).

Qian Jiao, Yu Gao, and Yinghe Zhao (2021). “The Carbon-to-H_2, CO-to-H_2 conversion factors, and carbon abundance on kiloparsec scales in nearby galaxies.” In: *MNRAS* 504.2, pp. 2360–2380. DOI: 10.1093/mnras/stab1035. arXiv: 2104.05985 [astro-ph.GA] (cited on pages 69, 103, 104).

María J. Jiménez-Donaire, Toby Brown, Christine D. Wilson, Ian D. Roberts, Nikki Zabel, Sara L. Ellison, Mallory Thorp, Vicente Villanueva, Ryan Chown, Dhruv Bisaria, Alberto D. Bolatto, Alessandro Boselli, Barbara Catinella, Aeree Chung, Luca Cortese, Timothy A. Davis, Claudia D. P. Lagos, Bumhyun Lee, Laura C. Parker, Kristine Spekkens, Adam R. H. Stevens, and Jiayi Sun (2023). “VERTICO. III. The Kennicutt-Schmidt relation in Virgo cluster galaxies.” In: *A&A* 671, A3, A3. DOI: 10.1051/0004-6361/202244718. arXiv: 2211.16521 [astro-ph.GA] (cited on page 136).

María J. Jiménez-Donaire, Diane Cormier, Frank Bigiel, Adam K. Leroy, Molly Gallagher, Mark R. Krumholz, Antonio Usero, Annie Hughes, Carsten Kramer, David Meier, Eric Murphy, Jérôme Pety, Eva Schinnerer, Andreas Schruba, Karl Schuster, Kazimierz Sliwa, and Neven Tomicic (2017). “^{13}CO/C^{18}O Gradients across the Disks of Nearby Spiral Galaxies.” In: *ApJL* 836.2, L29, p. L29. DOI: 10.3847/2041-8213/836/2/L29. arXiv: 1701.01734 [astro-ph.GA] (cited on pages 14, 40, 55).

W. A. Joye and E. Mandel (2003). “New Features of SAOImage DS9.” In: *Astronomical Data Analysis Software and Systems XII*. Ed. by H. E. Payne, R. I. Jedrzejewski, and R. N. Hook. Vol. 295. Astronomical Society of the Pacific Conference Series, p. 489 (cited on pages 63, 123).

J. Kainulainen, H. Beuther, T. Henning, and R. Plume (2009). “Probing the evolution of molecular cloud structure. From quiescence to birth.” In: *A&A* 508.3, pp. L35–L38. DOI: 10.1051/0004-6361/200913605. arXiv: 0911.5648 [astro-ph.GA] (cited on page 158).

J. Kamenetzky, J. Glenn, N. Rangwala, P. Maloney, M. Bradford, C. D. Wilson, G. J. Bendo, M. Baes, A. Boselli, A. Cooray, K. G. Isaak, V. Lebouteiller, S. Madden, P. Panuzzo, M. R. P. Schirm, L. Spinoglio, and R. Wu (2012). “Herschel-SPIRE Imaging Spectroscopy of Molecular Gas in M82.” In: *ApJ* 753.1, 70, p. 70. DOI: 10.1088/0004-637X/753/1/70. arXiv: 1205.0006 [astro-ph.GA] (cited on pages 35, 45, 84, 94).

J. Kamenetzky, N. Rangwala, and J. Glenn (2017). “Warm and cold molecular gas conditions modelled in 87 galaxies observed by the Herschel SPIRE Fourier transform spectrometer.” In: *MNRAS* 471.3, pp. 2917–2931. DOI: 10.1093/mnras/stx1595. arXiv: 1706.09900 `[astro-ph.GA]` (cited on pages 8, 67).

J. Kamenetzky, N. Rangwala, J. Glenn, P. R. Maloney, and A. Conley (2014). “A Survey of the Molecular ISM Properties of Nearby Galaxies Using the Herschel FTS.” In: *ApJ* 795.2, 174, p. 174. DOI: 10.1088/0004-637X/795/2/174. arXiv: 1409.7062 `[astro-ph.GA]` (cited on pages 7, 35, 39, 44, 45, 67, 94).

M. V. Kazandjian, R. Meijerink, I. Pelupessy, F. P. Israel, and M. Spaans (2012). “Diagnostics of the molecular component of photon-dominated regions with mechanical heating.” In: *A&A* 542, A65, A65. DOI: 10.1051/0004-6361/201118641. arXiv: 1203.5058 `[astro-ph.CO]` (cited on page 67).

M. V. Kazandjian, R. Meijerink, I. Pelupessy, F. P. Israel, and M. Spaans (2015). “Diagnostics of the molecular component of photon-dominated regions with mechanical heating. II. Line intensities and ratios.” In: *A&A* 574, A127, A127. DOI: 10.1051/0004-6361/201322805. arXiv: 1403.7000 `[astro-ph.GA]` (cited on page 67).

Jr. Kennicutt Robert C. (1998). “The Global Schmidt Law in Star-forming Galaxies.” In: *ApJ* 498.2, pp. 541–552. DOI: 10.1086/305588. arXiv: astro-ph/9712213 `[astro-ph]` (cited on pages 2, 68, 136).

Robert C. Kennicutt and Neal J. Evans (2012). “Star Formation in the Milky Way and Nearby Galaxies.” In: *ARA&A* 50, pp. 531–608. DOI: 10.1146/annurev-astro-081811-125610. arXiv: 1204.3552 `[astro-ph.GA]` (cited on pages 3, 11).

Woong-Tae Kim, Woo-Young Seo, James M. Stone, Doosoo Yoon, and Peter J. Teuben (2012). “Central Regions of Barred Galaxies: Two-dimensional Non-self-gravitating Hydrodynamic Simulations.” In: *ApJ* 747.1, 60, p. 60. DOI: 10.1088/0004-637X/747/1/60. arXiv: 1112.6055 `[astro-ph.GA]` (cited on page 158).

Jin Koda, Akihiko Hirota, Fumi Egusa, Kazushi Sakamoto, Tsuyoshi Sawada, Mark Heyer, Junichi Baba, Samuel Boissier, Daniela Calzetti, Jennifer Donovan Meyer, Bruce G. Elmegreen, Armando Gil de Paz, Nanase Harada, Luis C. Ho, Masato I. N. Kobayashi, Nario Kuno, Amanda M. Lee, Barry F. Madore, Fumiya Maeda, Sergio Martín, Kazuyuki Muraoka, Kouichiro Nakanishi, Sachiko Onodera, Jorge L. Pineda, Nick Scoville, and Yoshimasa Watanabe (2023). “Diverse Molecular Structures across the Whole Star-forming Disk of M83: High-fidelity Imaging at 40 pc Resolution.” In: *ApJ* 949.2, 108, p. 108. DOI: 10.3847/1538-4357/acc65e. arXiv: 2303.12108 `[astro-ph.GA]` (cited on page 138).

S. König, S. Aalto, S. Muller, J. S. Gallagher, R. J. Beswick, C. K. Xu, and A. Evans (2016). “Deep ALMA imaging of the merger NGC 1614. Is CO tracing a massive inflow of non-starforming gas?" In: *A&A* 594, A70, A70. DOI: 10.1051/0004-6361/201628535. arXiv: 1603.05405 `[astro-ph.GA]` (cited on page 13).

John Kormendy and Jr. Kennicutt Robert C. (2004). "Secular Evolution and the Formation of Pseudobulges in Disk Galaxies." In: *ARA&A* 42.1, pp. 603–683. DOI: 10.1146/annurev.astro.42.053102.134024. arXiv: astro-ph/0407343 `[astro-ph]` (cited on page 158).

K. Kreckel, I. -T. Ho, G. A. Blanc, B. Groves, F. Santoro, E. Schinnerer, F. Bigiel, M. Chevance, E. Congiu, E. Emsellem, C. Faesi, S. C. O. Glover, K. Grasha, J. M. D. Kruijssen, P. Lang, A. K. Leroy, S. E. Meidt, R. McElroy, J. Pety, E. Rosolowsky, T. Saito, K. Sandstrom, P. Sanchez-Blazquez, and A. Schruba (2019). "Mapping Metallicity Variations across Nearby Galaxy Disks." In: *ApJ* 887.1, 80, p. 80. DOI: 10.3847/1538-4357/ab5115. arXiv: 1910.07190 `[astro-ph.GA]` (cited on pages 70, 145).

Kathryn Kreckel, I. -Ting Ho, Guillermo A. Blanc, Simon C. O. Glover, Brent Groves, Erik Rosolowsky, Frank Bigiel, Médéric Boquíen, Mélanie Chevance, Daniel A. Dale, Sinan Deger, Eric Emsellem, Kathryn Grasha, Jenny J. Kim, Ralf S. Klessen, J. M. Diederik Kruijssen, Janice C. Lee, Adam K. Leroy, Daizhong Liu, Rebecca McElroy, Sharon E. Meidt, Ismael Pessa, Patricia Sanchez-Blazquez, Karin Sandstrom, Francesco Santoro, Fabian Scheuermann, Eva Schinnerer, Andreas Schruba, Dyas Utomo, Elizabeth J. Watkins, and Thomas G. Williams (2020). "Measuring the mixing scale of the ISM within nearby spiral galaxies." In: *MNRAS* 499.1, pp. 193–209. DOI: 10.1093/mnras/staa2743. arXiv: 2009.02342 `[astro-ph.GA]` (cited on page 70).

Nico Krieger, Jürgen Ott, Henrik Beuther, Fabian Walter, J. M. Diederik Kruijssen, David S. Meier, Elisabeth A. C. Mills, Yanett Contreras, Phil Edwards, Adam Ginsburg, Christian Henkel, Jonathan Henshaw, James Jackson, Jens Kauffmann, Steven Longmore, Sergio Martín, Mark R. Morris, Thushara Pillai, Matthew Rickert, Erik Rosolowsky, Hiroko Shinnaga, Andrew Walsh, Farhad Yusef-Zadeh, and Qizhou Zhang (2017). "The Survey of Water and Ammonia in the Galactic Center (SWAG): Molecular Cloud Evolution in the Central Molecular Zone." In: *ApJ* 850.1, 77, p. 77. DOI: 10.3847/1538-4357/aa951c. arXiv: 1710.06902 `[astro-ph.GA]` (cited on pages 37, 39, 42, 56, 137).

J. M. D. Kruijssen, J. E. Dale, S. N. Longmore, D. L. Walker, J. D. Henshaw, S. M. R. Jeffreson, M. A. Petkova, A. Ginsburg, A. T. Barnes, C. D. Battersby, K. Immer, J. M. Jackson, E. R. Keto, N. Krieger, E. A. C. Mills, Á. Sánchez-Monge, A. Schmiedeke, S. T. Suri, and Q. Zhang (2019). "The dynamical evolution of molecular clouds near the Galactic Centre - II. Spatial structure and kinematics of simulated clouds." In: *MNRAS* 484.4, pp. 5734–5754. DOI: 10.1093/mnras/stz381. arXiv: 1902.01860 `[astro-ph.GA]` (cited on page 57).

Mark R. Krumholz (2015). "Notes on Star Formation." In: *arXiv e-prints*, arXiv:1511.03457, arXiv:1511.03457. DOI: 10.48550/arXiv.1511.03457. arXiv: 1511.03457 `[astro-ph.GA]` (cited on page 151).

Craig Alan Kulesa (2002). “Molecular hydrogen and its ions in dark interstellar clouds and star forming regions.” PhD thesis. University of Arizona (cited on page 100).

Nario Kuno, Naoko Sato, Hiroyuki Nakanishi, Akihiko Hirota, Tomoka Tosaki, Yasuhiro Shioya, Kazuo Sorai, Naomasa Nakai, Kota Nishiyama, and Baltsar Vila-Vilaró (2007). “Nobeyama CO Atlas of Nearby Spiral Galaxies: Distribution of Molecular Gas in Barred and Nonbarred Spiral Galaxies.” In: *PASJ* 59, pp. 117–166. DOI: 10.1093/pasj/59.1.117. arXiv: 0705.2678 `[astro-ph]` (cited on page 158).

J. H. Lacy, R. Knacke, T. R. Geballe, and A. T. Tokunaga (1994). “Detection of Absorption by H 2 in Molecular Clouds: A Direct Measurement of the H 2:CO Ratio.” In: *ApJL* 428, p. L69. DOI: 10.1086/187395 (cited on pages 35, 44, 85, 94).

Philipp Lang, Sharon E. Meidt, Erik Rosolowsky, Joseph Nofech, Eva Schinnerer, Adam K. Leroy, Eric Emsellem, Ismael Pessa, Simon C. O. Glover, Brent Groves, Annie Hughes, J. M. Diederik Kruijssen, Miguel Querejeta, Andreas Schruba, Frank Bigiel, Guillermo A. Blanc, Mélanie Chevance, Dario Colombo, Christopher Faesi, Jonathan D. Henshaw, Cinthya N. Herrera, Daizhong Liu, Jérôme Pety, Johannes Puschnig, Toshiki Saito, Jiayi Sun, and Antonio Usero (2020). “PHANGS CO Kinematics: Disk Orientations and Rotation Curves at 150 pc Resolution.” In: *ApJ* 897.2, 122, p. 122. DOI: 10.3847/1538-4357/ab9953. arXiv: 2005.11709 `[astro-ph.GA]` (cited on pages 14, 15, 20, 70, 144).

William D. Langer and Arno A. Penzias (1990). “12C/ 13C Isotope Ratio across the Galaxy from Observations of 13C 18O in Molecular Clouds.” In: *ApJ* 357, p. 477. DOI: 10.1086/168935 (cited on pages 14, 37).

R. B. Larson (1981). “Turbulence and star formation in molecular clouds.” In: *MNRAS* 194, pp. 809–826. DOI: 10.1093/mnras/194.4.809 (cited on page 4).

Ryan Leaman, Francesca Fragkoudi, Miguel Querejeta, Gigi Y. C. Leung, Dimitri A. Gadotti, Bernd Husemann, Jesus Falcón-Barroso, Patricia Sánchez-Blázquez, Glenn van de Ven, Taehyun Kim, Paula Coelho, Mariya Lyubenova, Adriana de Lorenzo-Cáceres, Marie Martig, Inma Martinez-Valpuesta, Justus Neumann, Isabel Pérez, and Marja Seidel (2019). “Survival of molecular gas in a stellar feedback-driven outflow witnessed with the MUSE TIMER project and ALMA.” In: *MNRAS* 488.3, pp. 3904–3928. DOI: 10.1093/mnras/stz1844. arXiv: 1907.13142 `[astro-ph.GA]` (cited on pages 15, 20, 46, 47).

Adam K. Leroy, Alberto Bolatto, Karl Gordon, Karin Sandstrom, Pierre Gratier, Erik Rosolowsky, Charles W. Engelbracht, Norikazu Mizuno, Edvige Corbelli, Yasuo Fukui, and Akiko Kawamura (2011). “The CO-to-H_2 Conversion Factor from Infrared Dust Emission across the Local Group.” In: *ApJ* 737.1, 12, p. 12. DOI: 10.1088/0004-637X/737/1/12. arXiv: 1102.4618 `[astro-ph.CO]` (cited on pages 8, 12, 67, 138).

Adam K. Leroy, Alberto D. Bolatto, Eve C. Ostriker, Erik Rosolowsky, Fabian Walter, Steven R. Warren, Jennifer Donovan Meyer, Jacqueline Hodge, David S. Meier, Jürgen Ott, Karin Sandstrom, Andreas Schruba, Sylvain Veilleux, and Martin Zwaan (2015). "ALMA Reveals the Molecular Medium Fueling the Nearest Nuclear Starburst." In: *ApJ* 801.1, 25, p. 25. DOI: 10.1088/0004-637X/801/1/25. arXiv: 1411.2836 `[astro-ph.GA]` (cited on pages 12, 39, 59).

Adam K. Leroy, Annie Hughes, Daizhong Liu, Jérôme Pety, Erik Rosolowsky, Toshiki Saito, Eva Schinnerer, Andreas Schruba, Antonio Usero, Christopher M. Faesi, Cinthya N. Herrera, Mélanie Chevance, Alexander P. S. Hygate, Amanda A. Kepley, Eric W. Koch, Miguel Querejeta, Kazimierz Sliwa, David Will, Christine D. Wilson, Gagandeep S. Anand, Ashley Barnes, Francesco Belfiore, Ivana Bešlić, Frank Bigiel, Guillermo A. Blanc, Alberto D. Bolatto, Mèdèric Boquien, Yixian Cao, Rupali Chandar, Jérémy Chastenet, I. -Da Chiang, Enrico Congiu, Daniel A. Dale, Sinan Deger, Jakob S. den Brok, Cosima Eibensteiner, Eric Emsellem, Axel García-Rodríguez, Simon C. O. Glover, Kathryn Grasha, Brent Groves, Jonathan D. Henshaw, María J. Jiménez Donaire, Jaeyeon Kim, Ralf S. Klessen, Kathryn Kreckel, J. M. Diederik Kruijssen, Kirsten L. Larson, Janice C. Lee, Ness Mayker, Rebecca McElroy, Sharon E. Meidt, Angus Mok, Hsi-An Pan, Johannes Puschnig, Alessandro Razza, Patricia Sánchez-Bl'azquez, Karin M. Sandstrom, Francesco Santoro, Amy Sardone, Fabian Scheuermann, Jiayi Sun, David A. Thilker, Jordan A. Turner, Leonardo Ubeda, Dyas Utomo, Elizabeth J. Watkins, and Thomas G. Williams (2021a). "PHANGS-ALMA Data Processing and Pipeline." In: *ApJS* 255.1, 19, p. 19. DOI: 10.3847/1538-4365/abec80. arXiv: 2104.07665 `[astro-ph.IM]` (cited on pages 18, 19, 29, 71).

Adam K. Leroy, Erik Rosolowsky, Antonio Usero, Karin Sandstrom, Eva Schinnerer, Andreas Schruba, Alberto D. Bolatto, Jiayi Sun, Ashley. T. Barnes, Francesco Belfiore, Frank Bigiel, Jakob S. den Brok, Yixian Cao, I. -Da Chiang, Mélanie Chevance, Daniel A. Dale, Cosima Eibensteiner, Christopher M. Faesi, Simon C. O. Glover, Annie Hughes, María J. Jiménez Donaire, Ralf S. Klessen, Eric W. Koch, J. M. Diederik Kruijssen, Daizhong Liu, Sharon E. Meidt, Hsi-An Pan, Jérôme Pety, Johannes Puschnig, Miguel Querejeta, Toshiki Saito, Amy Sardone, Elizabeth J. Watkins, Axel Weiss, and Thomas G. Williams (2022). "Low-J CO Line Ratios from Single-dish CO Mapping Surveys and PHANGS-ALMA." In: *ApJ* 927.2, 149, p. 149. DOI: 10.3847/1538-4357/ac3490. arXiv: 2109.11583 `[astro-ph.GA]` (cited on page 81).

Adam K. Leroy, Eva Schinnerer, Annie Hughes, Erik Rosolowsky, Jérôme Pety, Andreas Schruba, Antonio Usero, Guillermo A. Blanc, Mélanie Chevance, Eric Emsellem, Christopher M. Faesi, Cinthya N. Herrera, Daizhong Liu, Sharon E. Meidt, Miguel Querejeta, Toshiki Saito, Karin M. Sandstrom, Jiayi Sun, Thomas G. Williams, Gagandeep S. Anand, Ashley T. Barnes, Erica A. Behrens, Francesco Belfiore, Samantha M. Benincasa, Ivana Bešlić, Frank Bigiel, Alberto D. Bolatto, Jakob S. den Brok, Yixian Cao, Rupali Chandar, Jérémy Chastenet, I. -Da Chiang, Enrico Congiu, Daniel A. Dale, Sinan Deger, Cosima Eibensteiner, Oleg V. Egorov, Axel García-Rodríguez, Simon C. O. Glover, Kathryn Grasha, Jonathan D. Henshaw, I. -Ting Ho, Amanda A.

Kepley, Jaeyeon Kim, Ralf S. Klessen, Kathryn Kreckel, Eric W. Koch, J. M. Diederik Kruijssen, Kirsten L. Larson, Janice C. Lee, Laura A. Lopez, Josh Machado, Ness Mayker, Rebecca McElroy, Eric J. Murphy, Eve C. Ostriker, Hsi-An Pan, Ismael Pessa, Johannes Puschnig, Alessandro Razza, Patricia Sánchez-Blázquez, Francesco Santoro, Amy Sardone, Fabian Scheuermann, Kazimierz Sliwa, Mattia C. Sormani, Sophia K. Stuber, David A. Thilker, Jordan A. Turner, Dyas Utomo, Elizabeth J. Watkins, and Bradley Whitmore (2021b). "PHANGS-ALMA: Arcsecond CO(2-1) Imaging of Nearby Star-forming Galaxies." In: *ApJS* 257.2, 43, p. 43. DOI: 10.3847/1538-4365/ac17f3. arXiv: 2104.07739 `[astro-ph.GA]` (cited on pages 14, 18, 70–72, 138, 139, 164).

Adam K. Leroy, Antonio Usero, Andreas Schruba, Frank Bigiel, J. M. Diederik Kruijssen, Amanda Kepley, Guillermo A. Blanc, Alberto D. Bolatto, Diane Cormier, Molly Gallagher, Annie Hughes, Maria J. Jiménez-Donaire, Erik Rosolowsky, and Eva Schinnerer (2017). "Millimeter-wave Line Ratios and Sub-beam Volume Density Distributions." In: *ApJ* 835.2, 217, p. 217. DOI: 10.3847/1538-4357/835/2/217. arXiv: 1611.09864 `[astro-ph.GA]` (cited on page 39).

Adam K. Leroy, Fabian Walter, Frank Bigiel, Antonio Usero, Axel Weiss, Elias Brinks, W. J. G. de Blok, Robert C. Kennicutt, Karl-Friedrich Schuster, Carsten Kramer, H. W. Wiesemeyer, and Hélène Roussel (2009). "Heracles: The HERA CO Line Extragalactic Survey." In: *AJ* 137.6, pp. 4670–4696. DOI: 10.1088/0004-6256/137/6/4670. arXiv: 0905.4742 `[astro-ph.CO]` (cited on page 14).

Adam K. Leroy, Fabian Walter, Elias Brinks, Frank Bigiel, W. J. G. de Blok, Barry Madore, and M. D. Thornley (2008). "The Star Formation Efficiency in Nearby Galaxies: Measuring Where Gas Forms Stars Effectively." In: *AJ* 136.6, pp. 2782–2845. DOI: 10.1088/0004-6256/136/6/2782. arXiv: 0810.2556 `[astro-ph]` (cited on pages 1, 136, 160).

Adam K. Leroy, Fabian Walter, Karin Sandstrom, Andreas Schruba, Juan-Carlos Munoz-Mateos, Frank Bigiel, Alberto Bolatto, Elias Brinks, W. J. G. de Blok, Sharon Meidt, Hans-Walter Rix, Erik Rosolowsky, Eva Schinnerer, Karl-Friedrich Schuster, and Antonio Usero (2013). "Molecular Gas and Star Formation in nearby Disk Galaxies." In: *AJ* 146.2, 19, p. 19. DOI: 10.1088/0004-6256/146/2/19. arXiv: 1301.2328 `[astro-ph.CO]` (cited on pages 3, 68, 137, 158).

Lihwai Lin, Hsi-An Pan, Sara L. Ellison, Francesco Belfiore, Yong Shi, Sebastián F. Sánchez, Bau-Ching Hsieh, Kate Rowlands, S. Ramya, Mallory D. Thorp, Cheng Li, and Roberto Maiolino (2019). "The ALMaQUEST Survey: The Molecular Gas Main Sequence and the Origin of the Star-forming Main Sequence." In: *ApJL* 884.2, L33, p. L33. DOI: 10.3847/2041-8213/ab4815. arXiv: 1909.11243 `[astro-ph.GA]` (cited on page 68).

Ming-Yi Lin, R. I. Davies, E. K. S. Hicks, L. Burtscher, A. Contursi, R. Genzel, M. Koss, D. Lutz, W. Maciejewski, F. Müller-Sánchez, G. Orban de Xivry, C. Ricci, R. Riffel, R. A. Riffel, D. Rosario, M. Schartmann, A. Schnorr-Müller, T. Shimizu, A. Sternberg, E. Sturm, T. Storchi-Bergmann, L. Tacconi, and S. Veilleux (2018). "LLAMA: nuclear stellar properties of Swift-BAT AGN and matched inactive galaxies." In: *MNRAS* 473.4, pp. 4582–4611. DOI: 10.1093/mnras/stx2618. arXiv: 1710.04098 [astro-ph.GA] (cited on page 15).

S. T. Linden, E. J. Murphy, D. Dong, E. Momjian, Jr. Kennicutt R. C., D. S. Meier, E. Schinnerer, and J. L. Turner (2020). "The Star Formation in Radio Survey: 3-33 GHz Imaging of Nearby Galaxy Nuclei and Extranuclear Star-forming Regions." In: *ApJS* 248.2, 25, p. 25. DOI: 10.3847/1538-4365/ab8a4d. arXiv: 2004.10230 [astro-ph.GA] (cited on pages 14, 37).

Daizhong Liu, Emanuele Daddi, Eva Schinnerer, Toshiki Saito, Adam Leroy, John D. Silverman, Francesco Valentino, Georgios E. Magdis, Yu Gao, Shuowen Jin, Annagrazia Puglisi, and Brent Groves (2021). "CO Excitation, Molecular Gas Density, and Interstellar Radiation Field in Local and High-redshift Galaxies." In: *ApJ* 909.1, 56, p. 56. DOI: 10.3847/1538-4357/abd801. arXiv: 2101.06646 [astro-ph.GA] (cited on page 39).

Daizhong Liu, Yu Gao, Kate Isaak, Emanuele Daddi, Chentao Yang, Nanyao Lu, and Paul van der Werf (2015). "High-J CO versus Far-infrared Relations in Normal and Starburst Galaxies." In: *ApJL* 810.2, L14, p. L14. DOI: 10.1088/2041-8205/810/2/L14. arXiv: 1504.05897 [astro-ph.GA] (cited on page 39).

Daizhong Liu, Eva Schinnerer, Yixian Cao, Adam Leroy, Antonio Usero, Erik Rosolowsky, J. M. Diederik Kruijssen, Mélanie Chevance, Simon C. O. Glover, Mattia C. Sormani, Alberto D. Bolatto, Jiayi Sun, Sophia K. Stuber, Yu-Hsuan Teng, Frank Bigiel, Ivana Bešlić, Kathryn Grasha, Jonathan D. Henshaw, Ashley T. Barnes, Jakob S. den Brok, Toshiki Saito, Daniel A. Dale, Elizabeth J. Watkins, Hsi-An Pan, Ralf S. Klessen, Eric Emsellem, Gagandeep S. Anand, Sinan Deger, Oleg V. Egorov, Christopher M. Faesi, Hamid Hassani, Kirsten L. Larson, Janice C. Lee, Laura A. Lopez, Jérôme Pety, Karin Sandstrom, David A. Thilker, Bradley C. Whitmore, and Thomas G. Williams (2023). "PHANGS-JWST First Results: Stellar-feedback-driven Excitation and Dissociation of Molecular Gas in the Starburst Ring of NGC 1365?" In: *ApJL* 944.2, L19, p. L19. DOI: 10.3847/2041-8213/aca973. arXiv: 2212.09652 [astro-ph.GA] (cited on pages 94, 158).

Daizhong Liu, Eva Schinnerer, Toshiki Saito, Erik Rosolowsky, Adam Leroy, Antonio Usero, Karin Sandstrom, Ralf S. Klessen, Simon C. O. Glover, Yiping Ao, Ivana Bešlić, Frank Bigiel, Yixian Cao, Jérémy Chastenet, Mélanie Chevance, Daniel A. Dale, Yu Gao, Annie Hughes, Kathryn Kreckel, J. M. Diederik Kruijssen, Hsi-An Pan, Jérôme Pety, Dragan Salak, Francesco Santoro, Andreas Schruba, Jiayi Sun, Yu-Hsuan Teng, and Thomas Williams (2022). "CI and CO in Nearby Spiral Galaxies – I. Line Ratio and Abundance Variations at $\sim$200 pc Scales." In: *arXiv e-prints*, arXiv:2212.09661, arXiv:2212.09661. arXiv: 2212.09661 [astro-ph.GA] (cited on pages 94, 101).

Tie Liu, Yuefang Wu, and Huawei Zhang (2013). “Gaseous CO Abundance—An Evolutionary Tracer for Molecular Clouds.” In: *ApJL* 775.1, L2, p. L2. DOI: 10.1088/2041-8205/775/1/L2. arXiv: 1306.0046 [astro-ph.SR] (cited on page 67).

S. N. Longmore, J. Bally, L. Testi, C. R. Purcell, A. J. Walsh, E. Bressert, M. Pestalozzi, S. Molinari, J. Ott, L. Cortese, C. Battersby, N. Murray, E. Lee, J. M. D. Kruijssen, E. Schisano, and D. Elia (2013). “Variations in the Galactic star formation rate and density thresholds for star formation.” In: *MNRAS* 429.2, pp. 987–1000. DOI: 10.1093/mnras/sts376. arXiv: 1208.4256 [astro-ph.GA] (cited on pages 37, 42, 56).

Anan Lu, Hope Boyce, Daryl Haggard, Martin Bureau, Fu-Heng Liang, Lijie Liu, Woorak Choi, Michele Cappellari, Laurent Chemin, Mélanie Chevance, Timothy A. Davis, Laurent Drissen, Jacob S. Elford, Jindra Gensior, J. M. Diederik Kruijssen, Thomas Martin, Etienne Massé, Carmelle Robert, Ilaria Ruffa, Laurie Rousseau-Nepton, Marc Sarzi, Gabriel Savard, and Thomas G. Williams (2022). “WISDOM project - XI. Star formation efficiency in the bulge of the AGN-host Galaxy NGC 3169 with SITELLE and ALMA.” In: *MNRAS* 514.4, pp. 5035–5055. DOI: 10.1093/mnras/stac1583. arXiv: 2206.03316 [astro-ph.GA] (cited on page 136).

S. C. Madden, D. Cormier, S. Hony, V. Lebouteiller, N. Abel, M. Galametz, I. De Looze, M. Chevance, F. L. Polles, M. -Y. Lee, F. Galliano, A. Lambert-Huyghe, D. Hu, and L. Ramambason (2020). “Tracing the total molecular gas in galaxies: [CII] and the CO-dark gas.” In: *A&A* 643, A141, A141. DOI: 10.1051/0004-6361/202038860. arXiv: 2009.00649 [astro-ph.GA] (cited on pages 12, 67, 138).

Fumiya Maeda, Fumi Egusa, Kouji Ohta, Yusuke Fujimoto, and Asao Habe (2023). “Statistical Study of the Star Formation Efficiency in Bars: Is Star Formation Suppressed in Gas-rich Bars?” In: *ApJ* 943.1, 7, p. 7. DOI: 10.3847/1538-4357/aca664. arXiv: 2211.15681 [astro-ph.GA] (cited on pages 136, 137).

J. P. McMullin, B. Waters, D. Schiebel, W. Young, and K. Golap (2007). “CASA Architecture and Applications.” In: *Astronomical Data Analysis Software and Systems XVI*. Ed. by R. A. Shaw, F. Hill, and D. J. Bell. Vol. 376. Astronomical Society of the Pacific Conference Series, p. 127 (cited on page 63).

David S. Meier and Jean L. Turner (2004). “Dynamically Influenced Molecular Clouds in the Nucleus of NGC 6946: Variations in the CO Isotopic Line Ratios.” In: *AJ* 127.4, pp. 2069–2084. DOI: 10.1086/382904. arXiv: astro-ph/0401325 [astro-ph] (cited on page 13).

S. N. Milam, C. Savage, M. A. Brewster, L. M. Ziurys, and S. Wyckoff (2005). “The ^{12}C/^{13}C Isotope Gradient Derived from Millimeter Transitions of CN: The Case for Galactic Chemical Evolution.” In: *ApJ* 634.2, pp. 1126–1132. DOI: 10.1086/497123 (cited on pages 5, 14, 37, 92).

Sanghyuk Moon, Woong-Tae Kim, Chang-Goo Kim, and Eve C. Ostriker (2021). “Star Formation in Nuclear Rings with the TIGRESS Framework.” In: *ApJ* 914.1, 9, p. 9. DOI: 10.3847/1538-4357/abfa93. arXiv: 2104.10349 [astro-ph.GA] (cited on pages 156, 165).

Kana Morokuma-Matsui, Kazuo Sorai, Yoshimasa Watanabe, and Nario Kuno (2015). “Stacking analysis of ^{12}CO and ^{13}CO spectra of NGC 3627: Existence of non-optically thick ^{12}CO emission?” In: *PASJ* 67.1, 2, p. 2. DOI: 10.1093/pasj/psu126. arXiv: 1409.7982 [astro-ph.GA] (cited on pages 57, 69).

John Moustakas, Jr. Kennicutt Robert C., Christy A. Tremonti, Daniel A. Dale, John-David T. Smith, and Daniela Calzetti (2010). “Optical Spectroscopy and Nebular Oxygen Abundances of the Spitzer/SINGS Galaxies.” In: *ApJS* 190.2, pp. 233–266. DOI: 10.1088/0067-0049/190/2/233. arXiv: 1007.4547 [astro-ph.CO] (cited on pages 15, 70, 91).

Kazuyuki Muraoka, Kazuo Sorai, Yusuke Miyamoto, Moe Yoda, Kana Morokuma-Matsui, Masato I. N. Kobayashi, Mayu Kuroda, Hiroyuki Kaneko, Nario Kuno, Tsutomu T. Takeuchi, Hiroyuki Nakanishi, Yoshimasa Watanabe, Takahiro Tanaka, Atsushi Yasuda, Yoshiyuki Yajima, Shugo Shibata, Dragan Salak, Daniel Espada, Naoko Matsumoto, Yuto Noma, Shoichiro Kita, Ryusei Komatsuzaki, Ayumi Kajikawa, Yu Yashima, Hsi-An Pan, Nagisa Oi, Masumichi Seta, and Naomasa Nakai (2019). “CO Multi-line Imaging of Nearby Galaxies (COMING). VI. Radial variations in star formation efficiency.” In: *PASJ* 71, S15, S15. DOI: 10.1093/pasj/psz015. arXiv: 1901.11197 [astro-ph.GA] (cited on page 137).

Eric J. Murphy, Dillon Dong, Adam K. Leroy, Emmanuel Momjian, James J. Condon, George Helou, David S. Meier, Jürgen Ott, Eva Schinnerer, and Jean L. Turner (2015). “Microwave Continuum Emission and Dense Gas Tracers in NGC 3627: Combining Jansky VLA and ALMA Observations.” In: *ApJ* 813.2, 118, p. 118. DOI: 10.1088/0004-637X/813/2/118. arXiv: 1508.06284 [astro-ph.GA] (cited on page 74).

Desika Narayanan, Mark Krumholz, Eve C. Ostriker, and Lars Hernquist (2011). “The CO-H_2 conversion factor in disc galaxies and mergers.” In: *MNRAS* 418.1, pp. 664–679. DOI: 10.1111/j.1365-2966.2011.19516.x. arXiv: 1104.4118 [astro-ph.CO] (cited on pages 68, 69).

Desika Narayanan, Mark R. Krumholz, Eve C. Ostriker, and Lars Hernquist (2012). “A general model for the CO-H_2 conversion factor in galaxies with applications to the star formation law.” In: *MNRAS* 421.4, pp. 3127–3146. DOI: 10.1111/j.1365-2966.2012.20536.x. arXiv: 1110.3791 [astro-ph.GA] (cited on pages 8, 12, 67–69, 99, 111, 113, 114, 137, 138, 157, 158).

M. Nimori, A. Habe, K. Sorai, Y. Watanabe, A. Hirota, and D. Namekata (2013). “Dense cloud formation and star formation in a barred galaxy.” In: *MNRAS* 429.3, pp. 2175–

2182. DOI: 10.1093/mnras/sts487. arXiv: 1207.5315 `[astro-ph.GA]` (cited on page 101).

Atsushi Nishimura, Kazuki Tokuda, Kimihiro Kimura, Kazuyuki Muraoka, Hiroyuki Maezawa, Hideo Ogawa, Kazuhito Dobashi, Tomomi Shimoikura, Akira Mizuno, Yasuo Fukui, and Toshikazu Onishi (2015). "Revealing the Physical Properties of Molecular Gas in Orion with a Large-scale Survey in J = 2-1 Lines of ^{12}CO, ^{13}CO, and C^{18}O." In: *ApJS* 216.1, 18, p. 18. DOI: 10.1088/0067-0049/216/1/18. arXiv: 1412.0790 `[astro-ph.GA]` (cited on page 67).

Tomoharu Oka, Tetsuo Hasegawa, Fumio Sato, Masato Tsuboi, Atsushi Miyazaki, and Masahiro Sugimoto (2001). "Statistical Properties of Molecular Clouds in the Galactic Center." In: *ApJ* 562.1, pp. 348–362. DOI: 10.1086/322976 (cited on page 13).

Matthew E. Orr, Christopher C. Hayward, Philip F. Hopkins, T. K. Chan, Claude-André Faucher-Giguère, Robert Feldmann, Dušan Kereš, Norman Murray, and Eliot Quataert (2018). "What FIREs up star formation: the emergence of the Kennicutt-Schmidt law from feedback." In: *MNRAS* 478.3, pp. 3653–3673. DOI: 10.1093/mnras/sty1241. arXiv: 1701.01788 `[astro-ph.GA]` (cited on page 166).

Donald E. Osterbrock and Gary J. Ferland (2006). *Astrophysics of gaseous nebulae and active galactic nuclei*. University Science Books (cited on page 28).

Eve C. Ostriker and Chang-Goo Kim (2022). "Pressure-regulated, Feedback-modulated Star Formation in Disk Galaxies." In: *ApJ* 936.2, 137, p. 137. DOI: 10.3847/1538-4357/ac7de2. arXiv: 2206.00681 `[astro-ph.GA]` (cited on page 166).

Hsi-An Pan and Nario Kuno (2017). "Variation in GMC Association Properties across the Bars, Spiral Arms, Inter-arms, and Circumnuclear Region of M100 (NGC 4321) Extracted from ALMA Observations." In: *ApJ* 839.2, 133, p. 133. DOI: 10.3847/1538-4357/aa60c2. arXiv: 1702.04124 `[astro-ph.GA]` (cited on pages 101, 125).

Padelis P. Papadopoulos, Thomas G. Bisbas, and Zhi-Yu Zhang (2018). "New places and phases of CO-poor/C I-rich molecular gas in the Universe." In: *MNRAS* 478.2, pp. 1716–1725. DOI: 10.1093/mnras/sty1077. arXiv: 1804.09654 `[astro-ph.GA]` (cited on pages 12, 67).

Padelis P. Papadopoulos, Paul van der Werf, E. Xilouris, Kate G. Isaak, and Yu Gao (2012a). "The Molecular Gas in Luminous Infrared Galaxies. II. Extreme Physical Conditions and Their Effects on the X $_{co}$ Factor." In: *ApJ* 751.1, 10, p. 10. DOI: 10.1088/0004-637X/751/1/10. arXiv: 1202.1803 `[astro-ph.CO]` (cited on pages 8, 39, 59, 60, 68, 96, 98, 104, 114, 137).

Padelis P. Papadopoulos, Paul P. van der Werf, E. M. Xilouris, K. G. Isaak, Yu Gao, and S. Mühle (2012b). "The molecular gas in luminous infrared galaxies - I. CO lines, extreme physical conditions and their drivers." In: *MNRAS* 426.4, pp. 2601–2629.

DOI: 10.1111/j.1365-2966.2012.21001.x. arXiv: 1109.4176 [astro-ph.CO] (cited on pages 8, 13).

Camilo H. Peñaloza, Paul C. Clark, Simon C. O. Glover, and Ralf S. Klessen (2018). “CO line ratios in molecular clouds: the impact of environment.” In: *MNRAS* 475.2, pp. 1508–1520. DOI: 10.1093/mnras/stx3263. arXiv: 1711.01221 [astro-ph.GA] (cited on page 69).

Fernando Pérez and Brian E. Granger (2007). “IPython: a System for Interactive Scientific Computing.” In: *Computing in Science and Engineering* 9.3, pp. 21–29. DOI: 10.1109/MCSE.2007.53. URL: http://ipython.org (cited on page 162).

I. Pessa, E. Schinnerer, F. Belfiore, E. Emsellem, A. K. Leroy, A. Schruba, J. M. D. Kruijssen, H. -A. Pan, G. A. Blanc, P. Sanchez-Blazquez, F. Bigiel, M. Chevance, E. Congiu, D. Dale, C. M. Faesi, S. C. O. Glover, K. Grasha, B. Groves, I. Ho, M. Jiménez-Donaire, R. Klessen, K. Kreckel, E. W. Koch, D. Liu, S. Meidt, J. Pety, M. Querejeta, E. Rosolowsky, T. Saito, F. Santoro, J. Sun, A. Usero, E. J. Watkins, and T. G. Williams (2021). “Star formation scaling relations at ∼100 pc from PHANGS: Impact of completeness and spatial scale.” In: *A&A* 650, A134, A134. DOI: 10.1051/0004-6361/202140733. arXiv: 2104.09536 [astro-ph.GA] (cited on pages 3, 68, 137, 166).

Max Pettini and Bernard E. J. Pagel (2004). “[OIII]/[NII] as an abundance indicator at high redshift.” In: *MNRAS* 348.3, pp. L59–L63. DOI: 10.1111/j.1365-2966.2004.07591.x. arXiv: astro-ph/0401128 [astro-ph] (cited on pages 139, 145).

L. S. Pilyugin and E. K. Grebel (2016). “New calibrations for abundance determinations in H II regions.” In: *MNRAS* 457.4, pp. 3678–3692. DOI: 10.1093/mnras/stw238. arXiv: 1601.08217 [astro-ph.GA] (cited on page 145).

Jaime E. Pineda, Paola Caselli, and Alyssa A. Goodman (2008). “CO Isotopologues in the Perseus Molecular Cloud Complex: the X-factor and Regional Variations.” In: *ApJ* 679.1, pp. 481–496. DOI: 10.1086/586883. arXiv: 0802.0708 [astro-ph] (cited on page 12).

Rebecca L. Pitts and Peter J. Barnes (2021). “Census of High- and Medium-mass Protostars. V. CO Abundance and the Galactic X_{CO} Factor.” In: *ApJS* 256.1, 3, p. 3. DOI: 10.3847/1538-4365/ac063d. arXiv: 2106.02047 [astro-ph.GA] (cited on page 138).

Rebecca L. Pitts, Peter J. Barnes, and Frank Varosi (2019). “On the diagnostic power of FIR/sub-mm SED fitting in massive galactic molecular clumps.” In: *MNRAS* 484.1, pp. 305–331. DOI: 10.1093/mnras/sty3360. arXiv: 1810.07708 [astro-ph.GA] (cited on page 100).

Planck Collaboration et al. (2011). “Planck early results. XIX. All-sky temperature and dust optical depth from Planck and IRAS. Constraints on the “dark gas” in our Galaxy.”

In: *A&A* 536, A19, A19. DOI: 10.1051/0004-6361/201116479. arXiv: 1101.2029 [astro-ph.GA] (cited on page 12).

P. Planesas, L. Colina, and D. Perez-Olea (1997). "Circumnuclear molecular gas and star formation in starburst galaxies." In: *A&A* 325, pp. 81–97 (cited on pages 14, 15, 37).

M. Querejeta, E. Schinnerer, S. Meidt, J. Sun, A. K. Leroy, E. Emsellem, R. S. Klessen, J. C. Muñoz-Mateos, H. Salo, E. Laurikainen, I. Bešlić, G. A. Blanc, M. Chevance, D. A. Dale, C. Eibensteiner, C. Faesi, A. García-Rodríguez, S. C. O. Glover, K. Grasha, J. Henshaw, C. Herrera, A. Hughes, K. Kreckel, J. M. D. Kruijssen, D. Liu, E. J. Murphy, H. -A. Pan, J. Pety, A. Razza, E. Rosolowsky, T. Saito, A. Schruba, A. Usero, E. J. Watkins, and T. G. Williams (2021). "Stellar structures, molecular gas, and star formation across the PHANGS sample of nearby galaxies." In: *A&A* 656, A133, A133. DOI: 10.1051/0004-6361/202140695. arXiv: 2109.04491 [astro-ph.GA] (cited on pages 136, 139, 144, 158).

Miguel Querejeta, Jérôme Pety, Andreas Schruba, Adam K. Leroy, Cinthya N. Herrera, I-Da Chiang, Sharon E. Meidt, Erik Rosolowsky, Eva Schinnerer, Karl Schuster, Jiayi Sun, Kimberly A. Herrmann, Ashley T. Barnes, Ivana Bešlić, Frank Bigiel, Yixian Cao, Mélanie Chevance, Cosima Eibensteiner, Eric Emsellem, Christopher M. Faesi, Annie Hughes, Jaeyeon Kim, Ralf S. Klessen, Kathryn Kreckel, J. M. Diederik Kruijssen, Daizhong Liu, Nadine Neumayer, Hsi-An Pan, Toshiki Saito, Karin Sandstrom, Yu-Hsuan Teng, Antonio Usero, Thomas G. Williams, and Antoine Zakardjian (2023). "A sensitive, high-resolution, wide-field IRAM NOEMA CO(1-0) survey of the very nearby spiral galaxy IC 342." In: *A&A* 680, A4, A4. DOI: 10.1051/0004-6361/202143023. arXiv: 2310.06501 [astro-ph.GA] (cited on pages 152, 166).

L. Ramambason, V. Lebouteiller, S. C. Madden, F. Galliano, C. T. Richardson, A. Saintonge, I. De Looze, M. Chevance, N. P. Abel, S. Hernandez, and J. Braine (2023). "Molecular gas distribution and CO-to-H2 conversion factors in CO-faint low-metallicity dwarf galaxies." In: *arXiv e-prints*, arXiv:2306.14881, arXiv:2306.14881. DOI: 10.48550/arXiv.2306.14881. arXiv: 2306.14881 [astro-ph.GA] (cited on page 138).

Michael W. Regan and Peter J. Teuben (2004). "Bar-driven Mass Inflow: How Bar Characteristics Affect the Inflow." In: *ApJ* 600.2, pp. 595–612. DOI: 10.1086/380116 (cited on page 158).

Q. Remy, I. A. Grenier, D. J. Marshall, and J. M. Casandjian (2017). "Cosmic rays, gas and dust in nearby anticentre clouds. I. CO-to-H_2 conversion factors and dust opacities." In: *A&A* 601, A78, A78. DOI: 10.1051/0004-6361/201629632. arXiv: 1703.05237 [astro-ph.HE] (cited on pages 8, 12, 67).

Florent Renaud, Frédéric Bournaud, Emanuele Daddi, and Axel Weiß (2019). "Three regimes of CO emission in galaxy mergers." In: *A&A* 621, A104, A104. DOI: 10.1051/0004-6361/201834397. arXiv: 1811.06547 [astro-ph.GA] (cited on pages 67, 69, 138).

Florent Renaud, Katarina Kraljic, and Frédéric Bournaud (2012). "Star Formation Laws and Thresholds from Interstellar Medium Structure and Turbulence." In: *ApJL* 760.1, L16, p. L16. DOI: 10.1088/2041-8205/760/1/L16. arXiv: 1210.2355 `[astro-ph.CO]` (cited on page 158).

Julia Roman-Duval, Mark Heyer, Christopher M. Brunt, Paul Clark, Ralf Klessen, and Rahul Shetty (2016). "Distribution and Mass of Diffuse and Dense CO Gas in the Milky Way." In: *ApJ* 818.2, 144, p. 144. DOI: 10.3847/0004-637X/818/2/144. arXiv: 1601.00937 `[astro-ph.GA]` (cited on page 105).

Erik Rosolowsky, Annie Hughes, Adam K. Leroy, Jiayi Sun, Miguel Querejeta, Andreas Schruba, Antonio Usero, Cinthya N. Herrera, Daizhong Liu, Jérôme Pety, Toshiki Saito, Ivana Bešlić, Frank Bigiel, Guillermo Blanc, Mélanie Chevance, Daniel A. Dale, Sinan Deger, Christopher M. Faesi, Simon C. O. Glover, Jonathan D. Henshaw, Ralf S. Klessen, J. M. Diederik Kruijssen, Kirsten Larson, Janice Lee, Sharon Meidt, Angus Mok, Eva Schinnerer, David A. Thilker, and Thomas G. Williams (2021). "Giant molecular cloud catalogues for PHANGS-ALMA: methods and initial results." In: *MNRAS* 502.1, pp. 1218–1245. DOI: 10.1093/mnras/stab085. arXiv: 2101.04697 `[astro-ph.GA]` (cited on pages 101, 125, 127, 157).

Amélie Saintonge and Barbara Catinella (2022). "The Cold Interstellar Medium of Galaxies in the Local Universe." In: *ARA&A* 60, pp. 319–361. DOI: 10.1146/annurev-astro-021022-043545. arXiv: 2202.00690 `[astro-ph.GA]` (cited on pages 1, 136).

Amélie Saintonge, Guinevere Kauffmann, Jing Wang, Carsten Kramer, Linda J. Tacconi, Christof Buchbender, Barbara Catinella, Javier Graciá-Carpio, Luca Cortese, Silvia Fabello, Jian Fu, Reinhard Genzel, Riccardo Giovanelli, Qi Guo, Martha P. Haynes, Timothy M. Heckman, Mark R. Krumholz, Jenna Lemonias, Cheng Li, Sean Moran, Nemesio Rodriguez-Fernandez, David Schiminovich, Karl Schuster, and Albrecht Sievers (2011). "COLD GASS, an IRAM legacy survey of molecular gas in massive galaxies - II. The non-universality of the molecular gas depletion time-scale." In: *MNRAS* 415.1, pp. 61–76. DOI: 10.1111/j.1365-2966.2011.18823.x. arXiv: 1104.0019 `[astro-ph.CO]` (cited on pages 136, 160).

Amélie Saintonge, Linda J. Tacconi, Silvia Fabello, Jing Wang, Barbara Catinella, Reinhard Genzel, Javier Graciá-Carpio, Carsten Kramer, Sean Moran, Timothy M. Heckman, David Schiminovich, Karl Schuster, and Stijn Wuyts (2012). "The Impact of Interactions, Bars, Bulges, and Active Galactic Nuclei on Star Formation Efficiency in Local Massive Galaxies." In: *ApJ* 758.2, 73, p. 73. DOI: 10.1088/0004-637X/758/2/73. arXiv: 1209.0476 `[astro-ph.CO]` (cited on pages 136, 158).

K. Sakamoto, S. K. Okumura, S. Ishizuki, and N. Z. Scoville (1999). "Bar-driven Transport of Molecular Gas to Galactic Centers and Its Consequences." In: *ApJ* 525.2, pp. 691–701. DOI: 10.1086/307910. arXiv: astro-ph/9906454 `[astro-ph]` (cited on page 158).

K. M. Sandstrom, A. K. Leroy, F. Walter, A. D. Bolatto, K. V. Croxall, B. T. Draine, C. D. Wilson, M. Wolfire, D. Calzetti, R. C. Kennicutt, G. Aniano, J. Donovan Meyer, A. Usero, F. Bigiel, E. Brinks, W. J. G. de Blok, A. Crocker, D. Dale, C. W. Engelbracht, M. Galametz, B. Groves, L. K. Hunt, J. Koda, K. Kreckel, H. Linz, S. Meidt, E. Pellegrini, H. -W. Rix, H. Roussel, E. Schinnerer, A. Schruba, K. -F. Schuster, R. Skibba, T. van der Laan, P. Appleton, L. Armus, B. Brandl, K. Gordon, J. Hinz, O. Krause, E. Montiel, M. Sauvage, A. Schmiedeke, J. D. T. Smith, and L. Vigroux (2013). “The CO-to-H_2 Conversion Factor and Dust-to-gas Ratio on Kiloparsec Scales in Nearby Galaxies.” In: *ApJ* 777.1, 5, p. 5. DOI: 10.1088/0004-637X/777/1/5. arXiv: 1212.1208 [astro-ph.CO] (cited on pages 2, 8, 13, 15, 48, 49, 58, 62, 67, 69, 95, 102–104, 107, 110, 114, 120, 137, 138).

Francesco Santoro, Kathryn Kreckel, Francesco Belfiore, Brent Groves, Enrico Congiu, David A. Thilker, Guillermo A. Blanc, Eva Schinnerer, I. -Ting Ho, J. M. Diederik Kruijssen, Sharon Meidt, Ralf S. Klessen, Andreas Schruba, Miguel Querejeta, Ismael Pessa, Mélanie Chevance, Jaeyeon Kim, Eric Emsellem, Rebecca McElroy, Ashley T. Barnes, Frank Bigiel, Médéric Boquien, Daniel A. Dale, Simon C. O. Glover, Kathryn Grasha, Janice Lee, Adam K. Leroy, Hsi-An Pan, Erik Rosolowsky, Toshiki Saito, Patricia Sanchez-Blazquez, Elizabeth J. Watkins, and Thomas G. Williams (2022). “PHANGS-MUSE: The H II region luminosity function of local star-forming galaxies.” In: *A&A* 658, A188, A188. DOI: 10.1051/0004-6361/202141907. arXiv: 2111.09362 [astro-ph.GA] (cited on page 70).

Eva Schinnerer, Torsten Böker, Eric Emsellem, and Ute Lisenfeld (2006). “Molecular Gas Dynamics in NGC 6946: A Bar-driven Nuclear Starburst “Caught in the Act”.” In: *ApJ* 649.1, pp. 181–200. DOI: 10.1086/506265. arXiv: astro-ph/0605702 [astro-ph] (cited on page 158).

Maximilien R. P. Schirm, Christine D. Wilson, Tara J. Parkin, Julia Kamenetzky, Jason Glenn, Naseem Rangwala, Luigi Spinoglio, Miguel Pereira-Santaella, Maarten Baes, Michael J. Barlow, Dave L. Clements, Asantha Cooray, Ilse De Looze, Oskar Ł. Karczewski, Suzanne C. Madden, Aurélie Rémy-Ruyer, and Ronin Wu (2014). “Herschel-SPIRE Fourier Transform Spectrometer Observations of Excited CO and [C I] in the Antennae (NGC 4038/39): Warm and Cold Molecular Gas.” In: *ApJ* 781.2, 101, p. 101. DOI: 10.1088/0004-637X/781/2/101. arXiv: 1312.2522 [astro-ph.GA] (cited on page 39).

Maarten Schmidt (1959). “The Rate of Star Formation.” In: *ApJ* 129, p. 243. DOI: 10.1086/146614 (cited on page 2).

F. L. Schöier, F. F. S. van der Tak, E. F. van Dishoeck, and J. H. Black (2005). “An atomic and molecular database for analysis of submillimetre line observations.” In: *A&A* 432.1, pp. 369–379. DOI: 10.1051/0004-6361:20041729. arXiv: astro-ph/0411110 [astro-ph] (cited on pages 16, 27).

Andreas Schruba, J. M. Diederik Kruijssen, and Adam K. Leroy (2019). “How Galactic Environment Affects the Dynamical State of Molecular Clouds and Their Star Formation Efficiency.” In: *ApJ* 883.1, 2, p. 2. DOI: 10.3847/1538-4357/ab3a43. arXiv: 1908.04306 `[astro-ph.GA]` (cited on page 136).

Andreas Schruba, Adam K. Leroy, J. M. Diederik Kruijssen, Frank Bigiel, Alberto D. Bolatto, W. J. G. de Blok, Linda Tacconi, Ewine F. van Dishoeck, and Fabian Walter (2017). “Physical Properties of Molecular Clouds at 2 pc Resolution in the Low-metallicity Dwarf Galaxy NGC 6822 and the Milky Way.” In: *ApJ* 835.2, 278, p. 278. DOI: 10.3847/1538-4357/835/2/278. arXiv: 1701.02748 `[astro-ph.GA]` (cited on page 138).

Andreas Schruba, Adam K. Leroy, Fabian Walter, Frank Bigiel, Elias Brinks, W. J. G. de Blok, Gaelle Dumas, Carsten Kramer, Erik Rosolowsky, Karin Sandstrom, Karl Schuster, Antonio Usero, Axel Weiss, and Helmut Wiesemeyer (2011). “A Molecular Star Formation Law in the Atomic-gas-dominated Regime in Nearby Galaxies.” In: *AJ* 142.2, 37, p. 37. DOI: 10.1088/0004-6256/142/2/37. arXiv: 1105.4605 `[astro-ph.CO]` (cited on pages 2, 26, 52, 56, 68, 81, 136).

Andreas Schruba, Adam K. Leroy, Fabian Walter, Frank Bigiel, Elias Brinks, W. J. G. de Blok, Carsten Kramer, Erik Rosolowsky, Karin Sandstrom, Karl Schuster, Antonio Usero, Axel Weiss, and Helmut Wiesemeyer (2012). “Low CO Luminosities in Dwarf Galaxies.” In: *AJ* 143.6, 138, p. 138. DOI: 10.1088/0004-6256/143/6/138. arXiv: 1203.4231 `[astro-ph.CO]` (cited on pages 12, 68).

N. Z. Scoville, Min Su Yun, D. P. Clemens, D. B. Sanders, and W. H. Waller (1987). “Molecular Clouds and Cloud Cores in the Inner Galaxy.” In: *ApJS* 63, p. 821. DOI: 10.1086/191185 (cited on pages 12, 71).

D. Seifried, S. Haid, S. Walch, E. M. A. Borchert, and T. G. Bisbas (2020). “SILCC-Zoom: H_2 and CO-dark gas in molecular clouds - the impact of feedback and magnetic fields.” In: *MNRAS* 492.1, pp. 1465–1483. DOI: 10.1093/mnras/stz3563. arXiv: 1906.01015 `[astro-ph.GA]` (cited on page 69).

Piyush Sharda, Shyam H. Menon, Christoph Federrath, Mark R. Krumholz, James R. Beattie, Katherine E. Jameson, Kazuki Tokuda, Blakesley Burkhart, Roland M. Crocker, Charles J. Law, Amit Seta, Terrance J. Gaetz, Nickolas M. Pingel, Ivo R. Seitenzahl, Hidetoshi Sano, and Yasuo Fukui (2022). “First extragalactic measurement of the turbulence driving parameter: ALMA observations of the star-forming region N159E in the Large Magellanic Cloud.” In: *MNRAS* 509.2, pp. 2180–2193. DOI: 10.1093/mnras/stab3048. arXiv: 2109.03983 `[astro-ph.GA]` (cited on page 138).

Y. Sheffer, M. Rogers, S. R. Federman, N. P. Abel, R. Gredel, D. L. Lambert, and G. Shaw (2008). “Ultraviolet Survey of CO and H_2 in Diffuse Molecular Clouds: The Reflection of Two Photochemistry Regimes in Abundance Relationships.” In: *ApJ* 687.2, pp. 1075–1106. DOI: 10.1086/59148410.48550/arXiv.0807.0940. arXiv: 0807.0940 [astro-ph] (cited on pages 94, 100).

Kartik Sheth, Stuart N. Vogel, Michael W. Regan, Michele D. Thornley, and Peter J. Teuben (2005). “Secular Evolution via Bar-driven Gas Inflow: Results from BIMA SONG.” In: *ApJ* 632.1, pp. 217–226. DOI: 10.1086/432409. arXiv: astro-ph/0505393 [astro-ph] (cited on page 158).

Rahul Shetty, Simon C. Glover, Cornelis P. Dullemond, and Ralf S. Klessen (2011a). “Modelling CO emission - I. CO as a column density tracer and the X factor in molecular clouds.” In: *MNRAS* 412.3, pp. 1686–1700. DOI: 10.1111/j.1365-2966.2010.18005.x. arXiv: 1011.2019 [astro-ph.GA] (cited on pages 3, 69).

Rahul Shetty, Simon C. Glover, Cornelis P. Dullemond, Eve C. Ostriker, Andrew I. Harris, and Ralf S. Klessen (2011b). “Modelling CO emission - II. The physical characteristics that determine the X factor in Galactic molecular clouds.” In: *MNRAS* 415.4, pp. 3253–3274. DOI: 10.1111/j.1365-2966.2011.18937.x. arXiv: 1104.3695 [astro-ph.GA] (cited on page 69).

Yoshito Shimajiri, Yoshimi Kitamura, Masao Saito, Munetake Momose, Fumitaka Nakamura, Kazuhito Dobashi, Tomomi Shimoikura, Hiroyuki Nishitani, Akifumi Yamabi, Chihomi Hara, Sho Katakura, Takashi Tsukagoshi, Tomohiro Tanaka, and Ryohei Kawabe (2014). “High abundance ratio of ^{13}CO to C^{18}O toward photon-dominated regions in the Orion-A giant molecular cloud.” In: *A&A* 564, A68, A68. DOI: 10.1051/0004-6361/201322912. arXiv: 1403.2930 [astro-ph.GA] (cited on page 14).

Yancy L. Shirley (2015). “The Critical Density and the Effective Excitation Density of Commonly Observed Molecular Dense Gas Tracers.” In: *PASP* 127.949, p. 299. DOI: 10.1086/680342. arXiv: 1501.01629 [astro-ph.IM] (cited on page 16).

Kazimierz Sliwa, Christine D. Wilson, Daisuke Iono, Alison Peck, and Satoki Matsushita (2014). “Around the Ring We Go: The Cold, Dense Ring of Molecular Gas in NGC 1614.” In: *ApJL* 796.1, L15, p. L15. DOI: 10.1088/2041-8205/796/1/L15. arXiv: 1410.6982 [astro-ph.GA] (cited on pages 13, 35, 45, 67, 85, 88, 92, 94, 106).

Kazimierz Sliwa, Christine D. Wilson, Satoki Matsushita, Alison B. Peck, Glen R. Petitpas, Toshiki Saito, and Min Yun (2017). “Luminous Infrared Galaxies with the Submillimeter Array. V. Molecular Gas in Intermediate to Late-stage Mergers.” In: *ApJ* 840.1, 8, p. 8. DOI: 10.3847/1538-4357/aa689b. arXiv: 1703.07121 [astro-ph.GA] (cited on pages 9, 13, 39, 45, 67, 85, 88, 92, 94, 106, 137, 138).

Kazimierz Sliwa, Christine D. Wilson, Glen R. Petitpas, Lee Armus, Mika Juvela, Satoki Matsushita, Alison B. Peck, and Min S. Yun (2012). “Luminous Infrared Galaxies with the Submillimeter Array. III. The Dense Kiloparsec Molecular Concentrations of Arp 299.” In: *ApJ* 753.1, 46, p. 46. DOI: 10.1088/0004-637X/753/1/46. arXiv: 1204.6659 [astro-ph.GA] (cited on pages 44, 106).

Rowan J. Smith, Simon C. O. Glover, Paul C. Clark, Ralf S. Klessen, and Volker Springel (2014). “CO-dark gas and molecular filaments in Milky Way-type galaxies.” In: *MNRAS* 441.2, pp. 1628–1645. DOI: 10.1093/mnras/stu616. arXiv: 1403.1589 `[astro-ph.GA]` (cited on page 100).

Smithsonian Astrophysical Observatory (2000). *SAOImage DS9: A utility for displaying astronomical images in the X11 window environment*. ascl: 0003.002 (cited on pages 63, 123).

V. V. Sobolev (1960). *Moving envelopes of stars*. Harvard University Press (cited on pages 6, 28).

T. J. Sodroski, N. Odegard, E. Dwek, M. G. Hauser, B. A. Franz, I. Freedman, T. Kelsall, W. F. Wall, G. B. Berriman, S. F. Odenwald, C. Bennett, W. T. Reach, and J. L. Weiland (1995). “The Ratio of H 2 Column Density to 12CO Intensity in the Vicinity of the Galactic Center.” In: *ApJ* 452, p. 262. DOI: 10.1086/176297 (cited on page 13).

Ulysses J. Sofia, James T. Lauroesch, David M. Meyer, and Stefan I. B. Cartledge (2004). “Interstellar Carbon in Translucent Sight Lines.” In: *ApJ* 605.1, pp. 272–277. DOI: 10.1086/382592. arXiv: astro-ph/0401510 `[astro-ph]` (cited on page 94).

P. M. Solomon, A. R. Rivolo, J. Barrett, and A. Yahil (1987). “Mass, Luminosity, and Line Width Relations of Galactic Molecular Clouds.” In: *ApJ* 319, p. 730. DOI: 10.1086/165493 (cited on pages 1, 12, 66).

Kazuo Sorai, Nario Kuno, Kohta Nishiyama, Yoshimasa Watanabe, Hidenori Matsui, Asao Habe, Akihiko Hirota, Yuko Ishihara, and Naomasa Nakai (2012). “Properties of Molecular Gas in the Bar of Maffei 2.” In: *PASJ* 64, 51, p. 51. DOI: 10.1093/pasj/64.3.51 (cited on page 101).

Mattia C. Sormani and Ashley T. Barnes (2019). “Mass inflow rate into the Central Molecular Zone: observational determination and evidence of episodic accretion.” In: *MNRAS* 484.1, pp. 1213–1219. DOI: 10.1093/mnras/stz046. arXiv: 1901.00867 `[astro-ph.GA]` (cited on pages 3, 68).

Mattia C. Sormani, Robin G. Tress, Simon C. O. Glover, Ralf S. Klessen, Cara D. Battersby, Paul C. Clark, H. Perry Hatchfield, and Rowan J. Smith (2020). “Simulations of the Milky Way’s Central Molecular Zone - II. Star formation.” In: *MNRAS* 497.4, pp. 5024–5040. DOI: 10.1093/mnras/staa1999. arXiv: 2004.06731 `[astro-ph.GA]` (cited on page 156).

A. W. Strong, I. V. Moskalenko, O. Reimer, S. Digel, and R. Diehl (2004). “The distribution of cosmic-ray sources in the Galaxy, γ-rays and the gradient in the CO-to-H_2 relation.” In: *A&A* 422, pp. L47–L50. DOI: 10.1051/0004-6361:2004017210.48550/arXiv.astro-ph/0405275. arXiv: astro-ph/0405275 `[astro-ph]` (cited on page 95).

Jiayi Sun, Adam K. Leroy, Eve C. Ostriker, Annie Hughes, Erik Rosolowsky, Andreas Schruba, Eva Schinnerer, Guillermo A. Blanc, Christopher Faesi, J. M. Diederik Kruijssen, Sharon Meidt, Dyas Utomo, Frank Bigiel, Alberto D. Bolatto, Mélanie Chevance, I-Da Chiang, Daniel Dale, Eric Emsellem, Simon C. O. Glover, Kathryn Grasha, Jonathan Henshaw, Cinthya N. Herrera, Maria Jesus Jimenez-Donaire, Janice C. Lee, Jérôme Pety, Miguel Querejeta, Toshiki Saito, Karin Sandstrom, and Antonio Usero (2020a). "Dynamical Equilibrium in the Molecular ISM in 28 Nearby Star-forming Galaxies." In: *ApJ* 892.2, 148, p. 148. DOI: 10.3847/1538-4357/ab781c. arXiv: 2002.08964 `[astro-ph.GA]` (cited on pages 68, 72, 149).

Jiayi Sun, Adam K. Leroy, Eve C. Ostriker, Sharon Meidt, Erik Rosolowsky, Eva Schinnerer, Christine D. Wilson, Dyas Utomo, Francesco Belfiore, Guillermo A. Blanc, Eric Emsellem, Christopher Faesi, Brent Groves, Annie Hughes, Eric W. Koch, Kathryn Kreckel, Daizhong Liu, Hsi-An Pan, Jérôme Pety, Miguel Querejeta, Alessandro Razza, Toshiki Saito, Amy Sardone, Antonio Usero, Thomas G. Williams, Frank Bigiel, Alberto D. Bolatto, Mélanie Chevance, Daniel A. Dale, Jindra Gensior, Simon C. O. Glover, Kathryn Grasha, Jonathan D. Henshaw, María J. Jiménez-Donaire, Ralf S. Klessen, J. M. Diederik Kruijssen, Eric J. Murphy, Lukas Neumann, Yu-Hsuan Teng, and David A. Thilker (2023). "Star Formation Laws and Efficiencies across 80 Nearby Galaxies." In: *ApJL* 945.2, L19, p. L19. DOI: 10.3847/2041-8213/acbd9c. arXiv: 2302.12267 `[astro-ph.GA]` (cited on pages 1, 68, 115, 136, 137, 150, 152, 160, 166).

Jiayi Sun, Adam K. Leroy, Erik Rosolowsky, Annie Hughes, Eva Schinnerer, Andreas Schruba, Eric W. Koch, Guillermo A. Blanc, I. -Da Chiang, Brent Groves, Daizhong Liu, Sharon Meidt, Hsi-An Pan, Jérôme Pety, Miguel Querejeta, Toshiki Saito, Karin Sandstrom, Amy Sardone, Antonio Usero, Dyas Utomo, Thomas G. Williams, Ashley T. Barnes, Samantha M. Benincasa, Frank Bigiel, Alberto D. Bolatto, Médéric Boquien, Mélanie Chevance, Daniel A. Dale, Sinan Deger, Eric Emsellem, Simon C. O. Glover, Kathryn Grasha, Jonathan D. Henshaw, Ralf S. Klessen, Kathryn Kreckel, J. M. Diederik Kruijssen, Eve C. Ostriker, and David A. Thilker (2022). "Molecular Cloud Populations in the Context of Their Host Galaxy Environments: A Multiwavelength Perspective." In: *AJ* 164.2, 43, p. 43. DOI: 10.3847/1538-3881/ac74bd. arXiv: 2206.07055 `[astro-ph.GA]` (cited on pages 3, 68, 109, 138, 139, 144, 149–151, 157).

Jiayi Sun, Adam K. Leroy, Eva Schinnerer, Annie Hughes, Erik Rosolowsky, Miguel Querejeta, Andreas Schruba, Daizhong Liu, Toshiki Saito, Cinthya N. Herrera, Christopher Faesi, Antonio Usero, Jérôme Pety, J. M. Diederik Kruijssen, Eve C. Ostriker, Frank Bigiel, Guillermo A. Blanc, Alberto D. Bolatto, Médéric Boquien, Mélanie Chevance, Daniel A. Dale, Sinan Deger, Eric Emsellem, Simon C. O. Glover, Kathryn Grasha, Brent Groves, Jonathan Henshaw, Maria J. Jimenez-Donaire, Jenny J. Kim, Ralf S. Klessen, Kathryn Kreckel, Janice C. Lee, Sharon Meidt, Karin Sandstrom, Amy E. Sardone, Dyas Utomo, and Thomas G. Williams (2020b). "Molecular Gas Properties on Cloud Scales across the Local Star-forming Galaxy Population." In: *ApJL* 901.1, L8, p. L8.

DOI: 10.3847/2041-8213/abb3be. arXiv: 2009.01842 [astro-ph.GA] (cited on pages 2, 3, 21, 58, 68, 108, 110, 155, 157).

Jiayi Sun, Adam K. Leroy, Andreas Schruba, Erik Rosolowsky, Annie Hughes, J. M. Diederik Kruijssen, Sharon Meidt, Eva Schinnerer, Guillermo A. Blanc, Frank Bigiel, Alberto D. Bolatto, Mélanie Chevance, Brent Groves, Cinthya N. Herrera, Alexander P. S. Hygate, Jérôme Pety, Miguel Querejeta, Antonio Usero, and Dyas Utomo (2018). "Cloud-scale Molecular Gas Properties in 15 Nearby Galaxies." In: *ApJ* 860.2, 172, p. 172. DOI: 10.3847/1538-4357/aac326. arXiv: 1805.00937 [astro-ph.GA] (cited on pages 19, 21, 58, 72).

Qing-Hua Tan, Yu Gao, Zhi-Yu Zhang, and Xiao-Yang Xia (2011). "^{12}CO, ^{13}CO and C^{18}O observations along the major axes of nearby bright infrared galaxies." In: *Research in Astronomy and Astrophysics* 11.7, pp. 787–810. DOI: 10.1088/1674-4527/11/7/005. arXiv: 1103.5540 [astro-ph.CO] (cited on page 14).

X. D. Tang, C. Henkel, K. M. Menten, Y. Gong, S. Martín, S. Mühle, S. Aalto, S. Muller, S. García-Burillo, S. Levshakov, R. Aladro, M. Spaans, S. Viti, H. M. Asiri, Y. P. Ao, J. S. Zhang, X. W. Zheng, J. Esimbek, and J. J. Zhou (2019). "ALMA view of the ^{12}C/^{13}C isotopic ratio in starburst galaxies." In: *A&A* 629, A6, A6. DOI: 10.1051/0004-6361/201935603. arXiv: 1906.06638 [astro-ph.GA] (cited on page 92).

Yu-Hsuan Teng (2024). *ElthaTeng/multiline-bayesian-modeling: Multi-line RADEX + Bayesian Modeling Pipeline*. Version v1.0.0. DOI: 10.5281/zenodo.10845936. URL: https://doi.org/10.5281/zenodo.10845936 (cited on pages 7, 163).

Yu-Hsuan Teng, I-Da Chiang, Karin M. Sandstrom, Jiayi Sun, Adam K. Leroy, Alberto D. Bolatto, Antonio Usero, Eve C. Ostriker, Miguel Querejeta, Jérémy Chastenet, Frank Bigiel, Médéric Boquien, Jakob den Brok, Yixian Cao, Mélanie Chevance, Ryan Chown, Dario Colombo, Cosima Eibensteiner, Simon C. O. Glover, Kathryn Grasha, Jonathan D. Henshaw, María J. Jiménez-Donaire, Daizhong Liu, Eric J. Murphy, Hsi-An Pan, Sophia K. Stuber, and Thomas G. Williams (2024). "Star Formation Efficiency in Nearby Galaxies Revealed with a New CO-to-H$_2$ Conversion Factor Prescription." In: *ApJ* 961.1, 42, p. 42. DOI: 10.3847/1538-4357/ad10ae. arXiv: 2310.16037 [astro-ph.GA] (cited on pages 9, 164, 166).

Yu-Hsuan Teng and Naomi Hirano (2020). "Physical Conditions and Kinematics of the Filamentary Structure in Orion Molecular Cloud 1." In: *ApJ* 893.1, 63, p. 63. DOI: 10.3847/1538-4357/ab7cca. arXiv: 2003.02459 [astro-ph.GA] (cited on pages 39, 84).

Yu-Hsuan Teng, Karin M. Sandstrom, Jiayi Sun, Munan Gong, Alberto D. Bolatto, I-Da Chiang, Adam K. Leroy, Antonio Usero, Simon C. O. Glover, Ralf S. Klessen, Daizhong Liu, Miguel Querejeta, Eva Schinnerer, Frank Bigiel, Yixian Cao, Mélanie Chevance, Cosima Eibensteiner, Kathryn Grasha, Frank P. Israel, Eric J. Murphy, Lukas Neumann, Hsi-An Pan, Francesca Pinna, Mattia C. Sormani, J. D. Smith, Fabian Walter, and Thomas G. Williams (2023). “The Physical Drivers and Observational Tracers of CO-to-H_2 Conversion Factor Variations in Nearby Barred Galaxy Centers.” In: *ApJ* 950.2, 119, p. 119. DOI: 10.3847/1538-4357/accb86. arXiv: 2304.04732 [astro-ph.GA] (cited on pages 9, 137, 138, 146, 147, 149–152, 156, 163, 165, 166).

Yu-Hsuan Teng, Karin M. Sandstrom, Jiayi Sun, Adam K. Leroy, L. Clifton Johnson, Alberto D. Bolatto, J. M. Diederik Kruijssen, Andreas Schruba, Antonio Usero, Ashley T. Barnes, Frank Bigiel, Guillermo A. Blanc, Brent Groves, Frank P. Israel, Daizhong Liu, Erik Rosolowsky, Eva Schinnerer, J. D. Smith, and Fabian Walter (2022). “Molecular Gas Properties and CO-to-H_2 Conversion Factors in the Central Kiloparsec of NGC 3351.” In: *ApJ* 925.1, 72, p. 72. DOI: 10.3847/1538-4357/ac382f. arXiv: 2111.05844 [astro-ph.GA] (cited on pages 9, 67, 68, 70–72, 83, 84, 88, 92, 94–99, 101, 103, 104, 107, 116, 119, 120, 129, 130, 137, 138, 151, 156, 163, 166).

A. G. G. M. Tielens (2010). *The Physics and Chemistry of the Interstellar Medium* (cited on page 66).

Aditya Togi and J. D. T. Smith (2016). “Lighting the Dark Molecular Gas: H_2 as a Direct Tracer.” In: *ApJ* 830.1, 18, p. 18. DOI: 10.3847/0004-637X/830/1/18. arXiv: 1607.08036 [astro-ph.GA] (cited on pages 3, 11).

Selçuk Topal, Estelle Bayet, Martin Bureau, Timothy A. Davis, and Wilfred Walsh (2014). “Molecular gas properties of the giant molecular cloud complexes in the arms and inter-arms of the spiral galaxy NGC 6946.” In: *MNRAS* 437.2, pp. 1434–1455. DOI: 10.1093/mnras/stt1976. arXiv: 1310.4493 [astro-ph.CO] (cited on page 39).

Robin G. Tress, Rowan J. Smith, Mattia C. Sormani, Simon C. O. Glover, Ralf S. Klessen, Mordecai-Mark Mac Low, and Paul C. Clark (2020a). “Simulations of the star-forming molecular gas in an interacting M51-like galaxy.” In: *MNRAS* 492.2, pp. 2973–2995. DOI: 10.1093/mnras/stz3600. arXiv: 1909.10520 [astro-ph.GA] (cited on page 156).

Robin G. Tress, Mattia C. Sormani, Simon C. O. Glover, Ralf S. Klessen, Cara D. Battersby, Paul C. Clark, H. Perry Hatchfield, and Rowan J. Smith (2020b). “Simulations of the Milky Way’s central molecular zone - I. Gas dynamics.” In: *MNRAS* 499.3, pp. 4455–4478. DOI: 10.1093/mnras/staa3120. arXiv: 2004.06724 [astro-ph.GA] (cited on page 158).

R. Tunnard and T. R. Greve (2016). “How Dense is Your Gas? On the Recoverability of LVG Model Parameters.” In: *ApJ* 819.2, 161, p. 161. DOI: 10.3847/0004-637X/819/2/161. arXiv: 1602.01095 [astro-ph.GA] (cited on pages 27, 29, 35).

Dyas Utomo, Alberto D. Bolatto, Tony Wong, Eve C. Ostriker, Leo Blitz, Sebastian F. Sanchez, Dario Colombo, Adam K. Leroy, Yixian Cao, Helmut Dannerbauer, Ruben Garcia-Benito, Bernd Husemann, Veselina Kalinova, Rebecca C. Levy, Damian Mast, Erik

Rosolowsky, and Stuart N. Vogel (2017). “The EDGE-CALIFA Survey: Variations in the Molecular Gas Depletion Time in Local Galaxies.” In: *ApJ* 849.1, 26, p. 26. DOI: 10.3847/1538-4357/aa88c0. arXiv: 1704.03481 `[astro-ph.GA]` (cited on pages 1, 136, 137).

F. F. S. van der Tak, J. H. Black, F. L. Schöier, D. J. Jansen, and E. F. van Dishoeck (2007). “A computer program for fast non-LTE analysis of interstellar line spectra. With diagnostic plots to interpret observed line intensity ratios.” In: *A&A* 468.2, pp. 627–635. DOI: 10.1051/0004-6361:20066820. arXiv: 0704.0155 `[astro-ph]` (cited on pages 6, 26, 63, 83, 84, 124).

Vicente Villanueva, Alberto D. Bolatto, Stuart Vogel, Tobias Brown, Christine D. Wilson, Nikki Zabel, Sara Ellison, Adam R. H. Stevens, María Jesús Jiménez Donaire, Kristine Spekkens, Mallory Tharp, Timothy A. Davis, Laura C. Parker, Ian D. Roberts, Dhruv Basra, Alessandro Boselli, Barbara Catinella, Aeree Chung, Luca Cortese, Bumhyun Lee, and Adam Watts (2022). “VERTICO. IV. Environmental Effects on the Gas Distribution and Star Formation Efficiency of Virgo Cluster Spirals.” In: *ApJ* 940.2, 176, p. 176. DOI: 10.3847/1538-4357/ac9d3c. arXiv: 2210.05381 `[astro-ph.GA]` (cited on page 136).

Pauli Virtanen, Ralf Gommers, Travis E. Oliphant, Matt Haberland, Tyler Reddy, David Cournapeau, Evgeni Burovski, Pearu Peterson, Warren Weckesser, Jonathan Bright, Stéfan J. van der Walt, Matthew Brett, Joshua Wilson, K. Jarrod Millman, Nikolay Mayorov, Andrew R. J. Nelson, Eric Jones, Robert Kern, Eric Larson, CJ Carey, İlhan Polat, Yu Feng, Eric W. Moore, Jake Vand erPlas, Denis Laxalde, Josef Perktold, Robert Cimrman, Ian Henriksen, E. A. Quintero, Charles R Harris, Anne M. Archibald, Antônio H. Ribeiro, Fabian Pedregosa, Paul van Mulbregt, and SciPy 1.0 Contributors (2020). “SciPy 1.0: Fundamental Algorithms for Scientific Computing in Python.” In: *Nature Methods* 17, pp. 261–272. DOI: https://doi.org/10.1038/s41592-019-0686-2 (cited on pages 63, 123, 162).

Keiichi Wada and Asao Habe (1995). “Bar-driven fuelling to a galactic central region in a massive gas disc.” In: *MNRAS* 277.2, pp. 433–444. DOI: 10.1093/mnras/277.2.433. arXiv: astro-ph/9506056 `[astro-ph]` (cited on page 158).

John S. Ward, Jonas Zmuidzinas, Andrew I. Harris, and Kate G. Isaak (2003). “A ^{12}CO J=6-5 Map of M82: The Significance of Warm Molecular Gas.” In: *ApJ* 587.1, pp. 171–185. DOI: 10.1086/368175 (cited on pages 35, 44, 85).

Y. Watanabe, K. Sorai, N. Kuno, and A. Habe (2011). “Refined molecular gas mass and star-formation efficiency in NGC 3627.” In: *MNRAS* 411.3, pp. 1409–1417. DOI: 10.1111/j.1365-2966.2010.17746.x (cited on pages 12, 74, 83).

Thomas G. Williams, Martin Bureau, Timothy A. Davis, Michele Cappellari, Woorak Choi, Jacob S. Elford, Satoru Iguchi, Jindra Gensior, Fu-Heng Liang, Anan Lu, Ilaria Ruffa, and Hengyue Zhang (2023). “WISDOM Project - XVII. Beam-by-beam properties of the molecular gas in early-type galaxies." In: *MNRAS* 525.3, pp. 4270–4298. DOI: 10.1093/mnras/stad2455. arXiv: 2308.05146 `[astro-ph.GA]` (cited on page 138).

Thomas G. Williams, Kathryn Kreckel, Francesco Belfiore, Brent Groves, Karin Sandstrom, Francesco Santoro, Guillermo A. Blanc, Frank Bigiel, Médéric Boquien, Mélanie Chevance, Enrico Congiu, Eric Emsellem, Simon C. O. Glover, Kathryn Grasha, Ralf S. Klessen, Eric Koch, J. M. Diederik Kruijssen, Adam K. Leroy, Daizhong Liu, Sharon Meidt, Hsi-An Pan, Miguel Querejeta, Erik Rosolowsky, Toshiki Saito, Patricia Sánchez-Blázquez, Eva Schinnerer, Andreas Schruba, and Elizabeth J. Watkins (2022). "The 2D metallicity distribution and mixing scales of nearby galaxies." In: *MNRAS* 509.1, pp. 1303–1322. DOI: 10.1093/mnras/stab3082. arXiv: 2110.10697 `[astro-ph.GA]` (cited on page 70).

Christine D. Wilson, Bruce G. Elmegreen, Ashley Bemis, and Nathan Brunetti (2019). "The Kennicutt-Schmidt Law and Gas Scale Height in Luminous and Ultraluminous Infrared Galaxies." In: *ApJ* 882.1, 5, p. 5. DOI: 10.3847/1538-4357/ab31f3. arXiv: 1907.05432 `[astro-ph.GA]` (cited on pages 151, 166).

T. L. Wilson and R. Rood (1994). "Abundances in the Interstellar Medium." In: *ARA&A* 32, pp. 191–226. DOI: 10.1146/annurev.aa.32.090194.001203 (cited on pages 5, 37, 92).

Mark G. Wolfire, David Hollenbach, and Christopher F. McKee (2010). "The Dark Molecular Gas." In: *ApJ* 716.2, pp. 1191–1207. DOI: 10.1088/0004-637X/716/2/1191. arXiv: 1004.5401 `[astro-ph.GA]` (cited on pages 12, 67).

J. G. A. Wouterloot, C. Henkel, J. Brand, and G. R. Davis (2008). "Galactic interstellar ^{18}O/{Î7}O ratios - a radial gradient?" In: *A&A* 487.1, pp. 237–246. DOI: 10.1051/0004-6361:20078156. arXiv: 0805.3399 `[astro-ph]` (cited on pages 14, 37).

E. L. Wright, P. R. M. Eisenhardt, A. K. Mainzer, M. E. Ressler, R. M. Cutri, T. Jarrett, J. D. Kirkpatrick, D. Padgett, R. S. McMillan, M. Skrutskie, S. A. Stanford, M. Cohen, R. G. Walker, J. C. Mather, D. Leisawitz, T. N. Gautier III, I. McLean, D. Benford, C. J. Lonsdale, A. Blain, B. Mendez, W. R. Irace, V. Duval, F. Liu, D. Royer, I. Heinrichsen, J. Howard, M. Shannon, M. Kendall, A. L. Walsh, M. Larsen, J. G. Cardon, S. Schick, M. Schwalm, M. Abid, B. Fabinsky, L. Naes, and C.-W. Tsai (2010). "The Wide-field Infrared Survey Explorer (WISE): Mission Description and Initial On-orbit Performance." In: *AJ* 140, 1868, pp. 1868–1881. DOI: 10.1088/0004-6256/140/6/1868. arXiv: 1008.0031 `[astro-ph.IM]` (cited on page 161).

Yoshiyuki Yajima, Kazuo Sorai, Yusuke Miyamoto, Kazuyuki Muraoka, Nario Kuno, Hiroyuki Kaneko, Tsutomu T. Takeuchi, Atsushi Yasuda, Takahiro Tanaka, Kana Morokuma-Matsui, and Masato I. N. Kobayashi (2021). "CO Multi-line Imaging of Nearby Galaxies (COMING). IX. ^{12}CO(J = 2-1)/^{12}CO(J = 1-0) line ratio on kiloparsec scales." In: *PASJ* 73.2, pp. 257–285. DOI: 10.1093/pasj/psaa119. arXiv: 2012.08523 `[astro-ph.GA]` (cited on pages 49, 81).

Y. T. Yan, C. Henkel, C. Kobayashi, K. M. Menten, Y. Gong, J. S. Zhang, H. Z. Yu, K. Yang, J. J. Xie, and Y. X. Wang (2023). "Direct measurements of carbon and sulfur isotope ratios in the Milky Way." In: *A&A* 670, A98, A98. DOI: 10.1051/0004-6361/202244584. arXiv: 2212.03252 `[astro-ph.GA]` (cited on page 92).

Benhui Yang, P. C. Stancil, N. Balakrishnan, and R. C. Forrey (2010). "Rotational Quenching of CO due to H_2 Collisions." In: *ApJ* 718.2, pp. 1062–1069. DOI: 10.1088/0004-637X/718/2/1062. arXiv: 1004.3923 `[astro-ph.SR]` (cited on page 27).

Atsushi Yasuda, Nario Kuno, Kazuo Sorai, Kazuyuki Muraoka, Yusuke Miyamoto, Hiroyuki Kaneko, Yoshiyuki Yajima, Takahiro Tanaka, Kana Morokuma-Matsui, Tsutomu T. Takeuchi, and Masato I. N. Kobayashi (2023). "CO multi-line imaging of nearby galaxies (COMING). XII. CO-to-H_2 conversion factor and dust-to-gas ratio." In: *PASJ* 75.4, pp. 743–786. DOI: 10.1093/pasj/psad034. arXiv: 2305.07827 `[astro-ph.GA]` (cited on page 138).

Kijeong Yim, Tony Wong, Rui Xue, Richard J. Rand, Erik Rosolowsky, J. M. van der Hulst, Robert Benjamin, and Eric J. Murphy (2014). "The Interstellar Medium and Star Formation in Edge-On Galaxies. II. NGC 4157, 4565, and 5907." In: *AJ* 148.6, 127, p. 127. DOI: 10.1088/0004-6256/148/6/127. arXiv: 1408.5905 `[astro-ph.GA]` (cited on pages 35, 85).

Lisa M. Young, David S. Meier, Martin Bureau, Alison Crocker, Timothy A. Davis, and Selçuk Topal (2021). "The Evolution of NGC 7465 as Revealed by Its Molecular Gas Properties." In: *ApJ* 909.2, 98, p. 98. DOI: 10.3847/1538-4357/abe126. arXiv: 2101.11652 `[astro-ph.GA]` (cited on page 57).

Lisa M. Young, David S. Meier, Alison Crocker, Timothy A. Davis, and Selçuk Topal (2022). "Down but Not Out: Properties of the Molecular Gas in the Stripped Virgo Cluster Early-type Galaxy NGC 4526." In: *ApJ* 933.1, 90, p. 90. DOI: 10.3847/1538-4357/ac7149. arXiv: 2204.02382 `[astro-ph.GA]` (cited on page 7).

Yuxuan Yuan, Mark R. Krumholz, and Blakesley Burkhart (2020). "Understanding biases in measurements of molecular cloud kinematics using line emission." In: *MNRAS* 498.2, pp. 2440–2455. DOI: 10.1093/mnras/staa2432. arXiv: 2007.13488 `[astro-ph.GA]` (cited on page 151).